

BOJANA OBRADOVIĆ

Cell and Tissue Engineering



Springer

ACADEMIC MIND

University of Belgrade - Faculty of Technology and Metallurgy
Beograd, 2011.

Redactor
Bojana Obradović, Ph. D.

Cell and Tissue Engineering

 Springer

ACADEMIC MIND
University of Belgrade - Faculty of Technology and Metallurgy

CELL AND TISSUE ENGINEERING

Redactor

Bojana Obradović, Ph. D.

University of Belgrade, Faculty of Technology and Metallurgy

Reviewers

Dijana Bugarski, Ph. D.

University of Belgrade, Institute for Medical Research

Ljiljana Mojović, Ph. D.

University of Belgrade, Faculty of Technology and Metallurgy

© 2012

ACADEMIC MIND, Belgrade, Serbia

UNIVERSITY OF BELGRADE, Faculty of Technology and Metallurgy

SPRINGER-VERLAG, Berlin Heidelberg, Germany

Design of cover page

Zorica Marković, Academic Painter

Printed in Serbia by

Planeta print, Belgrade

Circulation

300 copies

ISBN 978-86-7466-408-7

ISBN 978-3-642-21912-2

NOTICE: No part of this publication may be reproduced, stored in a retrieval system, or transmitted in any form or by any means, electronic, mechanical, photocopying, recording or otherwise, without the prior written permission of the publishers. All rights reserved by the publishers.

Authors

Narine Sarvazyan, Ph.D., Associate Professor, Pharmacology and Physiology Department, The George Washington University, USA

Djuro Koruga, Ph.D., Djuro Koruga, Ph.D., Professor, Faculty of Mechanical Engineering, University of Belgrade, Serbia

Dr Aleksandar Jeremić, Department of Physiology, Wayne State University School of Medicine, USA

Bhanu P. Jena, Ph.D., Professor, Department of Physiology/ NanoBioScience Institute, Wayne State University School of Medicine, USA

Srboljub M. Mijailovich, Sc.D., Harvard School of Public Health, Harvard University, USA

Dimitrije Stamenović, Ph.D., Associate Professor, Department of Biomedical Engineering, Boston University, USA

Ilka Bischofs-Pfeifer, Ph.D., Department of Bioengineering, University of California Berkeley, USA

Konstantinos A. Lazopoulos, Ph.D., Associate Professor, School of Applied Sciences (SEMFE), National Technical University of Athens, Greece

Béla Suki, Ph.D., Professor, Department of Biomedical Engineering, Boston University, USA

Erzsébet Bartolák-Suki, M.D., CelluTraf Sci, Boston, USA

Biancamaria Baroli, Ph.D., Assistant Professor, Faculty of Pharmacy, University of Cagliari, Italy

Warren L. Grayson, Ph.D., Professor, Department of Biomedical Engineering, Columbia University, USA

Gordana Vunjak-Novaković, Ph.D., Professor, Department of Biomedical Engineering, Columbia University, USA

Bojana Obradović, Ph.D., Associate Professor, Faculty of Technology and Metallurgy, University of Belgrade, Serbia

Adrian Neagu, PhD, Associate Professor, Department of Biophysics and Medical Informatics, Victor Babes University of Medicine and Pharmacy Timisoara, Romania; Adjunct Professor, Department of Physics and Astronomy, University of Missouri-Columbia, USA

Ioan Kosztin, PhD, Associate Professor, Department of Physics and Astronomy, University of Missouri-Columbia, USA

Karoly Jakab, Ph.D., Department of Physics and Astronomy, University of Missouri-Columbia, USA

Bogdan Barz, Department of Physics and Astronomy, University of Missouri-Columbia, USA

Monica Neagu, Ph.D., Department of Biophysics and Medical Informatics, Victor Babeş University of Medicine and Pharmacy Timișoara, Romania

Richard Jamison, Department of Physics and Astronomy, University of Missouri-Columbia, USA

Gabor Forgacs, Ph.D., Professor, Department of Physics and Astronomy and Department of Biology, University of Missouri-Columbia, USA

PREFACE

Cell and tissue engineering are multidisciplinary fields with two primary goals: understanding fundamental principles of cell and tissue structure and function, and development of new therapeutic options to address the clinical problem of tissue failure. Over the past two decades there was a tremendous progress in these fields based on advances in molecular biology, biochemistry, medicine and pharmacy as well as in material science and engineering disciplines. Due to the large volume of literature published in these fields, there is a need for apt organization of acquired knowledge to provide resources and assistance for different audiences.

The book *Cell and Tissue Engineering* was inspired by the talks presented at the International Summer School in Cell and Tissue Engineering held at the Faculty of Technology and Metallurgy, University of Belgrade, July 1-8, 2006. Graduate students of engineering and life sciences from many different countries were introduced to the principals and new approaches in cell and tissue engineering. The book contains selected lectures presented at the School, adapted to include both the fundamentals and the current trends in cell and tissue engineering, in a way useful both to a novice and an expert in the field. We expect that it will also be used as a textbook or complementary reading in biomedical engineering courses.

The book is composed of 13 chapters all of which are written by the leading experts. It is organized to gradually assemble an insight in cell and tissue function starting from a molecular (nano) level, extending to a cellular (micro) level and finishing at the tissue (macro) level. In specific, biological, physiological, biophysical, biochemical, medical, and engineering aspects are covered from the standpoint of the development of functional substitutes of biological tissues for potential clinical use. Topics in the area of cell engineering include cell membrane biophysics, structure and function of the cytoskeleton, cell-extracellular matrix interactions, and mechanotransduction. In the area of tissue engineering the focus is on the *in vitro* cultivation of functional tissue equivalents based on the integrated use of isolated cells, biomaterials, and bioreactors. The book also reviews novel techniques for cell and tissue imaging and characterization, some of which are described in detail such as atomic force microscopy.

Mathematical modeling methods are also presented as valuable and indispensable tools in cell and tissue engineering. Numerous illustrations enhance the quality and ease of use of the presented material.

We hope that the book Cell and Tissue Engineering will be valuable for academic and scientific communities especially in the Western Balkan region as one of the few books in these fields providing a resource and stimulus for biomedical engineering research and education.

Bojana Obradović

CONTENTS

1. CREATION OF LIVING TISSUE: AN ENGINEERING FEAT	1
1.1. OPTIONS ON THE TABLE	1
1.2. COMPLEXITY OF BIOLOGICAL ORGANS	2
1.3. SIZING UP THE CHALLENGE.....	4
1.4. TISSUE ENGINEERING	6
2. CLASSICAL AND QUANTUM INFORMATION PROCESSING IN DNA-PROTEIN CODING.....	9
2.1. INTRODUCTION	9
2.2 BASIC FACTS	11
2.3. DNA-PROTEIN SYSTEM MODELING.....	13
2.3.1. Energy approach.....	13
2.3.2. Information approach	14
2.3.3. Synergy approach.....	16
2.4 HOW DOES THE DNA-PROTEIN INFORMATION SYSTEM WORK?.....	17
2.4.1. New considerations in mechanisms of DNA action.....	17
2.4.2. Hydrogen bonds as a central enigma of life	18
2.4.3. Synergy of classical and quantum information	19
2.4.4. Violation of the synergetic DNA-protein information channel and cancer	21
2.5. SUMMARY	23
3. UNRAVELING THE MEMBRANE FUSION IN SECRETORY CELLS AT THE NM-LEVEL: A NANOBIOENGINEERING APPROACH.....	27
3.1. INTRODUCTION	27
3.2. POROSOME: A NEW CELLULAR STRUCTURE	30
3.3. POROSOME: ISOLATION AND RECONSTITUTION.....	34
3.4. SNARE-INDUCED MEMBRANE FUSION	37
3.5. REGULATION OF SECRETORY VESICLE SWELLING: INVOLVEMENT IN EXPULSION OF VESICULAR CONTENTS	39
3.6. MOLECULAR UNDERSTANDING OF CELL SECRETION	40
4. BIOPHYSICAL AND BIOCHEMICAL DETERMINANTS OF CONTRACTILE FORCE GENERATION, REGULATION, AND FUNCTION.....	44
4.1. THE FUNDAMENTAL PROBLEM OF MUSCLE CONTRACTION	44
4.1.1 Structure of skeletal muscle	44
4.1.2. What makes muscles shorten?.....	46
4.1.3. The cross-bridge cycle.....	47
4.1.4. Swinging lever arm and power stroke	49
4.1.5. Atomic structures of actin and myosin	50
4.2. BUILDING A COMPREHENSIVE MODEL OF MUSCLE CONTRACTION	51
4.2.1. What is the appropriate model to start with?.....	52
4.2.2 Energy landscape of myosin binding to actin.....	53
4.2.3. Extensibility of actin and myosin filaments	54
4.2.4. Calcium regulation	55
4.3 MATHEMATICAL FOUNDATIONS OF SLIDING FILAMENT THEORY AND COMPUTATIONAL METHODS THEORETICAL MODELS OF MUSCLE CONTRACTION.....	57
4.3.1. Basic concepts and definitions	57

4.3.2. A probabilistic formulation of cross-bridge kinetics	58
4.3.3. Rules for strain-dependent cross-bridge transition rates	60
4.3.4. Stochastic strain dependent binding in 3D sarcomere lattice	62
4.3.5. Probabilistic and stochastic numerical solutions	62
4.4. THEORETICAL MODELS OF MUSCLE CONTRACTION	63
4.4.1 Huxley's sliding filament model in extensible filament lattice	63
4.4.2. Stochastic strain dependent binding in 3D sarcomere lattice	69
4.4.3. Thin filament regulation in skeletal muscle	72
4.4.4. The latch regulatory scheme in smooth muscle.....	79
5. CYTOSKELETAL PRESTRESS AS A DETERMINANT OF DEFORMABILITY AND RHEOLOGY OF ADHERENT CELLS	92
5.1. INTRODUCTION	92
5.2. WHAT IS PRESTRESS?	93
5.3. STATICS: PRESTRESS AND CELL DEFORMABILITY	94
5.3.1. Measurements of cytoskeletal prestress and stiffness	96
5.3.1.1. <i>Traction Microscopy</i>	96
5.3.1.2. <i>Magnetic Twisting Cytometry</i>	97
5.3.2. Modeling of the steady-state mechanical behavior of the CSK.....	98
5.3.2.2. <i>Prestress induced stiffness of the CSK</i>	101
5.4. DYNAMICS: PRESTRESS AND CELL RHEOLOGY	103
5.4.1. Mechanisms that link cytoskeletal prestress to rheology	106
5.4.1.1. <i>Tensegrity and cytoskeletal rheology</i>	106
5.4.1.2. <i>Myosin cross-bridge kinetics</i>	108
5.4.1.3. <i>Cytoskeletal remodeling</i>	108
5.4.1.4. <i>Activation energy</i>	108
5.4.1.5. <i>Actin network dynamics</i>	109
5.4.1.6. <i>Dynamics of individual polymer chains under sustained tension</i>	110
5.5. CONCLUSIONS.....	113
6. CELL AND TISSUE ORGANIZATION IN SOFT MATERIALS: INSIGHT FROM MATHEMATICAL AND BIOPHYSICAL MODELLING.....	119
6.1. INTRODUCTION	119
6.1.1. Overview of cell and tissue organization principles for adherent cells	119
6.1.2. Classification of mechanical signals and biological responses	120
6.1.3. Effect of substrate mechanics on cell behavior	121
6.1.4. Sensing substrate mechanics: Active mechanosensing	121
6.2. A PRIMER ON ELASTICITY THEORY	123
6.3. TOWARDS A SYSTEM UNDERSTANDING OF THE INFLUENCE OF SUBSTRATE MECHANICS ON CELL AND TISSUE ORGANIZATION	125
6.3.1. Modeling cellular scale effects.....	125
6.3.2. Modeling tissue scale effects.....	128
6.3.3. Modeling subcellular scale effects	130
6.4. OUTLOOK.....	132
7. SUBSTRATE STRETCHING AND ORIENTATION OF ACTIVE CELLS AS A STABILITY PROBLEM.....	135
7.1. INTRODUCTION	135
7.2. MECHANICS PRELIMINARIES.....	139
7.3. THE NONLINEAR HOMOGENEOUS STRAIN FIELD OF A STRESS FIBER	142
7.4. THE EQUILIBRIUM PLACEMENTS OF THE STRESS-FIBERS.....	145
7.5. GLOBALLY STABLE EQUILIBRIUM PLACEMENTS.....	148

7.6. APPLICATIONS	151
7.7. DISCUSSION	152
8. ROLES OF MECHANICAL FORCES AND EXTRACELLULAR MATRIX PROPERTIES IN CELLULAR SIGNALING IN THE LUNG.....	158
8.1. INTRODUCTION	158
8.2. MAIN CONSTITUENTS OF THE LUNG CONNECTIVE TISSUE.....	160
8.2.1. Properties of collagens	160
8.2.2. Properties of elastic fibers	161
8.2.3. Properties of proteoglycans	161
8.2.4. Interstitial cells	162
8.2.5. Air-liquid interface and surface tension	163
8.2.6. Interaction among the tissue components.....	163
8.3. MECHANICAL PROPERTIES OF THE NORMAL LUNG.....	164
8.3.1. Molecular, fibril and fiber elasticity	164
8.3.2. Elasticity of lung collagen, alveolar wall, tissue strip and whole lung.....	166
8.4. EFFECTS OF MECHANICAL FORCES ON THE LUNG PARENCHYMA	168
8.4.1. Mechanical forces, cell signaling and biomechanical properties of the ECM....	168
8.4.2. Mechanical forces in the diseased lung	170
8.5. SUMMARY	172
9. ENZYME SIGNALING: IMPLICATIONS FOR TISSUE ENGINEERING.....	179
9.1. INTRODUCTION	180
9.2. GENERAL PROPERTIES OF ENZYMES.....	181
9.3. METALLOPROTEINASES IN SIGNALING	183
9.3.1. MMPs in diseases.....	183
9.3.2. Types and Structure of MMPs.....	184
9.3.3. Activation and inhibition of MMPs.....	187
9.3.4. Pharmacological manipulations of MMPs	188
9.4. GENERAL CONSIDERATIONS FOR TISSUE ENGINEERING	190
10. HYDROGELS IN TISSUE ENGINEERING	197
10.1. INTRODUCTION	197
10.2. WHAT IS A HYDROGEL?.....	199
10.3. METHODS OF PREPARATION	200
10.3.1. Chemical hydrogel preparation	200
10.3.2. Physical hydrogel preparation	201
10.3.2.1. Hydrogels obtained by ionic interactions.....	202
10.3.2.2. Hydrogels obtained by crystallization	202
10.3.2.3. Hydrogels obtained from amphiphilic block and graft co-polymers	203
10.3.2.4. Hydrogels obtained by hydrogen bond interactions	204
10.3.2.5. Hydrogels obtained by protein interactions	204
10.4. HYDROGEL PROPERTIES	205
10.4.1. Swelling.....	205
10.4.2. Responsive hydrogels.....	206
10.4.3. Surface properties.....	207
10.4.4. Degradability	208
10.5. METHODS OF CHARACTERIZATION	208
10.6. BIOMEDICAL / TISSUE ENGINEERING APPLICATIONS.....	209
11. BIOREACTORS IN TISSUE ENGINEERING	217
11.1. INTRODUCTION: WHAT ARE TISSUE-ENGINEERING BIOREACTORS?..	217
11.2. MASS TRANSPORT CONSIDERATIONS	218

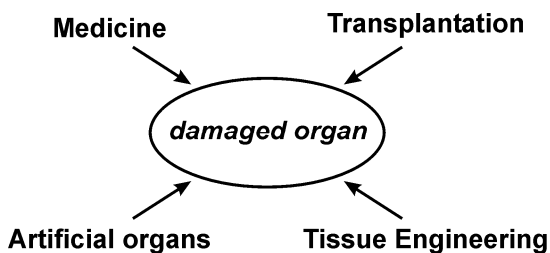
11.3. BIOPHYSICAL REGULATION.....	219
11.3.1. Engineered Bone	219
11.3.2. Engineered Cartilage	221
11.3.3. Engineered Myocardium	223
11.4. SUMMARY	223
12. APPROACHES TO MATHEMATICAL MODELING OF TISSUE ENGINEERING SYSTEMS	228
12.1. INTRODUCTION	228
12.2. CHARACTERIZATION OF IN VITRO CULTIVATING CONDITIONS.....	231
12.2.1. Hydrodynamic environment.....	232
12.2.2. Modeling of mass transfer.....	234
12.2.2.1. <i>Mass transport through the tissue by diffusion</i>	234
12.2.2.2. <i>Enhancement of mass transport through the tissue by convection</i>	239
12.3. CORRELATIONS OF CULTIVATING CONDITIONS WITH THE CELL RESPONSE AND TISSUE PROPERTIES	242
12.3.1. Correlations of hydrodynamic conditions with the tissue growth	242
12.3.2. Mathematical model of GAG accumulation in engineered cartilage constructs.....	244
12.4. CONCLUSION	247
13. COMPUTATIONAL MODELING OF TISSUE SELF-ASSEMBLY.....	251
13.1. THE MODELING APPROACH TO MORPHOGENESIS	251
13.2. IN SILICO TISSUE ENGINEERING	253
13.3. A LATTICE MODEL OF LIVING TISSUES.....	254
13.4. MONTE CARLO SIMULATIONS OF THE SELF -ASSEMBLY OF LIVING CELLS	258
Index.....	273

CREATION OF LIVING TISSUE: AN ENGINEERING FEAT

Narine Sarvazyan*

1.1. OPTIONS ON THE TABLE

The main purpose of tissue engineering is to repair a damaged organ or its part. However, it is only one of the four options to do so (Fig.1.1). The others include pharmacological treatment, replacement with transplant or implantation of an artificial organ. What are the advantages or disadvantages of tissue engineering as compared to these three alternatives approaches? Let's start with medicine. It is the most common way to treat an ailing person and the one which takes most of the healthcare R&D budget. With few exceptions, however, pharmacological treatments are aimed at reversibly damaged tissues. Tissues that have lost their functional



or structural integrity are not amenable to drug-mediated therapies, leaving standard medicine powerless against diseases in late stages or severe cases.

Figure 1.1. Why tissue engineering?

The second option is organ transplantation. Attempts to replace organs can be traced all way back to 1000 BC when American Indians performed successful nose transplants. Today essentially all organs, with the

* Pharmacology and Physiology Department, The George Washington University, Washington, DC, U.S.A.

exception of the brain, have been successfully transplanted from one human being to another. However, the demand far exceeds the supply: a rough estimate for the annual need of an organ replacement is around 10% of the general population (this includes all types of tissue grafts including dental, blood, skin and others). At the same time the number of available organs from human donors is extremely limited. In addition to the inherent availability problem, organ transplantation is associated with immunorejection and side-effects of immunosuppressants.

The third option noted in Fig.1.1 is the creation of artificial organs. Not long ago, it was considered to be an easily achievable goal. Indeed, we are living in the 21st century, when people inhabit space stations, nanoscale robots and 200-story buildings are commonplace, and gigabits of information can be packed into a tiny iPOD. Did you ever wonder why, with all the advances in physical and material sciences, scientists can't simply engineer a small filtering device (i.e., kidney) or a low pressure fluid pump (i.e., heart)?

In fact, they did try. The first artificial heart called Jarvik-7 was tested in the early eighties, but it was soon banned due to low life expectancy (6 months). On July 2, 2001, after nearly three decades of research, an artificial heart of a different design was implanted in a patient. Despite the device cost (\$100K) and all of the efforts which were spent on its development, the recipients of the AbioCor heart have lived an average of only 5 months after the operation. In September of 2006, under the Humanitarian Device Exemption, the FDA has approved the use of AbioCor for end-stage heart failure patients whose other treatment options have been exhausted. It is clear, however, that an artificial heart as a mainstream treatment or a long-term solution remains an elusive goal.

There are two main reasons why, with few notable exceptions (i.e., prosthetics), the use of artificial organs still eludes us. The first reason is that when an artificial device is placed into a living person, it changes the way the body responds to a variety of stressors. The resulting diffuse inflammatory reaction increases the likelihood of clot formation, leading to deadly outcomes such as infarct or stroke. The second reason is that organs which carry out seemingly simple tasks are not that simple. The goal of the next section is give you an appreciation as to why it is so, and why option #4, tissue engineering, maybe the best approach after all.

1.2. COMPLEXITY OF BIOLOGICAL ORGANS

There are many aspects that make the replacement of biological organs with artificial ones a challenging task (Fig. 1.2). First, one has to remember that it took several billion years of evolution to optimize

biological organs (Fig. 1.3). In contrast, the effort of a graduate student or a team of investigators is limited to a few years of trial and error.

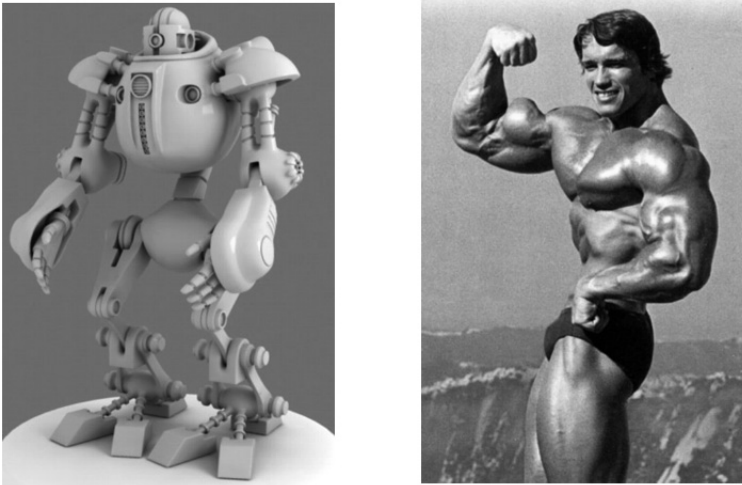


Figure 1.2. Artificial organs vs. Tissue Engineering: 1) optimal design; 2) self-renewable, repairable & rechargeable; 3) wide dynamic range with control feedback; 4) Multiple functions, some of them still hidden.

Second, the device needs not only to function, but be self-renewable, self-rechargeable and self-repairable (Fig. 1.2). Self-renewable means that as the intrinsic parts of an organ wear down, the system must be able to replace them with new material. In biological tissue these processes occur on two levels: the level of individual macromolecules (i.e. there is a continuous turnover of proteins, DNA, phospholipids) and the level of whole cells (via apoptosis of irreversibly damaged or unwanted cells). Self-rechargeable means that for the organs that perform mechanical functions (heart, skeletal muscle, gut) or are electrically active (the brain is an obvious example, but the rest of the organs also rely on electrical activity of excitable cells), energy has to be converted and stored on a continuous basis. The energy is produced by combining organic substances with oxygen within cells, but the organ's design has to include an efficient way to extract food and oxygen from circulating blood and to deliver them to individual cells. Finally, self-repairable means that in addition to gradual wear and tear, all organs experience accidental damage, being it a sudden hit, internal abscess, or rupture of a blood vessel. Parts of the living body have to be able to self-heal on a daily basis.

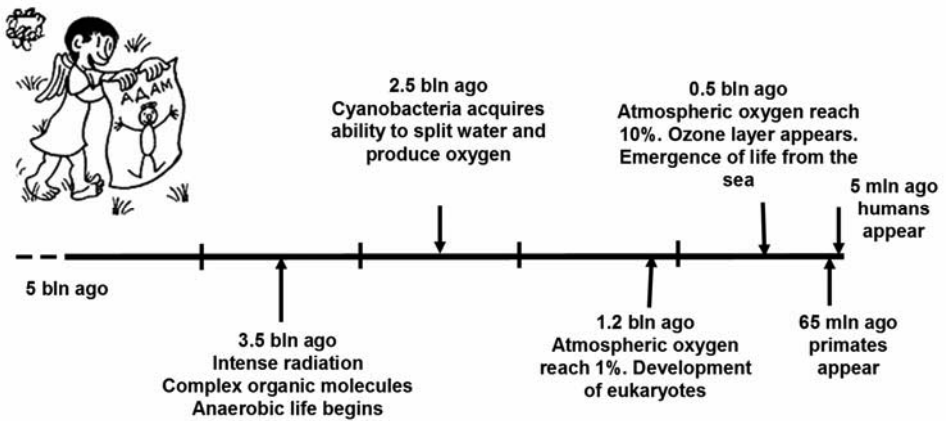


Figure 1.3. Milestones of biological evolution

The third aspect of why it is so challenging to replace a biological organ is the wide dynamic range under which the device has to be able to operate. Take a kidney for example: to adjust for your fluid intake, the kidney can produce urine which is 30 times more dilute (or concentrated) than so-called normal values. During strenuous exercise, the heart can increase its output 6 times, from 5 to 30 liters per minute! The most impressive (and humorous) example, is our brain – just think how much or how little of its functional capacity can be used. An amazing feedback system that employs both neuronal and hormonal controls regulates performance of each organ, tying it tightly to the needs of the body.

Finally, the fourth aspect of biological tissue design is that each organ has multiple functions, many of them still hidden. In order to efficiently “replace” an organ, the artificial device has to be able to accomplish at least most of these functions. Let us consider what will it take to replace an organ.

1.3. SIZING UP THE CHALLENGE

Ask yourself, what would be the simplest organ to “engineer”: the heart, lung, kidney? What about an organ without solid structure or a need for capillaries? Can you think of such an organ? Do you know that blood is not just a fluid, but considered to be an essential liquid organ? Its apparent lack of solid structure may give aspiring engineers the erroneous impression that it would be easy to replace. Unfortunately, despite decades of large scale efforts fueled by both healthcare and military budgets, we still do not have an effective blood substitute. The main components of

blood are plasma, erythrocytes (red blood cells or RBCs), platelets (main players in the coagulation cascade) and several types of white blood cells (main carriers of immune function of the body). Why don't we focus on just one type of blood cell, the simplest of all – the erythrocyte? Let's see how all the factors considered in Fig. 1.2 apply on the a level of the erythrocyte. It will give the reader, our future tissue engineer, a glimpse as to what challenges nature has in store for anyone who will be trying to mimic it.

RBCs are small, 7 micron-wide bags filled with hemoglobin, which carries oxygen to the cells (Fig. 1.4A). RBCs are the most numerous cells in our body with a concentration of 5 billion cells per cubic cm of blood. They are continuously produced in bone marrow. The old cells are filtered out by the spleen based on their flexibility with each passage of blood through the circulation loop. The average lifespan of an RBC is about 4 months. The main goal of these cells is to carry hemoglobin. In fact during its maturation from a reticulocyte, an RBC gets rid of its nucleus in order to increase the space available for hemoglobin. In addition, the absence of a nucleus makes RBCs more flexible, which, together with their concave shape (Fig. 1.4A), transforms these cells into ideal carriers that can to squeeze through narrow capillaries (Fig. 1.4B). The latter are often more narrow (3-5 micron) than the RBC itself, so the RBC bends and folds in order to get through. The surface of an RBC is covered in a complex coat of carbohydrates, which makes RBCs stick to each other at low velocities and makes blood a highly non-Newtonian fluid. It also helps RBCs to carry out their additional function – hemostasis (i.e., the ability of blood to maintain its own volume). When blood vessels experiences an internal rupture, a complex system of soluble factors is activated (the so-called complement system), interacts with the glycocalix coat of an RBC, and entraps them in a net of self-contracting myosin fibers. This produces a “cork” that prevents further loss of blood and eventually leads to wall repair (Fig. 1.4C).

Another important function of RBCs is to carry away CO₂ from tissues to the lungs, using the carbonic anhydrase system. RBCs are also the main carriers of catalase – a major antioxidant enzyme which eliminates hydrogen peroxide. The latter is formed from superoxide which escapes the hemoglobin-oxygen complex. What about the last aspect mentioned in Fig. 1.2, point #4? How one can replace an organ, without understanding the full range of its functions? One of “hidden” functions of RBCs became clear very recently. A decade ago a Nobel prize in medicine was given for the discovery of nitric oxide. This small molecule is an essential factor which regulates the diameter of blood vessels. The fact that hemoglobin, oxygen and superoxide (all of which can rapidly scavenge nitric oxide) are

sequestered within RBC, increases local availability of nitric oxide allowing it to regulate the vessel's tone (Fig. 1.4D).

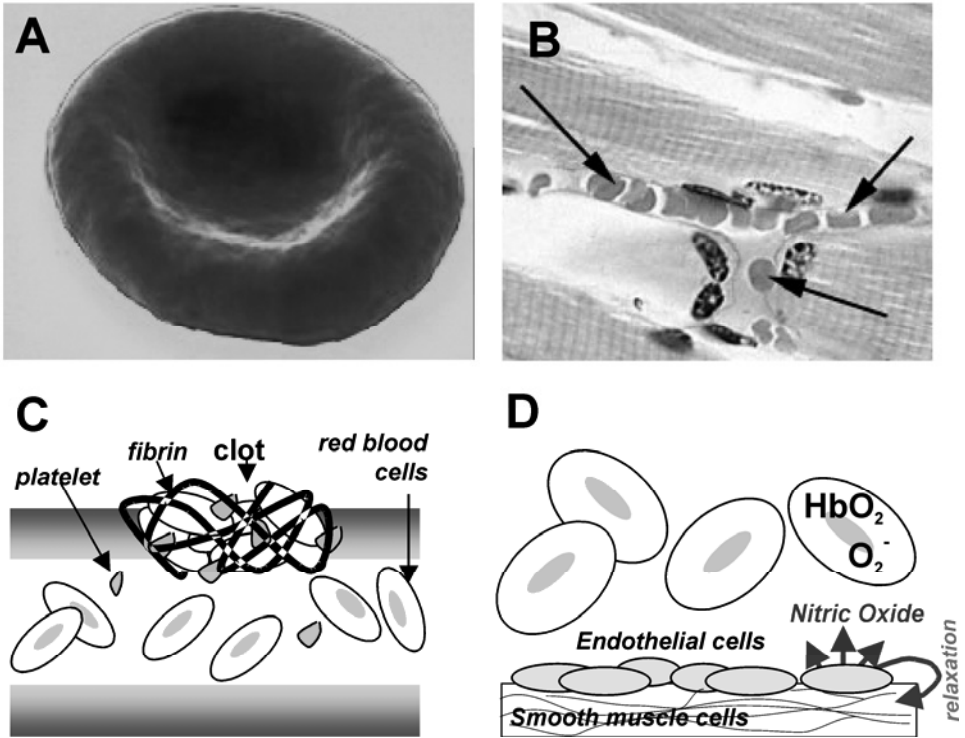


Figure 1.4. Red blood cells and their many functions. A) Picture of an erythrocyte showing its unique concave shape. B) RBCs (arrows) squeezing thru a capillary. One can see 2-micron wide sarcomeres in striated muscle surrounding the vessel. C) A cartoon of a ruptured vessel in which RBC serve their “cork” function. D) A cartoon that illustrates the “container” function of RBC, which ensures availability of nitric oxide to smooth muscle cells surrounding the vessels.

We only touched on the complexity of what can be considered to be the simplest cell of the simplest organ. I hope this gave you some appreciation as to why it might be a better idea to recreate tissues (in other words “tissue engineer” them), rather than to replace them with artificial ones.

1.4. TISSUE ENGINEERING

So what is tissue engineering? The discipline is relatively young – the term itself was coined about twenty years ago. It is defined as an interdisciplinary field that applies the principles of biology and engineering to the development of viable substitutes which restore,

maintain, or improve the function of human tissues. It comprised of the three components shown in Fig. 1.5. To date, the main problem lies in the fact that while we know that Nature uses these three components to create a tissue, we really don't know HOW. The whole situation resembles a childhood experience, to which any engineer can relate to. Remember disassembling a mechanical clock and then wondering how to put it back together? Arguably one can correlate today's shortage of students interested in engineering to the disappearance of mechanical clocks in most households. Today, the field of tissue engineering is suffering a similar "clock" experience: we know individual elements of living tissue, but we have little idea how they all come together to make a functioning organ.

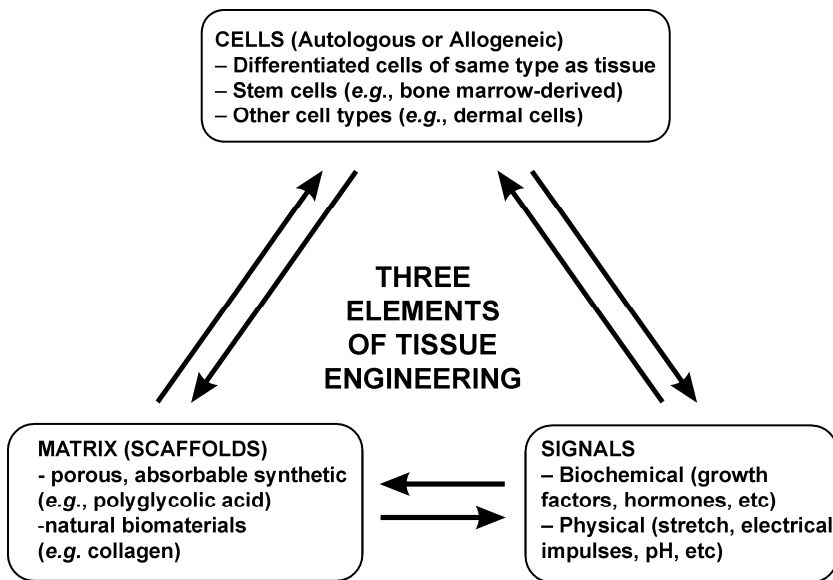


Figure 1.5. Tissue engineering: an emerging interdisciplinary field, which applies the principles of biology and engineering to the development of viable substitutes which restore, maintain, or improve the function of human tissues.

Tissue engineering holds the tremendous promise of curing diseases or accidental body damage. Because of that promise, its potential risks are often overlooked. In other words, one needs to exercise caution that the tissue engineering solution does not create a larger problem than that which is being solved. For example, one needs to be aware that by harvesting tissue for the isolation of cells, one places the donor site and surrounding tissue at risk of degeneration. Another example might be the fact that implants often accelerate the breakdown of surrounding tissues.

This book is intended to serve as an introduction to students who are entering the tissue engineering field. If it succeeds, some of its readers may decide to become the next generation of engineers recreating biological tissue from its individual components. If you are one of these brave souls, be aware that in addition to a solid engineering background, you will have to learn many subjects, including cell biology, healing and inflammation, biomaterials and scaffolds, stem cells and gene therapy, components of the extracellular matrix, biomaterials used in tissue engineering, immunology, cell culture techniques and other adjacent fields. The reward for your efforts, however, is life itself. After all, who do you think was the first tissue engineer? Whether you believe it was God or Nature, you'll have some very famous predecessors. Good luck!

CLASSICAL AND QUANTUM INFORMATION PROCESSING IN DNA-PROTEIN CODING

Djuro Koruga*

2.1. INTRODUCTION

In scientific fields, it is crucially important to understand how internal structure relates to the external form. The internal molecular structure of DNA is the key to understand how it works, but it is too far to be fully understood. Biomolecules are complex nanosystems, in which structure, energy, and information are coupled in non-conventional way. Standard model of DNA is based on classical (biochemical) signaling approach. According to nowadays knowledge, the main function of DNA is protein coding. However, it is not the complete function of this system because there are nonprotein-coding sequences, which have been considered as “junk” (Figure 2.1). Traditional view of gene activity in eukaryotes is based on individual genes, which comprise *exon* sequences that code for segments of protein separated by non-coding *intron* sequences. When a gene is active, it is entirely transcribed as RNA, but then the intronic RNA is spliced out and the exonic RNA is assembled as messenger RNA. In other words, the cell translates the messenger RNA into protein while breaking down and recycling the intronic RNA, which serves to no purpose. However, a new view of gene activity in eukaryotes is modification of the previous one, where some of the intronic RNA and even some of the assembled exonic RNA may play a direct regulatory role by interacting with the DNA, RNA, and proteins¹.

Schrödinger’s book *What is Life?* has had an enormous influence on the development of molecular biology, stimulating scientists such as Crick and

* Department of Biomedical Engineering, Faculty of Mechanical Engineering, University of Belgrade, Belgrade, Serbia

Watson to explore double helix of DNA as the basis of life^{2,3}. One of the central points in the book is the statement “that the most essential part of a living cell-the chromosome fiber -may suitably be called *an aperiodic crystal*” against to periodic crystal in classical physics. This leads to idea how DNA works as a classical information system based on double helix and ternary coding system with $4^3=64$ coding words⁴. Many years later it was recognized that the genetic ternary code, which codes amino and imino acids in proteins, also, may be represented as a classical binary code $2^6=64$ ^{5,6,7}.

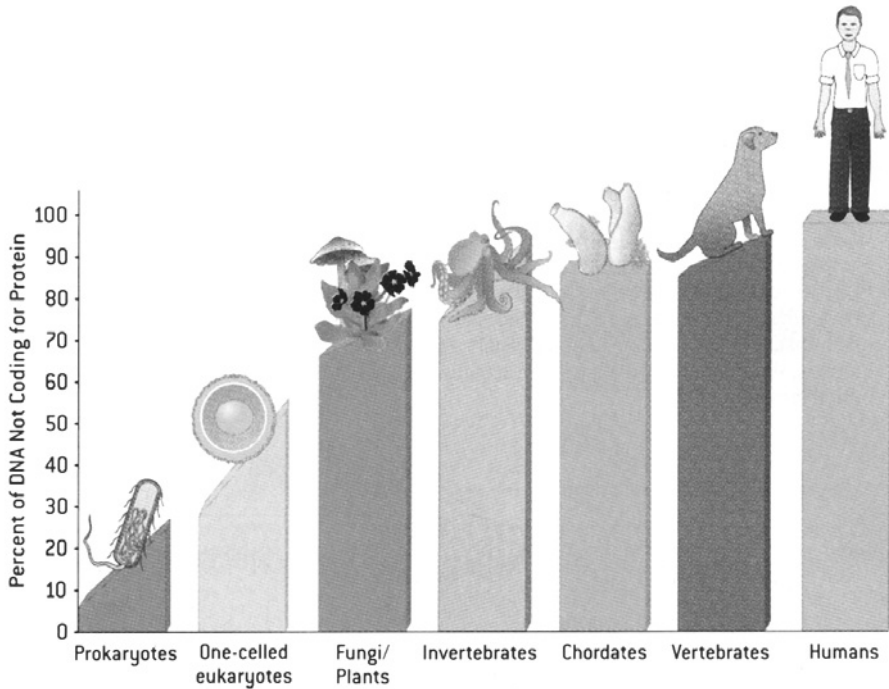


Figure 2.1. Nonprotein-coding sequences and organisms’ complexity¹

Since 1943, scientists have been only looking at one segment of Schrödinger’s idea and they developed a classical approach to understanding how DNA-protein system works. In his book Schrödinger clearly indicated that DNA is “unexplainable by classical physics”, and he recommended to do research of DNA from quantum mechanics point of view. But, for some reason, no scientist yet paid serious attention to consider DNA-protein as a quantum system. There were many trials to calculate energetic state of DNA and proteins, as separate systems, from both classical and quantum mechanical points of view, but without satisfactory results. Reasons for unsatisfactory results lie in a crude blunder, because

DNA and proteins could not be investigated separately. Proteins are other side of the DNA “coin”, and from quantum entanglement approach they have to be consider as a unique system.

2.2 BASIC FACTS

It is well known that proteins are the second side of DNA code². From structure-information point of view, each triplet of four nucleic acids (A,T,C,G in DNA, or A,U,C,G in RNA) represents one of 19 amino acids and one triplet corresponds to an imino acid. Those 20 structures are building blocks of each protein chain as a part of DNA chemical ternary code. This means that any alone amino or imino acid is a primary chemical entity (Fig. 2.2, left). In protein chain, amino acids are not alone, because each of them is split on left and right side from C_α atom (Fig. 2.2, right). In this way each amino acid, except for the first one (N-terminal) and the last one (C-terminal) builds half of two different peptide plains. Primary property of each peptide plain and protein chain, as assembly of peptide plains, is a physical one. Amino acid is split into $+1/2$ (Ψ angle) and $-1/2$ (Φ angle) parts. Alpha carbon atom is a joint point of two peptide plains which may rotate around it, one by angle Φ and the other by angle Ψ , providing possibilities that “peptide plain spins” may have many spin precession states in space. However, the side group R is a place where chemical interaction is possible (Fig. 2.3). Only proline (imino acid) side group has a direct physical feed-back to the previous peptide plain with a minimal value of atom displacement from its equilibrium state.

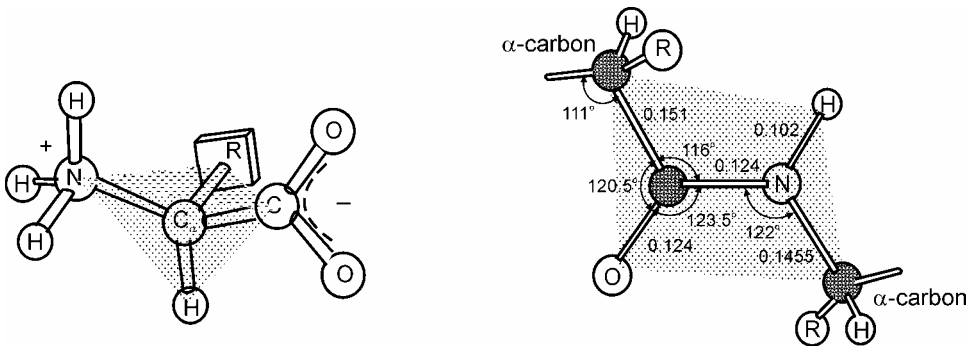


Figure 2.2 Amino acid is chemically structural-information entity of DNA code system. It is a tetragonal structure of N and C groups, C_α , and H atoms, and group of atoms R (left). Distances between atoms in peptide plains are in 10^{-10} m. Peptide plain is unity of half of each two neighboring amino acids in protein chain (right), except two amino acids which make N-and C-terminal.

Classical (chemical) ternary DNA code system is important to form proteins, but in a protein chain, it has a limited role. More important role has the classical (physical) binary code, while the primary role has the code based on quantum phenomena. Key point is the force constant of O...H between two peptide plains via hydrogen bond with 80 N/m (Table 2.1). In general, force constants are several times smaller in a peptide plain than in non-living matter (value of 434 N/m is C-C_α in a peptide plain, while value of 2500 N/m is C-C in diamond, Table 2.1).

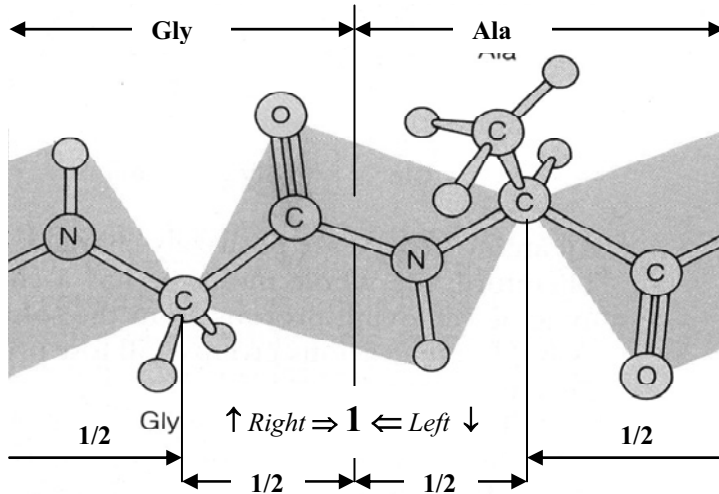


Figure 2.3 Peptide plain is physically the energy-information entity of a DNA-protein code system, while the side group R of an amino acid is the part which saves the chemical property of the DNA code system⁸

Table 2.1. Atom-atom interaction force constants, atom's displacement and time of action in peptide plane (*p.p* denotes the peptide plain, while *max* denotes values in other structures)

	Force constant k_f (N/m)		Displacement d (pm)		
	<i>p.p</i>	<i>max</i>		<i>Min</i>	<i>Max</i>
N - H	540	635	C	25	85
N - C	1600	2100	C _α	28	42
C - O	1400	1900	N	20	50
C - C	434	2500	O	18	45
O - H	550	780	H	25	120
O...H	80	120			
Time of action			~10 ⁻¹³ s		

Binary coding approach of DNA opens a possibility to investigate proteins “as second side of DNA code”. Both classical and quantum mechanics points of view may be applied. Since 2002, the Lagrangian (classical mechanics) and Hamiltonian (quantum mechanical) criteria have been used to calculate energy state of each atom in a peptide plain and in a protein chain as a system of peptide plains^{8,9,10}.

2.3. DNA-PROTEIN SYSTEM MODELING

2.3.1. Energy approach

The basic criteria for decision if the peptide plain possesses quantum mechanical property is testing its atoms action. If its action is near to Planck constant value, than from energy point of view, we can say that some entity possesses quantum mechanical property. We know that Planck constant h is $6,626 \times 10^{-34}$ Js. However, we should define the limiting value of atomic action (h^*) in peptide plain to still be quantum mechanical. As we know, the Planck constant is a link between energy (E) and electromagnetic wave oscillation (ν), as $E=h\nu$. Comparison of the electrical and magnetic interactions between two electron charges in neighboring atoms in relative motion in the peptide plain may give the solution. We know that it is not easy to calculate the magnetic interaction between two charged particles in motion relative to an observer O in a form similar to the electric interaction given by Coulomb’s law. However, we may compare orders of magnitude of the magnetic and electrical interactions. Considering two charges q and q' of neighboring atoms moving at velocities \mathbf{v} and \mathbf{v}' relative to the observer, we may simplify the formulas, in order to obtain only orders of magnitude. Thus, we can say that the electrical force produced by q' on q as measured by O is qE . The magnetic field produced by q' may be determined by the use of equation:

$$\mathbf{B} = 1/c^2 (\mathbf{v} \times \mathbf{E}) \quad (2.1)$$

The order of magnitude of \mathbf{B} is then is $\mathbf{v}'E/c^2$ and the magnetic force on q is then of the order of:

$$q\mathbf{v}\mathbf{B}=(\mathbf{v}\mathbf{v}'/c^2)q\mathbf{E} \quad (2.2)$$

Since, qE is the electrical force on q , than the ratio *magnetic force/electrical force* is $(F_M/F_E) \approx \mathbf{v}\mathbf{v}'/c^2$. If the velocities of the charges are small compared to the velocity of light c , the magnetic force is negligible compared to the electrical force and in many cases can be ignored. The orbital velocity of valence electrons in atoms is $\sim 10^6$ m/s, which gives $F_M/F_E \approx 10^{-4}$. This means that the existence of quantum action (h^*) could

be $6,626 \times 10^{-34} < h^* < 6,626 \times 10^{-30}$. In this action area, from the energy point of view, simultaneously exist both classical and quantum phenomena. So, this action area is perfect one for natural spontaneous synergetic classical/quantum processing, which we can call *fractal mechanical*. According to this approach “one theory is as strong as the opposite one”. Therefore, if action is $h^* > 6,626 \times 10^{-30}$ Js than phenomena are pure classical, while if it is $6,626 \times 10^{-34}$ Js, it is pure quantum.

The Planck constant h , as action, can be expressed as a product of F (force), d (displacement from equilibrium state) and t (time of action) as

$$h = F \times d \times t \quad (Js) \quad (2.3)$$

We can calculate F as a product of a force constant k_f and bond length x between any two coupling atoms in the peptide plain as:

$$F = k_f \times x \quad (2.4)$$

Bond lengths x_i are: C_α -C=132 pm, C_α -N=145 pm, C-O=124 pm, N-H=102 pm. By applying the eq. (2.4), the force between C_α -C can be calculated as:

$$F_{C_\alpha-C} = 434 \times 132 \times 10^{-12} = 57.28 \times 10^{-9} \text{ N}$$

Minimal action between C_α -C is then according to the eq. (2.3):

$$h_{\min}^* = (57.28 \times 10^{-9}) \times (25 \times 10^{-12}) \times 10^{-13} = 1.43 \times 10^{-31} \text{ Js}$$

while the maximal action is:

$$h_{\max}^* = (57.28 \times 10^{-9}) \times (85 \times 10^{-12}) \times 10^{-13} = 4.86 \times 10^{-31} \text{ Js}$$

Since, the action value for any two coupling atoms in the peptide plain is smaller than $h^* = 6,626 \times 10^{-30}$ Js and higher than $h = 6,626 \times 10^{-34}$, we can conclude that the peptide plain from the energy point of view, is a *fractional* entity (neither classical nor quantum). Since the peptide plane is a part of a protein, as coding matter, we should investigate DNA-protein coding (information) process as a synergy of *classical* and *quantum*.

2.3.2. Information approach

It has been shown that the genetic code is almost an example of a binary Gray code⁶. However, for the first time, it is shown that genetic code follows the binary-code tree and the Farey tree, corresponding to the Watson-Crick table and Gray code model of the genetic code at the same time⁷.

For example, in Watson-Crick notation², the amino acid arginine (*arg*) may be coded by a ternary code of nucleic acids as: AGA, AGG, CGU, CGC, CGA and CGG. However, in SDR (Swanson-Doolittle-Rakočević^{5,6,7}) notation it can be coded by a binary code as: 111010,

111011, 101100, 101101, 101110 and 101111. Both notations are valid for the amino acid as a separate entity. However, an amino acid loses the exclusive identity in a protein chain, because it is split in two peptide plains and residues (R). This structural transformation opens a possibility to transform classical binary SDR code into a quantum one (Table 2.2). Saving and converting the classical code is possible because of energy-information conditions of the peptide plain, which possesses both necessary and sufficient conditions for the existence of separate classical and quantum codes as well as their synergetic one. In other words, in a protein chain, the classical binary code of DNA, is both saved as itself and transformed into a quantum one.

Definition:

If and only if a classical information channel exists based on the binary code system, 2^n , which divisor function is $\sigma(n) = 2n$, with a property $\sigma(q) = q+1$ (for $n=q$, where q is a prime number), than the matter, which internal action (h^) lies between $6,626 \times 10^{-34}$ and $6,626 \times 10^{-30}$, possesses the quantum code system $\sigma(2n) = 2^{n+1} - 1$, as a number of quantum coding states of wave function Ψ in the quantum communication channel.*

Classical binary information (0,1) of DNA is the initialization factor for the quantum register, and then through computational steps and superposition into two-qubit states: $|11\rangle$, $|10\rangle$, $|01\rangle$ and $|00\rangle$ of left and right sides of an amino acid in two neighboring peptide planes (Table 2.2). This conformation change gives a quantum code $2^{6+1} - 1$ of a protein chain with 127 code words. Quantum code is a synergy of structure-energy-information of amino acid-peptide plain-protein chain (*aa-pp-pc*) complex. Implementation of “*aa-pp-pc*” algorithm represents a millstone for quantum information processing, not because of the result itself, but because it provides the possibility of studying molecular basis of life.

If we consider the peptide plain as the two-qubit state $|\psi\rangle = a|\uparrow\rangle_L \otimes |\uparrow\rangle_R + b|\downarrow\rangle_L \otimes |\downarrow\rangle_R$ with the property $|a|^2 + |b|^2 = 1$, than for general values of a and b , the peptide plain is entangled system of two amino acids. If the subsystems L (*left*) and R (*right*) are in states $|\psi\rangle_L$ and $|\psi\rangle_R$, respectively, the combined system is in a direct product state which we denote by $|\psi\rangle_L \otimes |\psi\rangle_R$. We can call direct product states simply as product states with the notation $|\uparrow\uparrow\rangle$ for $|\uparrow\rangle_L \otimes |\uparrow\rangle_R$.

Table 2.2: Relationship between classical ternary code (nucleic acids), classical binary code (nucleic acids-amino acids), and quantum code (amino acids {a.a}-peptide plain {p.p}-protein chain {p.c}) for arginine (*arg*)¹⁰.

Classical DNA code: 4 ³	Classical DNA binary code: 2 ⁶	Quantum DNA code: 2 ⁶⁺¹ -1		
		Left side of a.a in p.p.	Two-qubit state	Right side of a.a in p.p.
AGA	111010	1111	11⟩	1010
AGG	111011	1111		0111
CGU	101100	0101	01⟩	0100
CGC	101101	1010		1010
CGA	101110	1010	10⟩	1101
CGG	101111	1101		0111

Action: $6,626 \times 10^{-34} < \hbar^* < 6,626 \times 10^{-30}$ [Js]

Wave function: $\psi(t) = \frac{1}{2} (|\uparrow\rangle + e^{-i\omega_{SB}t} |\downarrow\rangle)$ [qubits]

2.3.3. Synergy approach

The synergy approach results in a synergy of matter-energy-information presented in the Fig. 2.4.

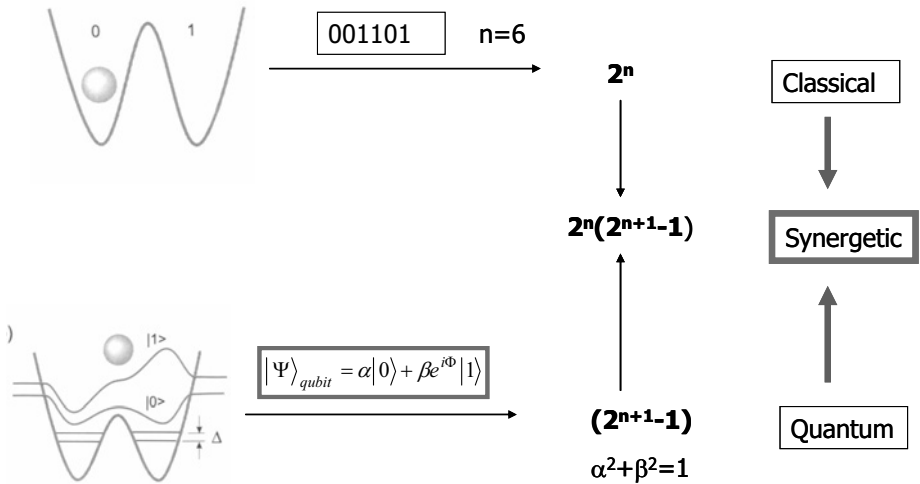


Figure 2.4. Synergy of classical (*bit*) and quantum (*qubits*) information codes of peptide plains in a protein chain based on the perfect numbers law⁹

According to the solution, the synergy of classical and quantum phenomena of the peptide plane is based on the perfect numbers law. Bearing in mind that the classical DNA code is $4^3=2^6=64$, and its quantum code in a protein chain is $2^{6+1}-1=127$, means that DNA-protein code system is a synergetic one. Also, it is an entanglement system $2^6(2^{6+1}-1)$ based on 8128 code words. Number 8128 is the fourth perfect number with a weak asymmetry of its divisors, and we can say that left and right sides of living matter possess small asymmetry because its structure, as a coding matter, is driven by the perfect number law.

2.4 HOW DOES THE DNA-PROTEIN INFORMATION SYSTEM WORK?

2.4.1. New considerations in mechanisms of DNA action

There are many things to learn about DNA, but we tried to select the most important one: the structure-function relationship. DNA is a structure made of three building blocks: phosphates, sugars, bases, and these compounds are linked together forming a double helix structure. Key points for our consideration are connections between outside hydrogen bonds (phosphor interactions with outside water molecules) and inner hydrogen bonds (base-pairs connections trough gaps).

The phosphate group is essentially a rigid tetrahedron, having a phosphorus atom at its center and one oxygen atom at each vertex. Freedom of rotation for adjacent links of the chain is provided via sugar carbon atoms. The calculation tells us something that agrees closely with experiments: almost all DNA double helices have 10 (“B” form), 11 (“A” form), and 12 (“Z” form) phosphates per turn of the helix, within each stand. Flexibility of sugar-phosphate chains, trough freedom of rotation of adjacent links, gives these three possibilities of DNA form. However, in all cases, the bases fill compactly the surface of “DNA cylinder” and successfully protect the centers of the double helices from the surrounding water. Polarized water molecules fully interact with phosphorous groups via hydrogen bonds. However, the center of the double helix, as quasi 1D dimensional space consists of discrete units of two and three hydrogen bonds, which bases A=T and G ≡ C are formed by the genetic code law.

Why “A” form of DNA is dominant in nature? From structural and energetic points of view, all three forms look similar. However, careful consideration shows that “B” and “Z” forms have some jagged features in their sugar-phosphate chain as irregularities in the packing of bases on the inside of the helix¹¹. Law of bases packing is the second key point in new considerations how DNA works. If DNA is a primary information device

in living systems then its structure has to be organized by optimal information coding law. Coding systems may be defined in different ways but sphere packing approach is a basic one¹². If the structure of DNA is designed by the sphere packing law then the form “A” (number 11) is optimal for digital transmission of information. Packing of spheres (atoms and globular proteins) gives that the optimal coding number could be 11,13, 35, and 37, with specific state of 10,12 and 35^{12,13}. There is equivalence of spheres packing in helix (coding number 11 and 13) and the packing on sphere surface (coding number 12). Bearing in mind that DNA is primary information device, coding number 11 is the first optimal number from the set of optimal numbers. Coding number 13 is the next optimal number and should be important for protein structure design, because it represents the second side of DNA code. It is known that microtubule (MT) is a coding structure with 13 subunits and possess $K_1[13,2^6,5]$ code, capable to transmit digital information¹³. Cell structure is organized from a central focal region near the nucleus called the microtubule organizing center (MTOC). The principle component of this center is the centriole, an organelle that consists of two perpendicular microtubule cylinders. Each of these cylinders is made up of 27 microtubules organized in nine MT triplets. The centriole has three main movements: (1) rotation, (2) twisting, and (3) duplication during cell division. Centrioles and MTOC play key roles in dynamic coordination of cell cytoplasm and activities. Many scientists call MTOC and cytoskeleton as “cortex” and “cell-brain”, respectively. Experiments have shown an unexpected effect, when cell is separated into two parts: one with nucleus and cytoplasm, the other with centriole with some cytoplasm. The “new” cell with the nucleus cannot produce a new centriole, in spite that DNA is responsible to make protein tubulin, which is a basic component of MT. In other words, microsurgical removal of the centriole blocks the cell reproduction and a new centriole generation (Moriotis and Schliwa,1991). Since coding systems 11 (DNA) and 13 (MT) are functionally closely interconnected and arise from the same sphere packing law, those two systems are entangled. This means that only cells, which have both nucleus and centriole have normal biological properties of mitosis (cell division) and general functionality.

2.4.2. Hydrogen bonds as a central enigma of life

The first potential importance of hydrogen bonding in the structure and function of biological macromolecules was predicted by the earliest investigators¹⁴. According to Linus Pauling, the concept of the hydrogen bond is to be attributed to M. L. Huggins and independently to W. M. Latimir and W. H. Rodebush, who proposed it in 1919 and 1920, respectively. Bearing in mind that most biological systems contain water fractions rang-

ing from 60% to 80%, importance of hydrogen bonds has become the most relevant for understanding how biomolecular machinery, as a complex system, works. In water, there are two types of bonds that are related to hydrogen: *hydrogen bonds* between water molecules and *sigma bonds* within a single water molecule, between oxygen and hydrogen atoms. It is well known that a covalent bond may only be described by quantum mechanics, because each electron does not really belong to a single atom - it belongs to both simultaneously. For a long period of time, scientists believed that hydrogen bond could be perfectly understood by principles of electrostatic interactions described by the Coulomb's law (pre-20th century classical physics), based on attraction and repulsion between charged particles positioned at a distance from each other. However, recent experimental data indicate that hydrogen bond has a double identity: classical and quantum^{15,16}. This is the key point for understanding a new approach to how DNA and proteins are behaving in water solutions. However, water itself may be a coding structure, via its hydrogen bonds, if it is organized in clusters. Some local areas of water, under the influence of DNA and microtubules, may be generators to organize water molecules in clusters as complementary coding forms. In human organisms of all water, 60% is free water, while 40% is captured by biomolecules. Estimation gives that only 5% of free water may be in cluster forms by the sphere packing law of coding number 12. Other 95% of free water is in form of "chaos" with local polymerized islands. In other words, we indeed do not know how water is dynamically organized in living systems.

According to the coding approach based on sphere packing, optimal water organization should be as a hydrogen-bonded $(\text{H}_2\text{O})_n$ polyhedron $5^{12}6^n$ ($n=0,2,4,\dots$), where 5^{12} represents 12 pentagons and n different number of hexagons¹⁷. Through hydrogen bonds dynamics, this water clathrate possess spherical coding system $2^5=32$. Bearing in mind that arrangement of water, based on number 12, may represent a coding system, which is a part of optimal information peak (11,12 and 13) of sphere packing, than water hydrogen-bonded polyhedron is both compatible and complementary coding system with the genetic code (DNA and proteins).

This means that "junk" sequence in genetic code may be an active regulatory factor of system complexity, like asymmetry, trough microtubules (cilia and centrioles) and water in living systems¹⁸. However, water organization could be the main problem of satisfactory functionality of "junk" sequence via hydrogen bonds.

2.4.3. Synergy of classical and quantum information

We found from both classical and quantum calculations that $A=T$, $C\equiv G$ in DNA, and the peptide plain in protein, possess two major oscillations:

acoustical (phonon) and optical (electrical)⁸. This indicates that both classical and quantum mechanical approaches yield same phenomenological results for those structures. Reason for similar results is a simple one: for stationary quantum state Hamilton is a sum of kinetic (T) and potential (V) energy, while Lagrangian is a difference between them when the system is in equilibrium with external forces. We have two similar pictures, one classical (type **C**) another quantum (type **Q**), of the same object.

The classical channel, type **C**, is based on the binary code system, like $2^6=64$, while the second is quantum one. The communication channel in form 2^n in the peptide plain gives the solution, $\sigma(2^n) = 2^{n+1} - 1$, what is exactly the number of quantum states in the communication channel¹⁹. From the unity point of view [coupling 2^n and $2^{n+1} - 1$ as $2^n(2^{n+1} - 1)$] we might say that *synergy* contains communication of 2^n (*classical*) code and of $2^{n+1} - 1$ (*quantum*) code by the *fractal* principle: from *one* through *two* to *three* appearing as *One*²⁰.

The most important entity of the classical information theory is the *bit*, which can have either the value «0» or «1» with both values separated by a large energy gap so that the unwanted spontaneous transition from one to the other value is impossible or extremely unlikely (the bit error rate in standard channels of telecommunication is 10^{-9} – 10^{-12}).

The quantum mechanical analogy of the bit is the quantum bit or *qubit*²¹. It is a quantum system with two states $|0\rangle$ and $|1\rangle$ forming Hilbert space as an orthogonal basis in the qubit space. In contrast to the classical bit, it is possible to crate qubits (Table 2.2, *down-left*) in a coherent superposition of $|0\rangle$ and $|1\rangle$, with the general state being $|\Psi\rangle_{qubit} = \alpha|0\rangle + \beta e^{i\phi}|1\rangle$, where $\alpha^2 + \beta^2 = 1$. Since biological molecules like DNA⁷, microtubules and clathrin²² are composed by the golden mean law then values α and β should be; $\alpha = \sqrt{\phi}$ and $\beta = \phi$ (where $\phi = 0.61803$ is value of the golden mean). One of the key differences between the familiar classical world we inhabit, and exotic quantum world, is the wire of superposition. It is the ability of quantum things to exist simultaneously in two different states.

Key point to understand biological communication system is the synergy of classical and quantum processes based on the perfect numbers and the golden mean laws¹⁰. Perfect numbers are positive integers n such that $n = s(n)$ where $s(n)$ is restricted divisor function $\sigma(n) = 2n$, where $\sigma(n)$ is the divisor function. The first four perfect numbers are 6, 28, 496, and 8128. For the first two perfect numbers their divisors are $1+2+3=6$, and $1+2+4+7+14=28$, respectively. Sum of reciprocate values of perfect number divisors is $H_a = \sum 1/\bar{d}_i = 2$ ($1/1+1/2+1/3+1/6 = 2$). Perfect numbers were deemed to have important numerological properties by the ancients, and were extensively studied by the ancient Greeks, including Euclid and Plato. Now, perfect numbers arise again as an important class of numbers

in information and control theories. From system organization point of view, the relationship *part-whole* is a crucial one. In modeling, combination of perfect numbers and harmonic numbers provides the best results for the control theory. Perfect numbers are connected with a class of Mersenne primes numbers in the form $M_p = 2^p - 1$.

Synergetic approach to processing free water - DNA interaction, and *vice versa*, might be considered as three channels to carry signals in a molecular system (Fig. 2.4). The first one is a classical channel (as binary system, 2^n) based on classical signal behavior (SDR code). The second is a hybrid one, which is based on *phonon-photon* coupling phenomena of phosphor-sugar-base group, which also works as binary 2^n system. The third one is the inner side of the DNA bases and may activate at the same time left *and* right sides of their hydrogen bonds ($2^n \times 2$), or only left *or* right side of them ($2^n \times 1/2$). In the first case, the communication system is of type **A** (*left-right* side is synchronized): $2^n \times 2 \times 2^n = 2^n$, or

$$2^n(2^{n+1}-1) = 0$$

where: 2^n represents a classical channel, while $2^{n+1}-1$ represents a quantum channel (Fig. 2.4).

In the second case, the system is of type **B** (there is not *photon-phonon* coupling during DNA or peptide plane hydrogen bonds oscillation). Left and right sides of DNA or peptide plane work separately, including the extreme case like *splitting*: $2^n/2 \times 2^n = 2^n/2$, or

$$2^{n-1}(2^n-1) = 0$$

For $n=6$, type **A** will give DNA working process by the fourth perfect number 8128, while type **B** will give solution by “non-perfect” number 2016. Type **A** has enough elements for right coding, both classical and quantum states, while the second one has not enough coding worlds for the quantum channel. Number 2016 is a symmetry breaking element between *the third* (496) and *the fourth* (8128) perfect numbers, because according to $2^{n-1}(2^n-1)$ formula, for $n=5$ the value will be 496. Since cluster water naturally works by 2^5 code ($n=5$), then when DNA code in same sequence of gene collapses from $n=6$ to $n=5$, then this event, as DNA disharmony, will transmit trough water very quickly in given region (“good news travel fast, bad even faster”)⁹.

2.4.4. Violation of the synergetic DNA-protein information channel and cancer

Cancer is one of the leading causes of death in the last century. Knowledge improvement in this field is a crucial one. However, our current knowledge about cancer is very limited. According to synergy of DNA-

microtubule-water coding system based on hydrogen bonds (perfect numbers and golden mean) we might consider cancer as symmetry breaking phenomena of hydrogen bonds¹⁰.

Following this approach let's present skin cancer and melanoma phenomena⁹. The epidermis is a dynamic renewing structure that provides life-sustaining protection from the environment. Keratinocytes and melanocytes are the major cell types responsible for the structure of the epidermis. They begin as stem cells in the basal epidermal layer. As keratinocytes move to the epidermal surface, the cells cease to divide and undergo morphological changes to form the spinous, granular, transition, and cornified layers²³. One melanocyte cell may overlap a few keratinocytes giving them melanin (the mechanism is yet unknown), which is responsible for protection from the environmental electromagnetic radiation (UV radiation) and neutralization of free radicals^{24,25}.

Also, collagen distortion below the basement membrane (lamina fibroreticularis) occurs when cancer penetrates from epidermis into dermis, and "opens the door" for metastases. From classical communication channels point of view, gene expression is responsible for it: normal collagen type I [$\alpha 1(I)_2\alpha 2(I)$], consists of two procollagen chains: $\alpha 1(I)$, which gene is located on chromosome 17 (q21-q22), and $\alpha 2(I)$, which gene is located on chromosome 7 (q21-q22). According to quantum theory, the quantum communication channel (entanglement) based on DNA hydrogen bonds, between keratinocyte or melanocyte and fibroblast cells, exists. When symmetry-breaking of hydrogen bonds happens in DNA, then automatically, through DNA-microtubule-water coding entanglement, the synergy of classical and quantum communication is broken (Fig. 2.5). There is experimental evidence that fibroblast cells and human melanoma cells interact as a function of tumor progression²⁶. If UV radiation damages DNA on chromosome 7, in keratinocyte or melanocyte cells, then through non-classical quantum channels this information will transfer to both centriole (damaged cell) and fibroblast cells in region. Centriole will become "wild" and will start to divide chromosomes irregularly. Nucleus of the initial cancer cell will become bigger than in a normal cell. The "wild" cell will be duplicated and number of them will rapidly increase because of a positive feedback control mechanism water-centriole will change perpendicularity of centriole pairs²⁷. From the other side, fibroblast cells will stop to synthesize collagen $\alpha 2(I)$. In the absence of $\alpha 2(I)$, procollagen chains during assembly into procollagen molecule will incorporate one more $\alpha 1(I)$ procollagen chain. This will result in collagen type I-trimer with structure [$\alpha 1(I)_3$]. In I-trimer links between procollagen chains do not fit well, and OH groups will be removed from collagen to make free water molecules. Volume of free water will increase for 20% in tissue. Similar situation

happens during skin aging and this is why people in age frequently have cancer²⁸.

When this type of collagen becomes dominant in a given tissue then lamina fibroreticularis (as a “woof” of basal lamina) becomes weak, because interconnection between procollagen chains into procollagen molecule, based on hydrogen bonds, is not adequate. Then, mass of skin cancer or melanoma, penetrate basal lamina and touch superficial arterio-venous plexus²⁹.

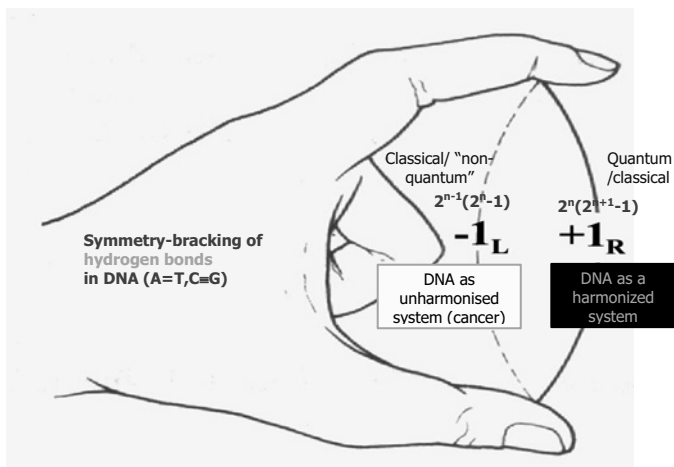


Figure 2.5. Symmetry breaking of DNA functionality: when there is a non adequate matching of hydrogen bonds between water-phosphate and hydrogen bonds of DNA pairs (A=T, C≡G) than functionality of DNA is violated (-1_L state). When hydrogen bonds matching is correct than classical and quantum channels make a synergy state (+1_R state)⁹

Bearing in mind that entanglement in biological tissues can produce effects in the classical channel (initial removal of collagen OH groups), then quantum entanglement of hydrogen bonds might be the key for understanding not only carcinoma but also the life itself. If so, the proverb, “every cloud has a silver lining” may have a sense.

2.5. SUMMARY

Hydrogen bonds look like a “soul” of biomolecule networks in cells and tissues as well as their complex intermolecular connections. They are a link between classical and quantum behaviors of matter on the molecular level, and they are a basic element for synergy of mass-energy and information in the living matter.

DNA is coded by 4th perfect number code $2^n(2^{n+1}-1)$ with 8128 code words, which is responsible for protein coding (*classical channel/quantum classical channel*) and system complexity coding (*quantum non-classical channel*) by entanglement. There is a mapping one-to-one from genetic code to proteins by the synergetic code. The synergetic code (*classical/quantum*) in protein chains is based on amino acids and peptide plains. Hydrogen bonds make body network with classical/quantum properties capable to form solitary wave.

Understanding DNA as a synergetic classical/quantum device, based on golden mean and the fourth perfect number, may help us not only for better understanding of the origin of life, but also for finding methods for prevention and healing the most illnesses. Bearing in mind that proteins are the second side of the DNA code, interaction and communication DNA-protein may be provided both through separate classical and quantum communications channels, and through the synergetic one. Applicability of the current genetic knowledge is limited because it is based only on classical information approach. However, the synergetic approach may open new possibilities for diagnosis and therapy of many illnesses including cancer.

DNA and water are in very delicate relationship. In normal situations, the first entity works by the fourth perfect number law, while the second entity by the third one. Thus, in normal situations, DNA-water system works harmonically. However, when for some reason DNA function collapses (from the fourth to the third perfect number law) then the information about the disharmonic state of DNA travels more smoothly through water than the harmonic one.

Acknowledgements

This work has been supported by the Ministry of Science of the Republic of Serbia, projects TR6349 (2005-2007) and 148028 (2006-2010).

References

1. Mattick S.J., Challenging the dogma: the hidden layer of non-protein-coding RNAs complex organisms, *BioEssays*, **25**(10), 930-939, 2003.
2. Watson J.D., F.H.C. Crick, Structures of deoxyribose nucleic acid, *Nature*, **171**, 737- 738, 1953.
3. Schrödinger E., *What is life? Mind and matter*, Cambridge University Press, Cambridge, 1967.
4. Crick F.H.C., The recent excitement in the coding problem, *Progress in Nucl. Acid Research*, **1**, 163-217, 1963.
5. Doolittle R., Similar amino acid sequences: chance or common ancestry, *Science*, **214**, 149-157, 1981.

6. Swanson A., A unifying concept for the amino acid code, *Bull. Math. Biology*, **46**(2), 187-203, 1984.
7. Rakočević M.M., The genetic code as a Golden mean determined system, *BioSystems*, **46**, 283-291, 1998.
8. Koruga D., A. Tomic, Z. Ratakaj, and L. Matija, Gibbson: Peptide plane as a unique biological nanostructure, *Materials Science Forum*, **453-454**, 529-536, 2004.
9. Koruga D., DNA as classical and quantum information system: Implication to gene expression in normal and cancer cells, *Arch Oncology*, **13**(3-4), 115-120, 2005.
10. Koruga D., A. Tomić, Ž. Ratakaj, L. Matija, Classical and quantum information channels in protein chain, *Materials Science Forum*, **518**, 491-496, 2006.
11. Calladine C.R., H.R. Drew, *Understanding DNA: The molecule and how it works*, Academic Press, San Diego, 1997.
12. Sloane N.J.A., The packing of spheres, *Scientific American*, **1**, 116-125, 1984
13. Koruga D., Microtubule screw symmetry: Packing of spheres as a latent bioinformation code, *Ann.NY Acad Sci*, **466**, 953-955, 1986.
14. Pauling L., R.B. Corey, H.R. Branson, The structure of proteins. Two hydrogen-bonded helical configurations of the polypeptide chain, *Proc.Nat. Acad. Sci USA*, **37**, 205-211, 1951.
15. Isaacs E.D., et. al, Covalency of the hydrogen bond in ice: A direct X-ray measurement, *Physical Review Letters*, **82**, 600-603, 1999.
16. Barbiellini B., A. Shukla, *Ab initio* calculations of the hydrogen bond, *Physical Review B*, **66**, 235101 (1-5), 2003.
17. Jeffrey G.A., *Introduction to hydrogen bonding*, Oxford University Press, New York-Oxford, 1997.
18. Kierszenbaum A.L., *Histology and cell biology*, Mobsy, St. Luis, 2002.
19. Ustinov A., Quantum computing using superconductors, in: R. Waser (ed.), *Nanoelectronics and information technology*, Wiley-VCH, Weinheim, pp.463-471, 2003.
20. Koruga D., *Fractal mechanics*, Megatrend University Press, Belgrade, 2008 (in press)
21. Nielsen A.M., L.I. Chuang, *Quantum computation and quantum information*, Cambridge University Press, Cambridge, 2000.
22. Koruga D., S. Hameroff, R. Loutfy, J. Withers, M. Sundereshan, *Fullerene C60: history, physics, nanobiology, nanotechnology*, Elsevier (North-Holland), Amsterdam, 1993.
23. Gawkrödger D.J., *Dermatology*, Elsevier, Amsterdam, 2003.
24. Varani J., Reduced fibroblast interaction with intact collagen as a mechanism for depressed collagen synthesis in photodamaged skin, *J. Invest Dermatol*, **122**, 1471-1479, 2004.
25. Van Den Bossche K., A. Naeyuert, J. Lambert, The quest for the mechanism of melanin transfer, *Trafic*, **7**, 1-10, 2006.
26. Coinil I., D. Theodorescu, S. Man, M. Herlyn, J. Jambrosic, and R.S. Kerbel, Fibroblast cell interactions with human melanoma cells affect tumor cell growth

- as a function of tumor progression, *Proc. Nat. Acad Sci, USA*, **88**, 6028-6032, 1991.
27. Koruga D., M. Andjelkovic, S. Jankovic, and S. Hameroff, Cytoskeleton as feed-back control system in neuron, in: *Artificial neural networks*, I. Aleksander, J. Taylor (eds), Elsevier, Amsterdam, pp. 399-402, 1992.
 28. Richard S., B. Querleux, J. Bittoun, O. Jolivet, L. Idy-Peretti, O. de Lacharriere, J.L. Leveque, Characterization of the skin *in vivo* by high resolution magnetic resonance imaging: water-behavior and aged-related effects, *J. Inves. Dermatoogy*, **100**, 705-709, 1993.
 29. Brinkley R.R., Managing the centrosome numbers game: from chaos to stability in cancer cell division, *TRENDS in Cell Biology*, **11**(1), 18-21, 2001.

UNRAVELING THE MEMBRANE FUSION IN SECRETORY CELLS AT THE NM-LEVEL: A NANOBIOENGINEERING APPROACH

Aleksandar M. Jeremic and Bhanu P. Jena*

3.1. INTRODUCTION

Secretion and membrane fusion are fundamental cellular processes regulating ER–Golgi transport, plasma membrane recycling, cell division, sexual reproduction, acid secretion, and the release of enzymes, hormones and neurotransmitters, to name just a few. It is therefore no surprise that defects in secretion and membrane fusion give rise to diseases like diabetes, Alzheimer's, Parkinson's, acute gastroduodenal diseases, gastroesophageal reflux disease, intestinal infections due to inhibition of gastric acid secretion, biliary diseases resulting from malfunction of secretion from hepatocytes, polycystic ovarian disease as a result of altered gonadotropin secretion, and Gitelman disease associated with growth hormone deficiency and disturbances in vasopressin secretion, are only a few examples. Understanding cellular secretion and membrane fusion helps not only to advance our understanding of these vital cellular and physiological processes, but in the development of drugs to help ameliorate secretory defects, provide insight into our understanding of cellular entry and exit of viruses and other pathogens, and in the development of smart drug delivery systems. Therefore, secretion and membrane fusion play an important role in health and disease. Studies^{1–18} in the last decade demonstrate that membrane-bound secretory vesicles dock and transiently fuse at the base of specialized plasma membrane structures called porosomes or fusion pores, to expel vesicular contents.

* Department of Physiology / NanoBioscience Institute, Wayne State University School of Medicine, Detroit, MI, U.S.A.

These studies further demonstrate that during secretion, secretory vesicles swell, enabling the expulsion of intravesicular contents through porosomes^{16–18}. With these findings^{1–18}, a new understanding of cell secretion has emerged and confirmed by a number of laboratories^{19–23}.

Throughout history, the development of new imaging tools has provided new insights into our perceptions of the living world and profoundly impacted human health. The invention of the light microscope almost 300 years ago was the first catalyst, propelling us into the era of modern biology and medicine. Using the light microscope, a giant step into the gates of modern medicine was made by the discovery of the unit of life, the cell. The structure and morphology of normal and diseased cells, and of disease causing microorganisms, were revealed for the first time using the light microscope. Then, in 1938, with the birth of the electron microscope (EM), dawned a new era in biology and medicine. Through the mid 1940s and 1950s, a number of subcellular organelles were discovered and their functions determined using the EM. Viruses, the new life forms were discovered and observed for the first time, and implicated in diseases ranging from the common cold to autoimmune disease (AIDS). Despite the capability of the EM to image biological samples at near nanometer resolution, sample-processing (fixation, dehydration, staining) results in morphological alterations, and is a major concern. Then in the mid 1980s, scanning probe microscopy evolved^{1,24}, further extending our perception of the living world to the near atomic realm. One such scanning probe microscope, the atomic force microscope (AFM), has helped overcome both limitations of light and electron microscopy, enabling determination of the structure and dynamics of single biomolecules and live cells in 3D, at near angstrom resolution. This unique capability of the AFM has given rise to a new discipline of ‘nanobioscience’, heralding a new era in biology and medicine.

Using AFM in combination with conventional tools and techniques, this past decade has witnessed advances in our understanding of cell secretion^{1–18} and membrane fusion^{9,15}, as noted earlier and briefly described in this review. The resolving power of the light microscope is dependent on the wavelength of the light used, and therefore, 250–300 nm in lateral and much less in depth resolution, can be achieved at best. The porosome or fusion pore in live secretory cells are cup-shaped structures, measuring 100–150 nm at its opening and 15–30 nm in relative depth in the exocrine pancreas, and just 10 nm at the presynaptic membrane of the nerve terminal. As a result, it had evaded visual detection until its discovery using the AFM^{3–8}. The development of the AFM²⁴ has enabled the imaging of live cells in physiological buffer at nm to subnanometer resolution. In AFM, a probe tip micro fabricated from silicon or silicon nitride and mounted on a cantilever spring is used to scan the surface of

the sample at a constant force. Either the probe or the sample can be precisely moved in a raster pattern using a xyz piezo tube to scan the surface of the sample (Fig. 3.1). The deflection of the cantilever measured optically is used to generate an isoforce relief of the sample²⁵. Force is thus used to image surface profiles of objects by the AFM, allowing imaging of live cells and subcellular structures at nm-resolution submerged in physiological buffer solutions. To image live cells, the scanning probe of the AFM operates in physiological buffers, and may do so under two modes: contact or tapping. In the contact mode, the probe is in direct contact with the sample surface as it scans at a constant vertical force. Although high-resolution AFM images can be obtained in this mode of AFM operation, sample height information generated may not be accurate since the vertical scanning force may depress the soft cell. However, information on the viscoelastic properties of the cell and the spring constant of the cantilever enables measurement of the cell height. In tapping mode on the other hand, the cantilever resonates and the tip makes brief contacts with the sample. In the tapping mode in fluid, vertical forces are virtually negligible. It is therefore important that the topology of living cells be obtained using both contact and tapping modes of AFM operation in fluid. The scanning rate of the tip over the sample also plays an important role on the quality of the image. Since cells are soft samples, a high-scanning rate would influence their shapes. Hence, a slow tip movement over the cell would be ideal and results in minimal distortion and better image resolution. Rapid cellular events may be further monitored by using section analysis. To examine isolated cells by the AFM, freshly cleaved mica coated with Cell-Tak have also been used with great success³⁻⁸. Also, to obtain optimal resolution, the contents of the bathing medium as well as the cell surface to be scanned should be devoid of any debris.

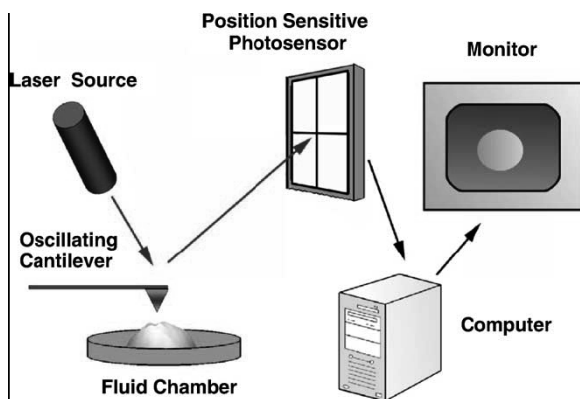


Fig. 3.1. Schematic diagram depicting key components of an atomic force microscope.

3.2. POROSOME: A NEW CELLULAR STRUCTURE

Earlier electrophysiological studies on mast cells suggested the existence of fusion pores at the cell plasma membrane (PM), which became continuous with the secretory vesicle membrane following stimulation of secretion²⁶. AFM has confirmed the existence of the fusion pore or porosome, and revealed its structure and dynamics in the exocrine pancreas^{3,4,7,8}, neuroendocrine cells^{5,6} and neurons¹⁴ at near nm resolution and in real time. Isolated live pancreatic acinar cells in physiological buffer, when imaged with the AFM^{3,4,7,8}, reveal at the apical PM a group of circular ‘pits’ measuring 0.4–1.2 μm in diameter which contain smaller ‘depressions’ (Fig. 3.2).

Figure 3.2. On the far left is an AFM micrograph depicting ‘pits’ (yellow arrow) and ‘depressions’ within (blue arrow), at the plasma membrane in live pancreatic acinar cells. On the right is a schematic drawing depicting depressions, at the cell plasma membrane, where membrane-bound secretory vesicles dock and fuse to release vesicular contents. Please see the Figure on the page 265.

Each depression averages between 100 and 150 nm in diameter, and typically 3–4 depressions are located within a pit. The basolateral membrane of acinar cells is devoid of either pits or depressions. High-resolution AFM images of depressions in live cells further reveal a cone-shaped morphology. The depth of each depression cone measures 15–30 nm. Similarly, growth hormone (GH) secreting cells of the pituitary gland and chromaffin cells, acinar cells of the exocrine pancreas, mast cells, and neurons, possess depressions at their PM, suggesting their universal presence in secretory cells. Exposure of pancreatic acinar cells to a secretagogue (mastoparan) results in a time-dependent increase (20–35%) in depression diameter, followed by a return to resting size on completion of secretion^{3,4,7,8} (Fig. 3.3). No demonstrable change in pit size is detected following stimulation of secretion³. Enlargement of depression diameter and an increase in its relative depth after exposure to secretagogues correlated with increased secretion. Conversely, exposure of pancreatic acinar cells to cytochalasin B, a fungal toxin that inhibits actin polymerization, results in a 15–20% decrease in depression size and a consequent 50–60% loss in secretion³ (Fig. 3.3).

Figure 3.3. Dynamics of depressions following stimulation of secretion. The top panel shows a number of depressions within a pit in a live pancreatic acinar cell. The scan line across three depressions in the top panel is represented graphically in the middle panel and defines the diameter and relative depth of the depressions; the middle depressions are represented by red arrowheads. The bottom panel represents percent of total cellular

amylase release in the presence and absence of the secretagogue Mas 7. Notice an increase in the diameter and depth of depressions, correlating with an increase in total cellular amylase release at 5 min after stimulation of secretion. At 30 min after stimulation of secretion, there is a decrease in diameter and depth of depressions, with no further increase in amylase release over the 5 min time point. No significant increase in amylase secretion or depressions diameter was observed in resting acini or those exposed to the nonstimulatory mastoparan analog Mas 17. Please see the Figure on the page 265.

Results from these studies suggested depressions to be the fusion pores in pancreatic acinar cells. Furthermore, these studies demonstrate the involvement of actin in regulation of both the structure and function of depressions. Analogous to pancreatic acinar cells, examination of resting GH secreting cells of the pituitary⁵ and chromaffin cells of the adrenal medulla⁶ also reveal the presence of pits and depressions at the cell PM (Fig. 3.4). The presence of porosomes in neurons, β -cells of the endocrine pancreas and in mast cells has also been demonstrated (Figs. 3.4 and 3.5)¹⁴. Depressions in resting GH cells measure 154 ± 4.5 nm (mean \pm S.E.) in diameter. Exposure of GH cells to a secretagogue results in a 40% increase in depression diameter (215 ± 4.6 nm; $P < 0.01$) but no appreciable change in pit size. The enlargement of depression diameter during secretion and the known effect that actin depolymerizing agents decrease depression size and inhibit secretion³ suggested depressions to be the fusion pores. However, a more direct determination of the function of depressions was required. This was achieved by immuno-AFM studies. AFM localization at depressions of gold-conjugated antibody to a secretory protein demonstrated secretion to occur through depressions^{4,5}. The membrane-bound secretory vesicles in exocrine pancreas called zymogen granules (ZGs) contain the starch digesting enzyme amylase. AFM micrographs demonstrated localization of amylase-specific antibodies tagged with colloidal gold at depressions following stimulation of secretion⁴ (Fig. 3.6).

Figure 3.4. AFM micrograph of depressions or porosomes or fusion pores in live secretory cell of the exocrine pancreas (A and B), the growth hormone secreting cell of the pituitary (C) and in the chromaffin cell (D). Note the ‘pit’ (white arrow heads) with four depressions (yellow arrow head). A high-resolution AFM micrograph is shown in (B). Bars = 40 nm for (A and B). Similarly, AFM micrographs of porosomes in β -cell of the endocrine pancreas (E) and mast cell (F) is shown. Note the 100–130 nm porosomes in the β -cell and the 70–80 nm porosomes in the mast cell. (G) Electron micrograph depicting a porosome (red arrow head) close to a microvilli (MV) at the apical plasma membrane (PM) of a pancreatic acinar cell. Note association of the porosome membrane (yellow arrow head), and the zymogen granule membrane (ZGM) (red arrow head) of a docked zymogen granule (ZG), the membrane-bound secretory vesicle of exocrine pancreas. Also a cross section of the ring at the mouth of the porosome is seen (blue arrow head)⁸. Please see the Figure on the page 266.

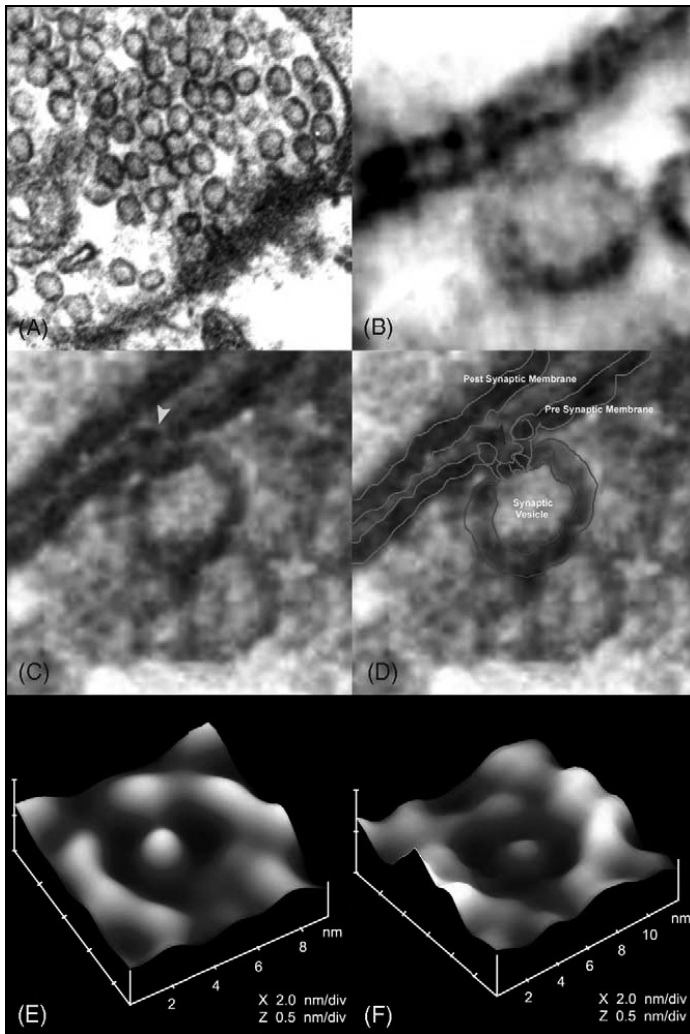


Figure 3.5. Electron micrograph of porosomes in neurons. (A) Electron micrograph of a synaptosome demonstrating the presence of 40–50 nm synaptic vesicles. (B–D) Electron micrograph of neuronal porosomes which are 10–15 nm cup-shaped structures at the presynaptic membrane (gray arrow head), where synaptic vesicles transiently dock and fuse to release vesicular contents. (E) Atomic force micrograph of a fusion pore or porosome at the nerve terminal in live synaptosome. (F) Atomic force micrograph of isolated neuronal porosome, reconstituted into lipid membrane.

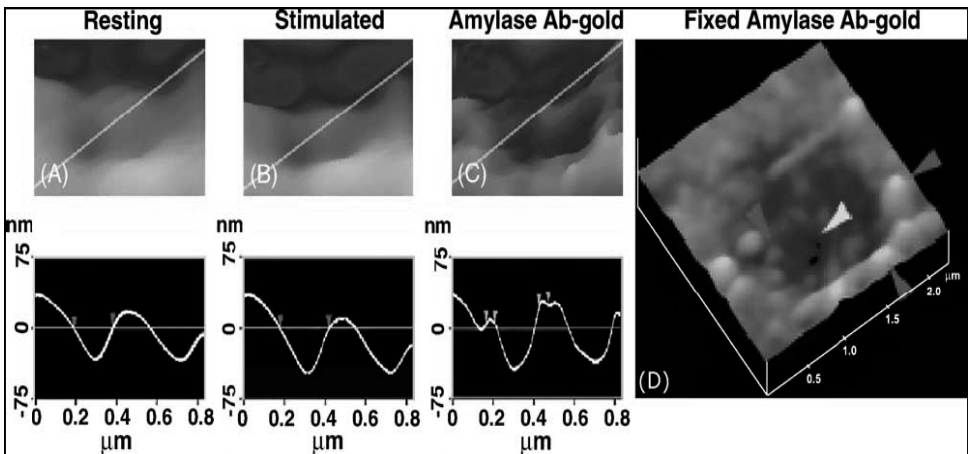


Figure 3.6. Depressions are fusion pores or porosomes. Porosomes dilate to allow expulsion of vesicular contents. (A and B) AFM micrographs and section analysis of a pit and two out of the four fusion pores or porosomes, demonstrating enlargement following stimulation of secretion. (C) Exposure of live cells to gold-conjugated amylase antibody (Ab) results in specific localization of immuno-gold to the porosome opening. Amylase is one of the proteins within secretory vesicles of the exocrine pancreas. (D) AFM micrograph of a fixed pancreatic acinar cell, demonstrating a pit and porosomes within, immunogold-labeling amylase at the site. Darker arrowheads point to immunogold clusters and the light gray arrowhead points to a porosome⁴.

These studies confirm depressions to be the fusion pores or porosomes in pancreatic acinar cells where membrane-bound secretory vesicles dock and fuse to release vesicular contents. Similarly, in somatotrophs of the pituitary, gold-tagged growth hormone-specific antibody is found to selectively localize at depressions following stimulation of secretion⁵, again identifying depressions in GH cells as fusion pores or porosomes. To determine the morphology of the porosome at the cytosolic side of the cell, pancreatic PM preparations were used. Isolated PM in buffer when placed on freshly cleaved mica, tightly adhere to the mica surface, enabling imaging by AFM. The PM preparations reveal scattered circular disks measuring 0.5–1 μm in diameter, with inverted cup-shaped structures within⁷. The inverted cups range in height from 10 to 15 nm. On a number of occasions, ZGs ranging in size from 0.4 to 1 μm in diameter were found associated with one or more of the inverted cups. This suggested the circular disks to be pits, and the inverted cups to be fusion pores or porosomes. To determine if the cup-shaped structures in isolated PM preparations are indeed porosomes, immuno-AFM studies were carried out. Since ZGs dock and fuse at the PM to release vesicular contents, it was hypothesized that if porosomes are these sites, then PM-associated t-SNAREs should localize at the base of porosomes. The t-SNARE protein SNAP-23, has been identified and implicated in secretion from pancreatic

acinar cells²⁷. A polyclonal mono-specific SNAP-23 antibody recognizing a single 23 kDa band in Western blots of pancreatic PM fraction, has been used in immuno-AFM studies. When the SNAP-23-specific antibody was added to the PM preparation during imaging with the AFM, the antibody selectively localized to the base of the cup-shaped structure, which is the tip of the inverted cup. These results demonstrate that the inverted cup-shaped structures in the isolated PM preparations are the porosomes observed from its cytosolic side^{7,8}. Target membrane proteins, SNAP-25 and syntaxin (t-SNARE) and secretory vesicle-associated membrane protein (v-SNARE), are part of the conserved protein complex involved in fusion of opposing bilayers^{28,9,15}. Since membrane-bounded secretory vesicles dock and fuse at porosomes to release vesicular contents, suggested t-SNAREs to associate at the porosome complex. It was therefore no surprise that the t-SNARE protein SNAP-23, implicated in secretion from pancreatic acinar cells, was located at the tip of the inverted cup (i.e., the base of the porosome) where secretory vesicles dock and fuse. The structure of the porosome was further demonstrated using transmission electron microscopy (TEM)^{7,8} (Fig. 3.4). TEM studies confirm the fusion pore to have a cup-shaped structure, with similar dimensions as determined from AFM measurement. Additionally, TEM micrographs reveal porosomes to possess a basket-like morphology, with three lateral and a number of vertically arranged ridge. A ring at the base of the complex is also identified⁷. Since porosomes are found to be stable structures at the cell PM, it was hypothesized that if ZGs were to fuse at the base of the structure, it would be possible to isolate ZG-associated porosomes. Indeed, TEM of isolated ZG preparations reveal porosomes associated with docked vesicles^{7,8}. As observed in whole cells, vertical structures were found to originate from within the porosome complex and appear attached to its membrane. As discussed later in this review, studies using full length recombinant SNARE proteins and artificial lipid membranes demonstrated that t- and v-SNAREs located in opposing bilayers interact in a circular array to form conducting pores⁹. Since similar circular structures are observed at the base of the porosome, and SNAP-23 immunoreactivity is found to localize at this site, suggests that the t-SNAREs present at the base of porosomes are possibly arranged in a ring pattern.

3.3. POROSOME: ISOLATION AND RECONSTITUTION

The size and shape of the immunisolated porosome complex was determined in greater detail when examined using both negative staining

TEM and AFM⁸. The images of the immunoisolated porosome obtained by both TEM and AFM were super-imposable⁸ (Fig. 3.7).

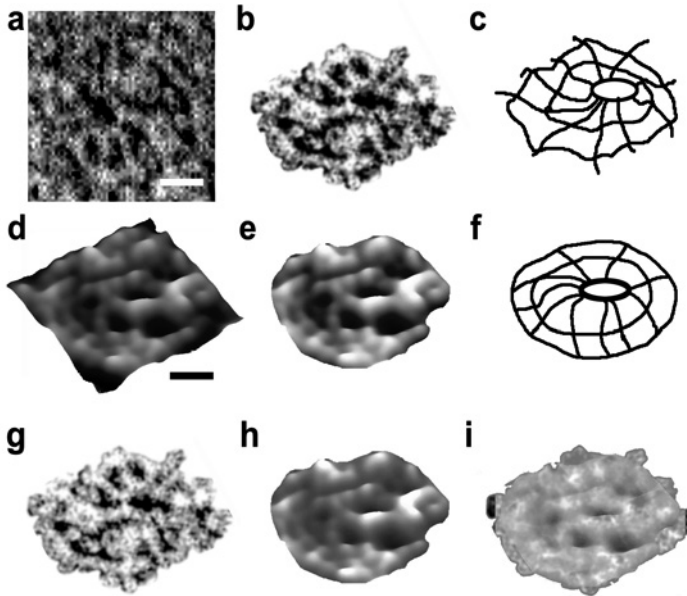


Figure 3.7. Negatively stained electron micrograph and atomic force micrograph of the immunoisolated fusion pore complex. (a) Negatively stained electron micrograph of an immunoisolated fusion pore complex from solubilized pancreatic plasma membrane preparations, using a SNAP-23 specific antibody. Note the three rings and the 10 spokes that originate from the inner smallest ring. This structure represents the protein backbone of the fusion pore complex. Bar = 30 nm. (b) The electron micrograph of the fusion pore complex, cut out from a, and (c) an outline of the structure presented for clarity. (d–f) AFM of the isolated pore complex in near physiological buffer. Bar = 30 nm. Note the structural similarity of the complex, imaged both by TEM (g) and AFM (h). The TEM and AFM images are super-imposable (i).

To further test whether the immunoisolated supramolecular complex was indeed the porosome, the complex was reconstituted into artificial liposomes, and the liposome-reconstituted complex examined using TEM⁸. Transmission electron micrographs reveal a 150–200 nm cup-shaped basket-like structure as observed of the porosome when co-isolated with ZGs (Fig. 3.8).

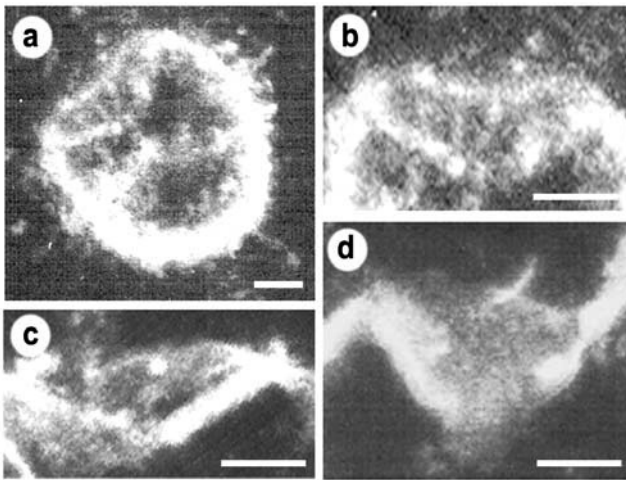


Figure 3.8. Electron micrographs of reconstituted porosome or fusion pore complex in liposomes showing a cup-shaped basket-like morphology. (a) A 500-nm vesicle with an incorporated porosome is shown. Note the spokes in the complex. The reconstituted complex at greater magnification is shown in b–d. Bar = 100 nm.

To test if the reconstituted porosome complex was functional, purified porosomes were reconstituted into lipid membranes in an electrophysiological bilayer setup (EPC9) and challenged with isolated ZGs. Both the electrical activity of the reconstituted membrane as well as the transport of vesicular contents from the cis to the trans compartment was monitored. Results of these experiments demonstrate that the lipid membrane-reconstituted porosomes are functional supramolecular complexes (Fig. 3.9)⁸. ZGs fused with the porosome-reconstituted bilayer, as demonstrated by an increase in capacitance and conductance, and in a time-dependent release of the ZG enzyme amylase from cis to the trans compartment of the bilayer chamber (Fig. 3.9B). Amylase is detected using immunoblot analysis of the buffer in the cis and trans chambers (Fig. 3.9B), using a previously characterized amylase-specific antibody⁴. As observed in immunoblot assays of isolated porosomes, chloride channel activities are also detected within the reconstituted porosome complex (Fig. 3.9C). Further, the chloride channel inhibitor DIDS, was found to inhibit current activity in the porosome-reconstituted bilayer. In summary, these studies demonstrate that the porosome in the exocrine pancreas is a 100–50 nm in diameter supramolecular cup-shaped lipoprotein basket at the cell PM, where membrane-bound secretory vesicles dock and fuse to release vesicular contents. Similar studies have now been performed in neurons, demonstrating both the structural (Fig. 3.5E and F) and functional reconstitution of the isolated neuronal porosome complex.

Figure 3.9. Lipid bilayer-reconstituted porosome complex is functional. (A) Schematic drawing of the bilayer setup for electrophysiological measurements. (B) Zymogen granules (ZGs) added to the cis side of the bilayer fuse with the reconstituted porosomes, as demonstrated by an increase in capacitance and current activities, and a concomitant time-dependent release of amylase (a major ZG content) to the trans side of the membrane. The movement of amylase from the cis to the trans side of the chamber was determined by immunoblot analysis of the contents in the cis and the trans chamber over time. (C) As demonstrated by immunoblot analysis of the immunisolated complex, electrical measurements in the presence and absence of chloride ion channel blocker DIDS, demonstrate the presence of chloride channels in association with the complex⁸. Please see the Figure on the page 266.

3.4. SNARE-INDUCED MEMBRANE FUSION

As eluded earlier, membrane fusion is mediated via a specialized set of proteins in the secretory vesicles and the plasma membrane. Three soluble *N*-ethylmaleimide-sensitive factor (NSF)-attachment protein receptors (SNAREs) have been implicated in membrane fusion²⁸. Target membrane proteins, SNAP-25 and syntaxin (t-SNARE) and secretory vesicle-associated membrane protein (v-SNARE), are part of the conserved protein complex involved in fusion of opposing bilayers²⁸. Although the structure of SNARE complex formed by interacting native³⁵ or recombinant^{36,37} t- and v-SNAREs was known from studies using electron microscopy^{35,36} and X-ray crystallography³⁷, the molecular mechanism of the involvement of SNAREs to bring about membrane fusion remained unknown until 2002⁹.

To determine the molecular mechanism of SNARE-induced membrane fusion, the structure and arrangement of SNAREs associated with lipid bilayers were examined using AFM (Fig. 3.10). The bilayer electrophysiological setup allowed measurements of membrane conductance and capacitance, prior to and after t-SNARE- or v-SNARE-reconstitution, and following exposure of v-SNARE or t-SNARE-reconstituted lipid vesicles. These studies demonstrate that the interaction of t-/v-SNARE proteins to form a pore or channel, is dependent on the presence of t-SNAREs and v-SNARE in opposing bilayers. Addition of purified recombinant v-SNARE to a t-SNARE-reconstituted lipid membrane increased only the size of the globular t-SNARE oligomer without influencing the electrical properties of the membrane⁹ (Fig. 3.10). However, when t-SNARE vesicles are added to v-SNARE reconstituted membrane, SNAREs assemble in a ring pattern (Fig. 3.10) and a stepwise increase in capacitance and conductance is observed (Fig. 3.10). Thus, t- and v-SNAREs are required to reside in opposing bilayers to allow appropriate t-/v-SNARE interactions leading to membrane fusion only in the presence of calcium^{9,15}.

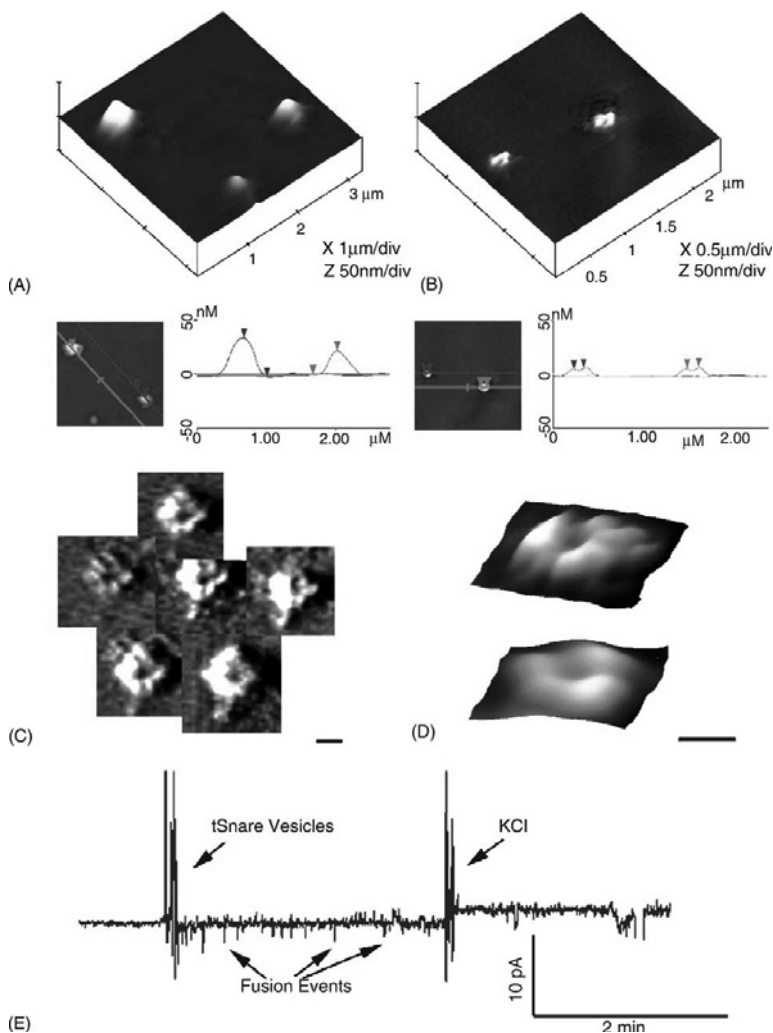


Figure 3.10. Pore-like structures are formed when t-SNAREs and v-SNARE in opposing bilayers interact. (A) Unfused v-SNARE vesicles on t-SNARE-reconstituted lipid membrane. (B) Dislodgement or fusion of v-SNARE-reconstituted vesicles with a t-SNARE-reconstituted lipid membrane, exhibit formation of pore-like structures due to the interaction of v- and t-SNAREs in a circular array. The size of the pores ranges between 50 and 150 nm (B–D). Several 3D AFM amplitude images of SNAREs arranged in a circular array (C) and some at higher resolution (D), illustrating a pore-like structure at the center is depicted. Scale bar is 100 nm. Recombinant t-SNAREs and v-SNARE in opposing bilayers drive membrane fusion. (E) When t-SNARE vesicles were exposed to v-SNARE-reconstituted bilayers, vesicles fused. Vesicles containing nystatin/ergosterol and t-SNAREs were added to the cis side of the bilayer chamber. Fusion of t-SNARE containing vesicles with the membrane observed as current spikes that collapse as the nystatin spreads into the bilayer membrane. To determine membrane stability, the transmembrane gradient of KCl was increased, allowing gradient-driven fusion of nystatin-associated vesicles⁹.

3.5. REGULATION OF SECRETORY VESICLE SWELLING: INVOLVEMENT IN EXPULSION OF VESICULAR CONTENTS

The molecular mechanism of vesicle swelling¹⁶⁻¹⁸ and its involvement in regulated expulsion of intravesicular contents¹⁴ has been established. Secretory vesicle swelling is critical for secretion⁴⁰⁻⁴³; however, the underlying mechanism of vesicle swelling was largely unknown until recently¹⁶⁻¹⁸. In most cells, an increase in secretory vesicle volume after stimulation of secretion has previously been suggested from electrophysiological measurements⁴⁴. However, direct evidence of secretory vesicle swelling in live cells was first demonstrated in pancreatic acinar cells using the AFM¹⁶. Isolated ZGs of the exocrine pancreas and parotid glands, possess Cl^- and ATP-sensitive, K^+ -selective ion channels at the vesicle membrane whose activities have been implicated in vesicle swelling. Additionally, secretion of ZG contents in permeabilized pancreatic acinar cells requires the presence of both K^+ and Cl^- ions. *In vitro* ZG-pancreatic plasma membrane fusion assays further demonstrate potentiation of fusion in the presence of GTP⁴³. $G_{\alpha i}$ protein has been implicated in the regulation of both K^+ and Cl^- ion channels in a number of tissues. Analogous to the regulation of K^+ and Cl^- ion channels at the cell plasma membrane, their regulation at the ZG membrane by a $G_{\alpha i3}$ protein has been demonstrated¹⁶. Isolated ZGs from exocrine pancreas swell rapidly in response to GTP¹⁶. These studies suggested the involvement of rapid water gating into ZGs following exposure to GTP. Therefore, when the possible involvement of water channels or aquaporins in ZG swelling was explored¹⁷, results from the study demonstrate the presence of aquaporin-1 (AQP1) at the ZG membranes and its participation in GTP-mediated vesicle water entry and swelling¹⁷.

To further understand the molecular mechanism of secretory vesicle swelling, the regulation of AQP1 in ZGs has been investigated¹⁸. Detergent-solubilized ZGs immunoprecipitated with monoclonal AQP-1 antibody, co-isolates AQP-1, PLA2, $G_{\alpha i3}$, potassium channel IRK-8, and the chloride channel ClC-2 ¹⁸. Exposure of ZGs to either the potassium channel blocker glyburide or the PLA2 inhibitor ONO-RS-082, blocked GTP-induced ZG swelling. RBC known to possess AQP-1 at the plasma membrane, also swell on exposure to the $G_{\alpha i}$ -agonist mastoparan, and respond similarly to ONO-RS-082 and glyburide, as do ZGs. Additionally, liposomes reconstituted with the AQP-1 immunisolated complex from solubilized ZGs, were found to swell in response to GTP. Glyburide or ONO-RS-082 abolished the GTP effect in reconstituted liposomes. Furthermore, immunisolated AQP1 and reconstituted into a planar lipid membrane demonstrate conductance, which is sensitive to glyburide and

an AQP-1-specific antibody. These results demonstrate a pathway and potassium channel involvement in AQP-1 regulation¹⁸, contributing to our understanding of the molecular mechanism of ZG swelling. Although secretory vesicle swelling is involved in membrane fusion⁴³, studies demonstrate that its primary role is in the expulsion of vesicular contents during secretion. The extent of swelling is directly proportional to the amount of intravesicular contents expelled^{14,45}.

3.6. MOLECULAR UNDERSTANDING OF CELL SECRETION

Fusion pores or porosomes are present in all secretory cells examined, from exocrine, endocrine, neuroendocrine, to neurons, where membrane-bound secretory vesicles dock and transiently fuse to expel vesicular contents. Porosomes in pancreatic acinar or growth hormone (GH)-secreting cells are cone-shaped structures at the plasma membrane, with a 100–150 nm diameter opening. Membrane-bound secretory vesicles ranging in size from 0.2 to 1.2 μm in diameter dock and fuse at porosomes to release vesicular contents. Following fusion of secretory vesicles at porosomes, only a 20–35% increase in porosome diameter is demonstrated. It is therefore reasonable to conclude that secretory vesicles “transiently” dock and fuse at the site. In contrast to accepted belief, if secretory vesicles were to completely incorporate at porosomes, the PM structure would distend much wider than what is observed. Furthermore, if secretory vesicles were to completely fuse at the plasma membrane, there would be a loss in vesicle number following secretion. Examination of secretory vesicles within cells before and after secretion demonstrates that the total number of secretory vesicles remains unchanged following secretion^{10,23}. However, the number of empty and partially empty vesicles increases significantly, supporting the occurrence of transient fusion. Earlier studies on mast cells also demonstrated an increase in the number of spent and partially spent vesicles following stimulation of secretion, without any demonstrable increase in cell size. Similarly, secretory granules are recaptured largely intact after stimulated exocytosis in cultured endocrine cells¹⁹. Other supporting evidence favoring transient fusion is the presence of neurotransmitter transporters at the synaptic vesicle membrane. These vesicle-associated transporters would be of little use if vesicles were to fuse completely at the plasma membrane to be compensatory endocytosed at a later time. In further support, a recent study reports that single synaptic vesicles fuse transiently and successively without loss of vesicle identity²⁰. Although the fusion of secretory vesicles at the cell plasma membrane occurs transiently, complete incorporation of membrane at the cell plasma membrane would occur when cells need to

incorporate signaling molecules like receptors, second messengers or ion channels.

The discovery of the porosome, and an understanding of the molecular mechanism of membrane fusion and the swelling of secretory vesicles required for expulsion of vesicular contents, provides an understanding of secretion and membrane fusion in cells at the molecular level. These findings have prompted many laboratories to work in the area and further confirm these findings. Thus, the porosome is a supramolecular structure universally present in secretory cells, from the exocrine pancreas to the neurons, and in the endocrine to neuroendocrine cells, where membrane-bound secretory vesicles transiently dock and fuse to expel vesicular contents. Hence, the secretory process in cells is a highly regulated event, orchestrated by a number of ions and biomolecules.

References

1. Horber J.K.H., M.J. Miles, Scanning probe evolution in biology. *Science*; **302**, 1002–1005, 2003.
2. Anderson L.L., Discovery of a new cellular structure—the porosome: elucidation of the molecular mechanism of secretion, *Cell Biol Int*, **28**, 3–5, 2004
3. Schneider S.W., K.C. Sritharan, J.P. Geibel, H. Oberleithner, B.P. Jena, Surface dynamics in living acinar cells imaged by atomic force microscopy: identification of plasma membrane structures involved in exocytosis, *Proc Natl Acad Sci USA*, **94**, 316–321, 1997.
4. Cho S.J., A.S. Quinn, M.H. Stromer, S. Dash, J. Cho, D.J. Taatjes, et al. Structure and dynamics of the fusion pore in live cells, *Cell Biol Int*, **26**, 35–42, 2002.
5. Cho S.J., K. Jeftinija, A. Glavaski, S. Jeftinija S, B.P. Jena, L.L. Anderson, Structure and dynamics of the fusion pores in live GH-secreting cells revealed using atomic force microscopy, *Endocrinology*, **143**, 1144–1148, 2002.
6. Cho S.J., A. Wakade, G.D. Pappas, B.P. Jena, Newstructure involved in transient membrane fusion and exocytosis, *Ann N Y Acad Sci*, **971**, 254–256, 2002.
7. Jena B.P., S.J. Cho SJ, A. Jeremic, M.H. Stromer, R. Abu-Hamdah, Structure and composition of the fusion pore, *Biophys J*, **84**, 1337–1343, 2003.
8. Jeremic A., M. Kelly, S.J. Cho, M.H. Stromer, B.P. Jena, Reconstituted fusion pore, *Biophys J*, **85**, 2035–2043, 2003.
9. Cho S.J., M. Kelly, K.T. Rognlien, J. Cho, J.K.H. Hoerber, B.P. Jena, SNAREs in opposing bilayers interact in a circular array to form conducting pores, *Biophys J*, **83**, 2522–2527, 2002.
10. Cho S.J., J. Cho, B.P. Jena, The number of secretory vesicles remains unchanged following exocytosis, *Cell Biol Int*, **26**, 29–33, 2002.
11. Jena B.P., Fusion pore in live cells, *NIPS*, **17**(6), 219–222, 2002.
12. Jena B.P., Fusion pore: structure and dynamics, *J Endocrinol*, **176**(2), 169–174, 2003.

13. Jena B.P., Exocytotic fusion: total or transient, *Cell Biol Int*, **21**(5), 257–259, 1997.
14. Jena B.P., Discovery of the porosome: revealing the molecular mechanism of secretion and membrane fusion in cells, *J Cell Mol Med*, **8**(1), 1–21, 2004.
15. Jeremic A., M. Kelly, J.H. Cho, S.J. Cho, J.K.H. Horber, B.P. Jena, Calcium drives fusion of SNARE-apposed bilayers, *Cell Biol Int*, **28**, 19–31, 2004.
16. Jena B.P., S.W. Schneider, J.P. Geibel, P. Webster, H. Oberleithner, K.C. Sritharan, Gi regulation of secretory vesicle swelling examined by atomic force microscopy, *Proc Natl Acad Sci USA*, **94**, 13317–13322, 1997.
17. Cho S.J., A.K. Sattar, E.H. Jeong, M. Satchi, J.A. Cho, S. Dash, et al., Aquaporin 1 regulates GTP-induced rapid gating of water in secretory vesicles, *Proc Natl Acad Sci USA*, **99**, 4720–4724, 2002.
18. Abu-Hamdah R., W.J. Cho, S.J. Cho, A. Jeremic, M. Kelly, A.E. Ilie, et al., Regulation of the water channel aquaporin-1: isolation and reconstitution of the regulatory complex, *Cell Biol Int*, **28**, 7–17, 2004.
19. Taraska J.W., D. Perrais, M. Ohara-Imaizumi, S. Nagamatsu, W. Almers, Secretory granules are recaptured largely intact after stimulated exocytosis in cultured endocrine cells, *Proc Natl Acad Sci USA*, **100**, 2070–2075, 2003.
20. Aravanis A.M., J.L. Pyle, R.W. Tsien, Single synaptic vesicles fusing transiently and successively without loss of identity, *Nature*, **423**, 643–647, 2003.
21. Tojima T., Y. Yamane, H. Takagi, T. Takeshita, T. Sugiyama, H. Haga H, et al., Three-dimensional characterization of interior structures of exocytotic apertures of nerve cells using atomic force microscopy, *Neuroscience*, **101**, 471–81, 2000.
22. Thorn P., K.E. Fogarty, I. Parker, Zymogen granule exocytosis is characterized by long fusion pore openings and preservation of vesicle lipid identity, *Proc Natl Acad Sci USA*, **101**, 6774–6779, 2004.
23. Lee J.S., M.S. Mayes, M.H. Stromer, C.G. Scanes, S. Jeftinija, L.L. Anderson, Number of secretory vesicles in growth hormone cells of pituitary remains unchanged after secretion, *Exp Biol Med*, **229**, 632–639, 2004.
24. Binnig G., C.F. Quate, C.H. Gerber, Atomic force microscope, *Phys Rev Lett*, **56**, 930–933, 1986.
25. Alexander S., L. Hellemans, O. Marti, J. Schneir, V. Elings, P.K. Hansma, An atomic resolution atomic force microscope implemented using an optical lever, *J Appl Phys*, **65**, 164–167, 1989.
26. Monck J.R., A.F. Oberhauser, J.M. Fernandez, The exocytotic fusion pore interface: a model of the site of neurotransmitter release, *Mol Membr Biol*, **12**, 151–156, 1995.
27. Gaisano H.Y., L. Sheu, P.P. Wong, A. Klip, W.S. Trimble, SNAP-23 is located in the basolateral plasma membrane of rat pancreatic acinar cells, *FEBS Lett*, **414**, 298–302, 1997.
28. Weber T., B.V. Zemelman, J.A. McNew, B. Westerman, M. Gmachl, F. Parlati, et al., SNAREpins: minimal machinery for membrane fusion, *Cell*, **92**, 759–772, 1988.
29. Bennett V., Spectrin-based membrane skeleton: a multipotential adaptor between plasma membrane and cytoplasm, *Physiol Rev*, **70**, 1029–1065, 1990.

30. Faigle W., E. Colucci-Guyon, D. Louvard, S. Amigorena, T. Galli, Vimentin filaments in fibroblasts are a reservoir for SNAP-23, a component of the membrane fusion machinery, *Mol Biol Cell*, **11**, 3485–3494, 2000.
31. Goodson H.V., C. Valetti, T.E. Kreis, Motors and membrane traffic, *Curr Opin Cell Biol*, **9**, 18–28, 1997.
32. Nakano M., S. Nogami, S. Sato, A. Terano, H. Shirataki, Interaction of syntaxin with α -fodrin, a major component of the submembranous cytoskeleton, *Biochem Biophys Res Commun*, **288**, 468–475, 2001.
33. Ohyama A., Y. Komiya, M. Igarashi, Globular tail of myosin-V is bound to vamp/synaptobrevin, *Biochem Biophys Res Commun*, **280**, 988–991, 2001.
34. Prekeris R., D.M. Terrian, Brain myosin V is a synaptic vesicle-associated motor protein: evidence for a Ca^{2+} -dependent interaction with the synaptobrevin–synaptophysin complex, *J Cell Biol*, **137**, 1589–1601, 1997.
35. Jeong E.H., P. Webster, C.Q. Khuong, A.K.M. Sattar, M. Satchi, B.P. Jena, The native membrane fusion machinery in cells, *Cell Biol Int*, **22**, 657–670, 1998.
36. Hanson P.I., R. Roth, H. Morisaki, R. Jahn, J.E. Heuser, Structure and conformational changes in NSF and its membrane receptor complexes visualized by quick-freeze/deep-etch electron microscopy, *Cell*, **90**, 523–535, 1997.
37. Sutton R.B., D. Fasshauer, R. Jahn, A.T. Brunger, Crystal structure of a SNARE complex involved in synaptic exocytosis at 2.4 Å resolution, *Nature*, **395**, 347–353, 1998.
38. Coorsen J.R., P.S. Blank, M. Tahara, J. Zimmerberg, Biochemical and functional studies of cortical vesicle fusion: the SNARE complex and Ca^{2+} sensitivity, *J Cell Biol*, **143**, 1845–1857, 1998.
39. Zimmerberg J., P.S. Blank, I. Kolosova, M.S. Cho, M. Tahara, J.R. Coorsen, A stage-specific preparation to study the Ca^{2+} -triggered fusion steps of exocytosis: rationale and perspectives, *Biochimie*, **82**, 303–314, 2000.
40. Alvarez de Toledo G., R. Fernandez-Chacon, J.M. Fernandez, Release of secretory products during transient vesicle fusion, *Nature*, **363**, 554–558, 1993.
41. Curran M.J., M.S. Brodwick, Ionic control of the size of the vesicle matrix of beige mouse mast cells, *J Gen Physiol*, **98**, 771–790, 1991.
42. Monck J.R., A.F. Oberhauser, G. Alvarez de Toledo, J.M. Fernandez, Is swelling of the secretory granule matrix the force that dilates the exocytotic fusion pore? *Biophys J*, **59**, 39–47, 1991.
43. Sattar A.K.M., R. Boinpally, M.H. Stromer, B.P. Jena, $\text{G}_{\alpha_{i3}}$ in pancreatic zymogen granule participates in vesicular fusion, *J Biochem*, **131**, 815–820, 2002.
44. Fernandez J.M., M. Villalon, P. Verdugo, Reversible condensation of the mast cell secretory products in vitro, *Biophys J*, **59**, 1022–1027, 1991.
45. Kelly M.L., W.J. Cho, A. Jeremic, R. Abu-Hamdah, B.P. Jena, Vesicle swelling regulates content expulsion during secretion, *Cell Biology Int*, **28**, 709–716, 2004.

BIOPHYSICAL AND BIOCHEMICAL DETERMINANTS OF CONTRACTILE FORCE GENERATION, REGULATION, AND FUNCTION

Srboljub M. Mijailovich*

4.1. THE FUNDAMENTAL PROBLEM OF MUSCLE CONTRACTION

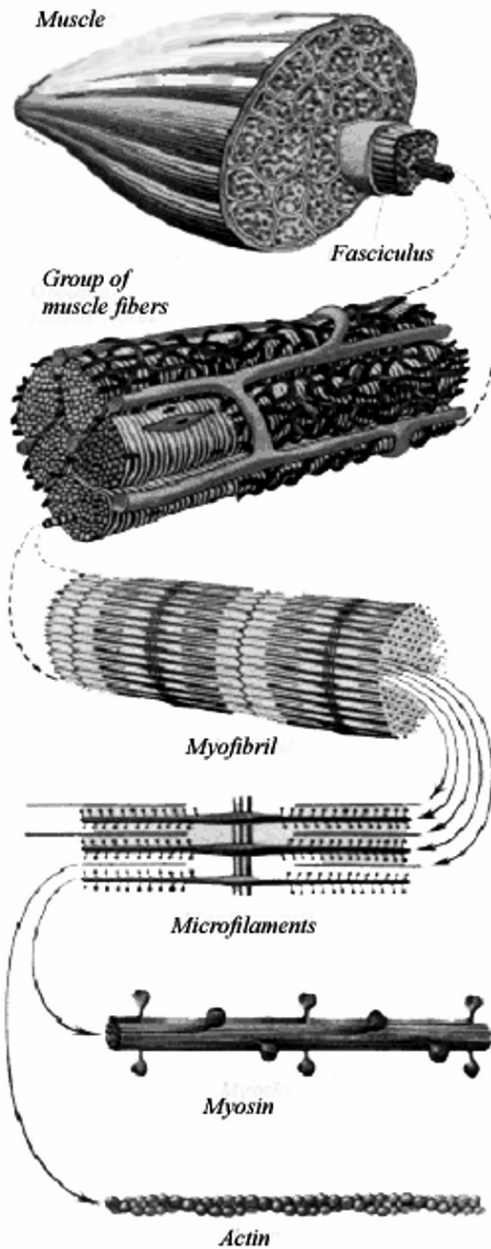
Understanding muscle contraction answers one of the fundamental questions posed in classical times, namely the nature of the *spiritus animalis*. The *spiritus animalis* was an intrinsic property of living things. Erasistratus (3rd century B.C.) of the Alexandrian school associated the *spiritus animalis* with the muscles. The *pneuma* was thought to course along the nerves and make the muscles swell and shorten. In the beginning of the 2nd. century A.D. Galen, the last classical physiologist, took over and expanded these ideas introducing a primitive metabolism involving the four humours. Furthermore, from a detailed anatomical examination of muscles, Galen concluded that muscles work in antagonistic pairs, and that muscles pull rather than push. From that time many mechanical models were proposed until 19th century when the concept of muscle as a chemical machine driven by isothermal combustion was first introduced by von Helmholtz. This was a beginning of the development on modern understanding of muscle contraction based on metabolic biochemistry, thermodynamics, and underlying molecular structure.

4.1.1 Structure of skeletal muscle

Fine structure of muscle can be observed by naked eye or by magnifying glass (Fig. 4.1 top panel). At finer scale multinucleated single cells, called

* Harvard School of Public Health, Harvard University, Boston, Massachusetts, USA.

muscle fibers, can be observed by optical microscope up to 0.2 μm . Skeletal muscle fiber is elongated having diameter of 10-60 μm and a length ranging for several mm to several cm. The fiber cytoplasm is divided into longitudinal threads or *myofibrils* each of about 1 μm wide.



The myofibrils are striated when they are stained by dyes and when they are examined optically, and they show distinctive dark (anisotropic, A) and bright (isotropic, I) bands (Fig. 4.2). The A bands are bisected transversely by a paler line called the H band, while the I bands are dissected by a thin dark line called Z band. Each myofibril is composed of arrays of myofilaments: Myosin (thick) filaments and Actin (thin) filaments (Fig. 4.2). These arrays are divided transversely by Z bands into serially repeating regions termed sarcomeres, each about 2-2.5 μm long dependent on the force acting in the muscle and state of excitation. The each of actin filaments is attached at one end to Z band and its other (free) end interdigitates with the myosin filaments. This interdigitation and molecular connection can be seen only by electron microscopy which has resolution of about 0.2nm. The molecular connections represent interaction of myosin molecules sticking out from myosin filament with the actin sites at actin filament.

Figure 4.1. The organizational hierarchy of skeletal muscle. From Gray's anatomy¹⁰.

4.1.2. What makes muscles shorten?

The contraction of voluntary muscles in all animals and humans takes place by the mutual sliding of two sets of interdigitating thick and thin filaments organized in sarcomeres each a few microns long which give muscle its cross striated appearance in the microscope (Fig. 4.2). The relative sliding of thick and thin filaments is brought about by “cross-bridges”, parts of the myosin molecules which stick out from the myosin filaments and interact cyclically with the thin filaments – transporting them by a kind of rowing action. During the process ATP (adenosine triphosphate) is hydrolyzed to ADP (adenosine diphosphate), and the hydrolysis of ATP provides the energy. The dichotomy of the action of ATP (a relaxing factor that drives contraction) remained an enigma to be explained later by Lymn and Taylor. In the mean time, the myosin molecule was characterized and was shown to consist of two heavy chains and two light chains. A soluble proteolytic fragment of myosin, heavy mero-myosin (which contains the globular “heads” of myosin) contains the ATPase activity¹⁹. The ATPase activity was later shown to reside in the “head” itself²⁰ often called S1 - which constitutes the morphological “cross-bridge”. The rest of myosin molecule forming a long α -helical coiled-coil is called S2.

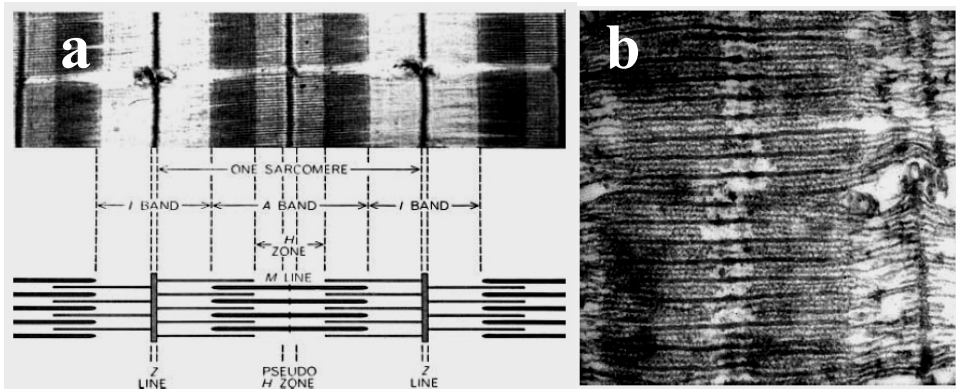


Figure 4.2. Fine structure of a sarcomere. (a) Longitudinal section of frog stratorious muscle, and diagram showing corresponding overlaying arrays of thicker (myosin) and thinner (actin) filaments; (b) Very thin longitudinal sections showing single layer of filament lattice, and hence individual thin and thick filaments, and cross-bridges between them⁶.

The first molecular theories, which appeared in the ‘30’s, were based on polymer science. They proposed that there was a rubber-like shortening of myosin filaments brought about by altering the state of ionization of the myosin. This aberration was corrected by the seminal works of HE Huxley

²³ and AF Huxley ²⁴ which showed that sarcomeres contained two sets of filaments (thick and thin), which glided over each other without altering their length. Hasselbach showed that the thick filaments contain the protein myosin. The question naturally arose – what made the filaments glide? Projections from the thick filaments, the myosin cross-bridges, were discovered by electron microscopy ¹ and subsequently shown both to be the site of the ATPase and also to be the motor elements producing force and movement between the filaments. Two conformations of the cross-bridge could be detected in insect flight muscle ²⁵. Progress was then rapid so that at a historic Cold Spring Harbor Symposium in 1972 the outline of the molecular mechanism of muscle contraction could be enunciated. The cross-bridge was thought to bind to actin in an initial (90°) conformation, go over to a angled (45°) conformation and then release ^{26,27}. For each cycle of activity one ATP would be hydrolyzed. The actual movement could be measured by physiological experiments on contracting muscle and was shown to be about 80-100 Å ²⁸. Since the cross-bridge was known to be an elongated structure, such a distance could be accommodated by a rotating or swinging cross-bridge model.

4.1.3. The cross-bridge cycle

Significant progress in understanding the structural, biochemical, and mechanical properties of biological motor proteins involved re-resolution of the significant states in the cross-bridge cycle, determination of structures of myosin and actin in these states, and measurements of the kinetics and the free energies of the state transitions set a stage for the development of structurally based model of muscle contraction. The detailed mechanism of transduction of chemical energy, derived from ATP hydrolysis, into mechanical work in the cross-bridge cycle is summarized in [Figure 4.3](#). The model consists of rapidly reversible low actin affinity (i.e. weak binding) states myosin·ATP, myosin·Pi·ADP, and actin-myosin·Pi·ADP, and slow detaching high affinity (i.e. strong binding) states actin-*myosin·Pi·ADP, actin-*myosin·ADP, and actin-myosin·ADP. A detailed description of the transitions between these states that also includes the power stroke is shown in the legend of [Figure 4.3](#). In the absence of ATP, the myosin cross-bridge binds tightly to actin filaments. However, it also binds and hydrolyses ATP. ATP binding brings about a rapid dissociation of the cross-bridge from actin ([Fig. 4.3](#), step 1). Thus the cross-bridge can bind either actin or ATP but to both only transiently. Solution kinetic observations were very important in establishing the relationship between the hydrolysis of ATP and the generation of force. A key feature of this process is the observation that transduction of the chemical energy released by the hydrolysis of ATP into directed mechanical force should oc-

cur during product release (ADP and inorganic phosphate, Pi) rather than during the hydrolysis step itself²⁷. Without actin, myosin is product-inhibited and is a poor ATPase. Mg-ATP rapidly dissociates the actomyosin complex on binding to the ATPase site of myosin; myosin then hydrolyzes ATP and forms a stable myosin-products complex; actin recombines with this complex and dissociates the products, initially the γ -phosphate ion thereby forming the original actin-myosin complex. Force is generated during the last step.

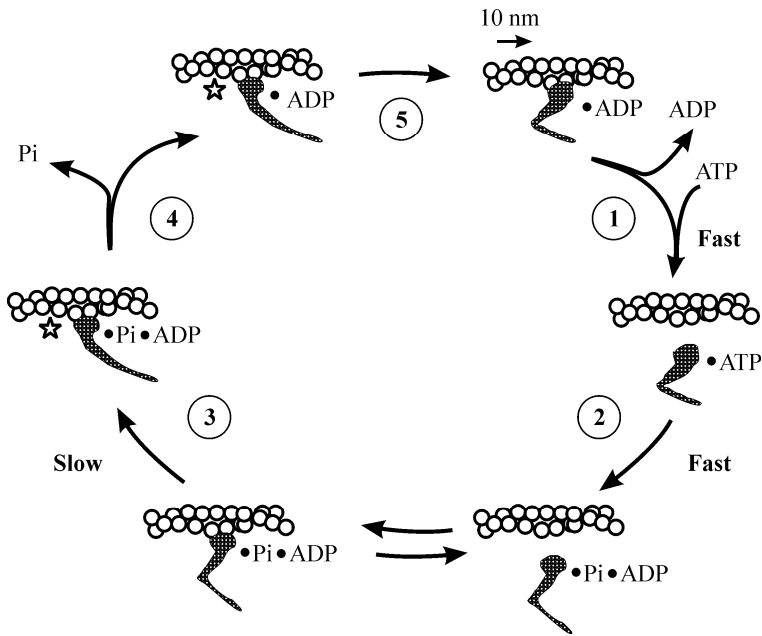


Figure 4.3. Cross-bridge cycle and actin-activated myosin ATPase cycle. Shown are only essential actin-activated myosin states and their transitions. In step 1, ATP binds to globular head of myosin molecule, which results in sufficient conformational change to cause the rapid dissociation of the myosin head from the actin filament; In step 2, the ATP is rapidly hydrolyzed to ADP and Pi, which remain tightly bound to the myosin rapidly forming a low affinity interaction with actin (i.e., by forming an actin-myosin-Pi-ADP complex); In step 3, a slow transition to an activated, high affinity pre-stroke form the actin-myosin complex (actin-*myosin-Pi-ADP). This slow state transition process limits the total cycle time; In step 4, this conversion to the high affinity form triggers the release of Pi which in step 5, triggers large conformational change that gives the lever arm motion of about 10 nm. This conformational change allows ADP to dissociate. The combination of steps 4 and 5 is referred to as “strongly bound-state time” as the myosin is strongly bound to actin throughout these steps. Dissociation of ADP allows rapid binding of ATP to myosin, and the cross-bridge cycle repeats (After Spudich¹²).

The model of cross-bridge cycle in Figure 4.3 is simplified to only essential states. There are, however, a number of intermediate states deter-

mined from biochemical studies in solution²⁹, but these biochemical states may not necessarily have corresponding structural states and *vice versa*. At this point, it is unclear to what degree these intermediate states are relevant for the physiology of muscle fibers, and a critical understanding of the role of these states in muscle contraction needs further investigation. In contrast, most of the sliding filament models presume that some transition rates between the states in Figure 4.3 are so fast that they can be merged into a single effective state, and yet, the transformation of chemical energy into mechanical work and, therefore, force production and shortening velocity may not be significantly affected.

4.1.4. Swinging lever arm and power stroke

The critical step in the transformation of chemical energy into mechanical work is entrenched in stepwise rotation (power stroke) of S1, originally called a tilting cross-bridge^{26,28}. The biochemical states associated with these mechanical states has been identified³⁰, and also recognized in recent structural studies^{11,12,31}. The structural studies of acto-myosin interaction envision that most of the cross-bridges bind to actin without rolling on the actin surface during the power stroke. The large rotation movements come from part of the myosin S1 fragment, so called swinging lever arm^{2,13,32,33} (Fig. 4.4a,b). A swinging lever arm also helps to explain why substantial changes in the cross-bridge orientation were difficult to see from x-ray diffraction studies³⁴: only a small fraction of the cross-bridge mass moves much during the power stroke.

Figure 4.4. Swinging lever arm hypothesis: **a)** Schematic representation of S1 (head portion) of the myosin molecule consisting of the binding and converter domain (fixed relative to actin filament, and swinging lever arm that during the “power stroke” pools on myosin tail (S2)) which is attached to myosin filament and causes relative movement of the myosin filament relative to the actin filament. **b)** A model for the “power strokes” of myosin motors shows about ~100 Å motion of the lever arm domain that is generated when the motor undergoes a transition from an ADP-Pi-bound state to an ADP/nucleotide-free conformation. Shown are the converter/lever arm positions in ADP-Pi (*yellow*) and nucleotide-free (*red*) states, the similar catalytic cores (*blue*), and the actin filament (*gray*; pointed end toward the top) (After Vale and Milligan¹³). Please see the Figure on the page 266.

The ‘swinging lever arm’ hypothesis for muscle contraction (Fig. 4.4) has been supported by results from a number of recent experiments³⁵⁻³⁷, crystal structures^{11,31,38,39} and cryo-EM images^{40,41}, and is now generally accepted as the mechanism of force generation by myosin, which is coupled to phosphate release². Despite the problems and uncertainties, current knowledge of the molecular events determining muscle contraction is highly advanced with a good measure of agreement about the biochemi-

cal cross-bridge cycle, the mechanism of force generation and its relation to biochemical events, and the kinetic and structural differences of myosins in fast and slow muscles. Consequently, the swinging myosin cross-bridge hypothesis of muscle contraction had become the textbook norm by 1972. However, regardless of all technological advances, it is still remarkably difficult to catch a bridge *in flagranti delicto*³². In fact the hypothesis had been modified over the years into a swinging lever arm hypothesis in which the bulk of the cross-bridge is envisaged to bind to actin with a more or less fixed geometry and only the distal (C-terminal) part of the myosin molecule moves³³ (Fig. 4.4).

4.1.5. Atomic structures of actin and myosin

Actin (thin filament) fibers (Fig. 4.5) are helical polymers of G-actin (i.e. globular-actin). The structure of monomeric actin which contains 365 residues and has a molecular weight of 42,000 was solved by protein crystallography as a 1:1 complex with the enzyme DNase I⁴². Orientated gels of actin fibers (F-actin), a helical copolymer of actin which has 13 molecules in 6 turns repeating every 360Å, yield x-ray fiber diagrams to about 6Å resolution. It was possible to determine the orientation of the G-actin monomer which best accounted for the F-actin fiber diagram⁴³ and thus arrive at an atomic model of the actin filament.

Figure 4.5. Atomic structure of actin. (a) G-Actin. ADP and the divalent cation are highlighted; (b) F-Actin; surface representation of 13 subunit repeat based on Ken Holmes' actin filament model. Please see the Figure on the page 266.

The cross-bridges comprise a part of the myosin molecule, namely subfragment-1 of heavy meromyosin (S1). The structure of chicken S1 (Fig. 4.6) has been solved by x-ray. This study shows the S1 (which has 884 residues) to be tadpole-like in form, with an elongated head, containing a 7-stranded β sheet and numerous associated α -helices forming a deep cleft, with the actin binding sites and nucleotide binding sites on opposite sides of the sheet. The cleft separates two parts of the molecule which are referred to as the 50K upper and 50K lower domains or actin binding domain. The C-terminal tail, sometimes called the “neck”, which also provides the connection to the thick filament forms an extended α -helix which binds two light chains. The ATP binding site contained the typical “P-loop” motive which is also found in the G-proteins.

Figure 4.6 Structure of myosin S1 fragment¹¹. It consists of myosin motor domain, converter domain and light chain binding domain (lever arm). Please see the Figure on the page 267.

By fitting the atomic structures of f-actin and S1 into three dimensional cryo-electron microscope reconstructions, an atomic model of the actin myosin complex is developed ² (Fig. 4.7). In particular, this model establishes the spatial orientation of the S1 myosin fragment in the active complex. For example, cleft in myosin extends from the ATP binding site to the actin binding site and the opening and closing of this cleft is very likely to provide the communication between the ATP site and the actin binding site. The actin binding site spans the 50K upper and lower domains and the ATP binding site extends from the 50K upper domain into the 50K lower domain. Furthermore, the very extended C-terminal α -helical neck of S1 is ideally placed to be a lever arm. The lever arm joins onto the bulk of the molecule via a small compact “converter domain” ³⁹ which lies just distal to a broken α -helix containing two reactive thiol groups known as SH1 and SH2. Numerous experiments point to the putative “hinge” for the lever arm being in the SH1-SH2 region of the molecule ³³.

Figure 4.7 Beginning and end of myosin’s working stroke. (a) model of the pre-power stroke state of myosin docked to actin; (b) Model of post power stroke ². Please see the Figure on the page 267.

4.2. BUILDING A COMPREHENSIVE MODEL OF MUSCLE CONTRACTION

The above biochemical and structural findings, taken together with the cross-bridge forces, the sliding distance generated for each enzymatic cycle of the acto-myosin ATPase, and the duration of cross-bridge attachment measured in motility assays, are a base for developing structurally based sliding filament models of muscle contraction. This is a formidable task because the distortion effect imposed by the extensibility of thin and thick filaments further complicates the relationship between in vitro measurements and the measurements in intact fibers.

A growing body of experimental evidence from the molecular studies, in many ways conflicting, needs to be reconciled with the physiological data in intact fibers. The main problem in interpreting these data is the wide range of values obtained by single molecule measurements (Table 4.1); many possible interpretations are consistent with these experimental data. Currently, there is no consistent approach or systematic framework for dealing with this problem.

Table 4.1. Experimental data of skeletal myosin II and smooth muscle myosin II

<i>Parameter</i>	<i>Motility Assay</i>	<i>Intact Fibers</i>
Cross-bridge force/head (at $V = 0$)	1 - 7 pN	3.4 – 6 pN
Cross-bridge stiffness	0.4 – 0.7 pN/nm	2 pN/m
Stroke Displacements	5 – 20 nm	5 – 10 nm
Distance/ATP ($F=0$)	5-30 nm	240 nm
Cycle Time		
Skeletal	80 ms	40 ms
Smooth	380 ms	400 ms
Duty Ratio	0.035 - 0.14	0.2 – 0.7

4.2.1. What is the appropriate model to start with?

The latest generation of sliding filament models can be divided into two groups: *probabilistic models* that consider mean values of state probabilities, state transition fluxes, and cycle fluxes, and *stochastic models* that consider fluctuations at the state level, between cycle and state, and the fluctuation in state probabilities. Probabilistic models are based on mean probability of a large ensemble of cross-bridges (i.e. projections from myosin filament whether they are attached to actin or not⁴⁴) to be in particular biochemical state, and these probabilities can be applied to smaller subensembles that contain cross-bridges with the actin site in the neighborhood of particular distance x , measured from the position where the cross-bridge force is equal to zero. Stochastic models are based on a biased random walk of any one cross-bridge. Both of these models are rooted in the sliding filament hypothesis from the 1950's^{23,24} and they differ only in the description of the ensemble of myosin molecules: probabilistic approach first defined by A.F. Huxley in his 1957 paper¹ and stochastic formulated by T.L. Hill⁴⁴.

The integration of the biochemical acto-myosin cycle (Fig. 4.3) into a sarcomere lattice (i.e. sliding filament model) can be summarized as follows. Each myosin head that is anchored in the thick filament can bind stereospecifically to adjacent sites on the thin filament. The myosin head contains a lever arm that amplifies *any* small change in conformation that occurs when different ligands bind at, or dissociate from, the nucleotide binding site (Fig. 4.4). The resulting conformational change creates a moment acting on the proximal end of the lever arm and causing its distal end to move⁴⁵. The distal end arm movement is simultaneously accommodated by the compliance of elastic elements within the neck of the molecule, presumably in S2 (i.e. coiled-coil part of myosin molecule which

connects myosin fragment S1 and myosin filament), and the compliance of the actin and myosin filaments.

4.2.2 Energy landscape of myosin binding to actin

A crucial aspect of myosin action is the way in which mechanical forces affect its chemistry and *vice versa*. The biochemical acto-myosin cycle, first proposed by Lymn and Taylor²⁷ and further refined by the inclusion of a number of intermediate states^{29,46,47}, leads to the development of cross-bridge models that more closely integrate relevant structural, biochemical, and biophysical properties of contracting muscle obtained at the fundamental level of the individual interacting molecules. A simplified scheme of the hydrolysis cycle that regulates the affinity of the myosin (head) for the actin filament is shown in Figure 4.8a, and parallels the structural picture drawn in Figure 4.3. Myosin with bound ATP has a low affinity for actin, but the “primed” head, which is the product of ATP splitting, binds readily. Once the head is attached, the rapid release of P_i provokes a major rotation, or “power stroke,” of the lever arm. Subsequently, ADP dissociates only slowly, giving rise to a change of conformation of (as yet) unspecified size. This event is immediately followed by the binding of ATP, which destabilizes the acto-myosin interaction and causes the head to detach, thereby completing the cycle. Biochemical measurements in solution provided the actual change in the free energy levels and in the rate transition constants between the states (the minima in parabolas shown in Fig. 4.8b); however, these data did not include any strain dependence induced by the cross-bridge force generation.

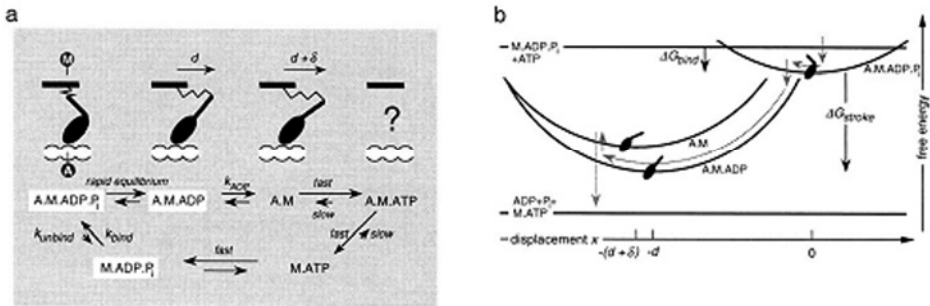


Figure 4.8. a) Biochemical cycle of myosin, showing the conformation of the head domain that corresponds to each chemical state. M labels the point of attachment of the head to the thick filament and A labels the binding site on the thin filament. Because of the fast reactions, only the three states boxed in white are populated to a significant degree; b) because of the linear elastic element in the myosin neck, the free energy of attached states varies quadratically with the displacement x of A relative to M (the elastic strain of A·M·ADP· P_i is taken to be zero at $x = 0$). The gray arrows indicate the typical reaction pathway of a myosin molecule over an actin-activated myosin ATPase cycle. (After Duke,^{14,15}).

T.L. Hill introduced the thermodynamic arguments that constrain the strain-dependence of the reaction rates^{44,48} and also included power-stroke transition²⁸. The ratio of forward and reverse state transition rate constants between any two states is determined by the free energy difference. If this is a function of the strain, as it will be if at least one of the states is attached to actin, then at least one of the rate constants must be strain dependent. The functional form of the dependencies, however, is undetermined. A rational approach to this problem, taken here, is to adopt Kramers' theory of chemical reactions⁴⁹, in which the rate depends exponentially on the free energy required to effect the transition. Because the free energy barrier is modified by changes in the elastic energy associated with conformational changes, the strain dependence of reaction rates is determined by the parameters that specify the structural properties of the molecule—the effective spring constant κ and the displacement d of the distal point of the lever after carrying out the power stroke. A hypothetical energy landscape that includes a quadratic free energy relationship caused by linear elastic spring located in the myosin neck (or S2) is shown in [Figure 4.8b](#). The additional distance moved by the lever on ADP release, observed in smooth muscle myosin II^{50,51} causes a jump to a slightly higher energy level. It is worth emphasizing that this approach provides more precise theoretical constraints than previous models^{1,52-54}, which include rate constants that are arbitrary functions of the strain. Moreover, structural changes alone may be responsible for the strain dependence, and these changes are necessary for each reaction that involves an alteration of ligand. This approach has been used by Smith and Geeves^{55,56} and further elaborated by Smith⁵⁷ in a probabilistic model, while Duke^{14,15} introduced an elegant stochastic model.

4.2.3. Extensibility of actin and myosin filaments

The existence of thin and thick filament extensibility introduces previously unrecognized complications into the sliding filament model of muscle contraction. Two independent laboratories have firmly established that the actin filament, and probably the myosin filament as well, exhibit extensibility comparable to or larger than that of the cross-bridge itself^{16,17}. Goldman and A.F. Huxley⁵⁸ have pointed out that this new evidence invites reexamination of the theory of muscle contraction at the most basic level. Following on this work, we have shown, for example, that when filaments are extensible, small rapid length changes of the sarcomere are not experienced simultaneously or to the same extent by all attached cross-bridges⁵⁹. Extensibility implies that relative displacements between thick and thin filament are nonuniform within the region of overlap, cross-bridge strains vary systematically along the region of overlap, local shortening events

occur even during an isometric contraction, and local shortening reduces force substantially below what would be expected in a rigid filament system. As such, in a system with extensible filaments the connections between macroscopic mechanical events and underlying molecular events are distorted, and the distortions are not necessarily small. For example, it is well established that during muscle activation the development of muscle stiffness leads development of force⁷. This finding was long held to imply that myosin heads first attach in a state that generates stiffness but no force, and then go through a transition to a second state that generates both stiffness and force⁶⁰. We now know, however, that even with models that possess only one bound state, development of stiffness must lead development of force as a result of dynamics attributable to filament extensibility. This is because small relative movements between filaments can induce inhibition of cross-bridge force during power stroke⁵⁹. Thus, the mechanical behaviors of muscle must be re-examined in the context of thick and thin filament extensibility.

4.2.4. Calcium regulation

In vertebrate striated and smooth muscles calcium regulation comprises another essential mechanism of muscle contraction that must be described accurately at the molecular level in order to correctly link macroscopic muscle behavior to underlying molecular events. Incorporation of this critical process is necessary for proper interpretation of experimental data obtained during stimulations of varying intensities and consequent (transient) contractile responses.

In vertebrate striated muscle, calcium regulation occurs via additional actin-associated proteins, namely tropomyosin, whose filaments overlap end-to-end to span the actin filament, and the inhibitory component (TnI) of troponin. In 1973, Haslegrove and Huxley⁶¹ proposed a steric-blocking model in which tropomyosin has two discrete orientations on actin, one of which blocks myosin binding. However, recent X-ray diffraction studies of skinned fibers and oriented filaments, and EM reconstructions of isolated thin filaments, have shown three tropomyosin orientations, supportive of the three-state regulatory model proposed earlier by McKillop and Geeves⁶². In the absence of calcium, Tm sits in a ‘blocked’ position that prevents myosin binding. With calcium, Tm shifts to a ‘closed’ position that allows weak binding but not force-generation. Thermally activated movements to an “open” position allow force generation which is reinforced by strongly-bound myosin.

The first quantitative model of regulation by the thin filament was proposed by T.L. Hill and colleagues⁶³, which predates observation of the third regulatory state. Hill’s models incorporate end-to-end Tm interac-

tions, which enhance the number of actin sites that can be cooperatively regulated by Tm beyond the 7 sites associated with one Tm molecule; this enhanced cooperative feature is missing from the quantitative three-state model formulated by McKillop and Geeves⁶². Near-neighbor interactions between tropomyosins are included in Hill's model of thin filament regulation, but in a structurally unrealistic way by modifying end-to-end Tm interactions. Geeves and co-workers have confirmed the existence of end-to-end interactions in various Tm and Tm-Tn systems and from various lines of evidence suggested that a model of weakly-interacting rigid 7-site Tm filaments should be replaced by a model of more strongly-interacting flexible tropomyosins, forming a chain spanning the actin filament. A quantitative model of this kind has now been developed and tested on solution data^{64,65}.

In contrast, in smooth muscle (SM), the primary mechanism of activation by calcium is through phosphorylation of 20 kDa myosin light chain (MLC₂₀) by myosin light chain kinase (MLCK)^{66,67}. In absence of Ca²⁺ dephosphorylation of MLC₂₀ in intact SM precedes muscle relaxation. In effect phosphorylation is envisioned as “turning on“ cross-bridges analogous to Ca²⁺ activation in skeletal muscle. However, this is an oversimplified model. In reality, SM can maintain maximal tension in the presence of Ca²⁺ levels well below those necessary to trigger maximal contraction, even at phosphorylation levels of MLC₂₀ and rates of ATP hydrolysis of only 20-40% of maximum. These findings, together with the facts that (1) the cross-bridge cycling rate can vary without changes in MLC₂₀; (2) phosphorylation levels of MLC₂₀ are linearly related to Mg²⁺ ATPase activity of myosin filaments; and (3) steady state phosphorylation levels of MLC₂₀ are directly related to intracellular Ca²⁺ concentrations, suggesting that steady state tension and steady state ATP hydrolysis must be influenced by factors other than the number of active myosin heads.

This led to the latch hypothesis of Hai and Murphy^{3,68} where a new bound state, the “latch state”, was introduced. The latch state is created primarily by dephosphorylation of bound phosphorylated myosin heads. Dynamic behavior of a four state cross-bridge model that includes the latch state was intensively studied by Mijailovich et al.⁶⁹, Fredberg et al.⁷⁰ in airway SM, and by Yu et al.⁷¹ in invertebrate SM. Model predictions agreed remarkably well with experimental data from whole and permeabilized smooth muscle fibers.

4.3 MATHEMATICAL FOUNDATIONS OF SLIDING FILAMENT THEORY AND COMPUTATIONAL METHODS

THEORETICAL MODELS OF MUSCLE CONTRACTION

4.3.1. Basic concepts and definitions

Length scales. Striated muscle is organized at three length scales, which are those of the whole muscle, the half-sarcomere and a single myosin head. In smooth muscle, the sarcomere is replaced by a non-periodic lattice of actin and myosin filaments. To deal with extensible filaments and cooperative thin-filament regulation, models must be constructed at the level of the half-sarcomere or its equivalent in smooth muscle, since the kinetics of myosin heads are coupled by dynamic strains even when the length of the sarcomere is fixed. The geometry of the filament lattice is required and varies with the type of muscle²¹. Here we will consider two different scales of organization. A *local* (nano) scale describes the kinetics of actin-myosin interactions (cross-bridge cycle) for a single myosin head and also includes some aspect of thin filament regulation, and a *global* scale at the sarcomere level.

Sarcomeric models can be formulated in terms of the relative position and orientations of all myosin heads relative to neighboring actin sites on surrounding thin filaments, which determine the rate of myosin binding, and specified cross-bridge states for each myosin molecule. For rigid filaments, the strain-dependence of transition rates can be applied equally to all heads in the half-sarcomere because the global deformation is uniform (affine) along the sarcomere. However, for the extensible filaments the global strains do not map equally to all heads, thus, in that case, local condition at the level of each myosin head should be known to correctly account for rate dependence of state transition rates. We achieved this using a multi-scale approach described below.

Probabilistic methods are based on mean state populations of biochemical actin-myosin states in a large ensemble of cross-bridges; these probabilities can be applied to subensembles of cross-bridges with a given distance x between myosin and nearest actin site, so that cross-bridge force is proportional to x . The original sliding-filament model was formulated in terms of state probabilities by A.F. Huxley¹, and most subsequent models have followed this approach (e.g. Hill⁴⁸, Eisenberg et al.⁵², Pate and Cooke⁷²).

Stochastic methods describe transitions of a single cross-bridge between these states as a kinetically-based Markov process. They are traditionally implemented by Monte-Carlo simulations, which generate sampled time sequences of events for every cross-bridge in the sarcomeric model. The kinetic Monte-Carlo algorithm is very simple: the same rate

constants are used to generate the probability of a transition in a suitably small time interval (one Monte-Carlo step), which triggers a transition according to the value of a random number uniformly distributed in (0, 1). Such simulations are computationally expensive but are best implemented by using specially-developed sparse matrix solution methods⁷³⁻⁷⁶.

4.3.2. A probabilistic formulation of cross-bridge kinetics

Here we will briefly present a multi-scale approach applicable to sliding filament models in extensible filament lattice⁵⁹. We consider two length scales: a global scale, at the sarcomere level, that provides local strains acting on individual cross-bridges, and a local (nano) scale where molecular state transitions are accounted for. The global spatial coordinate is denoted X , and local spatial variable is denoted x . The mathematical formulation of the sliding filament model at the level of a single myosin-S1 head (local scale) is given in terms of the state probability $p_i(X, x, t)$, the probability of the head being attached to the thin filament (actin) at an actin site displaced by distance x at time t (Eulerian formulation) at global location X along the thick filament (myosin). Let us consider X as the only parameter that we will use later for the description of *global* field equations of an extensible filament system. We focus here on the molecular kinetics exclusively at the *local* (molecular) scale. The subscript i identifies the particular actin-S1 myosin state and runs from 1 to the total number of states n used in the cross-bridge cycle. The myosin may be detached or bound to actin.

The strain dependent state transitions between myosin states are governed by conservation laws expressed as field equations. In vector form, this system of partial differential equations becomes,

$$D \mathbf{p}(X, x, t) / Dt = \mathbf{M}(x) \mathbf{p}(X, x, t) \quad (4.1)$$

Let us first focus on myosin strain dependent states only. In this case $\mathbf{M}(x, t) \equiv \mathbf{M}_x(x)$, where the components of $\mathbf{M}_x(x)$ are built from rate constants $k_{ij}(x)$ for the transition from state i to state j , i.e.

$\mathbf{M}_x(x) = k_{ji}(x) - \sum_{i=1}^n k_{ij}(x) \delta_{ij}$, where $\delta_{ij} = 1$ if $i = j$ and 0 otherwise. Each

component of the vector $\mathbf{p}(X, x, t)$ is the probability of finding the myosin head in one of its n states at time t , for a myosin such that x is the position of the nearest active site on actin relative to the equilibrium position of the cross-bridge on the myosin filament¹. The operator D/Dt is the material or convective derivative $\partial/\partial t - V(X, t)\partial/\partial x$, where $V(X, t)$ is the shortening velocity of the actin filament relative to myosin filament at position X from the M-band.

Although the transition matrix $\mathbf{M}_x(x)$ is of order $n \times n$, it has rank $n-1$ because the structure of eq. (4.1) preserves the normalization of probabilities, which says that myosin must be in some state of the complete set. It can be shown that this condition is a consequence of the lack of independence of the rows of the transition matrix; the sum of all the rows is a column of zeros, i.e. $\mathbf{M}_x(x)$ is singular. To find unique solution of eq. (4.1), it is necessary to replace in $\mathbf{M}_x(x)$ one row by the constraint equation coefficients derived from the above preservation of probabilities^{55,56,69} (i.e. the sum of all $p_i(X, x, t)$ at particular x and t is equal to 1).

The instantaneous force was computed from the first spatial moment of cross-bridge probability distributions of all attached states, while the state populations are computed from the zeroth moment of the state probability distributions. The rate of ATP consumption was separately computed from the fluxes for each of the transition processes that consume ATP, e.g. dissociations of myosin from actin, or phosphorylation of myosin light chains.

The generalization to regulation. Following the rules described at the beginning of this section, we derive the rate transition matrix $\mathbf{M}(x, t)$ for a particular acto-myosin binding scheme by expanding the cross-bridge rate transition matrix $\mathbf{M}_x(x)$ to the two population of states: i) the states with Ca^{2+} bound to troponin in skeletal and cardiac muscle, or phosphorylated myosin states in smooth muscle; and ii) the states without Ca^{2+} bound to troponin, or unphosphorylated states, respectively. The transitions between these two populations of states are defined by the calcium concentration and thus these rate constants may also depend on time varying calcium concentration $\text{Ca}(t)$.

The Generalization to Extensible Filaments. When filaments are extensible, the main difficulty is that the relative sliding velocity V , vary not only with time but also with (global) position X along the thin filaments⁵⁹. Eq. (4.1) must be solved *locally* at each position, and then embedded into *global* field equations that describe the distribution of stresses and strains in filaments, which vary on the scale of the length of filament overlap in the half sarcomere. Because relative displacements between thick and thin filament and $V(X, t)$ depend simultaneously on boundary conditions and cross-bridge tractions, $\tau(X, t)$ generated by myosin binding (eq. 4.1) to actin, in turn, explicitly depend on $V(X, t)$, the problem needs to be solved iteratively (Fig. 4.9). The global system of field equations, and the strategy to solving them are described in detail in Mijailovich et al.⁵⁹.

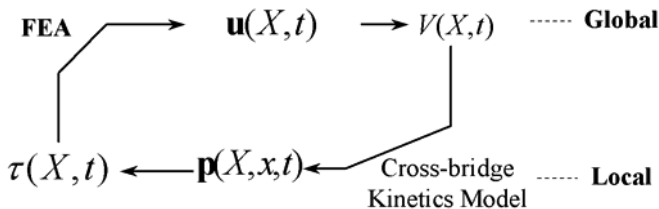


Figure 4.9 Iterative scheme used for the solution of the sliding extensible filament model. *Global scale:* From known distribution of cross-bridge tractions along thick and thin filament overlap, $\tau(X,t)$, and prescribed boundary conditions at the ends of the sarcomere we calculate the filament strains, $\epsilon(X,t)$, and displacements, $\mathbf{u}(X,t)$, and heretofore, relative velocity between the filaments, $V(X,t)$, by solving the *global* field equations (Eq. 7, see below). *Local scale:* From the known $V(X,t)$ and parameters of the cross-bridge model we calculate the state probabilities, $\mathbf{p}(X,x,t)$, by solving the system of partial differential equations (eq. 4.1). Finally, from the known $\mathbf{p}(X,x,t)$ we calculate $\tau(X,t)$. Being an implicit scheme, the simultaneous satisfaction of all global and local equations requires iterations at each time step such that all equations are satisfied to a preset tolerance. The same iterative scheme applies to models proposed in other parts of the project.

4.3.3. Rules for strain-dependent cross-bridge transition rates

In principle, strain-dependent rates $k_{ij}(x)$ of cross-bridge transitions can be deduced from structural features of myosin and a binding region on an actin filament when both are tethered as in the sarcomere. The literature abounds with *ad hoc* strain-dependent functions whose only justification is through the predictions of the resulting model. However, in practice it is necessary to postulate simple reaction pathways and how they might be modified by tethering. With the atomic structures of both molecules at hand, it now becomes possible. T.L. Hill has emphasized that the ratio of forward to backward rates must satisfy Gibbs' thermodynamic identity

$$K_{ij}(x) \equiv k_{ij}(x)/k_{ji}(x) = \exp\left[-(G_j(x) - G_i(x))/k_B T\right] \quad (4.2)$$

in terms of the Gibbs energies of the initial and final states, including the elastic strain energy derived from the tension^{48,77}. Thus each rate constant $k_{ij}(x)$ is composed of a strain-independent factor k_{ij} which, in principle, is the rate observed in a solution-kinetic experiment under the same conditions, and a x -dependent (strain-dependent) factor which tends to be equal to 1 when the molecules are not tethered.

The physics behind models of strain-dependent thermally-activated chemical reaction rates originates from the transition-state theory⁷⁸ as updated by Kramers⁴⁹. To the logarithmic accuracy, the rate of reaction is

limited by the energy barrier presented by the point of highest Gibbs energy on the reaction path. For example,

1. For binding $M \cdot ADP \cdot P_i \rightleftharpoons A \cdot M \cdot ADP \cdot P_i$ the activation energy is supplied by thermal (Brownian) fluctuations. The elastic element of the detached myosin molecule fluctuates thermally and the strain-dependent binding rate varies with displacement between associated actin and myosin site, x_o

$$k_1(x) = k_{bind} \exp(-\kappa x_o^2 / 2k_B T) \quad (4.3a)$$

where $k_{bind} = k_{P_i}$ is overall binding rate of $M \cdot ADP \cdot P_i$ to actin, T is absolute temperature and k_B is Boltzmann's constant. The reverse reaction occurs at a constant rate $k_{-1} = k_{unbind}$.

2. Two states $A \cdot M \cdot ADP \cdot P_i$ and $A \cdot M \cdot ADP$ are assumed to be in dynamic equilibrium because the forward/backward reaction between them is rapid. Also the P_i release is accompanied by a large (negative) change in chemical free energy $\Delta G_{stroke} = \Delta G_{P_i}$. Thus, to define the population of these states it suffices to specify the ratio of forward and reverse rates (i.e., ratio of the relative probabilities of these post- and pre-power stroke states) that also includes the change in elastic energy of the power stroke:

$$k_{-2}(x) / k_2(x) = \exp[-\Delta G_{stroke} - (\kappa d^2 / 2k_B T)(2x/d + 1)] \quad (4.3b)$$

where d is displacement of the lever arm after carrying out the power stroke.

3. For strain dependent ADP release (i.e., $A \cdot M \cdot ADP \rightarrow A \cdot M$), the difference between initial and final strain energies gives the forward rate as:

$$k_3(x) = k_{ADP^0} \exp\left[(-\kappa \delta^2 / 2k_B T)(2x/\delta + 1)\right] \quad (4.3c)$$

where δ is displacement that lever arm must move to open the nucleotide pocket and allow ADP release, and k_{ADP^0} is the rate of ADP release when the elastic element is relaxed. ATP binding is much faster than the reverse rate k_{-3} , and thus any strain dependence due to conformational change has almost no effect. It is therefore reasonable to take k_3 to be constant. Furthermore, ATP-mediated detachment is sufficiently faster than the reverse reaction that the latter can be safely neglected.

All forms satisfy detailed balancing. Various modifications can be envisaged. For example, binding becomes a much flatter function of x if the head is able to make a rotationally-flexible bond to actin and this step is rate-limiting for any subsequent transition to a stereo-specific state. The

rate of binding may also change with variations of myosin affinity caused by mismatch of the pitch of actin (and myosin) filament(s), generating target zones as observed by Steffen et al. ⁷⁹. The rate of the force-generating step should not become arbitrarily large at negative x , and an x -independent rate is expected when strain-energy favors the post-force state sufficiently ⁷⁷. Similar comments apply to eq. (4.3c), which controls the rate of ADP release by coupling the opening of the nucleotide pocket to an additional swing of the lever arm ^{56,57}. Some strain-dependence of this step seems to be required to generate the Fenn effect, as envisaged in Huxley's 1957 model.

4.3.4. Stochastic strain dependent binding in 3D sarcomere lattice

For comprehensive understanding of coupling between the rates of biochemical processes and mechanical forces actin on molecular bonds precise information of strains acting on the molecular bonds is necessary. We are developing 3D model of sarcomere that includes stochastic strain dependent binding between discrete (exact) locations of myosin molecules and actin binding sites. This approach to 3D binding defines myosin-actin interactions in the context of target zones, which are prescribed by the spatial arrangement of actin and myosin filaments in the sarcomeric hexagonal lattice ^{79,80}. The 3-D mechanokinetic model for the muscle half-sarcomere includes: (i) extensible filaments, (ii) allow all feasible head-site of actin-myosin interactions in the 3-D filament lattice, (iii) discrete head positions on myofilaments, and (iv) the heads bind to target zones on F-actin. In our comprehensive analysis we used stochastic (Monte Carlo) simulations. Because we calculate the molecular at forces for each molecular bond at any instant of time the modulation of biochemical transition caused by these forces can be precisely taken into account.

4.3.5. Probabilistic and stochastic numerical solutions

For simplicity, we will only point out the numerical methods that we will use to solve the above equations, and our references were the methods are described in detail. The solution of eq. (4.1) is obtained by methods of characteristics ⁵⁹, and the finite element nonlinear iterative procedures for solution in 1D, and in 3D sarcomere are described in Mijailovich et al. ^{59,69}, and Kojic et al. ^{81,82}. Monte Carlo simulations of myosin stochastic binding are explained in Smith et al. ^{64,65,83,84}.

4.4. THEORETICAL MODELS OF MUSCLE CONTRACTION

4.4.1 Huxley's sliding filament model in extensible filament lattice

In 1957, Huxley proposed the first molecular model of muscle contraction in which myosin heads participate *independently* in individual, force-generating ATPase cycles. The model considers only two myosin states: detaches state when myosin is dissociated from actin, and attached state when myosin is bound to actin. The transitions between these states are defined by state transition matrix:

$$M(x) = \begin{bmatrix} f(x) & g(x) \\ 1 & 1 \end{bmatrix} \quad (4.4)$$

where $f(x)$ is binding rate unbound myosin heads, and $g(x)$ is dissociation rate of myosin heads bound to actin. For simplicity we assumed only one myosin head active for binding per myosin molecule, historically called cross-bridge. Strain dependence of binding rates is defined as in the original work of A.F. Huxley¹:

$$\left. \begin{aligned} f(x) &= \begin{cases} 0, & x < 0 \\ f_1 x, & 0 \leq x \leq h \\ 0, & h < x \end{cases} \\ g(x) &= \begin{cases} g_2, & x < 0 \\ g_1 x, & 0 \leq x \end{cases} \end{aligned} \right\} \quad (4.5)$$

The second row in state transition matrix (eq. 4.4) represents normalization that constrains the probabilities of bound and unbound states to be equal to 1 at any x .

The Distribution of Axial Filament Strains During Isometric Force Development. The isometric preparation is one where the sarcomere is held at fixed overall length. With rigid filaments, this global isometric condition implies local isometric conditions. With extensible filaments, however, there will be systematic local length changes and nonzero local relative velocities of actin vs. myosin even when overall sarcomere length is held fixed. These in turn will have an immediate effect both on the stiffness and the force developed, as these are direct functions of filament strain and local relative velocities.

We begin with a given set of distributions of attached cross-bridges $p(X, x, t)$. Here X is position along myosin filament. Initially, $p(X, x, t)$ is equal to zero relaxed muscle, or might be defined from steady state solution at full tetany prior to a quick shortening simulation. These distribu-

tions in x determine an initial set of tractions, $\tau(X, x)$ in X . The tractions are defined as

$$\tau(X, t) = c \int_{-\infty}^{+\infty} x p(X, x, t) dx \quad (4.6)$$

where $c = k_{XB} / l_a l_m$, k_{XB} is cross-bridge stiffness, l_a and l_m are distances respectively between successive actin sites and successive myosin heads, and $p(X, x, t)$ is the fraction of cross-bridges (at global coordinate X) at local position x that are attached. For X distribution of tractions at any instant, we solve the mechanical equilibrium field equations prescribed in terms of the displacements:

$$\left. \begin{aligned} K_m \frac{\partial^2 u_m(X, t)}{\partial X^2} &= -\tau(X, t) \\ K_a \frac{\partial^2 u_a(X, t)}{\partial X^2} &= +\tau(X, t) \end{aligned} \right\} \quad (4.7)$$

The interface condition, eq. (4.7), includes the distribution of attached cross-bridges which are calculated from first order hyperbolic partial differential eq. (4.1) and it depends on the local relative velocity between filaments. In turn, the deformation of filaments and heretofore, relative velocity, depends on traction distribution along the filaments. This makes the problem simultaneously dependent on the tractions defined at a local level and relative velocity defined at global level. The solution of the problem is obtained numerically by the method of characteristics for local tractions and by finite-element method for the actin and myosin filament deformations by using an iterative scheme described in ⁵⁹.

We solved the field equations for isometric force development beginning with the filaments in a resting state, with strain everywhere zero at $t = 0$. Furthermore, the probability of cross-bridge to be attached is also taken to be 0. At $t = 0^+$, Ca^{2+} is assumed to have flooded the sarcomere, with its associated relief of the troponin/tropomyosin inhibitory complex, and allowing cross-bridges to begin attaching. We examined the time rate of evolution of both the stiffness and the force.

Force Development. We focused on isometric force development because the effect of filament extensibility in this circumstance is significant and, as we will demonstrate, challenges the interpretation of experimental evidence that rest on current theories of muscle mechanics. We quantitatively assessed the nonuniform relative filament displacement, cross-bridge strain and, importantly, the local shortening velocities that - even at constant over-

all sarcomere length - depress force below that which would have developed if the filaments had been inextensible. We show that filament extensibility may be a major effect contributing to the difference in the timing of force versus the timing of stiffness development, and the evolving relationship between stiffness of number of cross-bridges attached.

The temporal evolution of force and the distributions of attached cross-bridges are shown in Figure 4.10. The cross-bridge distributions at early times are triangular in shape reflecting the shape of stain dependent rate function, $f(x)$, while the distributions approach a rectangular shape at large times, reflecting the equilibration between binding and dissociation rates, $(f(x)/(f(x) + g(x)))$.

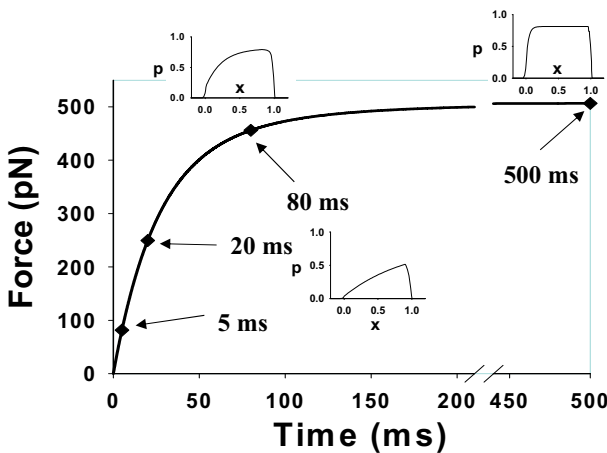


Figure 4.10. Force development calculated from Huxley's cross-bridge model in extensible sarcomere lattice. Inserts represent probability distributions of attached cross-bridges, $p(x,t)$, at different instants during force development.

During force development, an extensible filament system displays the following three characteristics that are quite different than obtained from the rigid filament model: 1) changes of muscle stiffness lead changes of force (Fig. 4.11); 2) stiffness is prominently dissociated from the number of attached cross-bridges during force development (Fig. 4.12a); and 3) estimates of cross-bridge stiffness are significantly higher than previously assessed by inextensible filament models (Fig. 4.12b).

The temporal relationship of developing stiffness versus force is an important part of the interpretation of experimental evidence in terms of the kinetics of myosin attachment rates and the multi-state hypothesis, and that multi-state binding is necessary to account for the experimental observations in rigid filament models of muscle mechanics. This interpretation supports the widely accepted notion that cross-bridges can be attached in more than one state, namely an early state that is non-force producing and, later, through a conformational change, a second state that is force producing
5,11,12,28,85. Although this mechanism provides an explanation for the sign of

the difference in stiffness and force development, the force lag is quantitatively too short⁷. Other, longer lasting non-force producing states may exist and there may be mechanisms of long range cooperativity⁷ that could also account for the observed lag.

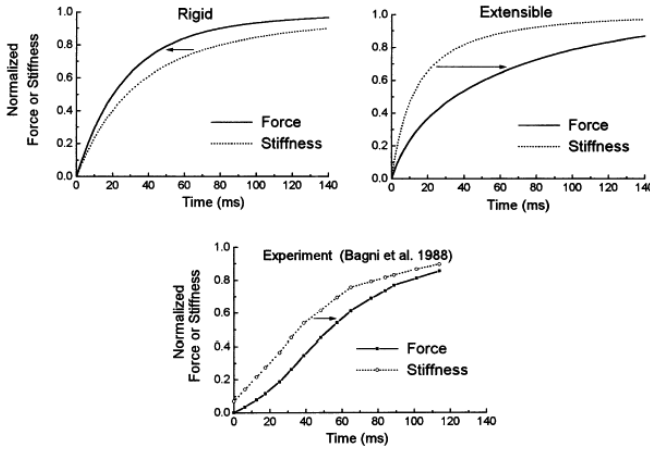


Figure 4.11. Upper panels: The time evolution of normalized force (indicated by the *dashed lines*) and normalized stiffness (*solid lines*) in the rigid and extensible filament models. Note that stiffness *lags* force in the rigid filament model and stiffness *leads* force in the extensible filament model. Lower panel: For comparison, the experimental points of Bagni et al.⁷ are shown. Note that stiffness *leads* force in the experimental preparation, consistent with the extensible filament model, and inconsistent with the rigid filament model.

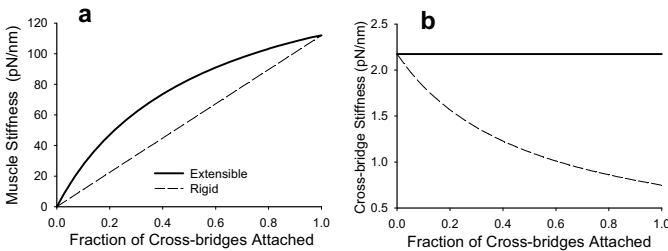


Figure 4.12 The relationship of developing overall muscle stiffness and the cross-bridge stiffness to the fraction of total number of cross-bridges attached. **a)** Muscle stiffness dissociates from number of cross-bridges attached (N_{att}) in extensible filament model, whereas it is strictly proportional to N_{att} in rigid case. **b)** The assessed cross-bridge stiffness from rigid filament model is markedly lower at higher N_{att} , then correctly calculated from extensible filament case.

On the other hand, we propose an alternative mechanism (which does not preclude the existence of multiple binding states or cooperativity, but does

not require such postulates) found simply in the consequences of extensible filaments, even with a single force producing binding state. The other two important issues regarding number of attached cross-bridges and the cross-bridge stiffness are still under debate because of conflicting experimental evidence from motility assays and intact fibers^{86,87}, may, in part, be explained by the distortion effect originated from filament extensibility. Moreover, the reformulated analysis also implies that the local behavior of one myosin head must depend on the state of myosin binding at neighboring attachment sites. This cooperativity occurs exclusively through local sliding velocities (i.e. nonuniform change of relative displacements), which can be significant even during isometric force development. The resulting cooperativity of myosin binding is grounded in fiber mechanics and follows inevitably from filament extensibility. This issue raises the question of whether the cross-bridges are independent force generators, as assumed in number of sliding filament models^{1,14,15,54-57,72,85,88,89}, or whether the action of one depends on the action of other cross-bridge, perhaps remote, connected by extensible filaments?

Why are the Implications of Filament Extensibility Difficult to Anticipate?

The reason is that small changes globally (i.e. at the scale of the sarcomere) may induce large and important changes at the molecular scale where the myosin head interacts with the actin filament. The relative displacement between the extensible thick and thin filaments of only a few nanometers can alter biochemical cross-bridge cycling and, therefore, cross-bridge force generation. For example, during isometric force development growing cross-bridge tractions (i.e. cross-bridge force per unit length) transfer loads *locally* between filaments, causing them to extend and, therefore, to slide *locally* relative to one another even during a contraction in which the muscle is not allowed to shorten. At full tetany relative displacements between the extensible filaments are nonuniform over scales of 4-5 nm, that is, about the length of the power stroke (5-11 nm). The nonuniformity of the relative displacements in some cases can be large, for example during force (re)development after a step change in length. On a local (molecular) scale, then, the very notion of “isometric” force (re)development becomes a logical impossibility, even when spot-follower servo technology is brought into play to regulate sarcomere length. Such behavior implies, even with a slight degree of filament extensibility, as reported by H.E. Huxley et al.¹⁶ and Wakabayashi et al.¹⁷, that: 1) relative displacement between the two filaments must be nonuniform along the region of filament overlap, 2) cross-bridge strain must vary systematically along the overlap region, and importantly, 3) the local shortening velocities, even at constant overall sarcomere length, reduce force well below the level that would have developed if the filaments had been inextensible. In [Figure 4.13](#) are shown the distributions of tractions and ten-

sions in actin and myosin filaments and their relative velocities during force redevelopment (T1-T2 transition). Evolution of cross-bridge tractions was calculated by the simplest two state model of Huxley¹, which may not be adequate to capture T1-T2 fast transients, yet is sufficiently accurate to show the magnitude of nonuniform tractions, and small but important sliding velocities. These tractions and relative velocities are directly related to the nonuniform imposed stretch on S2 (i.e., cross-bridge elastic element) by the sliding extensible filaments.

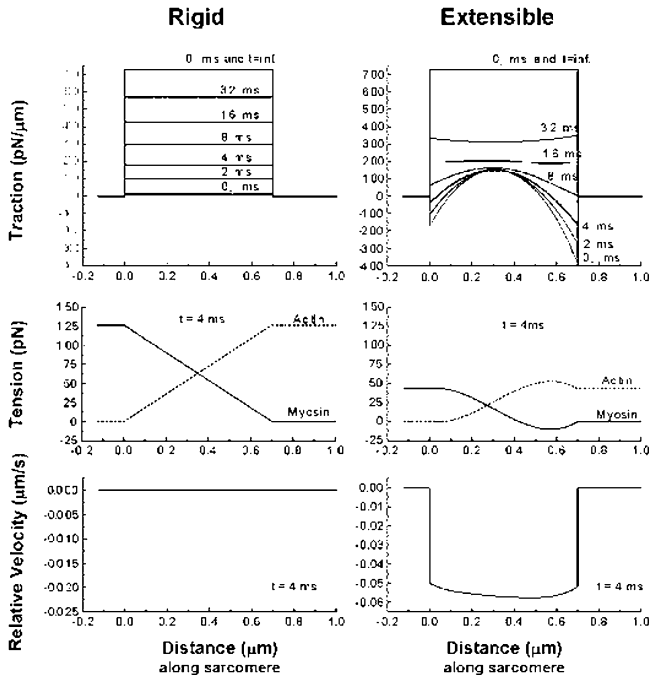


Figure 4.13 The axial distribution of tractions and tensions in actin and myosin filaments and their relative velocities as a function of axial position along (half) sarcomere, at selected times following a quick change in muscle length ($\Delta L = 4 \text{ nm}$, i.e., from full tetany isometric force to zero force (Ford et al.⁵). The left panel shows the evolving distributions for rigid fiber systems; the right panel shows the distributions for extensible fiber systems.

Observed from the position of a myosin molecule interacting with an actin filament, only local relative velocity and local relative displacement between the myosin actin binding sites are relevant for strain dependent attachment and detachment rates for that particular bridge. Thus, nonuniformly distributed strains imposed upon cross-bridges along the sliding filaments, directly affect all strain dependent state transition rate constants, i.e., biochemical reaction rates, during cross-bridge cycle shown in Figure 4.1, and consequently, the cross-bridge ability to generate force. Over time, this nonuniformity gradually becomes less prominent, relative velocities approach zero, and cross-bridges at different locations along the filaments experience less nonuniform stretch imposed by the sliding filaments. It is important to note that the local relative displacements and relative velocities in an extensible system are dissociated from the displace-

ment history observed at the level of the sarcomere. Thus, the interpretation of the experimental data by an extensible model may be quite different than by the one obtained from rigid filament model, which explicitly assumes that local relative displacements are exactly the same as displacements observed at the filament ends.

4.4.2. Stochastic strain dependent binding in 3D sarcomere lattice

A new 3D stochastic model, based on several updated four state myosin cycles, revealed several important issues not observed in other models. For simplicity we present here predictions based on Huxley's 1957 two state model described above. The predictions of time courses of the novel 3D stochastic model are in good agreement with the corresponding predictions of the mass action (i.e. probabilistic) model for both isometric force development and isotonic muscle shortening (Fig. 4.14).

Figure 4.14 A comparison between the predictions of the 3D sarcomere model of stochastic binding and the mass action model¹. Both models adequately predicted evolutions of (1) force development in fully activated muscle; and of (2) isotonic sarcomere shortening at zero load. All kinetics parameters are taken from¹, filament extensibility from^{16,17}, and exact dimensions of vertebrate hexagonal muscle lattice from^{21,22}. Please see the Figure on the page 267.

Some differences in the time courses can be attributed to fundamental differences between two models. While the 3D stochastic model takes in account exact number and location of myosin heads and corresponding actin sights and, therefore does not include any explicit assumptions, the probabilistic methods use fundamental assumption that the sum of all the state probability distributions, $p_i(X, x, t)$, at the same location X and the same cross-bridge strain x , is equal to one. The latter assumption causes that state probabilities are not normalizable, because this formulation assumes sufficient number of myosin heads to bind to all unoccupied actin sites. Because number of myosin heads is finite and precisely defined by stoichiometric ratio between number of myosin molecules and the number of actin monomers in a sarcomere lattice, this assumption is fundamentally wrong and can impose significant error in calculations of the fast transients and shortening velocities. This approach is modified by Piazzesi and Lombardi⁵⁴ and later used in Mijailovich's model of smooth muscle contraction⁵⁹ in order to conserve total number crossbridges i.e. myosin heads. Although this approach provided the model that can be normalized, i.e. the sum of the fractions of the crossbridges in each of actomyosin states is always one, the ratio between the number of attached and detached cross bridges must be specified, or calculated from a steady state solution of former approach. In contrast, 3D stochastic model does not require any

additional assumptions. In this model we imposed azimuthal dependence of the rate of myosin binding, based on measurements of reduced affinity of myosin to actin in a single molecule assay⁷⁹. Thus the differences in rates must be adjusted using an appropriated curve fitting method.

Consequently, the state transition rates will be different for the two alternative methods in contrast to the same used in Figures 4.14 and 4.15. Thus, the overall effect of contractile forces obtained from mass action models may not be satisfactorily accurate, except in several special cases.

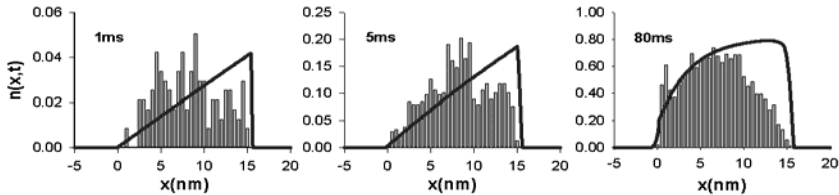


Figure 4.15. The distribution densities of cross-bridge forces of the 3D stochastic model (bars) and original Huxley¹ model (lines).

The novel finding in this simple analysis provides the physical insight into the differences of distribution of cross-bridge forces obtained by the two different methods (Fig. 4.15). For example, the effect of discrete binding affinities is clearly visible for early times (a half periodicity of actin monomers of 2.7 nm), while for later times this periodicity is less visible. This result clearly shows how filament extensibility smoothes otherwise digital matching between the myosin and actin. The principal differences in the distributions are, however, at higher levels of cross-bridge forces, whereas the number of cross-bridges predicted by 3D model is much smaller than predicted by mass action model. This result reflects a change in affinity of myosin to actin molecule, depending on their azimuthal matching within 3D sarcomere geometry (measured by single molecule techniques⁷⁹) which is not visible in the widely used mass action models. This finding is essential for the proper interpretation of coupling between the underlying biochemical process and the mechanical forces acting on cross-bridges. To precisely define mechanochemical strain dependent state transitions for each cross-bridge, it is necessary to know the exact amount of force acting on that bridge. This is especially important in the context of mechanical cooperativity among cross-bridges (see Mijailovich et al.⁵⁹), where the macroscopic velocity of muscle shortening or the velocity at filament ends in a sarcomere cannot directly map to molecular transitions. Bridging these scales is not a simple matter and requires rigorous treatment. The cross-bridges are not independent force generators (i.e., that local transition of one cross-bridge affects the transitions of other cross-bridges) and coupling between macroscopic variables (at scale of $\sim 1\text{mm}$)

needs precise recalculation to the scale of molecular interactions (of $\sim 1\text{nm}$).

In contrast to probabilistic models, this novel approach predicted oscillations in a fully developed isometric force (Fig. 4.16), muscle stiffness, and number of attached cross-bridges at different sarcomere lengths. These oscillations are direct consequence of discrete binding of myosin to actin sites in a 3-D lattice. The analysis of these spatial oscillations showed peaks at about 14.5 nm, and 7.3 nm. The former roughly corresponds to periodicity of myosin linings (14.3 nm), and the latter to the difference between myosin and actin periodicity (43 nm vs. 36.5 nm). The filament extensibility is insufficient to wipe out these match- mismatch-oscillations despite quite large variation in force in single myosin filaments (*symbols*). In contrast, rigid filaments simulations (*red line and symbols*, Fig. 4.16) show strong spatial periodicity at 2.7 nm, which corresponds to a half of actin spacing which is wiped out in extensible simulations. These oscillations are not observed in fiber experiments and possible reasons are that they are removed in striated muscle by slight length variations of filaments in series and in parallel, and possible slight bending of Z lines. Including these inter and intra sarcomere inhomogeneities in the model will smooth out the match-mismatch-oscillations and correctly predict observations in the fiber experiments, but only the model could assess magnitude of the variation of forces acting on individual myosin filaments. This result strongly emphasize importance of multiple-scale modeling: calculating average molecular forces from whole muscle fiber data may not correctly represent actual forces acting on molecular bonds and, therefore, how these forces mediate the biochemical relations. Thus, the essential information of coupling between mechanical forces and underlying biochemical processes is lost by not including variation of forces acting on individual myosin filaments as well as at individual acto-myosin bonds. Finally, the 3D stochastic model predictions are important in understanding the strengths and weaknesses of mass action models. This finding strongly suggests that a number of interpretations drawn from mass action models should be rethought, and revised.

Figure 4.16. Predictions of stochastic (Monte Carlo) simulations of the system of 3-D sarcomere with 20 myosin filaments. The isometric force (and also stiffness, and number of attached cross bridges) varies significantly at different sarcomere lengths. Symbols represent forces in individual myosin filaments. Both, extensible (*blue*) and rigid filaments (*red*) show the spatial periodicity of these oscillations (*right panel*). This periodicity is a consequence of spatial match-mismatch of positions of myosin heads and corresponding actin sites in 3-D sarcomere lattice. Please see the Figure on the page 267.

In a broader context, the above principles must apply for a proper understanding of molecular interactions at any interface between deformable bodies, such as between the cells and the extracellular matrix. This ap-

proach can be applied in the context of 3D meso-scale cell architecture coupled with the dynamics of cell adhesion to substrates for various cell types. This approach, when applied to contraction-adhesion coupling, will give the proper estimate of the variation of the forces acting on molecular bonds and corresponding biochemical state transition rates – essential information necessary for understanding integrative (patho)physiological processes such as tissue morphogenesis and remodeling, wound healing, fibrosis, cellular crawling, and invasion.

4.4.3. Thin filament regulation in skeletal muscle

The development of comprehensive models of thin filament regulation is in its embryonic phase. Structurally thin filament regulation of myosin binding is mediated by the presence of tropomyosin (Tm) and troponin (Tn) on the actin filament (Fig. 4.17).

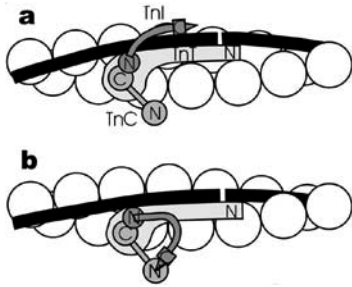


Figure 4.17. Schematic structure of the regulated actin tropomyosin-troponin (A-Tm-Tn) filament, showing a single chain of tropomyosin (Tm) molecules on one strand of the actin double helix. TnT is bound to one end of Tm and its N terminus overlaps the adjacent tropomyosin. The C terminus of TnC and the N terminal of TnI are bound to TnT. **a)** In the absence of calcium, the hands of the N-terminal region of TnC are ‘shut’ and the C terminus of TnI is bound to actin and blocks myosin binding to that site. **b)** When two calcium ions are bound to TnC, the hands of the N-terminal region are ‘open’ and bind a region of TnI near its C terminus, so that the myosin binding site is regulated only by tropomyosin. Based on models of Gagne and Tripet.

A number of models of the thin filament regulation are proposed and tested against in solution data⁶¹⁻⁶⁵. The implementation of these models in sliding filament models and lattice models is still lacking. For illustrative purpose we will present here the simplest four state model of muscle contraction and regulation. The model is derived from more complex the eight state mathematical model of Razumova et al.^{4,90}, that includes nearest-neighbor interactions: (i) between adjacent Tm-troponin regulatory units, (ii) between adjacent cycling cross-bridges, and (iii) in the case when an attached (force-bearing) cross-bridge facilitates the transition to the on state by a neighboring Tm-troponin regulatory unit. The model includes three state sliding filament model based on the energy landscape shown in Figure 4.8b.

Mathematical Details: The model consists of regulatory (Tm-Tn) unit, RU, that controls myosin access to the actin-binding site, and the three-state cross-bridge kinetics model (Fig. 4.18). The RU corresponds to a single Tm-Tn complex and relative to the segment of an actin filament can have two steric configurations: *closed* when actin affinity for myosin subfragment 1 (S1) is low (Fig. 4.17 a), and *open* when actin affinity for S1 is high (Fig. 4.17 b).

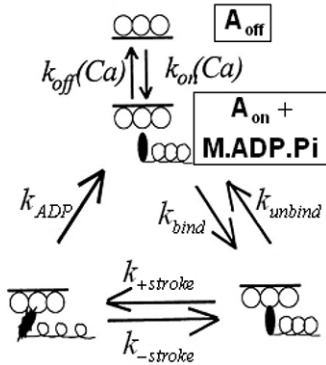


Figure 4.18. Four-state kinetic model of thin filament regulation and contraction (Razumova et al. ⁴). Thin filament has two configurations with respect to regulatory unit, RU (Tm-Tn complex): *open*, A_{on} , and *closed*, A_{off} . Cross-bridges can attach to the thin filament only when the RU is in the *open* configuration, while they are prohibited to bind when RU is in the *closed* configuration. Ca^{2+} binds and dissociates from the low-affinity of TnC site on the RU with rate constants of association, k^+ , and dissociation, k^- . When k^+ and k^- are much larger than the other rate coefficients, then Ca^{2+} binding and dissociation can be defined through the calcium dependence of $k_{on}(Ca)$ and $k_{off}(Ca)$ rate constants. The cross-bridge may be detached, $A_{on}+M.ADP.Pi$, or attached, $A_{on}.M.ADP.Pi$, $A_{on}.M.ADP..$ Attachment, power stroke, and detachment forward rate constants are denoted as k_{bind} , $k_{+stroke}$, and k_{ADP} respectively and backward rate constants k_{unbind} , $k_{-stroke}$ respectively.

Binding of Tm alone can induce two states, *closed* and *open* (with the equilibrium between them defined by $K_T = k_{on}^0 / k_{off}^0$), but without Ca^{2+} bound to troponin C (TnC) and the RU in *closed* configuration there is little probability that RU will be open. In cooperative fashion, binding of Ca^{2+} to TnC considerably enhances further binding of Ca^{2+} to TnC, which switches *on* a thin filament regulatory complex favoring further more formation of force-bearing cross-bridges. In activated muscle Ca^{2+} binds and dissociates from the low-affinity TnC site with rate constants of association, k^+ , and dissociation, k^- . Thus, we could have an actin state in one of the following four states: *open* and *closed* with Tm bound alone, A_{on}^0 and A_{off}^0 , respectively, and *open* and *closed* with bound Ca^{2+} to TnC, A_{on}^{Ca} and A_{off}^{Ca} , respectively. We assume a stoichiometry of one RU for every XB attachment site. This is very important assumption because actin sites in *closed* configuration can be treated in cross-bridge kinetics models as an additional detached state, where probability to attach a myosin head to actin is very low (i.e., zero). In addition to these states, we consider a tree-

state model that have one detached state, $A_{on}+M.ADP.Pi$, and two attached states, $A_{on}.M.ADP.Pi$ and $A_{on}.M.ADP$, in which A_{on} , that can be either with bound Ca^{2+} to TnC, A_{on}^{Ca} , or without bound Ca^{2+} to TnC, A_{on}^0 .

If we assume that Ca^{2+} -binding constants k^+ and k^- are much larger than other rate constants, and that these constants are independent of position of RU (i.e., whether the RU are *open* or *closed*), and also that they are independent of all transitions within the cross-bridge cycle, the original eight-state model of Razumova et al.⁴ can be reduced to the four-state model (Fig. 4.18). According to this reduced four-state model, the probabilities of myosin head to be in one of the four states is equivalent to the sum of the probabilities of same states with bound and without bound Ca^{2+} to TnC. The rate constants for transitions between RU *open* and closed states now depend on calcium concentration:

$$k_{on} = k_{on}^0 + (k_{on}^{Ca} - k_{on}^0) \frac{Ca}{Ca_{50} + Ca} \quad (4.8a)$$

$$k_{off} = k_{off}^0 + (k_{off}^{Ca} - k_{off}^0) \frac{Ca}{Ca_{50} + Ca} \quad (4.8b)$$

where Ca_{50} ($=k^-/k^+$) is the calcium concentration of half Ca^{2+} saturation of thin filament binding sites and Ca is current Ca^{2+} concentration.

The states in the four-state model, denoted for convenience by both numeric and generic state labels, may be grouped into two subpopulations: the states that collectively represent the population of cycling cross-bridges (1 = $A_{on}+M.ADP.Pi$, 2 = $A_{on}.M.ADP.Pi$, and 3 = $A_{on}.M.ADP$), and the state 4 = $A_{off}+M.ADP.Pi$ that represents the noncycling cross-bridge population (i.e., cross-bridges in $M.ADP.Pi$ state that do not have an available actin site, thus cannot execute its cycle). The 4×4 rate transition matrix $\mathbf{M}(x,t)$ describes the probability of transitions between these states and how these probabilities vary with strain (i.e. position, x) of the myosin head or the level of activation at any instant, $Ca(t)$. The elements of $\mathbf{M}(x,t)$ are derived from the transition-rate theory^{49,78}, and they include both the *strain-independent* transitions between detached states (i.e., $A_{off}+M.ADP.Pi$ and $A_{on}+M.ADP.Pi$), and *strain-dependent* transitions between cross-bridge cycling states.

To set $\mathbf{M}(x,t)$, we use the rate functions from eq. (4.3a-c) and the transition rates between detached states related to Ca^{2+} activation of the thin filament. The rate transition matrix is:

$$\mathbf{M}(x,t) = \begin{bmatrix} -k_1(x) - k_{-4}(Ca(t)) & k_{-1} & 0 & k_4(Ca(t)) \\ k_1(x) & -k_2(x) - k_{-1} & k_{-2}(x) & 0 \\ 0 & k_2(x) & -k_3(x) - k_{-2}(x) & 0 \\ k_{-4}(Ca(t)) & 0 & k_3(x) & -k_4(Ca(t)) \end{bmatrix} \quad (4.9)$$

The elements of matrix $\mathbf{M}(x,t)$ that define transition between the cycling cross-bridge states 1-3 are already defined in eqs. (4.3a-c): $k_1(x)$ depends on the overall rate of binding of $M \cdot ADP \cdot P_i$ to actin, k_{bind} ; the reverse reaction occurs at constant rate $k_{-1} = k_{unbound}$; $k_2(x)$ and $k_{-2}(x)$ (i.e., the overall rates denoted as $k_{+stroke}$ and $k_{-stroke}$ in Figure 4.18) are rapid forward/backward reaction rates between pre- and post-stroke states whose equilibrium depends on a large (negative) change in chemical free energy ΔG_{stroke} after the P_i release and size of power stroke d ; $k_3(x)$ (i.e., overall rate denoted as $k_{ADP}(x)$) defines the strain-dependent rate (limiting step) of ADP release (i.e., the slowest rate in sequence of events associated with ATP binding and hydrolysis (Figs 4.3 and 4.8)). The elements that define transition between open and closed position of RU are defined by the calcium concentration rate constants that may also depend on time: $k_4(Ca(t)) = k_{on}(Ca(t))$ and $k_{-4}(Ca(t)) = k_{off}(Ca(t))$ (eqs. 4.8a,b). However, these rate constants further depend on the state of its nearest-neighbors, i.e., the interactions: i) between adjacent Tm-troponin regulatory units, ii) between adjacent cycling cross-bridges, and iii) in the case when an attached (force-bearing) cross-bridge facilitated the transition to the on-state by neighboring Tm-troponin regulatory units. These transitions between *open* and *closed* configurations are also governed by Boltzmann statistics (i.e., Kramers' theory) similar to the previously described for strain-dependent rate transitions and, in general, the transitions depend on the state of nearest neighbors and the activation energies that drive these transitions. The higher is the activation energy, the smaller the probability that the transition will occur.

Cooperativity and Force-pCa Relationship. Cooperativity among the contractile processes of the myofilament system is widely accepted. Usually, cooperativity is defined by the Hill coefficient greater than 1. The Hill coefficient is a central parameter in the study of ligand-protein interactions, which measures the degree of cooperativity between subunits that bind the ligand in multisubunit proteins. In the thin filament regulation, we consider cooperativity as sequence of events that enhance force production and favor the occurrence of other events in the sequence. For example, Ca^{2+} binding to Troponin C (TnC) enhances the binding of more Ca^{2+} to TnC; the switching *on* of a thin filament regulatory complex favoring the

switching *on* of other regulatory complexes; the formation of a force-bearing cross-bridge favoring the formation of more force bearing cross-bridges. In the highly structured myofilament system, cooperativity almost certainly implies some kind of interaction between neighboring locations along the length of the filaments.

Here we consider three kinds of neighbor interactions that likely contribute to the cooperativity resulting in enhanced rate of myosin binding and, therefore force production. Tropomyosin thin-filament regulatory units may have neighbors in steric blocking positions (*off*) or steric permissive positions (*on*). The position of these neighbors influences the tendency for the regulatory unit to assume the *on* or *off* state. Likewise, the tendency of a myosin cross-bridge to achieve a force-bearing state may be influenced by neighboring cross-bridges in force-bearing states. Also, a cross-bridge in the force-bearing state may influence the tendency of a regulatory unit to enter the *on* state. We used a mathematical model to examine the influence of each of these three kinds of neighbor interactions on the steady-state force-pCa relation and on the dynamic force development and force redevelopment processes. Each neighbor interaction was unique in its effects on maximal Ca^{2+} -activated force, position, and symmetry of the force-pCa curve and on the Hill coefficient.

Ca^{2+} change was simulated by changing the Ca/Ca_{50} ratio between 0.01 and 100 (Fig. 4.19). The steady-state value of force predicted by the model was found for each Ca/Ca_{50} value and the resulting force- $\log(\text{Ca}/\text{Ca}_{50})$ curve was plotted. This was done for the baseline parameters – i.e., no neighbor interactions and no cooperativity. Then, the parameters grading the strength of neighbor interactions were individually changed to give in each case moderate and strong interactions and corresponding force- $\log(\text{Ca}/\text{Ca}_{50})$ curves for these conditions were obtained. Features of Force- $\log(\text{Ca}/\text{Ca}_{50})$ curve were evaluated and compared among the various conditions, including force during maximal Ca^{2+} activation, F_{\max} ; $\log(\text{Ca}/\text{Ca}_{50})$ at half F_{\max} , Hill coefficient, n_H , of the Hill equation fitted to the model-predicted force- $\log(\text{Ca}/\text{Ca}_{50})$ curve

$$F = \frac{1}{1 + \left(\frac{\text{Ca}}{\text{Ca}_{50}} \right)^{-n_H}}. \quad (4.10)$$

Curve asymmetry was assessed for fit to relationship over range $F/F_{\max} < 0.5$ vs. that for fit to relationship over the range $F/F_{\max} > 0.5$.

Figure 4.19 Effect of different types of myofilament neighbor interactions on Force-pCa interactions. The force is pN/actin filament, and pCa as log of the ratio of calcium current concentration, Ca^{2+} , and the concentration of half Ca^{2+} saturation, Ca_{50} . (a) Effect of RU-RU interaction on Force-pCa relationship. Three curves represent different

strength of interaction: no interaction (*dashed curve*, $u=1$), weak interaction (*red curve*, $u=2$), and strong interaction (*green curve*, $u=3$); (ii) The effect of XB-XB interaction.: no interaction (*dashed curve*, $v=1$), weak interaction (*red curve*, $v=2.5$), and strong interaction (*green curve*, $v=3.2$). The effect of XB-RU interaction: no interaction (*dashed curve*, $w=1$), weak interaction (*red curve*, $w=3$), and strong interaction (*green curve*, $w=5$). Please see the Figure on the page 268.

The differences among the three types of neighbor interactions are contrasted in the Force- $\log(\text{Ca}/\text{Ca}_{50})$ relationships shown in Figure 4.19. Increasing strength of RU-RU interaction increases maximal Ca^{2+} -activated force, shifts the curve predominantly to the right (especially at low Ca^{2+}), increases curve steepness, and introduces curve asymmetry (relatively slow departure from no-force baseline and rapid approach to saturation). Therefore, with increasing Ca^{2+} , RU-RU interaction and Ca^{2+} activation act synergistically and this interaction collectively promotes formation of the *on* state. Increasing strength of XB-XB interaction greatly increases maximal Ca^{2+} -activated force, shifts the curve to the right with weak interaction, and also increases curve steepness but only with strong interaction. Furthermore, it introduces distinct curve asymmetry, i.e. relatively rapid departure from no-force baseline, slower approach to saturation. Increasing strength of XB-RU interaction modestly increases maximal Ca^{2+} -activated force, but shifts the curve strongly to the left, increases curve steepness, and introduces distinct curve asymmetry.

Whereas all three types of interaction shared the effect of increasing the steepness of the force- $\log(\text{Ca}/\text{Ca}_{50})$ relationship, the RU-RU interaction easily had the greatest effect in this regard. Strong interaction between adjacent RUs created a condition that favored either all *off* or all *on*; if its neighbors were *off*, an RU tends to be held in the *off* position, but if its neighbors are *on* the RU tends to be held in the *on* position. In contrast, calcium binding promotes the transition from *off* to *on*. At low Ca^{2+} concentrations when most RU are *off*, neighbor interactions tend to hold the RU *off* even in the face of the weak effect of Ca^{2+} to promote the transition to *on*. These competing effects continue as Ca^{2+} concentrations are raised until there has been sufficient Ca^{2+} -induced transition to the *on* state that the neighbor interaction effects suddenly reverse and favor the transition to *on*.

As with increasing u (RU-RU interaction) and v (XB-XB), increasing the strength of XB-RU interaction also increased F_{max} . Increasing w from 1 (no interaction) to 5 (strong interaction) increased the maximum Ca^{2+} -activated force, F_{max} , by approximately 30%. The magnitude of these effects was more like for u than for v . However, unlike either u or v , increasing w caused a dramatic left shift in the normalized force- $\log(\text{Ca}/\text{Ca}_{50})$ curve (Fig. 4.19). The left-shifted curve was not symmetrical, having a higher n_H in the lower part ($n_H = 5.3$) than in the upper part ($n_H = 5.15$).

Similarly to effect of u , at maximal Ca^{2+} activation w also had very little effect on the rate of force development. Taken together, these diverse effects suggest that variations in all three kinds of nearest-neighbor interactions may be responsible for a wide variety of currently unexplained observations of myofilament contractile behavior.

Myofilament Kinetics in Isometric Twitch Dynamics. To better understand the relationship between kinetic processes of contraction and the dynamic features of an isometric twitch, we developed a mathematical model that included: (1) kinetics of cross-bridge cycling; (2) kinetics of thin filament regulatory processes; (3) serial and feedback interactions between these two kinetic processes; and (4) time course of calcium activation. From the model simulation of isometric twitch wave forms we evaluated morphometric features of twitch wave and assessed sensitivities of wave form morphometric features to the model kinetic model parameters. The impulse response of the cross-bridge showed that dynamic constants of the twitch transient were much faster than turnover number of steady-state cycling of cross-bridge, and that speed and duration of the twitch wave form were sensitive to cross-bridge cycle kinetic constants. In contrast the parameters of wave shape were not affected at all. In [Figure 4.20](#), time course of calcium transient and force transient raise (twitch wave) are shown.

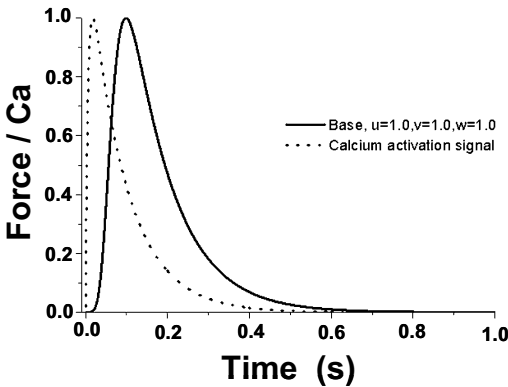


Figure 4.20. Isometric transient raise in tension (twitch) lags the calcium transient.

Note that the force response lags the calcium transient. When thin filament regulatory unit (RU) kinetics were added to cross-bridge cycle kinetics, the system impulse response slowed with only little effect on wave shape. When cooperative neighbor interactions between RU and cross-bridge were added, twitch wave shape (as well as amplitude, speed and duration) becomes sensitive to variation in cooperativity. Importantly, persistence and shape of the falling phase could be strongly modified. When kinetic coefficients of cross-bridge attachment depend on sarcomere

length, wave shape also changes. In contrast this change has not appeared when only sliding filament mechanisms were operative. Indeed, the force-length relationship proved to be highly sensitive to length-dependent cross-bridge attachment in combination with cooperative interactions. These model findings are the basis of hypotheses for the role of specific kinetic events of contraction in generating twitch wave form features in heart muscle.

4.4.4. The latch regulatory scheme in smooth muscle

The sliding filament theory of smooth muscle contraction is based on two concepts: population kinetics of cross-bridge attachment and detachment, and the latch regulatory scheme of Hai and Murphy³. We have chosen the latch regulatory scheme of Hai and Murphy because it is simple and it captures the central importance of phosphorylation of the 20 kDa myosin light chain (MLC₂₀).

Latch Regulatory Scheme – Static Equilibrium. Within the latch scheme, the attainment of the isometric steady state implies that the populations of four states of the four myosin states depicted in Figure 4.21 have come to an equilibrium set by a balance of seven rate processes (*arrows*), four of which are ATP dependent. Once enough time has passed to attain this balance, the muscle is then said to be in the *latch state*, and myosin has come to a binding equilibrium appropriate to isometric steady state. We will refer to this as the static equilibrium of myosin binding. In Hai and Murphy's scheme, therefore, the latch state corresponds to a static equilibrium of myosin binding associated with a particular distribution of myosin between the two attached species (the slowly cycling latch bridge AM, and the rapidly cycling cross-bridge, AM_p, where the subscript “p” denotes phosphorylated species). In summary, regardless of the mechanism of cycling rate regulation, every point on the static force-length characteristic of contracted airway smooth muscle corresponds to isometric steady state conditions and, therefore, static equilibrium of myosin binding.

Figure 4.21 Hai and Murphy's four-state model³: the latch regulatory scheme for Ca²⁺ dependent smooth muscle activation and Huxley's sliding filament model. A actin (thin filament); myosin cross-bridge states are M (detached, unphosphorylated); Mp (detached, phosphorylated); AM_p (attached, phosphorylated); AM (attached, unphosphorylated, also known as the latch bridge). k_1 - k_7 are first order rate constants from experimental data³. k_1 and k_6 represent Ca²⁺, calmodulin dependent myosin light chain kinase (MLCK) activity; k_2 and k_5 represent myosin light chain phosphatase (MLCP) activity, where k_5 drives the rapidly cycling cross-bridges, AM_p, to slowly cycling latch bridges, AM. k_3 and k_4 are the rate constants for attachment and detachment of phosphorylated cross-bridges, and k_7 is the rate for latch bridge detachment, all three dependent on cross-bridge displacements (x) through scaled Huxley's attachment and detachment (spatially distributed) rates. h :

range of displacements over which myosin has positive binding rate. Please see the Figure on the page 268.

A Sliding Filament Model with the Latch Regulatory Scheme. In contrast to the static equilibrium of myosin binding, in real physiological circumstances there are necessarily length and force fluctuations. For example, airways exhibit tidal excursions in their diameter during normal breathing. These tidal inflations impose upon the airway muscle tidal fluctuations in muscle load which, in turn, perturbs myosin binding by straining attached bridges, which according to Huxley's two state scheme (Fig. 4.12. right panel) increases rate of cross-bridge detachment and therefore decreases mean force, muscle stiffness, and number of attached cross-bridges, while ATP consumption increases^{69,70}. The mathematical synthesis of the ideas of Huxley with those of Hai and Murphy we refer to as the HHM theory⁷⁰.

The transitions between the four states are governed by seven rate constants (Fig. 4.21). Implicit in the scheme is that cross-bridges cannot attach to actin unless they are first phosphorylated, i.e. the muscle is regulated exclusively by Ca^{2+} dependent state transition rate constants, k_1 and k_6 (which may vary with time), mediated by calmodulin dependent myosin light chain kinase (MLCK). Hai and Murphy also assumed that the affinities of MLCK and myosin light chain phosphatase (MLCP) for both attached and detached cross-bridges are similar, i.e. $k_1 \approx k_6$ and $k_2 \approx k_5$.

We assessed the relationship between the time varying external load, level of muscle activation and acto-myosin dynamics by computing numerical solutions to the HHM theory. This theory can be written as four coupled partial differential equations that express conservation of each myosin species (eq. 4.1). Each of the four components of the vector $\mathbf{p}(x,t)$ corresponds to the population fraction of myosin in one of its four states (i.e. $p_M(x,t)$, $p_{M_p}(x,t)$, $p_{AM_p}(x,t)$, $p_{AM}(x,t)$) all of which vary both in time, t , and space, x , where x is the position of the active actin site on the actin filament relative to the equilibrium position of the cross-bridge on the myosin filament¹.

The 4x4 rate transition matrix $\mathbf{M}(x,t)$ describes the probability of transitions between these states, and how these probabilities vary with position of the myosin head. These probabilities are important because, with any relative movement between actin and myosin filaments, the myosin head may traverse regions that tend to favor attachment events, and some others that tend to favor detachment events; the latter dominate where x is large and or negative¹. The elements of $\mathbf{M}(x,t)$ include both the strain-independent transitions between M and M_p and between AM and AM_p (phosphorylation and dephosphorylation of 20kD myosin light chain are driven by action of kinases and phosphatases^{3,68}), and strain-dependent

transitions between Mp and AMp and between M and AM (attachment and detachment of myosin to actin^{1,68}). As such, $\mathbf{M}(x, t)$ governs the transition of chemical events into mechanical events and, importantly, the converse as well. To set $\mathbf{M}(x, t)$, we used the rate functions reported by Hai and Murphy after adapting them to include the increased rate of detachment (g_3) described by Zahalak⁹¹ in the region $x > h$, where h is the range for positive probability of attachment¹. The rate transition matrix is:

$$\mathbf{T}(x, t) = \begin{bmatrix} -k_1(t) & k_2 & 0 & g(x) \\ k_1(t) & -k_2 - f_p(x) & g_p(x) & 0 \\ 0 & f_p(x) & -k_5 - g_p(x) & k_6(t) \\ 0 & 0 & k_5 & -k_6(t) - g(x) \end{bmatrix} \quad (4.11)$$

where

$$f_p(x) = \begin{cases} 0, & x < 0 \\ f_{p1}x/h, & 0 \leq x \leq h \\ 0, & h < x \end{cases}$$

$$g_p(x) = \begin{cases} g_{p2}, & x < 0 \\ g_{p1}x/h, & 0 \leq x \leq h \\ (g_{p1} + g_{p3})x/h, & h < x \end{cases} \quad (4.12)$$

$$g(x) = \begin{cases} g_2, & x < 0 \\ g_1x/h, & 0 \leq x \leq h \\ (g_1 + g_3)x/h, & h < x. \end{cases}$$

$f_p(x)$ is the position dependent attachment rate of Mp, $g_p(x)$ is detachment rate of AMp, and $g(x)$ is the detachment rate of AM. The subscript p denotes phosphorylated myosin heads. Following Hai and Murphy^{3,68}, the attachment rate of unphosphorylated myosin (i.e. $M \rightarrow AM$) is negligible, which accounts for that 0 entry in \mathbf{T} . Note also that the Ca^{2+} dependent transition rates k_1 and k_6 to the phosphorylated states are explicitly shown as potential functions of time. The magnitude of the above rate dependent cross-bridge constants, defined by f_{p1} , g_{p1} , and g_1 , are chosen to match Murphy's position-independent state transition rate constants (shown in Fig. 4.21), k_3 , k_4 and k_7 , respectively, when relations (4.12) are averaged over x . Specifically, the linear character of the rate constants within $0 \leq x \leq h$ implies, for example, that the average of $f_p(x)$ is simply $f_{p1}/2$. Thus we take $f_{p1} = 2k_3$. g_{p1} and g_1 are evaluated similarly. Finally, we evaluated the other time constants to be $g_{p2} = 4(f_{p1} + g_{p1})$ and

$g_2 = 20 g_1$ as defined in Huxley¹, and $g_{p3} = 3g_{p1}$ and $g_3 = 3g_1$ as defined in Zahalak⁹¹.

Isometric Force Development and Oscillatory Length Fluctuations. Figure 4.22 shows transients of muscle force, stiffness, phosphorylation, and ATP consumption during force development and the effect of the imposition of length fluctuations after the isometric force is fully developed. Details about these dynamic transitions are explained in the legend to Figure 4.22. These are truly dynamic processes that may find their origin in both the populations of the cross-bridge states and in their strain distributions⁶⁹. When force is fully developed (~180 s), the final populations of the AMp and AM states depend upon the level of fractional phosphorylation. In the example shown, the steady state fractional phosphorylation is 0.375, for which the AM population ultimately exceeds the AMp population. This partitioning is typical for low levels of fractional phosphorylation and corresponds to the “latch state”³. However, imposition of sinusoidal length changes of 1% and 4% Lo upsets the isometric binding equilibrium and leads to a new perturbed equilibrium of myosin binding. The dynamic steady state has fewer attached bridges, lower mean force, lower stiffness, and higher mean ATP consumption, even though phosphorylation remains unchanged. These effects are caused by increased detachment of cross-bridges due to larger cross-bridge strains. It is interesting to note that the instantaneous force, F , and ATP_{cycl} vary substantially over the cycle, while instantaneous stiffness, K , and the populations of AM and AMp vary only modestly.

Figure 4.22. Evolution of mechanical and metabolic parameters during force development (0-180 s) and superimposed length variations of 1% (180-245 s) and 4% (245-305 s). **a)** During force development, phosphorylation⁹ peaks at about 5 s., following the Ca^{2+} transient (through k_l and k_o), while muscle force, F (dark green), and instantaneous stiffness, K (pink), monotonically increase. Superimposed length variations of 1% and 4% did not affect levels of myosin phosphorylation, but progressively depresses both mean F and mean K . While instantaneous F fluctuates more than 50% of its isometric value, instantaneous K only modestly varies over its mean value. **b)** State population transitions of M¹⁸, Mp (red) and AMp⁹ occurred quickly and the muscle force and stiffness develops mostly through rapid cross bridge cycling. Latch bridges (AM, blue) develop later, significantly slowing the apparent cross bridge cycling rates. Imposed strain variations decreases number of both AMp and AM bridges. Variation of all state populations is small compared to F . **c)** Total ATP consumption (black line) first drops, reflecting the early transient between M and Mp states, then increases following initial increase of cross bridge cycling rates (i.e. ATP_{cycl} , cyan line), and reaches a plateau at larger times (~ 180 s). Please see the Figure on the page 268.

The Implications of the Dynamic of Myosin Binding. Based on myosin binding dynamics, we simulated the macroscopic mechanical behavior and energetics and found that they are, for the most part, indistinguishable

from those determined experimentally both in terms of the threshold levels and the magnitude of the effects (Figs 4.23 and 4.24); solid lines correspond to predictions from HHM).

Figure 4.23. a) Steady state mean force, elastance, and hysteresivity as a function of strain amplitude at steady state level of phosphorylation of 0.375 mole Pi/Mole LC_{20} . Experimental data from maximally activated tracheal smooth muscle (from Fredberg et al. ⁸) normalized to 100% at $\epsilon = 0.25\%$, frequency 0.33 Hz) are shown by closed symbols \pm SD. The predictions of HHM theory are shown in the solid lines. **b)** Steady state mean force, elastance, and hysteresivity as a function of myosin light chain phosphorylation at fixed frequency of 0.33 Hz and Fixed amplitude of $\epsilon = 2\%$. Mean force, F , and Elastance, E , are normalized by the respective isometric values at 100% phosphorylation. Please see the Figure on the page 269.

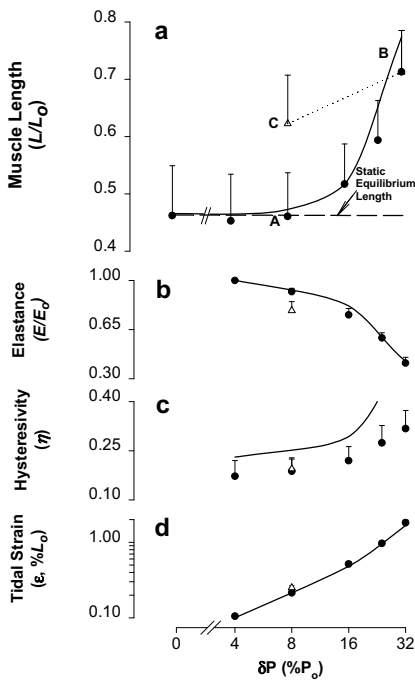


Figure 4.24 Pooled observations (*filled circles*, $n=6$; error bars denote SD between strips drawn only in one direction for clarity and predicted (*solid lines* computed from HHM theory) fully dynamically equilibrated values of **a)** muscle length (vs. force fluctuation amplitude); **b)** Loop stiffness (% of isometric value); **c)** Hysteresivity ; **d)** Tidal length change ϵ is $\Delta L/L_o$ in %.

On this basis we were persuaded that this seemingly complicated set of mechanical, biochemical, and metabolic effects of imposed load fluctuations may be largely accounted for by a single mechanism- myosin dynamics- and that these dynamics are perturbed by imposed load fluctuations. Simply put, the quantitative analysis shows that the fluctuations of load, such as imposed by the action of breathing, creates fluctuations that are big enough to perturb myosin binding and causes bridges to detach much sooner than they otherwise would have ⁷⁰. Premature detachment decreases the fraction of time that myosin remains attached to the actin filament, typically to less than 20% of its value in the isometric steady

state, and profoundly inhibits contractile function. As demonstrated in Figure 4.23 the mechanical effects are not small. Similarly, Figure 4.24 demonstrates that within physiological range of force fluctuations, the airway smooth muscle length is not governed by the isometric force generating capacity of the muscle, as had been assumed previously. It is governed by a dynamically-equilibrated steady state which requires as an essential feature a continuous supply of *external mechanical energy* (derived from tidal lung inflations *in vivo* or a servo controller simulating that action *in vitro*) that acts to perturb the binding of myosin to actin, drive the molecular state of the system far from thermodynamic equilibrium⁸, and biases the muscle towards lengthening (Fig. 4.24). Within the physiological range of force fluctuations in airway smooth muscle during normal breathing (i.e., when $\delta F \geq 8\%F_o$) the dynamically equilibrated length L is seen to substantially exceed the statically equilibrated length (i.e., when $\delta F = 0$). Compared with a static binding equilibrium, these perturbed states are characterized by substantially diminished bridge numbers and augmented rates of bridge turnover.

We now turn to the related question: how are these dynamic states attained, and how are metabolic and mechanical work related (i.e., the relationship between the cross-bridge cycling rates and energy consumption)? The ATPase activity computed from the net rate of bridge cycling (exclusive of phosphorylation events) is shown as ATP_{cycl} , and this quantity together with the additional ATP consumption associated with phosphorylation events defines the total, shown as ATP_{tot} (Fig. 4.22). The mechanical work done by the imposed strains on the muscle per load cycle is equal to the area enclosed by the force/length loop D ; the external power loss is given by the average work done on the muscle per unit time, or in terms of our previously defined quantities, by $Df = \eta E \Delta L^2 f \pi$ (for detail definitions see Mijailovich et al.⁶⁹). Figure 4.25 illustrates the relationship between external power loss and excess ATPase (over the isometric, ATP_{iso}) that is caused by tidal stretches ($ATP_{excess} = ATP_{cycl} - ATP_{iso}$). It is important to note that both chemical energy of ATPase and the mechanical power loss are energy dissipative processes, that are associated over wide frequency range and strain amplitudes below 4% (Fig. 4.25), but they dissociate for larger strain amplitudes.

The stretch-induced augmentation of the hysteresivity is attributable in part to a direct mechanical effect at the level of cyclic interaction of myosin and actin^{1,92}. Compared with isometric conditions, during tidal stretch the attached myosin molecule spends some fraction of each period in regions along the actin filament that favor rapid detachment. The greater the stretch amplitude, the greater is the fraction of detached bridges. Dashed lines in Figure 4.25 show excess ATPase (over the isometric) that is caused by tidal stretches. Increased time spent in regions favoring detachment

would, in turn, account for an increased rate of bridge turnover and an elevated value of η (Fig. 4.23).

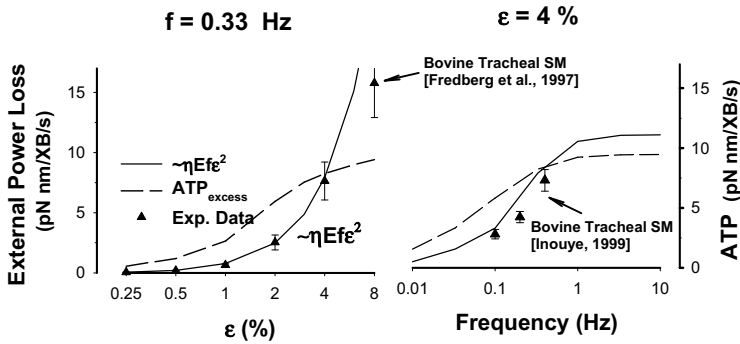


Figure 4.25 Rate of external energy loss (HHM prediction, *solid line*), and the experimental points (from Fredberg et al.⁸ *triangles* \pm SD) over the range of physiological strain amplitudes and frequencies. Also shown is ATP_{excess} (*dashed line*), where $ATP_{excess} = ATP_{cycl} - ATP_{iso}$ is the excess ATPase activity over ATP_{iso} , the isometric steady state cross-bridge ATPase. Both power energy loss and ATPase activity are calculated per a myosin molecule (XB). The free energy of ATP hydrolysis is assumed to be 100 pNnm.

In order to investigate the uncertainty of the HHM model rate constants at stretches above 4%, we also calculated power loss from the experimental data shown in Figure 4.23 (from Fredberg et al.^{8,70}). This is shown in Figure 4.25 (*triangles*). It agrees well with HHM predictions up to $\epsilon = 4\%$. At $\epsilon = 8\%$, however, we note two features. First, external power loss computed by HHM theory significantly overestimates the experimentally determined power loss. Second, the experimentally determined power loss is itself significantly higher than the HHM computed ATPase activity. These two observations imply only a weak coupling between external mechanical work (power) and the chemical energy (cyclic ATPase) required for maintaining steady state contraction. In summary, the perturbed equilibrium requires external work to break the cross-bridges, which in turn raises the myosin cycling rates and therefore the biochemical energy required to maintain that dynamic equilibrium. While the data and computational analysis suggest that perturbed myosin dynamics may be a major unifying concept, the data also suggest that myosin dynamics cannot be the whole answer, since HHM theory cannot by itself account for sustained effects of load history.

Acknowledgements

Parts of this text and several figures are adapted from books and papers of Professors K.C. Holmes, Y.C. Fung, H.E. Huxley, J.A. Spudich, R.D. Vale, T.A. Duke, and K.B. Campbell. This work is supported by NIH grants HL 33009 and AR048776.

References

1. Huxley A.F., Muscle structure and theories of contraction., *Progress in Biophys. and Biophys. Chem.*, **7**, 255-318, 1957.
2. Geeves M.A., K.C. Holmes, Structural mechanism of muscle contraction, *Annu Rev Biochem*, **68**, 687-728, 1999.
3. Hai C.M., R.A. Murphy, Cross-bridge phosphorylation and regulation of latch state in smooth muscle, *Am J Physiol*, **254**, C99-106, 1988.
4. Razumova M.V., A.E. Bukatina, K.B. Campbell, Different myofilament nearest-neighbor interactions have distinctive effects on contractile behavior, *Biophys J*, **78**, 3120-3137, 2000.
5. Ford L.E., A.F. Huxley, R.M. Simmons, Tension responses to sudden length change in stimulated frog muscle fibres near slack length, *J Physiol*, **269**, 441-515, 1977.
6. Huxley H.E., Fifty years of muscle and the sliding filament hypothesis, *Eur J Biochem*, **271**, 1403-1415, 2004.
7. Bagni M.A., G. Cecchi, M. Schoenberg, A model of force production that explains the lag between crossbridge attachment and force after electrical stimulation of striated muscle fibers, *Biophys J*, **54**, 1105-1114, 1988.
8. Fredberg J.J., D. Inouye, B. Miller, M. Nathan, S. Jafari, S.H. Raboudi, J.P. Butler, S.A. Shore, Airway smooth muscle, tidal stretches, and dynamically determined contractile states, *Am J Respir Crit Care Med*, **156**, 1752-1759, 1997.
9. Johnson P.R., M. Roth, M. Tamm, M. Hughes, Q. Ge, G. King, J.K. Burgess, J.L. Black, Airway smooth muscle cell proliferation is increased in asthma, *Am J Respir Crit Care Med*, **164**, 474-477, 2001.
10. Tsuda A., B.K. Stringer, S.M. Mijailovich, R.A. Rogers, K. Hamada, M.L. Gray, Alveolar cell stretching in the presence of fibrous particles induces interleukin-8 responses, *Am J Respir Cell Mol Biol*, **21**, 455-462., 1999.
11. Rayment I., W.R. Rypniewski, K. Schmidt-Base, R. Smith, D.R. Tomchick, M.M. Benning, D.A. Winkelmann, G. Wesenberg, H.M. Holden, Three-dimensional structure of myosin subfragment-1: a molecular motor, *Science*, **261**, 50-58, 1993.
12. Spudich J.A., How molecular motors work, *Nature*, **372**, 515-518, 1994.
13. Vale R.D., R.A. Milligan, The way things move: looking under the hood of molecular motor proteins, *Science*, **288**, 88-95, 2000.
14. Duke T.A., Molecular model of muscle contraction, *Proc Natl Acad Sci U S A*, **96**, 2770-2775, 1999.

15. Duke T., Cooperativity of myosin molecules through strain-dependent chemistry, *Philos Trans R Soc Lond B Biol Sci*, **355**, 529-538, 2000.
16. Huxley H.E., A. Stewart, H. Sosa, T. Irving, X-ray diffraction measurements of the extensibility of actin and myosin filaments in contracting muscle, *Biophys J*, **67**, 2411-2421, 1994.
17. Wakabayashi K., Y. Sugimoto, H. Tanaka, Y. Ueno, Y. Takezawa, Y. Amemiya, X-ray diffraction evidence for the extensibility of actin and myosin filaments during muscle contraction, *Biophys J*, **67**, 2422-2435, 1994.
18. Dracup K., A.A. Alonzo, J.M. Atkins, N.M. Bennett, A. Braslow, L.T. Clark, M. Eisenberg, K.C. Ferdinand, R. Frye, L. Green, M.N. Hill, J.W. Kennedy, E. Kline-Rogers, D.K. Moser, J.P. Ornato, B. Pitt, J.D. Scott, H.P. Selker, S.J. Silva, W. Thies, W.D. Weaver, N.K. Wenger, S.K. White, The physician's role in minimizing prehospital delay in patients at high risk for acute myocardial infarction: recommendations from the National Heart Attack Alert Program. Working Group on Educational Strategies To Prevent Prehospital Delay in Patients at High Risk for Acute Myocardial Infarction, *Ann Intern Med*, **126**, 645-651, 1997.
19. Szent-Gyorgyi A.G., Meromyosins, the subunits of myosin, *Arch Biochem Biophys*, **42**, 305-320, 1953.
20. Margossian S.S., S. Lowey, Substructure of the myosin molecule. 3. Preparation of single-headed derivatives of myosin, *J Mol Biol*, **74**, 301-311, 1973.
21. Squire J.M., *Molecular Mechanisms in Muscle Contraction.*, CRC Press, Inc, Boca Raton, Fl, 1990.
22. Squire J.M., Muscle filament lattices and stretch-activation: the match-mismatch model reassessed, *J Muscle Res Cell Motil*, **13**, 183-189, 1992.
23. Huxley H.E., E.J. Hanson, Changes in the cross-striations of muscle during contraction and stretch and their structural interpretation., *Nature*, **173**, 973-976, 1954.
24. Huxley A.F., R. Niedergerke, Structural changes in muscle during contraction., *Nature*, **173**, 971-973, 1954.
25. Reedy M.K., K.C. Holmes, R.T. Tregear, Induced changes in orientation of the cross-bridges of glycerinated insect flight muscle, *Nature*, **207**, 1276-1280, 1965.
26. Huxley H.E., The mechanism of muscular contraction, *Science*, **164**, 1356-1365, 1969.
27. Lynn R.W., E.W. Taylor, Mechanism of adenosine triphosphate hydrolysis by actomyosin, *Biochemistry*, **10**, 4617-4624, 1971.
28. Huxley A.F., R.M. Simmons, Proposed mechanism of force generation in striated muscle, *Nature*, **233**, 533-538, 1971.
29. Geeves M.A., The dynamics of actin and myosin association and the crossbridge model of muscle contraction, *Biochem J*, **274** (Pt 1), 1-14, 1991.
30. Hibberd M.G., D.R. Trentham, Relationships between chemical and mechanical events during muscular contraction, *Annu Rev Biophys Biophys Chem*, **15**, 119-161, 1986.
31. Rayment I., Holden H.M., M. Whittaker, C.B. Yohn, M. Lorenz, K.C. Holmes, R.A. Milligan, Structure of the actin-myosin complex and its implications for muscle contraction, *Science*, **261**, 58-65, 1993.

32. Cooke R., The mechanism of muscle contraction, *CRC Crit Rev Biochem*, **21**, 53-118, 1986.
33. Holmes K.C., The swinging lever-arm hypothesis of muscle contraction, *Curr Biol*, **7**, R112-118, 1997.
34. Piazzesi G., M. Reconditi, I. Dobbie, M. Linari, P. Boesecke, O. Diat, M. Irving, V. Lombardi, Changes in conformation of myosin heads during the development of isometric contraction and rapid shortening in single frog muscle fibres, *J Physiol*, **514 (Pt 2)**, 305-312, 1999.
35. Corrie J.E., B.D. Brandmeier, R.E. Ferguson, D.R. Trentham, J. Kendrick-Jones, S.C. Hopkins, U.A. van der Heide, Y.E. Goldman, C. Sabido-David, R.E. Dale, S. Criddle, M. Irving, Dynamic measurement of myosin light-chain-domain tilt and twist in muscle contraction, *Nature*, **400**, 425-430, 1999.
36. Molloy J.E., J.E. Burns, J. Kendrick-Jones, R.T. Tregear, D.C. White, Movement and force produced by a single myosin head, *Nature*, **378**, 209-212, 1995.
37. Suzuki Y., T. Yasunaga, R. Ohkura, T. Wakabayashi, K. Sutoh, Swing of the lever arm of a myosin motor at the isomerization and phosphate-release steps, *Nature*, **396**, 380-383, 1998.
38. Fisher A.J., C.A. Smith, J.B. Thoden, R. Smith, K. Sutoh, H.M. Holden, I. Rayment, X-ray structures of the myosin motor domain of Dictyostelium discoideum complexed with MgADP.BeFx and MgADP.AIF₄, *Biochemistry*, **34**, 8960-8972, 1995.
39. Houdusse A., A.G. Szent-Gyorgyi, C. Cohen, Three conformational states of scallop myosin S1, *Proc Natl Acad Sci U S A*, **97**, 11238-11243, 2000.
40. Walker M., H. White, B. Belknap, J. Trinick, Electron cryomicroscopy of actomyosin-S1 during steady-state ATP hydrolysis, *Biophys J*, **66**, 1563-1572, 1994.
41. Taylor K.A., H. Schmitz, M.C. Reedy, Y.E. Goldman, C. Franzini-Armstrong, H. Sasaki, R.T. Tregear, K. Poole, C. Lucaveche, R.J. Edwards, L.F. Chen, H. Winkler, M.K. Reedy, Tomographic 3D reconstruction of quick-frozen, Ca²⁺-activated contracting insect flight muscle, *Cell*, **99**, 421-431, 1999.
42. Holmes K.C., M. Tirion, D. Popp, M. Lorenz, W. Kabsch, R.A. Milligan, A comparison of the atomic model of F-actin with cryo-electron micrographs of actin and decorated actin, *Adv Exp Med Biol*, **332**, 15-22; discussion 22-14, 1993.
43. Holmes K.C., D. Popp, W. Gebhard, W. Kabsch, Atomic model of the actin filament, *Nature*, **347**, 44-49, 1990.
44. Hill T.L., *Free energy transduction in biology: The steady- state kinetics and thermodynamic formalism*, Academic Press, New York, NY, 1977.
45. Becker E.W., Kinetic equilibrium of forces and molecular events in muscle contraction, *Proc Natl Acad Sci U S A*, **97**, 157-161, 2000.
46. Geeves M.A., R.S. Goody, H. Gutfreund, Kinetics of acto-S1 interaction as a guide to a model for the crossbridge cycle, *J Muscle Res Cell Motil*, **5**, 351-361, 1984.
47. Geeves M.A., P.B. Conibear, The role of three-state docking of myosin S1 with actin in force generation, *Biophys J*, **68**, 194S-199S; discussion 199S-201S, 1995.
48. Hill T.L., Theoretical formalism for the sliding filament model of contraction of striated muscle. Part I, *Prog Biophys Mol Biol*, **28**, 267-340, 1974.

49. Kramers H.A., Brownian motion in a field of force and the diffusion model of chemical reactions. *Physica*, **7**, 284-304, 1940.
50. Whittaker M., E.M. Wilson-Kubalek, J.E. Smith, L. Faust, R.A. Milligan, H.L. Sweeney, A 35-A movement of smooth muscle myosin on ADP release, *Nature*, **378**, 748-751, 1995.
51. Veigel C., L.M. Coluccio, J.D. Jontes, J.C. Sparrow, R.A. Milligan, J.E. Molloy, The motor protein myosin-I produces its working stroke in two steps, *Nature*, **398**, 530-533, 1999.
52. Eisenberg E., T.L. Hill, Y. Chen, Cross-bridge model of muscle contraction. Quantitative analysis, *Biophys J*, **29**, 195-227, 1980.
53. Cooke P.H., F.S. Fay, R. Craig, Myosin filaments isolated from skinned amphibian smooth muscle cells are side-polar, *J Muscle Res Cell Motil*, **10**, 206-220, 1989.
54. Piazzesi G., V. Lombardi, A cross-bridge model that is able to explain mechanical and energetic properties of shortening muscle, *Biophys J*, **68**, 1966-1979, 1995.
55. Smith D.A., M.A. Geeves, Strain-dependent cross-bridge cycle for muscle, *Biophys J*, **69**, 524-537, 1995.
56. Smith D.A., M.A. Geeves, Strain-dependent cross-bridge cycle for muscle. II. Steady-state behavior, *Biophys J*, **69**, 538-552, 1995.
57. Smith D.A., A strain-dependent ratchet model for [phosphate]- and [ATP]-dependent muscle contraction, *J Muscle Res Cell Motil*, **19**, 189-211, 1998.
58. Goldman Y.E., A.F. Huxley, Actin compliance: are you pulling my chain?, *Biophys J*, **67**, 2131-2133, 1994.
59. Mijailovich S.M., J.J. Fredberg, J.P. Butler, On the theory of muscle contraction: filament extensibility and the development of isometric force and stiffness, *Biophys J*, **71**, 1475-1484, 1996.
60. Lombardi V., G. Piazzesi, The contractile response during steady lengthening of stimulated frog muscle fibres, *J Physiol*, **431**, 141-171, 1990.
61. Haselgrove J.C., H.E. Huxley, X-ray evidence for radial cross-bridge movement and for the sliding filament model in actively contracting skeletal muscle, *J Mol Biol*, **77**, 549-568, 1973.
62. McKillop D.F., M.A. Geeves, Regulation of the interaction between actin and myosin subfragment 1: evidence for three states of the thin filament, *Biophys J*, **65**, 693-701, 1993.
63. Hill T.L., E. Eisenberg, Theoretical considerations in the equilibrium binding of myosin fragments on F-actin, *Biophys Chem*, **11**, 271-281, 1980.
64. Smith D.A., R. Maytum, M.A. Geeves, Cooperative regulation of myosin-actin interactions by a continuous flexible chain I: actin-tropomyosin systems., *Biophys. J.*, **84**, 3155-3167, 2003.
65. Smith D.A., M.A. Geeves, Cooperative regulation of myosin-actin interactions by a continuous flexible chain II: actin-tropomyosin-troponin and regulation by calcium., *Biophys. J.*, **84**, 3168-3180, 2003.
66. Dillon P.F., M.O. Aksoy, S.P. Driska, R.A. Murphy, Myosin phosphorylation and the cross-bridge cycle in arterial smooth muscle, *Science*, **211**, 495-497, 1981.

67. Hartshorn D.J., in *Physiology of the Gastrointestinal Tract*; L.R. Johnson (ed.), Ravena Press, New York, pp. 423-482, 1987.
68. Hai C.M., R.A. Murphy, Regulation of shortening velocity by cross-bridge phosphorylation in smooth muscle, *Am J Physiol*, **255**, C86-94, 1988.
69. Mijailovich S.M., J.P. Butler, J.J. Fredberg, Perturbed equilibria of myosin binding in airway smooth muscle: bond-length distributions, mechanics, and ATP metabolism, *Biophys J*, **79**, 2667-2681, 2000.
70. Fredberg J.J., D.S. Inouye, S.M. Mijailovich, J.P. Butler, Perturbed equilibrium of myosin binding in airway smooth muscle and its implications in bronchospasm, *Am J Respir Crit Care Med*, **159**, 959-967, 1999.
71. Yu S.N., P.E. Crago, H.J. Chiel, Biomechanical properties and a kinetic simulation model of the smooth muscle I2 in the buccal mass of *Aplysia*, *Biol Cybern*, **81**, 505-513, 1999.
72. Pate E., R. Cooke, A model of crossbridge action: the effects of ATP, ADP and Pi, *J Muscle Res Cell Motil*, **10**, 181-196, 1989.
73. Davis T.A., P.-C. Yew, A nondeterministic parallel algorithm for general unsymmetric sparse LU, *Factorization. Siam J. Matrix Anal. Appl.*, **11**, 383-402, 1990.
74. Davis T.A., I. Duff, An unsymmetric-pattern multifrontal method for sparse LU factorization, *Siam J. Matrix Anal. Appl.*, **18**, 140-158, 1997.
75. Censor Y.D., D. Gordon, R. Gordon, Component averaging: An efficient iterative parallel algorithm for large and sparse unstructured problems, *Parallel Comp*, **27**, 777-808, 2001.
76. Censor Y., D. Gordon, R. Gordon, BICAV: a block-iterative parallel algorithm for sparse systems with pixel-related weighting, *IEEE Trans Med Imaging*, **20**, 1050-1060, 2001.
77. Wood J., R. Mann, A sliding-filament cross-bridge ensemble model of muscle contraction for mechanical transients, *Math. Biosci.*, **57**, 211-263, 1981.
78. Glasstone S., J. Laidler, K. Eyring, *The Theory of Rate Processes*, McGraw Hill, New York, 1941.
79. Steffen W., D. Smith, R. Simmons, J. Sleep, Mapping the actin filament with myosin, *Proc Natl Acad Sci U S A*, **98**, 14949-14954, 2001.
80. Simmons R.M., D.A. Smith, J. Sleep, Target zones on the actin filament and the myosin working stroke from optical trapping., *Biophys. J. (Annual Meeting Abstracts)*, **80** (1): 80, 2001.
81. Kojic M., The governing parameter method for implicit integration of viscoplastic constitutive relations for isotropic and orthotropic metals, *Int. J. Computational Mechanics*, **19**, 49-57, 1996.
82. Kojic M., N. Grujovic, R. Slavkovic, M. Zivkovic, A general orthotropic von Mises plasticity material model with mixed hardening - model definition and implicit stress integration procedure, *Transactions of ASME J Appl. Mechanics*, **63**, 376-382, 1996.
83. Smith D.A., Direct tests of muscle cross-bridge theories: predictions of a Brownian dumbbell model for position-dependent cross-bridge lifetimes and step sizes with an optically trapped actin filament, *Biophys J*, **75**, 2996-3007, 1998.

84. Smith D.A., W. Steffen, R.M. Simmons, J. Sleep, Hidden-Markov methods for the analysis of single-molecule actomyosin displacement data: the variance-Hidden-Markov method, *Biophys J*, **81**, 2795-2816, 2001.
85. Ford L.E., A.F. Huxley, R.M. Simmons, The relation between stiffness and filament overlap in stimulated frog muscle fibres, *J Physiol*, **311**, 219-249, 1981.
86. Cooke R., Actomyosin interaction in striated muscle, *Physiol Rev*, **77**, 671-697, 1997.
87. Stehle R., B. Brenner, Cross-bridge attachment during high-speed active shortening of skinned fibers of the rabbit psoas muscle: implications for cross-bridge action during maximum velocity of filament sliding, *Biophys J*, **78**, 1458-1473, 2000.
88. Pate E., H. White, R. Cooke, Determination of the myosin step size from mechanical and kinetic data, *Proc Natl Acad Sci U S A*, **90**, 2451-2455, 1993.
89. Bagni M.A., G. Cecchi, F. Colomo, C. Poggesi, Tension and stiffness of frog muscle fibres at full filament overlap, *J Muscle Res Cell Motil*, **11**, 371-377, 1990.
90. Razumova M.V., A.E. Bukatina, K. B. Campbell, Stiffness-distortion sarcomere model for muscle simulation, *J Appl Physiol*, **87**, 1861-1876, 1999.
91. Zahalak G.I., A comparison of the mechanical behavior of the cat soleus muscle with a distribution-moment model, *J Biomech Eng*, **108**, 131-140, 1986.
92. Eisenberg E., T.L. Hill, Muscle contraction and free energy transduction in biological systems, *Science*, **227**, 999-1006, 1985.

CYTOSKELETAL PRESTRESS AS A DETERMINANT OF DEFORMABILITY AND RHEOLOGY OF ADHERENT CELLS

Dimitrije Stamenović*

5.1. INTRODUCTION

Mechanotransduction – cellular response to mechanical stress – is governed by the cytoskeleton (CSK), an intracellular network of various biopolymers (actin microfilaments, microtubules, intermediate filaments, myosin, and crosslinking polymers) (cf. ¹). The CSK mechanically stabilizes the cell and actively generates contractile forces. To carry out certain behaviors (e.g., crawling, spreading, division, invasion, etc.), cells must modify their CSK to become highly deformable, almost fluid-like, whereas in order to maintain their structural integrity when mechanically stressed, the CSK must behave like an elastic solid. These responses are governed by material properties of the CSK as well as by stress-induced changes in biochemistry that modify the structure of the CSK. Although the mechanical properties of cells govern their form and function, and when abnormal, lead to a wide range of diseases ¹, little is known about biophysical and biochemical mechanisms by which cells control their deformability. In the past, tensegrity architecture ²⁻⁷, cytoskeletal remodeling (gel-sol transition) ⁸, cross-bridge kinetics ⁹, soft glass rheology ¹⁰, polymer network rheology ¹¹⁻¹⁴, and the percolation theory ¹⁵ have been invoked to explain this problem. They have provided useful insights into the mechanisms that govern cell deformability, but they also steered controversies, leaving many questions open and many issues to be reconciled. During the past decade, a growing body of evidence has indicated that me-

* Department of Biomedical Engineering, Boston University, Boston, Massachusetts, USA.

chanical prestress of the CSK has a central role in cell deformability and rheology. This chapter provides a brief survey of experimental and theoretical studies that describe the role of cytoskeletal prestress in the mechanical behavior of cells. The chapter is divided into two major parts: 1) statics - which deals with prestress and deformability (shape stability) of the CSK, and 2) dynamics which deals with the prestress and cytoskeletal rheology.

5.2. WHAT IS PRESTRESS?

The prestress is pre-existing tensile stress within the CSK even before application of external loads. It results from the action of tensional forces that are generated in contractile actin microfilaments which are transmitted over intermediate filaments, and resisted by adhesive tethers to the extracellular matrix (ECM) known as focal adhesions (Fig. 5.1), and by other CSK filaments (e.g., microtubules) inside the cell. The prestress can be modulated by activating or de-activating myosin contractile motors (e.g., through various agonists and antagonist such as histamine, isoproterenol, etc.) and also passively by mechanical distension of the cell (e.g., due to stretching of the ECM or due to swelling pressure of the liquid cytoplasm). One of the first pieces of evidence that cytoskeletal prestress is transferred to the ECM is provided by Harris et al.¹⁶ who showed that fibroblasts cultured on a malleable substrate cause the substrate to wrinkle as they contract (Fig. 5.2).

Figure 5.1. Cytoskeletal actin network (green) carries prestress which is transmitted to the extracellular matrix via focal adhesions (arrow). Blue indicates nuclei. Courtesy of Sui Huang and Donald E. Ingber. Please see the Figure on the page 269.

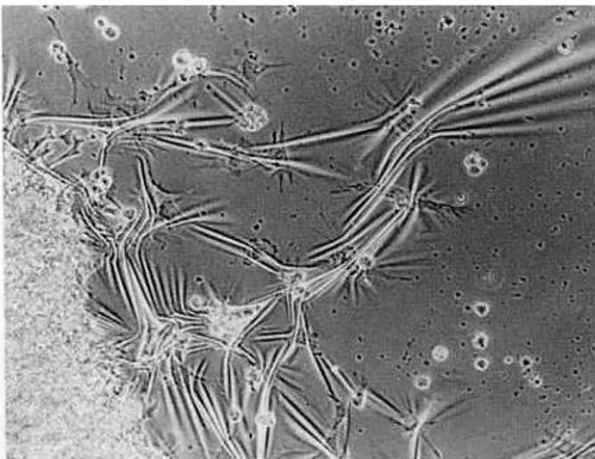


Figure 5.2. Evidence of prestress in living cells. Fibroblast cells cause silicon rubber substrate to wrinkle as they contract. From A.K. Harris, et al., Silicon rubber substrata: a new wrinkle in the study of cell locomotion, *Science* **208**, 177-179 (1980), (Ref. 16). Reprinted with permission from AAAS.

5.3. STATICS: PRESTRESS AND CELL DEFORMABILITY

The idea that mechanical prestress determines cell shape stability is rooted in the model that depicts the cell as a tensed cortical membrane surrounding pressurized liquid cytoplasm (cf. ^{17,18}). An instructive analogy is a rubber balloon filled with air. Air pressure inflates the balloon and provides tension in the rubber membrane, while this tension maintains shape to the balloon; the greater the air pressure (i.e., the greater the tension in the membrane), the more stable the shape of the balloon is. This idea was further advanced by Ingber who suggested that prestress in the tensed intracellular cytoskeletal lattice, rather than the cortical membrane, is primarily responsible for shape stability in adherent mammalian cells. Ingber introduced a special class of tensed, reticulated mechanical structures, known as “tensegrity” architecture^{*}, as a model of the CSK (cf. ²⁻⁴) (Fig. 5.3).

These are discrete structures comprised of a continuous network of cable-like tensile elements and isolated compression-bearing struts. These structures have no intrinsic shape stability like, for example metals or rubber, and require initial tension in the cable elements to maintain stability. This tension is balanced by compression in the struts and, if the structure is attached to the substrate, by anchoring forces at the substrate. Together, cables, struts and the substrate form a stable, self-equilibrated system. An illustrative example of tensegrity is camp tent; the cloth and ropes carry tension that is balanced by compression in the poles and by the pegs in the ground to which the ropes are tied.

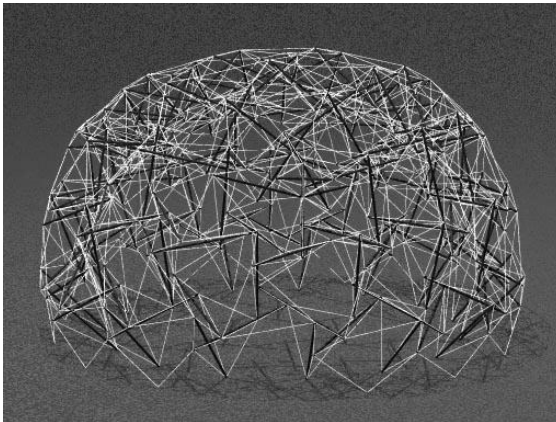


Figure. 5.3. A cable-and-strut tensegrity dome ("Dome Image ©1999 Bob Burkhardt"). In this structure tension in the cables (white lines) is partly balanced by the compression of the struts (thick black lines) and partly by the attachments to the substrate. From R. Burkhardt, *A Technology for Designing Tensegrity Domes and Spheres* (2007), (Ref. 20). Reprinted with permission of R. Burkhardt.

^{*} Tensegrity architecture is a building principle introduced by R. Buckminster Fuller ¹⁹ and is defined as a system through which structures are stabilized by continuous tension (i.e., prestress) carried by the structural members. Fuller referred to this architecture as “tensional integrity”, or shortly “tensegrity”.

The central mechanism by which tensegrity structures develop restoring stress in the presence of external loading is primarily by geometrical rearrangement of their pre-tensed members^{5,6}. The greater the pre-tension carried by these elements, the less geometrical rearrangement they undergo under an applied load, and thus, the less deformable (more rigid) the structure will be. Consequently, stiffness (G) increases in proportion with the level of the prestress (P)²¹.

$$G \propto P \tag{5.1}$$

Key premises of the cellular tensegrity model are: a) cytoskeletal prestress, carried by the network of actin and intermediate filaments, confers shape stability to the cell; and b) the prestress is partly balanced by tethering forces at the focal adhesions and partly by CSK-based compression-bearing elements such as microtubules (Fig. 5.4).

It is important to clarify that according to a mathematical definition of tensegrity, that is based on considerations of structural stability²², various tensile pre-stressed networks, including the cortical membrane model and the tensed cable network (e.g., spider web) also fall in the category of tensegrity structures. All these structures conform to eq. (5.1). They differ only by the manner in which they balance the prestress. However, in the structural mechanics literature, this difference is used to make a distinction between various types of prestressed structures and consequently, tensed cable nets and tensegrity architecture are considered as two distinct types of structures^{21,23}.

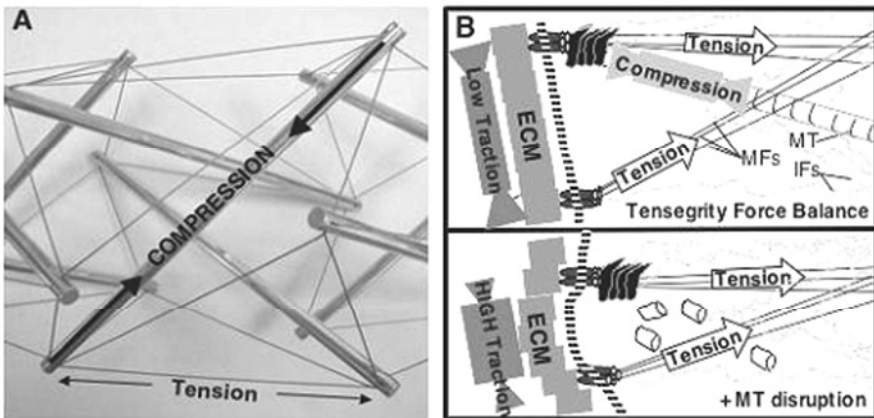


Figure 5.4. Tension-compression synergy in tensegrity. A) in a cable-and-strut model and B) in the cellular tensegrity model, where tension in actin microfilaments (MF) is balanced by compression of microtubules (MT) and tractional forces of the ECM. Disruption of MTs causes an increase in tractional forces. From N. Wang et al., *Proc Nat. Acad. Sci. USA* **98**, 7765-7770 (2001), (Ref. 7).

5.3.1. Measurements of cytoskeletal prestress and stiffness

5.3.1.1. Traction Microscopy

Traction microscopy is a technique for measuring traction that arises at the cell-substrate interface during cell contraction^{7,23-25}. Since traction must balance the cytoskeletal contractile stress, it is possible to compute the contractile stress. Cells are cultured sparsely on the apical surface of elastic polyacrylamide gel. The bottom surface of the gel is bonded to a glass plate and the lateral surfaces are free. Many fluorescent microbeads (0.2- μm diameter) are embedded near the apical surface. As the cell contracts, the motion of the microbeads is measured (Fig. 5.5A). From measured displacement field of the microbeads and known elastic properties of the gel (elastic modulus of $\sim 1\text{-}30\text{ kPa}$), traction (τ) can be calculated using equations from the theory of elasticity²⁵. By considering force balance of a free body diagram of an arbitrary section of the cell, the cytoskeletal prestress is obtained from τ and cell geometry (Fig. 5.5B).

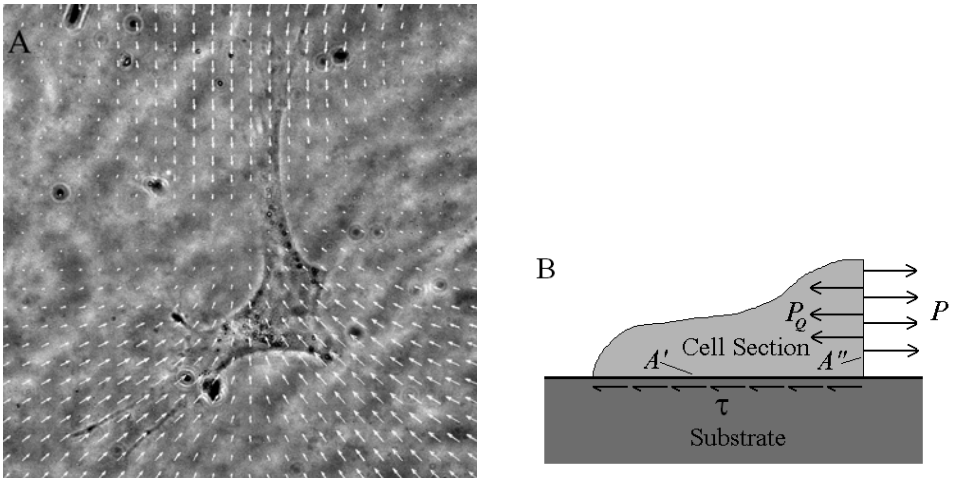


Figure 5.5. A) Displacement field of the substrate. A human airway smooth muscle cell cultured on a flexible polyacrylamide gel substrate contracts in response to histamine (10 μM). As a result, the substrate deforms causing fluorescent microbeads embedded in the gel to move (white arrows). **B) A free-body diagram of a cell section** depicting a three-way force balance between the actin CSK, substrate, and microtubules: $P_S = P - P_Q$ where P_S indicates the part of prestress (P) balanced by the substrate and P_Q indicates the part of P balanced by compression-supporting microtubules. Equilibrium requires that $\tau A' = P_S A''$ where A' and A'' are interfacial and cross-sectional areas of the cell section, respectively and τ is traction. Since τ , A' A'' can be directly measured, one can obtain P_S . From D. Stamenović, Models of cytoskeletal mechanics based on tensegrity. In: *Cytoskeletal Mechanics – Models and Measurements*, Cambridge University Press, New York (2006), pp. 103-128, (Ref. 23).

Note that only the fraction of the contractile prestress (P) that is balanced by the substrate (P_S) can be obtained from traction measurements (Fig. 5.5B). The other portion that is balanced by microtubules (P_Q) can be determined by chemically disrupting microtubules and repeating the traction measurements (Fig. 5.4B). The difference in the estimated prestress after and prior to disruption of microtubules corresponds to P_Q , i.e., $P_Q = P - P_S$ ²⁶.

5.3.1.2. Magnetic Twisting Cytometry

Magnetic twisting cytometry is a technique for measuring rheological properties of living cells. It originated in early 1950s²⁷ and has been improved and modified during past two decades^{10,28,29}. Ferromagnetic beads (4.5 μm -diameter) are coated with a peptide that binds specifically to mechanical integrin receptors on the cell apical surface (Fig. 5.6). Integrins physically connected to the actin CSK through a series of linking protein (vinculin, talin, α -actinin, etc.). Thus, by twisting beads attached to integrins we can directly probe mechanical properties of the CSK. Beads are initially magnetized in the horizontal plane. Then they are twisted by a magnetic field applied in the vertical plane. From the applied specific twisting torque and the corresponding horizontal bead displacement, stiffness is calculated from the ratio of the two. This ratio is multiplied by a geometrical factor in order to obtain the stiffness in the units of stress³⁰. The magnetic cytometer can operate in different loading modes, including a step loading and a harmonic (oscillatory) loading.

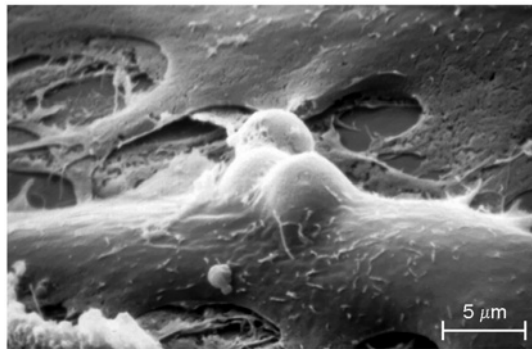


Figure 5.6. Magnetic cytometry technique. Ferromagnetic beads coated with the integrin-binding RGD (Arg-Gly-Asp) peptide attached to the apical surface of cultured human airway smooth muscle cells. From B. Fabry et al., Implications of heterogeneous bead behavior on cell mechanical properties measured with magnetic twisting cytometry, *Journal of Magnetism and Magnetic Materials* **194**, 120-125 (1999), (Ref. 29). Reprinted with permission from Elsevier Ltd.

There are other techniques for measuring cell stiffness including atomic force microscopy^{31,32} and micropipette aspiration^{17,33}. However, these techniques are non-specific in the sense that they do not probe directly the CSK, but rather apply load to the cell surface. Thus, the outcome of these measurements is influenced by the cell lipid membrane and other non-cytoskeletal structures.

Results of traction and magnetic cytometry measurements showed that the cell stiffness increases linearly with increasing cytoskeletal prestress (Fig. 5.7)^{7,23,24}. This is consistent with the *a priori* prediction of the tensegrity model (eq. 5.1). While these results do not necessarily prove tensegrity nor they disprove alternative models and interpretations, the weight of the evidence does suggest that the stiffness comes mainly from the prestress.

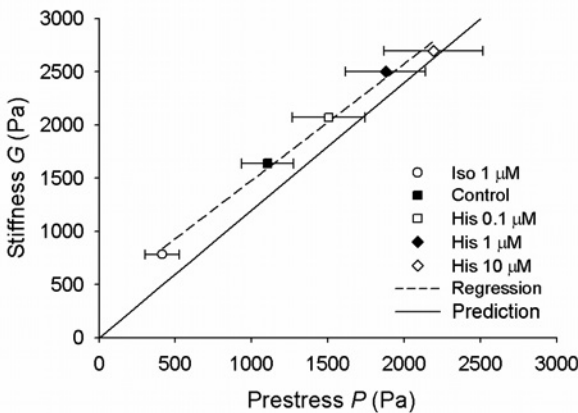


Figure 5.7. Cytoskeletal stiffness (G) vs. prestress (P) relationship measured in cultured human airway smooth muscle cells; G is measured by magnetic cytometry and P by traction microscopy. Both G and P are modulated by graded doses of contractile agonist histamine (His) and relaxant isoproterenol (Iso). Points are data \pm SE; dashed line is regression (slope = 1.1), solid line is model prediction (slope = 1.2; see section 5.3.2. 2 below). Reprinted with permission from the American Physiological Society (Ref. 24).

5.3.2. Modeling of the steady-state mechanical behavior of the CSK

To illustrate how these mechanisms arise from the cytoskeletal microstructure and how they predict various cell behaviors, we use an affine tensegrity model³⁴. The affine approximation effectively combines features of both continuum mechanics and discrete network modeling approaches and allows developing a model of a complex structure without having to rely on a detailed description of microstructural geometry or boundary conditions. The key premise of the affine approximation is that microstructural strains are related to the global (continuum) strain according to the laws of continuum mechanics. This approach allows one to interpret mechanical properties of a discrete structure (such as the CSK) in terms of quantities

that characterize a solid continuum (e.g., shear modulus). These quantities can be then used to study a particular boundary value problem in cellular mechanics using methods of continuum mechanics. Another advantage of the affine approach is that it yields explicit and mathematically transparent equations that describe various behaviors of cells and that can be easily implemented and experimentally tested. It does not require numerical and computationally-intensive calculations for obtaining those predictions.

The CSK of an isolated adherent cell is modeled as a network composed of tension-bearing cables interconnected with compression-supporting struts³⁴. The cables and struts are perfectly elastic. The structure is anchored to a rigid substrate. The cables play the role of actin microfilaments, whereas the struts play the role of microtubules. The cables carry pre-tension which is partly balanced by the compression of the struts, and partly by anchoring forces of the substrate. All junctions are assumed frictionless. The variational statement of equilibrium for the model is

$$\delta U = \sum_{i=1}^N F_i \delta l_i - \sum_{i=1}^M Q_i \delta L_i \quad (5.2)$$

where U is the potential of external macroscopic (continuum) stress, F_i and l_i are current forces and lengths of the cables ($i = 1, 2, 3, \dots, N$), Q_i and L_i are current forces and lengths of the struts ($i = 1, 2, 3, \dots, M$), and N and M denote the total number of cables and struts in the network, respectively. The negative sign in eq. (5.2) indicates compression. Because cables and struts are two-force members, F_i and Q_i depend only on l_i and L_i , respectively. The struts are slender and may buckle under compression. In that case, L_i indicates the end-to-end length (chord-length) of a strut. For mathematical simplicity, we do not include in eq. (5.2) the explicit contribution of intermediate filaments. To include this contribution, an additional term of the same mathematical form as the first term on the right-hand side of eq. (5.2) should be added.

5.3.2.1. Force balance between actin microfilaments, microtubules and the ECM

For uniform volume change, $U = \sigma V$, where σ is macroscopic isotropic stress and V is the current volume of the CSK. Then, according to the affine assumption, lengths change proportionally to $V^{1/3}$, i.e., $l_i \propto V^{1/3}$, and $L_i \propto V^{1/3}$. Thus, it follows from eq. (5.2) that

$$\sigma = \sum_{i=1}^N \frac{F_i l_i}{3V} - \sum_{j=1}^M \frac{Q_j L_j}{3V} = \frac{N \langle Fl \rangle}{3V} - \frac{M \langle QL \rangle}{3V}, \quad (5.3)$$

where $\langle \cdot \rangle$ indicates the average over all orientations. At the reference state, the first term on the right-hand side of eq. (5.3) represents the prestress (P) borne by the actin microfilament network; the second term represents the part of P balanced by microtubules (P_O). If $P > P_{MT}$, then σ on the left-hand side of eq. (5.3) indicates the part of P balanced by the ECM (P_S). Thus, $P_S = P - P_O$. Mechanical equilibrium of a section of the cell (see Fig. 5.5B) demands that mean traction (τ) at the cell-ECM interface and P_S are balanced, i.e.,

$$\tau A' = P_S A'' = (P - P_O) A'', \quad (5.4)$$

where A' and A'' are the interfacial and the cross-sectional areas of the cell section, respectively (Fig. 5.5B). (Strictly speaking, eq. (5.4) holds only when the cross-sectional surface A'' is perpendicular to the substrate and the force balance is in the direction of the normal to A'' .) Importantly, all variables in eq. (5.4) are measurable, which makes possible to evaluate contributions of actin filaments, ECM and microtubules to force balance across the CSK. For example, experimental data show that the contribution of microtubules (i.e. P_O) to changes in τ can vary from a few percent in highly spread cells (i.e. big A'), to up to 80% in poorly spread cells (i.e. small A') while P and A'' are maintained nearly constant^{23,35}.

A key assumption of the tensegrity model is that microtubules carry compression as they balance tension in the actin network. This is qualitatively supported by microscopic visualizations of microtubules of living cells that show that microtubules buckle as they oppose contraction of the actin network (Fig. 5.8)⁷.

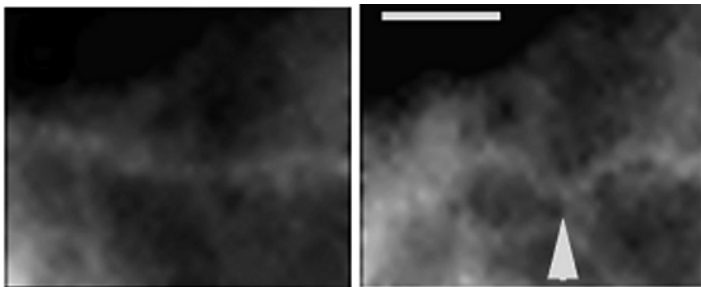


Figure 5.8 Local buckling of a microtubule in cultured endothelial cells. A microtubule appears fairly straight prior to cell contraction (left) and assumes a typical sinusoidal buckled shape (arrowhead) following contraction induced by thrombin (right). The scale bar is 2 μm . From N. Wang et al., Mechanical behavior in living cells consistent with the tensegrity model. *Proc. Nat. Acad. Sci. USA* **98**, 7765-7770 (2001), (Ref. 7).

It is not known, however, whether the compression that causes this buckling could balance a substantial fraction of the contractile prestress. To investigate this possibility, we carried out an energetic analysis of

buckling of microtubules²⁶. The assumption was that energy stored in microtubules during compression is transferred to a flexible substrate upon their disruption. Thus, an increase in elastic energy of the substrate following disruption of microtubules should indicate transfer of compression energy that was stored in microtubules prior to their disruption. Experimental data show that in spread human airway smooth muscle cells that are optimally stimulated with contractile agonists (i.e., the cytoskeletal contractile prestress is maintained constant at its optimal level), disruption of microtubules causes the energy stored in the substrate to increase on average by ~ 0.13 pJ²⁶. This result was then compared with results from a model in which the microtubules are assumed to be slender elastic rods laterally supported by intermediate filaments³⁶. Using the post-buckling equilibrium theory of Euler struts³⁷, we estimated that the energy stored during buckling of microtubules is ~ 0.18 pJ, which is close to the measured value of ~ 0.13 pJ²⁶. This is further evidence in support of the idea that microtubules are intracellular compression-bearing elements.

Taken together, the above results confirmed the existence of a complementary force balance between contractile forces carried by the actin network, compression in microtubules and traction forces that arise at the focal adhesion anchoring to the ECM, as predicted by the tensegrity. We next use the affine model to show how prestress confers stiffness to the CSK.

5.3.2.2. Prestress induced stiffness of the CSK

We consider a simple shear distortion of the CSK. In that case, the potential $U = V_0 \sigma_s \gamma$, where σ_s is the macroscopic shear stress γ is the corresponding macroscopic shear strain and V_0 is the reference volume occupied by the CSK. Thus it follows from eq. (5.2) that³⁴

$$\sigma_s = \frac{1}{V_0} \left(\sum_{i=1}^N F_i \frac{dl_i}{d\gamma} - \sum_{j=1}^M Q_j \frac{dL_j}{d\gamma} \right) = \frac{1}{V_0} \left(N \left\langle F \frac{dl}{d\gamma} \right\rangle - M \left\langle Q \frac{dL}{d\gamma} \right\rangle \right). \quad (5.5)$$

Taking the derivative of eq. (5.5) with respect to γ and evaluating it at the reference state (i.e., $\gamma = 0$), we obtain the shear modulus (G) as follows

$$G = \left. \frac{d\sigma_s}{d\gamma} \right|_{\gamma=0} = \frac{1}{V_0} \left[N \left\langle F \frac{d^2 l}{d\gamma^2} \right\rangle + N \left\langle \frac{dF}{dl} \left(\frac{dl}{d\gamma} \right)^2 \right\rangle - M \left\langle Q \frac{d^2 L}{d\gamma^2} \right\rangle - M \left\langle \frac{dQ}{dL} \left(\frac{dL}{d\gamma} \right)^2 \right\rangle \right]_{\gamma=0}. \quad (5.6)$$

To obtain quantitative predictions for G and compare them to experimental data, we assume a) the affine strain field and b) that at the refer-

ence state orientations of cables and struts are equally probable. The first assumption yields l and L as functions of γ , i.e.,

$$\frac{l}{l_0} = \frac{L}{L_0} = \sqrt{(1+\gamma)^2 \sin^2 \theta \cos^2 \psi + (1-\gamma)^2 \sin^2 \theta \sin^2 \psi + \cos^2 \theta}, \quad (5.7)$$

where ψ and θ are azimuth and latitude angles of the spherical coordinates, and l_0 and L_0 are reference lengths of cables and struts, respectively. The second assumption implies material isotropy and is used to calculate the average values, i.e.,

$$\langle f \rangle = \frac{1}{2\pi} \int_0^{2\pi} \int_0^{\pi/2} f(\theta, \psi) \sin \theta d\theta d\psi, \quad (5.8)$$

where f is any function and $\langle \cdot \rangle$ denotes an average value. By combining eqs. (5.3) and (5.6) – (5.8), we obtain that

$$G = 0.8(P - P_Q) + 0.2(BP - B_Q P_Q), \quad (5.9)$$

where $P = NF_0 l_0 / 3V_0$, $P_Q = MQ_0 L_0 / 3V_0$, $B = (dF/dl)_0 / (F_0/l_0)$, $B_Q = (dQ/dL)_0 / (Q_0/L_0)$, and subscript 0 indicates the reference state. The value of the non-dimensional cable stiffness B is determined from tensile tests of isolated acto-myosin filament interactions³⁸; $B \approx 2.4$ for a wide range of tensile force. The value of the non-dimensional strut stiffness B_Q is determined from buckling behavior of microtubules. We find experimentally that in highly spread cells $P_Q = 0.12P$ and the corresponding $B_Q \approx -0.7$ ²⁶. Substituting the above values for P_Q , B and B_Q into eq. (5.9), we obtain that $G \approx 1.2P$. This prediction is consistent with experimental data for cultured, highly spread airway smooth muscle cells (see Fig. 5.7).

The model also predicts how microtubules contribute to the overall stiffness of the CSK. Since microtubules and the substrate together balance the contractile prestress, disruption of microtubules would alter this balance and thus, according to eq. (5.9), affect cytoskeletal stiffness. Experimental data from cultured adherent cells show that disruption of microtubules causes either cell softening^{33,39,40}, stiffening^{41,42}, or no change in stiffness^{43,44}. Using eq. (5.9) and experimental data for the contribution of microtubules to balancing the prestress³⁵, we found that in highly spread cells stiffness slightly increases, whereas in poorly spread cells the stiffness decreases with disruption of microtubules³⁴. This finding is quantitatively consistent with experimental data from cultured human airway smooth muscle cells which show that disruption of microtubules by colchicine causes a 10% increase in cell stiffness⁴¹ whereas the model predicts an 8% increase³⁴.

One limitation of the affine approach is the assumption that local strains follow global strains, which leads to overestimate of elastic moduli (cf. ⁴⁵).

This can, in part explain, the slight quantitative discrepancy between the slopes of the G vs. P relationship predicted by the model and the one calculated from the experimental data; the model predicts the slope of 1.2 whereas experiments yield the slope of 1.1 (Fig. 5.7). Furthermore, this model cannot predict long-distance propagation of forces in the cytoplasm that has been observed in living cells^{15,46}, since the model presumes a continuum behavior which, in turn, implies that local loads produce only local deformations (in continuum mechanics this is known as the principle of local action). Nevertheless, the affine model has been successful in describing and predicting a number of essential mechanical properties of living cells such as prestress induced stiffening, the contribution of microtubules to cell stiffness and to load shift between the CSK and the ECM.

5.4. DYNAMICS: PRESTRESS AND CELL RHEOLOGY

The proportionality between stiffness and prestress (eq. 5.1) characterizes steady-state (static) behavior of prestressed structures where only elastic forces contribute to the overall stress. Under dynamic loadings, however, other forces (e.g., viscous forces) also come into play. Since viscous forces are an important component of the overall cellular stress, it is of considerable interest to investigate how the prestress affects dynamic behavior of the cell.

The oscillatory response of linear viscoelastic materials is characterized by the dynamic modulus (G^*), i.e., the complex stress to strain ratio. The real part of G^* is the elastic (storage) modulus (G') and the imaginary part is the viscous (loss) modulus (G''); $G^* = G' + iG''$, where $i = \sqrt{-1}$ is indicative of the out-of-phase behavior; phase $\phi = \text{atan}(G''/G')$ (cf.⁴⁷).

Data from the oscillatory measurements (0.1-1000 Hz) on cultured airway smooth muscle cells reveal that both G' and G'' increase with increasing prestress P , and that this dependence is accentuated at higher frequencies (Fig. 5.9)⁴⁸. While the dependence of G' on P was expected, based on the notion that the CSK determines cell elastic behavior (as explained in the previous sections), the dependence of G'' on P was not. The reason was the common belief that viscous properties of the cell are primarily determined by liquid cytoplasm and thus altering cytoskeletal prestress should bear little impact on G'' . These results, however, suggest that both elastic and viscous properties of the cell reside within the CSK where they are affected by the prestress.

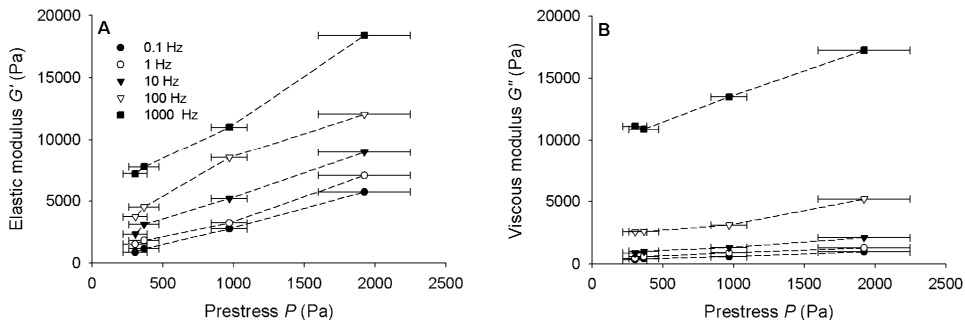


Figure 5.9. Rheological moduli vs. prestress relationships. A) Elastic modulus (G') and B) viscous modulus (G'') increase with increasing prestress (P). This dependence is accentuated at higher frequencies. Measurements were done on cultured human airway smooth muscle cells using the traction microscopy and magnetic cytometry techniques. The prestress was modulated pharmacologically by histamine and isoproterenol. Data means \pm SE. Reprinted with permission from the American Physiological Society (Ref. 48).

More insight into the cell dynamic behavior are obtained from replotting the data in [Figure 5.9](#) such that G' and G'' are functions of forcing frequency (f) on a log-log scale ([Fig. 5.10](#)). One can see that $\log G'$ increases linearly with $\log f$ over four decades of f . This, in turn, implies that G' changes with f according to a power law, $G' \sim f^\alpha$, where the power-law exponent α corresponds to the slope of the curve on the log-log scale ([Fig. 5.10](#)).

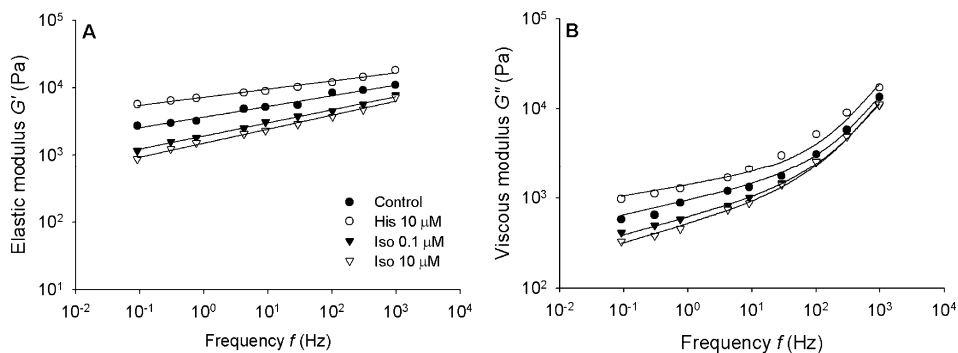


Figure 5.10. Rheological moduli vs. frequency relationships. A) Elastic modulus (G') in airway smooth muscle cells increases with increasing frequency (f) according to a power law for different levels of prestress (P). B) Frictional modulus (G'') also follows the power law up to 10 Hz, but above 10 Hz the power-law dependence increases and approaches the log-log slope of 1. Prestress is modulated pharmacologically by histamine (His) and isoproterenol (Iso). Data are means and black lines are best fits of eqs. (5.10). Reprinted with permission from the American Physiological Society (Ref. 48).

This power-law dependence persists at each level of P only the slope (i.e., α) changes; it decreases as P increases. Similar behavior has been observed in the case of G'' , except that at frequencies >10 Hz, the power-law dependence progressively increases and approaches unity at very high frequencies, indicative of Newtonian viscous behavior.

A power-law implies that cell rheology is not determined by a discrete number of time constants, rather by a continuous spectrum. This suggests that a single molecular process does not determine cell rheology, rather that it is result of many processes.

Fabry et al.¹⁰ recognized that the observed behaviors conform to a structural damping law (cf.⁴⁷). This is an empirical law which implies that the phase lag between frictional and elastic stresses is independent of f . According to the structural damping law, G' and G'' are given by the following equations

$$\text{a) } G' = G_0 \left(\frac{f}{f_0} \right)^\alpha \cos \frac{\alpha\pi}{2} \quad (5.10a)$$

$$\text{b) } G'' = G_0 \left(\frac{f}{f_0} \right)^\alpha \sin \frac{\alpha\pi}{2} + \mu f, \quad (5.10b)$$

where G_0 and f_0 are scaling factors for stiffness and frequency, respectively and $0 \leq \alpha \leq 1$ is directly related to the phase. The Newtonian viscous contribution μf is added to the equation for G'' to account for the behavior at high frequencies; μ is Newtonian viscosity. In the limit of $\alpha = 0$, $G' \propto G_0$, i.e., elastic solid of stiffness G_0 . In the limit of $\alpha = 1$, $G'' \propto f$, i.e., Newtonian viscous behavior. Thus, α is an index of transition between elastic solid-like and Newtonian fluid-like behavior. Since the slope of each curve corresponds to different value of P , it follows that α is related to P , and therefore P is an index of cell transition between a fluid-like and a solid-like behaviors. From these data and the G' vs. P , relationship (Fig. 5.9A), an empirical unique relationship between α and P was obtained⁴⁸. According to this relationship, α decreases with increasing P (Fig. 5.11), for all frequencies. This is consistent with experimentally obtained data for α and P . Taken together, these data show that there is a close association between α , an index of transition between fluid-like and solid-like behavior, and P , suggesting that cell rheological properties are controlled by P . This is an intriguing finding since it implies that the dynamic (rheological) behavior of the cell is controlled by the static prestress. However, the physical basis of this relationship remains an open question that we address in the following section.

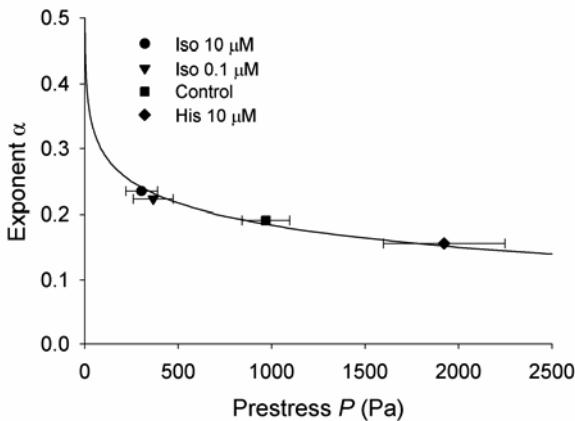


Figure 5.11. Power-law exponent (α) vs. prestress (P) relationship. By combining results from Figs. 5.9 and 5.10 it was obtained that α decreases with increasing P for all frequencies. An empirical relationship (solid line) is in agreement with experimental data on airway smooth muscle cells in which P is modulated by histamine (His) and isoproterenol (Iso). Data are means \pm SE. Reprinted with permission from the American Physiological Society (Ref. 48).

Several remarks are noteworthy. The data we show above are all obtained from only one cell type (human airway smooth muscle cells), with only one measuring technique (magnetic cytometry) and with only one method for modulating the prestress (pharmacological agonists), suggesting the possibility that those findings may be cell type- and experimental technique-dependent. However, very similar results have been also obtained with different cell types⁴⁹⁻⁵¹, using different techniques⁵¹, and by different methods for modulating the prestress^{50,52}, suggesting that the power-law rheology and its dependence on the prestress is general behavior of adherent cells.

5.4.1. Mechanisms that link cytoskeletal prestress to rheology

What is the physical basis for the observed relationship between the cytoskeletal prestress and cell rheology? In this section, we examine several potential mechanisms including tensegrity, cytoskeletal remodeling, energy activation theories, polymer network dynamics and molecular chain dynamics.

5.4.1.1. Tensegrity and cytoskeletal rheology

The original tensegrity idea considers static, elastic structures. Thus, it does not appear useful for describing the dynamic rheological behavior. However, by replacing elastic cable elements in a tensegrity system by viscoelastic elements, one can obtain a viscoelastic tensegrity model that can simulate the dynamic behavior of cells^{53,54}.

Sultan et al.⁵⁴ considered a simple six-strut tensegrity model (Fig. 5.12) where cable elements were simple Voigt models (i.e., linear spring and dashpot in parallel). A Voigt model has a single time constant and it does not change with changing tension in the cables. The idea was that through tensegrity mechanisms a qualitatively new viscoelastic behavior would emerge and that it would be consistent with the behavior observed in cells. The model was subjected to oscillatory loading. It yielded dependences of G' and G'' on prestress and on frequency of loading that are generally qualitatively consistent with experimental data. However, to obtain reasonable quantitative consistency (Fig. 5.13), it was necessary to assume that each cable has a different time constant, spanning the range of several orders of magnitude. There is no evidence that such degree of inhomogeneity exists in the CSK.

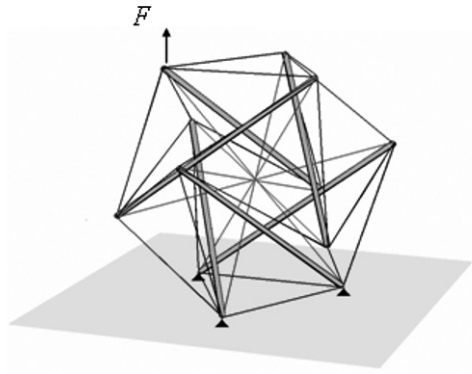


Figure 5.12. A six-strut tensegrity model with viscoelastic Voigt cables (black lines) and rigid struts (gray bars). The structure is loaded by a harmonic force (F).

It yielded dependences of G' and G'' on prestress and on frequency of loading that are generally qualitatively consistent with experimental data. However, to obtain reasonable quantitative consistency (Fig. 5.13), it was necessary to assume that each cable has a different time constant, spanning the range of several orders of magnitude. There is no evidence that such degree of inhomogeneity exists in the CSK.

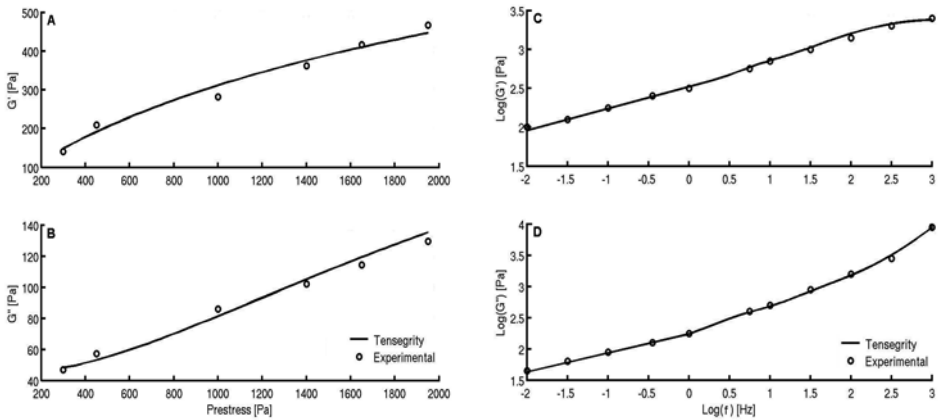


Figure 5.13. Viscoelastic behavior of the six-strut tensegrity model. A) The elastic modulus (G') and B) the viscous modulus (G'') increase with increasing prestress; C) G' and D) G'' also increase with increasing frequency (f). Lines are model's best fit to experimental data from airway smooth muscle cells. From C. Sultan et al., A computational tensegrity model predicts dynamic rheological behaviors in living cells, *Annals of Biomedical Engineering* **32**, 520-530 (2004), (Ref. 54). Reprinted with permission from Springer.

5.4.1.2. Myosin cross-bridge kinetics

It has been shown that during longitudinal extension of isolated smooth muscle strips their mean force, elastic stiffness and frictional losses increase in proportion with the number of attached myosin cross-bridges. As this number increases in response to contractile agonists, the cell contractile prestress, the stiffness and frictional losses increase in parallel⁹. Thus, the observed dependences of G' and G'' on the contractile prestress could reflect nothing more than the direct effect of myosin cross-bridge recruitment. Although one can not completely rule out this mechanism, several pieces evidence argue against this interpretation. First, a theoretical model of the cross-bridge kinetics⁵⁵ does not conform to the power-law. Second, muscle stiffness measured in longitudinal extension does not follow the power law-behavior.

5.4.1.3. Cytoskeletal remodeling

Contractile agonists (e.g., histamine), in addition to generating force in the acto-myosin contractile motors, also result in actin polymerization. Thus, the observed changes in G' and G'' during pharmacological treatments may be a result of agonist-induced cytoskeletal remodeling^{56,57}. Furthermore, actin gels near critical gelation point exhibit power law phenomena similar to the one observed in cells. However, it has been shown that agonist-induced actin polymerization may not be sufficient to explain the observed changes in G' and G'' in response to pharmacological treatments and that myosin contractile force generation also plays important role⁵⁸.

5.4.1.4. Activation energy

It is shown above that power-law exponent α is an index of cell's transition between fluid-like and solid-like behavior. This transition can be framed in terms of the Eyring's activation theory⁵⁹ as follows⁴⁸. Macroscopic deformation of the cytoskeletal lattice involves micorscale Brownian motions of its long molecular chains over energy barriers. These barriers may be intermolecular (e.g., resistance to sliding of molecular chains) or intramolecular (e.g., barriers associated with conformational changes of molecular chains). It has been shown that the relationship between macroscopic rate of strain ($\dot{\epsilon}$) and the applied stress (σ) is given as⁵⁹

$$\dot{\epsilon} \propto \sigma e^{-\Delta H / kT}, \quad (5.11)$$

where ΔH indicates the potential energy barrier, k is the Boltzmann's constant, and T is the absolute temperature. Eq. (5.11) is known as the Eyring's equation. In the limit of $\Delta H \rightarrow \infty$, i.e., very high energy barrier, it

follows from eq. (5.11) that $\dot{\epsilon} \rightarrow 0$, which implies a constant strain (ϵ) and the solid-like behavior. In the limit of $\Delta H \rightarrow 0$, i.e., very low energy barrier, it follows from eq. (5.11) that $\dot{\epsilon} \propto \sigma$, which implies the Newtonian fluid-like behavior. Thus, analogous to α in the power-law, ΔH is an index of transition between solid-like and fluid-like behavior. Because experimental findings show that α changes with the prestress⁴⁸, we speculate that ΔH may also change with prestress. One reason could be that under tension induced by the prestress, molecular chains of the CSK become taut, which in turn reduces their flexibility. A decrease in flexibility of these molecules increases the effective energy barrier associated with their conformational changes. Thus, modulations of cytoskeletal prestress might change the level of potential energy barriers within the CSK and thereby alter cellular rheological behaviors.

There are other energy activation theories that could explain the transition between solid and liquid states. One of them - soft glass rheology⁶⁰ derived from the soft matter physics – have become prominent during recent years. In this theory, however, the activation energy is thought to be greater than the thermal energy associated with Brownian motion. The pivotal idea of soft glass rheology is that soft glasses are non-equilibrium systems that flow slowly when stressed such that their material moduli scale with the time and frequency of loading according to a single weak power-law. This behavior indicates that the rheology of these materials is governed by timescale-invariant processes, regardless of the physical basis for this behavior. Soft glass rheology has been successful in describing the power-law rheology of cells^{10,49,61}. However, the physical basis of soft glass rheology in living cells has not yet been fully identified⁶². Furthermore, this theory cannot explain the dependence of material moduli on prestress.

5.4.1.5. Actin network dynamics

The rheological behavior of actin networks must necessarily reflect dynamics of actin filaments. Individual polymer chains, driven by Brownian motion, move in a snake-like fashion, called reptation, through the mesh of surrounding polymers. The extent of this motion determines deformability of the network; greater reptation means more deformable network. Humphrey et al.¹⁴ studied the oscillatory behavior of actin polymer gels with myosin dispersed in them. They found that activation of myosin causes a decrease of G' and G'' in those networks. This is opposite from the observations in cells where activation of myosin motors caused an increase in G' and G'' (see Fig. 5.9). A possible explanation for this discrepancy is that, within polymerized actin gel myosin activation does not induce contractile stress because there are no sites for mechanical anchorage

that could counterbalance this stress. Instead, the force generated by the myosin motors pushes the actin chains through the network, enhancing thereby their longitudinal motion and thus causing an apparent increase in gel fluidity. On the other hand, in living cells the contractile stress generated by the molecular motors is transmitted by the actin network to actin stress fibers, microtubules and, ultimately, via focal adhesions to the ECM which counterbalances this forces and stabilizes the CSK. Thus, contractile stress enhances stability rather than induces fluidity of the CSK of intact living cells⁴⁸.

5.4.1.6. Dynamics of individual polymer chains under sustained tension

A key difference between actin polymer networks *in vitro* and actin network within the CSK is that in the absence of external forces the former are stress-free, whereas the latter are under the influence of prestress. Consequently, actin polymer chains within the CSK are exposed to a sustained prestress-induced tension. We hypothesize that this tension bears influence on the dynamics of polymer chains and thereby on the rheological behavior of the entire CSK. We developed a model of polymer chain⁶³ that can simulate power-law creep behavior observed in living cells.

Earlier studies of the dynamics of individual actin polymer chains assume that they are linear elastic structures that fluctuate under the Brownian thermal aggitation. It was found that the dynamics of such chain is primarily entropic in nature and that yields a power law of constant exponent of 0.75^{11-13,64,65}, unlike in living cells where this exponent is smaller and changes with prestress ($\sim 0.1-0.4$)^{10,48-52,61,64,65}. By introducing non-linearity in the elasticity of the actin chain, we find that the observed dependence of the power-law exponent on the prestress can be reproduced.

We consider a chain comprised of N elastic bonds of unstretched length b_0 , connected by flexible joints of undeformed bond angle θ_0 . For simplicity, we model the chain as a two-dimensional system (Fig. 5.14A)⁶³. Due to topological constraints, the movement of a single chain within a polymer network is confined to a tube-like region bounded by its neighboring chains^{11,65,66}. Thus, the chain is built and is allowed to move inside a long, straight, rigid tube of a constant diameter (d). The elastic energy (U) stored in the chain is given by

$$U = \frac{1}{2} \sum_{i=1}^N K_1 \left(\frac{\Delta b_i}{b_0} \right)^2 + \frac{1}{4} \sum_{i=1}^N K_2 \left(\frac{\Delta b_i}{b_0} \right)^4 + \frac{1}{2} \sum_{i=1}^{N-1} K_\theta \Delta \theta_i^2, \quad (5.12)$$

where K_1 and K_2 are the linear and nonlinear bond stiffnesses, respectively, K_θ is the angular joint stiffness, Δb is the change in bond length relative to b_0 , and $\Delta \theta$ is the change in bond angle relative to θ_0 . The dynamics of the chain is driven by the motion of the joints as they thermal-

ly seek an energetically favorable position in a fixed neighborhood (Fig. 5.14B). The movement of a joint to its target position is probabilistically governed by the Monte Carlo algorithm⁶⁷ at a given temperature T . The probability $\propto \exp(-\Delta U/kT)$, where ΔU is the change of energy of the chain with respect to the original configuration calculated according to eq. (5.12). The resulting movement of the chain shows fluctuations similar to Brownian motions.

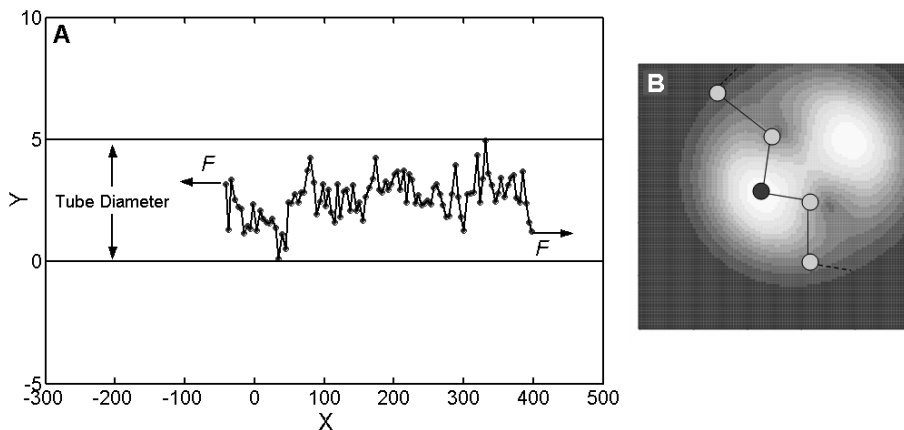


Figure 5.14. A two-dimensional elastically-jointed polymer chain model. A) The model is comprised of elastic bonds (black lines) connected by angular spring joints (gray circles). The chain is confined inside a straight tube of fixed diameter. Stretching forces (F) are applied in a stepwise manner at the end-bonds. Note that due to scaling in the X -direction the bond angles appear small, whereas initially they are close to $\sim 170^\circ$. B) A schematic depiction of a segment of the chain (joints are circles connected by bonds) with a joint (dark circle) seeking the most probable minimum energy configuration at temperature T . White and gray colors indicate high and low probabilities, respectively, of the possible positions of the joint.

The model produces creep curves that exhibit three distinct behaviors at a given prestress F_0 : an initial fast creep, a slow intermediate-time creep, and a steady state (Fig. 5.15A). The intermediate time creep behavior conforms to a power law, t^α . As F_0 increases the power-law rate of creep slows down the creep curves exhibit splay (Fig. 5.15A, inset), consistent with the experimental observations⁶¹. Consequently, the power-law exponent α decreases with increasing F_0 (Fig. 5.15B) which is also consistent with experimental data (see Fig. 5.11). Importantly, changes in N do not affect α , only the duration of creep; the greater the N , the longer the creep⁶³.

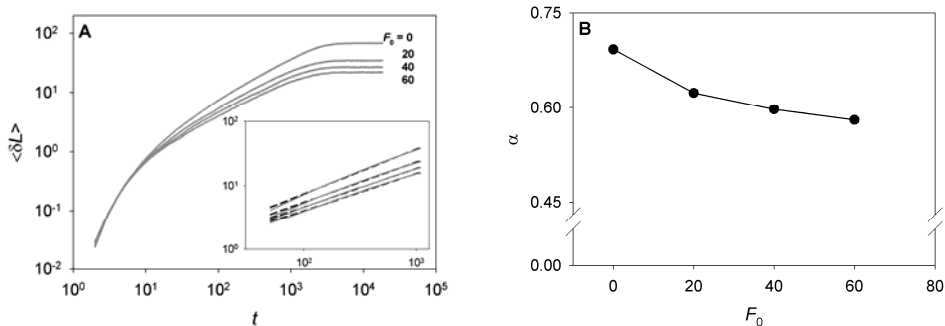


Figure 5.15. The creep response of the polymer chain model. A) The rate of creep slows down with increasing prestress ($F_0 = 0, 20, 40, 60$) such that the creep curves corresponding to different F_0 s exhibit a splay with increasing time (t) (*inset*). The creep curves are given as $\langle \delta L \rangle$ vs. t , where $\langle \cdot \rangle$ indicates the mean value calculated from five chains of $N = 350$ bonds. B) The creep power-law exponent α as decreases with F_0 . The values of α are obtained by fitting the power-law regime of the creep curve by a power-law function $\sim t^\alpha$ (black dashed lines in *inset* in Fig. 5.17A). All variables and parameters are non-dimensional. From N. Rosenblatt et al., Dynamics of prestressed semiflexible polymer chains as a model of cell rheology, *Physical Review Letters* **97**, 168101 (2006), (Ref. 63). Reprinted with permission from the American Physical Society.

The initial creep response of the chain is determined by the properties of its end-bonds. The power-law creep response, however, includes contributions from all bonds. The disturbance caused by the applied force at the end-bonds is not felt instantaneously throughout the chain. The onsets of creep are delayed throughout the chain with segments closer to the center having longer delays and faster creep than those at the ends. The cumulative effect of these delayed creep responses leads to the observed power-law behavior. The global creep response reaches the new steady state approximately when the central segment responds to the force perturbation⁶³.

To understand why nonlinear bond elasticity is critical for bringing forth the dependence of α on F_0 , we analyze internal chain segments' delayed creep responses. Due to this nonlinearity, both the effective bond stiffness and the global chain stiffness are higher at higher levels of F_0 . Since propagation speed scales with the square root of stiffness, this should result in a faster spread of the disturbance from the end-bonds toward the center of the chain. Thus, the leading edge of the disturbance propagates faster at higher F_0 . The increased effective chain stiffness also reduces the steady-state value of δL . Thus, an internal segment starts creeping earlier and attains a lower steady-state value of δL at higher values F_0 than at lower values. Consequently, the rate of creep of individual segments as well as the whole chain is necessarily slower the higher the F_0 is. In the chain with linearly elastic bonds, however, the chain's effective stiffness is virtually independent of F_0 and hence F_0 has a little effect on

the propagation speed and thereby on α ⁶³. Taken together, these findings suggest that nonlinear elasticity of single actin chains likely plays a key role in determining how the creep power-law exponent depends on prestress in living cells. These findings also imply that the dynamics of cytoskeletal actin chains is not entirely governed by the entropic contributions, and that the internal energy contributions that come through the elastic nonlinearity of the chain are critical.

Values of the creep power-law exponent α of the chain (Fig. 5.15B) are more than two times greater than the values reported for cells^{10,48-52,61,64,65}. This discrepancy may reflect the two-dimensional nature of our model. Furthermore, cross-linking and polydispersity on the cytoskeletal lattice may lead to a slower creep response of the network⁶⁸ than the creep response of a single polymer chain. Nevertheless, the overwhelming similarities between the chain model simulations and the fundamental rheological behaviors observed in cells suggest that the dynamics of prestressed single polymer chains is a key determinant of cell rheology.

5.5. CONCLUSIONS

The overwhelming body of evidence strongly suggests that the cytoskeletal prestress is a key determinant of deformability and rheological behaviors of adherent cells. The effect of the prestress on cell deformability and shape stability properties is consistent with the tensegrity model where the governing mechanisms are those of prestressed cytoskeletal architecture. On the other hand, the effect of the prestress on cell rheology can be traced to a lower scale – dynamics of single actin polymer chains. These results do not preclude the importance of other mechanisms including cytoskeletal remodeling, myosin cross-bridge kinetics, network dynamics, or energy activation processes. Rather, they elucidate different levels of organization in which those mechanisms function and may be regulated. Regardless of the underlying mechanisms, the observed role of the prestress provides a new perspective on a number of cellular functions that are critically dependent on cell contractility, cell mechanical distension and cell rheology.

There have been several important developments in the area of cell rheology and cytoskeletal dynamics since I presented this lecture at the Cell and Tissue Engineering Summer School, Belgrade, Serbia, 2006. It was reported that rheological properties of crosslinked and prestressed actin gels are both qualitatively and quantitatively similar to the behaviors observed in living cells suggesting that crosslinking and the prestress are key factors that determine cytoskeletal rheology^{69,70}. Cell softening (fluidization) in response to transient stretching has been explained by the soft

glass rheology model⁷¹. Finally, it has been shown that cells conform to a multiple power-law behavior over a physiological range of timescales rather than a single power law, as suggested by the soft glass rheology model⁷². This in turn implies that cell rheology is timescale dependent. Physical origins and physiological implications of these discoveries are still largely unexplained. Thus, an effective model of cell rheology needs to be developed such that it incorporate quantitative descriptions of cell behavior amenable to computational and structural analysis in the context of physiological relevant molecular structures in living cells. Only this way can biologists, bioengineers and biomaterial scientists use this type of model to understand the molecular basis of cellular mechanotransduction and mechanobiology.

Acknowledgements

This work was supported by NIH Grant HL-33009 and by World University Service (WUS) grant.

References

1. Ingber D.E., Mechanobiology and diseases of mechanotransduction, *Ann. Med.*, **35**, 564-577, 2003.
2. Ingber D.E., Cellular tensegrity revisited I. Cell structure and hierarchical systems biology, *J. Cell Sci.*, **116**, 1157-1173, 2003.
3. Ingber D.E., The architecture of life, *Sci. Am.*, **278**, 48-57, 1998.
4. Ingber D.E., S.R. Heidemann, P. Lamoroux, R.E. Buxbaum, Opposing views on tensegrity as a structural framework for understanding cell mechanics. *J. Appl. Physiol.*, **89**, 1663-1670, 2000.
5. Stamenović D., J.J. Fredberg, N. Wang, J.P. Butler, D.E. Ingber, A microstructural approach to cytoskeletal mechanics based on tensegrity, *J. Theor. Biol.*, **181**, 125-136, 1996.
6. Stamenović D., Effects of cytoskeletal prestress on cell rheological behavior. *Acta Biomater.*, **1**, 255-262, 2005.
7. Wang N., K. Naruse, D. Stamenović, J.J. Fredberg, S.M. Mijailovich, I.M. Tolić-Nørrelykke, T. Polte, R. Mannix, D.E. Ingber, Mechanical behavior in living cells consistent with the tensegrity model. *Proc. Natl Acad. Sci. USA*, **98**, 7765-7770, 2001.
8. Stossel T.P., On the crawling of animal cells, *Science* **260**, 1086-1094, 2004.
9. Fredberg J.J., K.A. Jones, M. Nathan, S. Raboudi, Y. S. Prakash, S.A. Shore, J.P. Butler, G.C. Sieck, Friction in airway smooth muscle: mechanism, latch, and implications in asthma, *J. Appl. Physiol.*, **81**, 2703-2712, 1996.
10. Fabry B., G.N. Maksym, J.P. Butler, M. Glogauer, D. Navajas, J.J. Fredberg, Scaling the microrheology of living cells, *Phys. Rev. Lett.*, **87**, 148102, 2001.
11. Dichtl M.A., E. Sackmann, Microrheometry of semiflexible actin networks through enforced single-filament reptation: Frictional coupling and

- heterogeneities in entangled networks, *Proc. Natl Acad. Sci. USA*, **99**, 6533-6538, 2002.
12. Gardel M.L., M.T. Valentine, J.C. Crocker, A.R. Bausch, D.A. Weitz, Microrheology of entangled F-actin solutions, *Phys. Rev. Lett.*, **91**, 158302, 2003.
 13. MacKintosh F.C., J. Käs, P.A. Janmey, Elasticity of semiflexible biopolymer networks, *Phys. Rev. Lett.*, **75**, 4425-4428, 1995.
 14. Humphrey D., C. Duggan, D. Saha, D. Smith, J. Käs, Active fluidization of polymer networks through molecular motors, *Nature* **416**, 413-416, 2002.
 15. Forgacs G., Of possible role of cytoskeletal filamentous networks in intracellular signaling: an approach based on percolation. *J Cell Sci.*, **108**, 2131-2143, 1995.
 16. Harris A.K., P. Wild, D. Stopak, Silicon rubber substrata: a new wrinkle in the study of cell locomotion, *Science* **208**, 177-179, 1980.
 17. Evans E., A. Yeung, Apparent viscosity and cortical tension of blood granulocytes determined by micropipet aspiration, *Biophys. J.*, **56**, 151-160, 1989.
 18. Hiramoto Y., Mechanical properties of sea urchin eggs. I. Surface force and elastic modulus of the cell membrane, *Exp. Cell Res.*, **56**, 201-208, 1963.
 19. Fuller B., Tensegrity, *Portfolio Artnews Annals*, **4**, 112-127, 1961.
 20. Burkhardt R., A technology for designing tensegrity domes and spheres. <http://www.channell.com/users/bobwb/prospect/prospect.htm>, 2004.
 21. Volokh K.Y., O. Vilnay, New cases of reticulated underconstrained structures, *Int. J Solids Struct.*, **34**, 1093-1104, 1997.
 22. Connelly R., A. Back, Mathematics and tensegrity, *Am. Sci.*, **86**, 142-151, 1998.
 23. Stamenović D., Models of cytoskeletal mechanics based on tensegrity. In: *Cytoskeletal Mechanics – Models and Measurements*, Cambridge University Press, New York, pp. 103-128, 2006.
 24. Wang N., I.M. Tolić-Nørrelykke, J. Chen, S.M. Mijailovich, J.P. Butler, J.J. Fredberg, D. Stamenović, Cell prestress. I. Stiffness and prestress are closely associated in adherent contractile cells. *Am. J. Physiol. Cell Physiol.*, **282**, C606-C616, 2002.
 25. Butler J.P., I.M. Tolić-Nørrelykke, J.J. Fredberg, Estimating traction fields, moments, and strain energy that cells exert on their surroundings. *Am. J. Physiol. Cell Physiol.*, **282**, C595-C605, 2002.
 26. Stamenović D., S.M. Mijailovich, I.M. Tolić-Nørrelykke, J. Chen, N. Wang, Cell prestress. II. Contribution of microtubules. *Am. J. Physiol. Cell Physiol.*, **282**, C617-C624, 2002.
 27. Crick F.H.C., A.F.W. Hughes, The physical properties of cytoplasm: a study by means of the magnetic particle method, *Exp. Cell Res.*, **1**, 37-80, 1950.
 28. Wang N., J.P. Butler, D.E. Ingber, Mechanotransduction across cell surface and through the cytoskeleton, *Science* **26**, 1124-1127, 1993.
 29. Fabry B., G.N. Maksym, R.D. Hubmayr, J.P. Butler, J.J. Fredberg, Implications of heterogeneous bead behavior on cell mechanical properties measured with magnetic twisting cytometry, *J. Magn. Magn. Mater.*, **194**, 120-125, 1999.
 30. Mijailovich S.M., M. Kojic, M. Zivkovic, B. Fabry, J.J. Fredberg, A finite element model of cell deformation during magnetic bead twisting, *J. Appl. Physiol.*, **93**, 1429-1436, 2002.

31. Alcaraz J., L. Buscemi, M. Grabulosa, X. Trepas, B. Fabry, R. Farre, D. Navajas, Microrheology of human lung epithelial cells measured by atomic force microscopy, *Biophys. J.*, **84**, 2071-2079, 2003.
32. Shroff S.G., D.R. Saner, R. Lal, Dynamic micromechanical properties of cultured rat arterial myocytes measured by atomic force microscopy, *Am. J. Physiol. Cell Physiol.*, **269**, C286-C292, 1995.
33. Sato M., D.P. Theret, L.T. Wheeler, N. Ohshima, R.M. Nerem, Application of the micropipette technique to the measurements of cultured porcine aortic endothelial cell viscoelastic properties. *ASME J. Biomech. Eng.*, **112**, 263-268, 1990.
34. Stamenović D., Microtubules may harden or soften cells, depending of the extent of cell distension, *J. Biomech.*, **38**, 1728-1732, 2005.
35. Hu S., J. Chen, N. Wang, Cell spreading controls balance of prestress by microtubules and extracellular matrix. *Front. Biosci.*, **9**, 2177-2182, 2004.
36. Brodland G.W., R. Gordon, Intermediate filaments may prevent buckling of compressively loaded microtubules, *ASME J. Biomech. Eng.*, **112**, 319-321, 1990.
37. Timoshenko S.P., J.M. Gere, *Theory of Elastic Stability*, McGraw-Hill, New York, 1988.
38. Ishijima A., H. Kojima, H. Higuchi, Y. Harada, T. Funatsu, T. Yanagida, Multiple- and single-molecule analysis of the actomyosin motor by nanometer-piconewton manipulation with a microneedle: unitary steps and forces, *Biophys. J.*, **70**, 383-400, 1996.
39. Wang N., Mechanical interactions among cytoskeletal filaments, *Hypertension* **32**, 162-165, 1998.
40. Potard U.S.B., J.P. Butler, N. Wang. Cytoskeletal mechanics in confluent epithelial cells probed through integrins and E-cadherins, *Am. J. Physiol. Cell Physiol.*, **272**, C1654-C1663, 1997.
41. Stamenović D., Z. Liang, J. Chen, N. Wang, The effect of cytoskeletal prestress on the mechanical impedance of cultured airway smooth muscle cells, *J. Appl. Physiol.*, **92**, 1443-1450, 2002.
42. Wu H.W., T. Kuhn, V.T. Moy, Mechanical properties of 1929 cells measured by atomic force microscopy: effects of anticytoskeletal drugs and membrane crosslinking, *Scanning*, **20**, 389-397, 1998.
43. Dennerll T.J., H.C. Joshi, V.L. Steel, R.E. Buxbaum, S.R. Heidemann, Tension and compression in the cytoskeleton II: quantitative measurements, *J. Cell Biol.*, **107**, 665-674, 1988.
44. Trickey W.R., T.P. Vail, F. Guilak, The role of the cytoskeleton in the viscoelastic properties of human articular chondrocytes, *J. Orthop. Res.*, **22**, 131-139, 2004.
45. Stamenović D., T.A. Wilson, The shear modulus of liquid foam, *ASME J. Appl. Mech.*, **51**, 229-231, 1984.
46. Hu S., J. Chen, B. Fabry, Y. Namaguchi, A. Gouldstone, D.E. Ingber, J.J. Fredberg, J.P. Butler, N. Wang, Intracellular stress tomography reveals stress and structural anisotropy in cytoskeleton of living cells. *Am. J. Physiol. Cell Physiol.*, **285**, C1082-C1090, 2003.
47. Fredberg J.J., D. Stamenović, On the imperfect elasticity of lung tissue, *J. Appl. Physiol.*, **67**, 2408-2419, 1989.

48. Stamenović D., B. Suki, B. Fabry, N. Wang, J.J. Fredberg, Rheology of airway smooth muscle cells is associated with cytoskeletal contractile stress. *J. Appl. Physiol.*, **96**, 1600-1605, 2004.
49. Fabry B., G.N. Maksym, J.P. Butler, M. Glogauer, D. Navajas, N.A. Taback, E.J. Millet, J.J. Fredberg, Time scale and other invariants of integrative mechanical behavior in living cells, *Phys. Rev. E* **68**, 041914, 2003.
50. Trepast X., M. Grabulosa, F. Puig, G.N. Maksym, D. Navajas, R. Farre, Viscoelasticity of human alveolar epithelial cells subjected to stretch, *Am. J. Physiol. - Lung Cell. Mol. Physiol.*, **287**, L1025-L1034, 2004.
51. Smith B.A., B. Tolloczko, J.G. Martin, P. Grütter, Probing the viscoelastic behavior of cultured airway smooth muscle cells with atomic force microscopy: stiffening induced by contractile agonist, *Biophys. J.*, **88**, 2994-3007, 2005.
52. Rosenblatt N., S. Hu, J. Chen, N. Wang, D. Stamenović, Distending stress of the cytoskeleton is a key determinant of cell rheological behavior, *Biochem. Biophys. Res. Comm.*, **321**, 617-622, 2004.
53. Cañadas P., V.M. Laurent, C. Oddou, D. Isabey, S. Wendling, A cellular tensegrity model to analyze the structural viscoelasticity of the cytoskeleton, *J. Theor. Biol.*, **218**, 155-173, 2002.
54. Sultan C., D. Stamenović, D.E. Ingber, A computational tensegrity model predicts dynamic rheological behaviors in living cells, *Ann. Biomed. Eng.*, **32**, 520-530, 2004.
55. Mijailovich S.M., J.P. Butler, J.J. Fredberg, Perturbed equilibrium of myosin binding in airway smooth muscle: bond-length distributions, mechanics, and ATP metabolism. *Biophys. J.*, **79**, 2667-2681, 2000.
56. Mehta D., S.J. Gunst, Actin polymerization stimulated by contractile activation regulates force development in canine tracheal smooth muscle, *J. Physiol. – London*, **519**, 829-840, 1999.
57. Tang D., D. Mehta, S.J. Gunst, Mechanosensitive tyrosine phosphorylation of paxillin and focal adhesion kinase in tracheal smooth muscle. *American Journal of Physiology Cell Physiology* **276**, C250-C258, 1999.
58. An S.S., R.E. Laudadio, J. Lai, R.A. Rogers, J.J. Fredberg, Stiffness changes in cultured airway smooth muscle cells, *Am. J. Physiol. Cell Physiol.*, **283**, C792-C801, 2002.
59. Halsey G., J.H. White, Jr., H. Eyring, Mechanical properties of textiles, I, *Text. Res. J.*, **15**, 295-311, 1945.
60. Sollich P., Rheological constitutive equation for a model of soft glassy materials, *Phys. Rev. E*, **58**, 738-759, 1998.
61. Lenormand G., Millet E., Fabry B., Butler J.P., Fredberg J.J., Linearity and time-scale invariance of the creep function in living cells. *J. Royal Soc. London Interface*, **1**, 91-97, 2004.
62. Gunst S.J., J.J. Fredberg, Invited Review: The first three minutes: smooth muscle contraction, cytoskeletal events, and soft glasses, *J. Appl. Physiol.*, **95**, 413-425, 2003.
63. Rosenblatt N., A.M. Alencar, A. Majumdar, B. Suki, D. Stamenović, Dynamics of prestressed semiflexible polymer chains as a model of cell rheology, *Phys. Rev. Lett.*, **97**, 168101, 2006.

64. Dimitrakopoulos P., J.F. Brady, Z-G. Wang, Short- and intermediate-time behavior of the linear stress relaxation in semiflexible polymer chains. *Phys. Rev. E*, **64**, 050803(R), 2001.
65. Morse D.C., Viscoelasticity of concentrated isotropic solution of semiflexible polymers. 2. Linear response, *Macromolecules* **31**, 7044-7067, 1998.
66. Doi M., S.F. Edwards, *The Theory of Polymer Dynamics*, Clarendon Press, Oxford, UK, 1986.
67. Metropolis N., S. Ulam, The Monte Carlo method, *J. Am. Stat. Assoc.*, **44**, 335-341, 1949.
68. Suki B., A.-L. Barabási, K.R. Lutchen, Lung tissue viscoelasticity: a mathematical framework and its molecular basis, *J. Appl. Physiol.*, **76**, 2749-2759, 1994.
69. Gardel M.L., F. Nakamura, J. Hartwig, J.C. Crocker, T.P. Stossel, D.A. Weitz, Stress-dependent elasticity of composite actin networks as a model for cell behavior, *Phys. Rev. Lett.*, **96**, 088102, 2006.
70. Mizuno D., C. Tardin, C.F. Schmidt, F.C. MacKintosh, Nonequilibrium mechanics of active cytoskeletal networks, *Science* **315**, 370-373, 2007.
71. Trepap X., L. Deng, S.S. An, D. Navajas, D.J. Tschumperlin, W.T. Gerthoffer, J.P. Butler, J.J. Fredberg, Universal physical responses to stretch in the living cell, *Nature* **447**, 592-595, 2007.
72. Stamenović D., N. Rosenblatt, M. Montoya-Zavala, B.D. Matthews, S. Hu, B. Suki, N. Wang, D.E. Ingber, Rheological behavior of living cells is timescale-dependent. *Biophys. J.*, **93**, L39-L41, 2007.

CELL AND TISSUE ORGANIZATION IN SOFT MATERIALS: INSIGHT FROM MATHEMATICAL AND BIOPHYSICAL MODELLING

Ilka B. Bischofs*

6.1. INTRODUCTION

6.1.1. Overview of cell and tissue organization principles for adherent cells

All complex organisms are hierarchically structured: the body is composed of organs each fulfilling a specialized function, organs contain specialized tissues and a tissue is an organized assembly of specialized cells and extracellular matrix (ECM). The ECM is mainly composed of a network of protofilaments like collagen or fibronectin which are secreted by the tissue's resident cells and is constantly remodeled by cells. The human body consists of about 10^{13} cells from more than 200 different cell types. What distinguishes a clot of cells and matrix from a functional tissue is its well defined organization. Functionality implies that cells differentiate into the tissue specific cell types, adopt specific cell positions and orientation in a tissue specific extra-cellular environment and maintain that organization through constant remodeling. The organization of cells and tissues is affected by many environmental signals which get integrated into cellular decision making. These signals drive cell differentiation but also affect cell orientation and positioning. For anchorage-dependent cells like fibroblasts or smooth muscle cells the factors which are known to influence cell orientation and cell locomotion can be broadly classified into three categories: chemical, topographical and mechanical cues ¹.

* Department of Bioengineering, University of California Berkeley, Berkeley, CA, USA.

Chemo- and haptotaxis are organization principles based on (physico)-chemical signals. Chemotaxis is the ability of cells to sense (soluble) chemical gradients and move towards attractants or away from repellents. Haptotaxis describes the migration of cells following gradients in adhesiveness of (specific) immobilized ligands. Cells also respond to topographic features such as curvature, where they typically prefer to orient along surfaces with a low curvature. Contact guidance is a very broad term coined already in the 1930ies by Peter Weiss who observed that cells orient along fibers comprising the extracellular matrix ². Today it is commonly associated with a strong topographic connotation. In this lecture we focus on mechanical cues driving cell and tissue organization. Mechanical cues can for instance result from forces resulting from blood pulsation, gravity, exercise etc., but also the mechanical properties of the matrix itself e.g. its rigidity.

6.1.2. Classification of mechanical signals and biological responses

Mechanical signals may be classified whether they result from *external sources* acting on cells, such as forces resulting blood pulsation, fluid flow, body movement, gravity. Alternatively mechanical signals can arise from *substrate mechanics* that is altered substrate rigidity or prestrain of the extra-cellular environment.

Mechanical effects may be classified based on the hierarchical scale of the biological response into subcellular scale effects (a), cellular scale effects (b) and supracellular or tissue scale effects (c). Subcellular effects occur as a result of mechano-specific signaling, e.g. Ca-fluxes mediated by stretch activated ion channels or mechanosensitive signaling at cell-matrix or cell-cell adhesions. These signaling events ultimately lead to cellular scale effects such as altered gene expression driving and maintaining cell differentiation; cellular reorganization of the cytoskeleton and cell morphology, including cell positioning and cell orientation. On the supracellular scale mechanical effects then lead to mechanosensitive cell differentiation, cell positioning and cell orientation that drive pattern formation and tissue morphogenesis.

To study the mechanical effects elicited from external sources or substrate mechanics several experimental methods have been devised ³. The mechano-response to external forces is studied in vitro mainly through experimental techniques such as (cyclic) cell stretchers (probing for b,c-effects), flow chambers (a,b), magnetic twisting cytometry and micropipettes (a,b).

The response of cells to altered mechanical properties of the environment has been mainly addressed via experiments using optical traps (a) and soft elastic substrates based on polyacrylamide (PAAM) or

polydimethylsiloxane (PDMS) gels (b,c). In this lecture we will focus primarily on signals generated by altered substrate mechanics.

6.1.3. Effect of substrate mechanics on cell behavior

For a long time the role of substrate mechanics on cell and tissue organization has been widely overseen by biologist, probably because standardized *in vitro* culture protocols utilize glass or plastic dishes. However glass and plastic dishes commonly employed for standard cell culturing have rigidities in the GPa regime. In contrast, most tissues have rigidities in the MPa to kPa regime and thus are 1000 - 100000 times softer than glass. For comparison, rubber has a Young modulus of MPa.

In order to study the effect of substrate mechanics on cell behavior *in vitro*, synthetic polymer gels are commonly used. PAAM and PDMS are synthetic polymer gels whose mechanical properties can be adjusted by the level of cross-linking and tuned within and beyond the physiologically relevant regime of kPa (nerve tissue) and several MPa (pressurized arteries) ¹. Biological responses that have been shown *in vitro* to be affected by substrate mechanics using the elastic substrate method involve all scales from subcellular to the tissue scale ⁴. On the subcellular scale, cell-matrix contacts have been shown to change their chemical compositions and size as the stiffness of the substrate increases. Cells spread better and form stress fibers when cultured on stiff versus compliant gels. This also affects the degree and distribution of forces generated by cells with larger forces being generated on stiffer matrices. On the cellular scale cell differentiation, cell locomotion (e.g. fibroblasts move from soft to stiff substrates), cell orientation (orientation towards the mechanically stiffer direction) have been shown to be responsive to substrate mechanics. Finally multi-cellular effects and rigidity dependent pattern formation has been demonstrated recently ⁵.

These *in vitro* findings have a broad impact on standard cell culturing but also on our understanding of diseases, morphogenesis and tissue engineering.

6.1.4. Sensing substrate mechanics: Active mechanosensing

Mechanical signals originating from external forces acting on cells “merely” require a translation of force into biochemical signaling events or can even exert their action directly, for instance by pulling the nucleus apart or rupturing the cytoskeleton. This is a common form of biological signaling where an extracellular cue, in this case a mechanical cue, is directly translated into an intracellular signal and thus an example of outside-in signaling. In contrast, signals originating from *substrate*

mechanics must *first* be translated into a *mechanical signal* which subsequently may trigger similar biochemical signaling pathways as those triggered directly by external forces. This process is therefore different from outside-in signaling since the cell must first “do” something to generate a cue from the substrate which subsequently is translated into a cellular signal. Thus it is an inside-outside-inside signaling event⁴. We therefore call this process *active mechanosensing* to indicate that sensing of substrate mechanics requires mechanical activity of the cell in addition to a sensory machinery⁶.

The mechanical activity of cells has been studied since the 1980ies when Harris and coworkers first pioneered the elastic substrate method and discovered that single cells can exert traction on their environment⁷. For example, fibroblasts exert overall tractions on soft substrates in the kPa regime. In general, the magnitude of cellular forces is *cell-type* specific and seems to correlate with the overall mechanical properties of the tissue: “rigid tissue – strong cells”, “soft tissue – weak cells”.

Today the measurement of cellular forces is a field on its own and known under the term *traction force microscopy*⁸. Different techniques have been employed for this purpose, including the use of soft gels with embedded markers for substrate displacement⁹, micro-structured soft substrates¹⁰ and arrays of soft micro needles which bend under the forces exerted by the cells¹¹. These techniques reconstruct force magnitude, direction (and position) from displacement data observed with a microscope^{12,13} and show that forces are non-uniformly transmitted to the substrate only at distinct cell-matrix adhesions, that is, focal complexes and larger focal adhesions, respectively. Typical stresses transmitted at focal adhesions amount to 5-6 nN/ μm^2 ^{10,11}. The main molecular force generating mechanism for cellular traction involves actomyosin based contractility and contributions from forces generated by actin polymerization. In both processes chemical energy in form of the cellular fuel ATP is converted into mechanical work. A single myosin motor can generate force in the *pN* regime which is also the typical force exerted by growing filaments pushing against a boundary. The level of mechanical activity is subject to cellular regulation mainly through upstream small Rho-GTPases such as Rho, Rac and Cdc42. These GTPases can dramatically affect the status of the cytoskeleton and regulate motor activity and actin polymerization¹⁴.

The forces generated inside the cell are transmitted to the exterior at cell-matrix contacts. Cell-matrix contacts are protein clusters based on trans-membrane receptors of the integrin family which recognize the RGD binding motif presented by ECM proteins such as fibronectin and collagen on the outside. On the cell interior integrins bind to the actin cytoskeleton via adapter molecules such as talin and vinculin. Proper activation of cell-

matrix contacts involves mechanical input from the environment. By restraining the retroactive motion of fibronectin coated beads using an optical trap, it was demonstrated that beads undergo “reinforcement” – a structural strengthening of cell-bead linkages- proportional to the level of internally generated force which also triggered signaling activity¹⁵. Similar rigidifying effects are also observed using magnetic twisting cytometry¹⁶. A combination of traction force microscopy and fluorescent analysis of focal adhesion size demonstrated a correlation of the level of focal adhesion size and the magnitude of force^{10,11}. In addition to that, externally applied forces lead to contact growth and strong signaling activity¹⁷. *Cell-matrix contacts therefore act as mechanosensors.*

In fact cell-matrix contacts are hot-spots of cellular signaling activity. More than 50 different proteins have been shown to localize with cell-matrix contacts among those both structural proteins as well as a plethora of signaling molecules (serine/tyrosine kinases and phosphatases such as FAK, Pax, Fyn, Src, etc.)^{18,19}. The exact identity of the mechanosensor is still mysterious: various studies suggested force induced conformational changes of proteins (several molecular candidates have been implied including integrin itself), collective reorganization of contacts upon force application, stretch activated ion channels²⁰. Recent experiments suggest that several mechanosensitive processes act simultaneously on different time scales²¹. They might also respond to different force levels. As such there may not be “the” mechanosensor but a collective action of mechanosensitive elements eliciting a context specific cell response.

6.2. A PRIMER ON ELASTICITY THEORY

Elasticity theory is a part of continuum mechanics and describes the influence of external forces on the shape and volume of solid bodies²². In the field of cell and tissue mechanics elasticity theory is often used to extract the elastic constant from measuring stress-strain relationships either macroscopically or microscopically using micro- and nano-indentation for example with an atomic force microscope. Elasticity theory is also used to calculate elastic fields from given force distributions or to calculate force distribution from elastic fields in traction force microscopy^{8,12}.

Under deformation a point located initially at r is displaced by a vector \mathbf{u} . The changes in *relative distance* between points after deformation define the strain *tensor* $u_{ij}(r)$. For example, if there were only displacements in the x - direction, the strain simply becomes:

$$u_{xx} = \frac{l-l_0}{l_0} = \frac{u_x(x+dx) - u_x(x)}{dx} = \frac{du_x}{dx}, \quad (6.1)$$

where l_0 and l are the distances between to points before and after deformation. In general, one can deform in all three directions yy , zz and also get mixed terms xy , yz , etc., which denote shear strain.

Elastic bodies resist deformation, that is, strain leads to internal forces that aim to push the material back into its initial positions. The force that acts on the surface of a volume element gives rise to a stress. Stress has units force per area and is a *tensor* like strain. The components of the stress tensor σ_{ij} are defined as the force per unit area in i direction acting on a surface element with outward normal j .

Stress is propagated in the medium because each volume element acts on its adjacent volume elements. For small strains the relationship between stress and strain is linear: $\sigma_{ij} = C_{ijkl}u_{kl}$. This formula is the three-dimensional analog of Hookes law that you know from high-school for describing the force-displacement relationship of a simple spring, $F=Kx$. Here F is force, K is spring constant and x is the displacement. In its three dimensional version, the “spring” constant C becomes the elastic constant tensor, which has 81 components. However most of them are related to each other by symmetry operations. For instance, *isotropic* materials, that is materials which “look the same” from all directions (i.e. they are “rotation invariant”), can change their volume and their shape independently. Hence, they are characterized by only *two* independent elastic moduli, the shear modulus, which describes the resistance to shape changes, and the bulk modulus, which describes the response to volume changes. Experimentally substrates are typically characterized by the Young modulus E and the Poisson ratio ν which can be extracted from a uniaxial stretch experiment. Suppose you are applying a tension σ_{zz} along the z -axis and measure the elongation along the direction of tension application. Then the Young modulus E is given by:

$$E = \frac{\sigma_{zz}}{u_{zz}}. \quad (6.2)$$

As the material is stretched along z , it will typically contract in the transverse direction. This effect is called *Poisson effect* and is quantified by the Poisson ratio ν :

$$\nu = -\frac{u_{xx}}{u_{zz}}. \quad (6.3)$$

For most synthetic substrates such as polyacrylamid or PDMS the assumption of linear, isotropic elasticity is typically good. Typical values

for synthetic substrates are $E=\text{MPa-Pa}$ and $\nu=0.3-0.5$. Note, when $\nu=0.5$ the material is incompressible, that is it can only change shape but not overall volume. For complex tissues the assumption of linear elasticity is often not satisfied and the mechanical behavior is more complex including non-linear stress-strain and viscous effects.

The typical problem of elasticity theory is to calculate the elastic fields from a given distribution of forces acting on the substrate by solving the *elastic boundary value problem*: Each point has to be in *mechanical equilibrium* and must fulfill the *boundary condition* at the surface(s) of the substrate. Two types of boundary conditions are commonly employed: *free and clamped* boundaries. For a free boundary the substrate is free to deform at the surface (e.g. free floating gels). In this case the normal tractions have to vanish at the surface. For a clamped boundary the displacements at the surface are fixed (e.g. the gel is polymerized against a rigid surface). *Green functions* are the *solutions* to elastic boundary value problems in response to a *unit point force density*. Once the Greens function is known you can calculate the elastic fields for *any* complicated force distribution by summing (or integrating) over the total force distribution. This is a result of the *superposition principle* that states that the field generated by n forces is simply the sum of the individual fields created by each of the n forces separately. Note that the superposition principle only applies for materials with a linear stress-strain relationship.

6.3. TOWARDS A SYSTEM UNDERSTANDING OF THE INFLUENCE OF SUBSTRATE MECHANICS ON CELL AND TISSUE ORGANIZATION

6.3.1. Modeling cellular scale effects

a) Modeling mechanical activity: The force multipole expansion

A useful concept to characterize a force distribution is its *force multipole expansion*¹². Given the force multipoles you can approximate how the elastic fields vary with distance r from the center of the force distribution without having to consider the fields generated by each force separately. The vector sum of all forces exerted by a cell in mechanical equilibrium is zero. In mathematical terms we say: the *force monopole* (the sum of all forces) vanishes. The first non-vanishing component of the force distribution is the *force dipole*. That is, the elastic field far away from the cell created by all cellular traction forces is approximately the same as the ones generated by two opposing forces F being separated a distance L from each other. In general, a force dipole is characterized by its dipole

strength P , which is the product of total force F and the force separation L . For a contractile cell like a fibroblast a typical value for a force dipole amounts to 10^{-11} J. Replacing the complex total force distribution of the cell by a force dipole is an approximation which works well if you are interested in the elastic fields at distances $r > L$. The Table 6.1 provides the long range decay of the elastic displacement and strain fields with distance for the lowest moments of a multipole expansion.

Table 6.1. Long range decay of the elastic displacement and strain fields with distance r for the lowest moments of a multiple expansion

Moment		Displacement	Strain
Monopole	P_i	$\sim 1/r$	$\sim 1/r^2$
Dipole	P_{ij}	$\sim 1/r^2$	$\sim 1/r^3$
Quadrupole	P_{ijk}	$\sim 1/r^3$	$\sim 1/r^4$

The concept of force dipoles is abstract and is therefore very versatile and not restricted to modeling single cells only. According to their symmetry you can classify force dipoles into isotropic or anisotropic dipoles. Isotropic dipoles do not have an orientation, for example it describes the action of a cell with stress fibers running in all directions. Anisotropic dipoles have an orientation but not a direction – front and back cannot be distinguished, e.g. a fibroblast with a well defined bipolar morphology and stress fibers running in one predominant direction. In addition to the action of a single cell in mechanical equilibrium, we can model the mechanical action of any force distribution in mechanical equilibrium using force dipoles, for instance, a single stress fiber or a colony of contractile cells.

b) Cell organization in soft materials: preference for effective stiffness

In this section we briefly discuss a phenomenological model which aims to mathematically predict the organization of single cells in soft materials. A more detailed and/or more mathematically rigorous treatment is found in Ref.^{6, 23}

To illustrate the main idea of the model, consider the force-build up when pulling on a spring with a spring constant K . In order to generate a force F , one has to invest energy to deform the spring. In mechanical equilibrium force F balances the counter force $F=Kx$, where x is the spring displacement. The deformation energy therefore is

$$W = \frac{1}{2} Kx^2 = \frac{F^2}{2K} \tag{6.4}$$

Hence the stiffer the spring (the environment), the more effective force is generated. In a mechanically anisotropic environment, i.e. if the cell is pulling at springs with different spring constants, the cell polarizes along the direction with the largest K or smallest W potentially because mechanosensitive signaling is activated more efficiently in this direction. Mathematically this describes the experimentally observed cellular preference for large effective stiffness in the environment.

More formally the model assumes that the cellular mechanical activity probing the environment can be modeled as an anisotropic force contraction dipole P . The environment is modeled as a linear elastic medium. The cellular preference for stiffness is then postulated as a cellular self-organization principle and mathematically expressed by the deformation energy W which in the framework of linear elasticity becomes:

$$W = \frac{1}{2} \int C_{ijkl} u_{ij} u_{kl} dV \quad (6.5)$$

In the presence of an external strain field the deformation energy changes by an amount proportional to the coupling of the force dipole tensor to the local external strain field:

$$\Delta W = P_{ij} u_{ij}^{ext} \quad (6.6)$$

By minimizing this quantity as a function of dipole orientation and position one can predict the optimal cell configuration in response to external prestrain. In order to make predictions for optimal cell configurations one has to calculate the stress and strain distribution in the substrate by solving the elastic equations. By using Green functions the mechanics can be solved analytically in some simple cases and W can be expressed as a function of cell orientation and cell position. For more complicated scenarios numerical procedures like finite element methods can be employed to solve the elastic equations. To identify the optimal configuration W is then minimized as a function of cell position and orientation.

The main success of this simple model is to explain a variety of findings which have been reported in the experimental literature within a *unifying* theoretical framework of effective stiffness preference. The model qualitatively captures durotaxis (locomotion of cells up a gradient in substrate rigidity) and mechanotaxis (locomotion towards tensile and away from compressive strain), orientation of cells along the direction of stress in uniaxially (pre)strained substrates and various orientation phenomena close to substrate boundaries. For example, a cell embedded in a three dimensional elastic space close a flat boundary (elastic halfspace) will feel the presence of the boundary. Dependent on whether the

boundary is free (surface can freely deform) or clamped (surface is rigidly fixed), the elastic material effectively softens (stiffens) towards the boundary. Hence cells prefer to orient away from a free boundary but towards a clamped. Similar effects are also observed at interfaces of materials with different rigidities. These boundary and interface effects are potentially very important in tissue engineering applications when creating interfaces between tissues and implants of grossly non-matched rigidities, e.g. a titanium implant surrounded by soft connective tissue.

6.3.2. Modeling tissue scale effects

a) *Elastic interactions of cells*

The above model also predicts the possibility of elastic cell-cell communication. For anisotropic contraction dipoles these interactions are long-ranged $\sim 1/r^3$ and strongly anisotropic. For two cells the optimal configuration predicted by the model is an alignment of cells. In this configuration each cell senses maximal effective stiffness due to the traction of the other cell because maximal *tension* is generated along the axis of contraction. At low cell density we therefore expect elastically interacting cells to form strings. In principle elastic interactions could manifest themselves in two important ways in tissues – in large scale pattern formation and in active modulation of the material properties of the substrate.

b) *Pattern formation due to elastic interactions*

When many mechanically active bipolar cells (like fibroblasts) are present they may elastically interact and engage in pattern formation. Refs. ^{24,25} predict “*phase diagrams*” for structure formation as a function of cell density, positioning and Poisson ratio as calculated for dipoles on top of an elastic substrate with Young modulus E and Poisson ratio ν . The model predicts three phases a robust *paraelastic* (or spin-glass) phase at low densities in which cells only locally align but the macroscopic structure is isotropic; an *antiferroelastic phase* for incompressible substrates at high densities, in which cells locally form ring-like structures; and a *ferroelastic phase* at high densities on highly compressible substrates, that is, an aligned structure of all cells pointing along a common direction. The phase diagrams were calculated under the assumption that cells were strongly interacting elastically with each other without any other competing organizing principles and at a low level of stochasticity which tends to randomize cell decisions. While the phase behavior of elastically interacting cells has not been studied experimentally yet, physiologically relevant might be the extended robust *paraelastic* or spin-glass phase. In

this phase cells only locally form aligned short stings but strings hardly interact with each other: the global pattern appears *disordered*. This is due to strong *lateral screening* of the elastic fields produced by a string of anisotropic force dipoles. Only at high densities cells tend to macroscopically order in the simulation and either form a *ferroelastic* phase, where all cells have their contractility directed along the same direction. This is an event of spontaneous *polarization* of the tissue where an anisotropic macroscopic cell stress builds-up, which will change the effective material properties of the substrate (which were isotropic) to that of an *anisotropic* composite material. In the *antiferroelastic* phase, cells form rings and the effective material properties stay isotropic. One can switch between these *phases* by altering *cell density* and *Poisson ratio*. When the stochasticity (or effective temperature) is increased the patterns start to look increasingly random. Note that the Young modulus E alters the effective temperature $T \sim 1/E$. Thus, on rigid substrates, cells are expected to stay unaffected by the mechanical signals generated by other cells and the patterns should look random.

The above results were obtained by *Monte Carlo simulations*. Monte Carlo simulations are a method frequently employed in statistical mechanics to simulate stochastic effects²⁶. In each simulation step you randomly chose a cell and vary its orientation; if W is decreased you accept the new configuration, if not, you accept the configuration with a probability $p = \exp(W/T)$ where T is the effective temperature of the system. In the calculation T is not a physical temperature but an effective measure for overall stochasticity, which lumps in several sources of stochasticity and randomness in substrate properties and cellular decision making. For large T all moves are accepted and the structure becomes increasingly random. In contrast for low T structures become *optimized* with respect to the elastic interactions.

c) Polarization and effective material properties

Even at low cell densities a tissue can polarize. When you apply a uniaxial external tension field force dipoles tend to align with tension, that is, cells are expected to align with the external uniaxial tensile strain field. This has been observed experimentally. As cells reorient their traction forces in response to an external field, they polarize the material or tissue. This will also change the *effective* material properties of the tissue. The tissue is expected to become more rigid, i.e. the apparent Young modulus increases, while the Poisson ratio typically decreases. This is a result of *elastic screening* effects similar to electrostatic screening of charges on a plate capacitor with a dielectric embedded. The polarization of the dielectric affects the electric field inside the plate capacitor. Similar effects

are predicted for polarizable tissues which will alter the effective material properties. This may contribute to *mechanical homeostasis* of a tissue and may be especially important for wound healing where often large elastic tension fields are present^{24,27}.

d) From synthetic substrates to physiological hydrogels

Similar cell organization effects to those observed on synthetic substrates have also been reported for tissue cells in physiological hydrogels, such as collagen gels²⁸⁻³⁰. While mechanical effects will be present also in these gels, the situation in physiological gels is certainly much more complicated to interpret than for synthetic elastic substrates – in part due to the competition of topographical and mechanical guidance principles and the potential for visco-elasticity governing substrate mechanics. There is a considerable body of theoretical models that have addressed the role of substrate topography through contact guidance³¹⁻³⁵. Most models are dynamic partial differentiation equation models and sometimes employ rather complicated models for describing the complexity of the environment. These models are conceptually very similar to the model described in this lecture in the sense that most argue that cell orient along fibers and fibers orient along strain, which results in an effective cell – strain coupling very similar to the theory of effective stiffness preference. In vivo both principles, contact guidance and mechanical guidance, are therefore expected to co-coordinately work together, that is, they are typically reinforcing each other rather than competing with each other.

6.3.3. Modeling subcellular scale effects

a) The two-spring model of active mechanosensing

The two-spring model of Ref.³⁶ is a generic dynamic model that aims to provide a conceptual framework for analyzing active mechanosensing and establish a connection between the principle of effective stiffness preference and subcellular processes. Recall that cellular forces transmitted at cell-matrix contacts are generated by actomyosin contractility. As motors pull, the spring gets strained and motors pull against the load exerted by the spring pulling back. For the static situation the energy $W=F^2/2K$ is stored in the spring. Therefore the stiffer the environment, the less energy has to be invested to build up a certain level of force. The dynamics of force generation can be derived from the power dW/dt invested into the spring. The stiffer the spring the faster force build-up occurs. The force build-up is stopped when bonds connecting the actin-cytoskeleton to the extracellular matrix are rupturing. Thus there may be competing time-scale for force build-up that determines the average level

of force generated at adhesions and therefore variations in K may trigger variations in focal adhesion mechanosensitive signaling activity. The average level of force is then given by:

$$F = \frac{F_s}{1 + kt_K} \quad (6.7)$$

where F_s is the force at which molecular motors stall, k is the rate constant governing the bond rupture and

$$t_K = \frac{F_s}{vK} \quad (6.8)$$

where v is the maximal motor velocity without load. The spring constant K is actually composed of a series arrangement of at least two mechanical elements: the external stiffness of the environment and the internal stiffness of the cell. Hence the term two spring model. For two springs in series the mechanical action of the combined springs is given by:

$$\frac{1}{K} = \frac{1}{K_{cell}} + \frac{1}{K_{ext}} \quad (6.9)$$

Hence the average force at a bond is dependent both on external parameters, the substrate rigidity, and internal parameters such as contractility, the strength of molecular bonding, the level of internal rigidity = inside-outside signaling. Inside-outside signaling determines the initial level of force that is build-up before putative feedback mechanisms kick in. Feedback could target various cellular processes including contractility, the level of reinforcement and thus affect the state of mechanosignaling.

b) Theoretical models for mechanotransduction at cell matrix contacts

There have been several theoretical models published to explain “the mechanosensor” in focal adhesion. All mathematical models are again generic and consider no molecular details. Instead they aim to explain the physical mechanisms of activation and/or growth behavior of focal adhesions and focal contacts. Some recent examples include the study of ligand density dependent configuration changes in focal adhesions that lead to asymmetric growth of adhesions. Here directional stress causes a non-uniform strain (and hence also a non-uniform ligand density) and thus a back-front asymmetry at the contact rim³⁷. Another model studies the growth of focal adhesions through plaque stress release³⁸ while others propose a cooperative force-dependent transition into a stable adhesion

state³⁹ or imply collective rupture effects of cell-matrix bonds that result in large forces on individual bonds triggering a mechanoresponse³⁶.

c) *Molecular models and mechanistic models*

There are no molecular or mechanistic models that take into account the molecular details of focal adhesions or focal contacts.

6.4. OUTLOOK

It becomes increasingly evident that substrate mechanics plays an important role in governing cell and tissue organization. To gain a system level understanding on its effects on cell and tissue organization, clearly more multi-scale experimentation and modeling is required to eventually generate a holistic view of the influence of matrix mechanics on cell and tissue organization. This will not only contribute to a better understanding of physiological situations but also be relevant for tissue engineering applications.

References and suggested readings

1. Wong J.Y., J.B. Leach, X.Q. Brown, Balance of chemistry, topography and mechanics at the cell-biomaterial interface: Issues and challenges for assessing the role of substrate mechanics on cell response. *Surf. Sci.*, **570**(1-2), 119-133. 2004.
2. Weiss P., In vitro experiments on the factors determining the course of the outgrowing nerve fiber. *J. Exp. Zool.*, **68**, 393-448. 1934
3. Schwarz U.S., I.B. Bischofs, Physical determinants of cell organization in soft media. *Med. Eng. Phys.*, **27**(9), 763-772. 2005
4. Discher D.E., P. Janmey, Y.-l. Wang, Tissue Cells Feel and Respond to the Stiffness of Their Substrate. *Science*, **310**(5751), 1139-1143. 2005
5. Guo W.-h., et al., Substrate Rigidity Regulates the Formation and Maintenance of Tissues, 10.1529/biophysj.105.070144. *Biophys. J.*, **90**(6), 2213-2220. 2006
6. Bischofs I.B., U.S. Schwarz, Cell organization in soft media due to active mechanosensing. *Proc. Natl Acad. Sci. USA*, **100**(16), 9274-9279. 2003.
7. Harris A.K., P. Wild, D. Stopak, Silicone-Rubber Substrata - New Wrinkle in the Study of Cell Locomotion. *Science*, **208**(4440), 177-179. 1980.
8. Dembo M., et al., Imaging the traction stresses exerted by locomoting cells with the elastic substratum method. *Biophys. J.*, **70**(4), 2008-2022. 1996.
9. Munevar S., Y.L. Wang, M. Dembo, Regulation of mechanical interactions between fibroblasts and the substratum by stretch-activated Ca²⁺ entry. *J. Cell Sci.*, **117**(1), 85-92. 2004

10. Balaban N.Q., et al., Force and focal adhesion assembly: a close relationship studied using elastic micropatterned substrates. *Nat. Cell Biol.*, **3**(5), 466-472. 2001.
11. Tan J.L., et al., Cells lying on a bed of microneedles: An approach to isolate mechanical force. *Proc. Natl Acad. Sci. USA*, **100**(4), 1484-1489. 2003.
12. Schwarz U.S., et al., Calculation of forces at focal adhesions from elastic substrate data: The effect of localized force and the need for regularization. *Biophys. J.*, **83**(3), 1380-1394. 2002.
13. Dembo M., Y.L. Wang, Stresses at the cell-to-substrate interface during locomotion of fibroblasts. *Biophys. J.*, **76**(4), 2307-2316. 1999.
14. Nobes C.D., A. Hall, Rho, rac, and cdc42 GTPases regulate the assembly of multimolecular focal complexes associated with actin stress fibers, lamellipodia, and filopodia. *Cell*, **81**(1), 53-62. 1995.
15. Choquet D., D.P. Felsenfeld, M.P. Sheetz, Extracellular matrix rigidity causes strengthening of integrin-cytoskeleton linkages. *Cell*, **88**(1), 39-48. 1997.
16. Wang N., J.P. Butler, D.E. Ingber, Mechanotransduction across the Cell-Surface and through the Cytoskeleton. *Science*, **260**(5111), 1124-1127. 1993.
17. Riveline D., et al., Focal contacts as mechanosensors: Externally applied local mechanical force induces growth of focal contacts by an mDial1-dependent and ROCK-independent mechanism. *J. Cell Biol.*, **153**(6), 1175-1185. 2001.
18. Zamir E., B. Geiger, Components of cell-matrix adhesions. *J. Cell Sci.*, **114**(20), 3577-3579. 2001.
19. Geiger B., et al., Transmembrane extracellular matrix-cytoskeleton crosstalk. *Nat. Revs Mol. Cell Biol.*, **2**(11), 793-805. 2001.
20. Vogel V., M. Sheetz, Local force and geometry sensing regulate cell functions. *Nat. Revs Mol. Cell Biol.*, **7**(4), 265-275. 2006.
21. Matthews B.D., et al., Integrins, Rho, cytoskeletal tension and mechanosensitive ion channels. *J. Cell Sci.*, **119**, 508-518. 2006.
22. Landau L.D., E.M. Lifshitz, *Theory of elasticity*. 3rd ed. Vol. 7. Butterworth-Heinemann, Oxford, 1999.
23. Bischofs I.B., S.A. Safran, and U.S. Schwarz, Elastic interactions of active cells with soft materials. *Phys. Rev. E*, **69**(2), 021911. 2004.
24. Bischofs I.B., U.S. Schwarz, Effect of Poisson Ratio on Cellular Structure Formation. *Phys. Rev. Lett.*, **95**(6), 068102-4. 2005.
25. Bischofs I.B., U.S. Schwarz, Collective effects in cellular structure formation mediated by compliant environments. *Acta Biomater.*, **2**, 253-265. 2006.
26. Allen M.P., D.J. Tildesley, *Computer Simulations of Liquids*. Oxford University Press, Oxford, 2001.
27. Zemel A., I.B. Bischofs, S.A. Safran, Active elasticity of gels with contractile cells. *Phys. Rev. Lett.*, **97**, 128103-128106. 2005.
28. Bell E., B. Ivarsson, C. Merrill, Production of a Tissue-Like Structure by Contraction of Collagen Lattices by Human-Fibroblasts of Different Proliferative Potential In vitro. *Proc. Natl Acad. Sci. USA*, **76**(3), 1274-1278. 1979.
29. Eastwood M., et al., Effect of precise mechanical loading on fibroblast populated collagen lattices: Morphological changes. *Cell Motil. Cytoskel.*, **40**(1), 13-21. 1998.

30. Gorton T.S., V.H. Barocas, R.T. Tranquillo, Confined compression of a tissue-equivalent: Collagen fibril and cell alignment in response to anisotropic strain. *J. Biomech. Eng.-Trans. ASME*, **124**(5), 568-575. 2002.
31. Murray J.D., G.F. Oster, Cell Traction Models for Generating Pattern and Form in Morphogenesis. *J. Math. Biol.*, **19**(3), 265-279. 1984.
32. Oster G.F., J.D. Murray, A.K. Harris, Mechanical Aspects of Mesenchymal Morphogenesis. *J. Embryol. Exp. Morphol.*, **78**(DEC), 83-125. 1983.
33. Murray J.D., G.F. Oster, A.K. Harris, A Mechanical Model for Mesenchymal Morphogenesis. *J. Math. Biol.*, **17**(1), 125-129. 1983.
34. Barocas V.H., R.T. Tranquillo, An anisotropic biphasic theory of tissue-equivalent mechanics: The interplay among cell traction, fibrillar network deformation, fibril alignment, and cell contact guidance. *J. Biomech. Eng.-Trans. ASME*, **119**(2), 137-145. 1997.
35. Barocas V.H., R.T. Tranquillo, A finite element solution for the anisotropic biphasic theory of tissue equivalent mechanics: The effect of contact guidance on isometric cell traction measurement. *J. Biomech. Eng.-Trans. ASME*, **119**(3), 261-268. 1997.
36. Schwarz U.S., T. Erdmann, I.B. Bischofs, Focal adhesions as mechanosensors: The two-spring model. *Biosystems*, **83**, 225-232. 2006.
37. Nicolas A., B. Geiger, S.A. Safran, Cell mechanosensitivity controls the anisotropy of focal adhesions. *Proc. Natl Acad. Sci. USA*, **101**(34), 12520-12525. 2004.
38. Shemesh T., B.G., Alexander D. Bershadsky, M. Kozlov, Focal adhesions as mechanosensors: A physical mechanism. *Proc. Natl Acad. Sci. USA*, **102**, 12383-12388. 2005.
39. Bruinsma R., Theory of Force Regulation by Nascent Adhesion Sites. *Biophys. J.*, **89**(1), 87-94. 2005.

SUBSTRATE STRETCHING AND ORIENTATION OF ACTIVE CELLS AS A STABILITY PROBLEM

Konstantinos A. Lazopoulos*

7.1. INTRODUCTION

Adherent cells change their orientation to substrate stretching. This is a mechanochemical process involving a mechanical stretching signal and cytoskeletal remodeling. Stress fibers, which are bundles of actin filaments are aligned with the long axis of the cells. Let us recall that the long axis of a cell is directed towards the highest contractile stress of the cell. The cell orientation depends also upon the magnitude of the extracellular strain and the contractility of the cell as well^{1,2,3}. Experimental evidence proves that the stress fibers orient away from the direction of the maximum extracellular stretching^{2,4,5}. Nevertheless, reduced contractility leads to stress fibers reorientation closer to substrate stretching⁴. Kaunas et al.⁶ have demonstrated the importance of the Rho in the development and orientation the stress fibers.

Butler et al.⁷, Bischofs et al.^{8,9} have presented studies of reorientation of the cells using elastic dipoles. Further, Lazopoulos and Stamenovic^{10,11} have presented a model for the cell reorientation under uniaxial strain, accepting large deformations based upon the Finite Elasticity principles. The basic idea was that the cell, under substrate stretching, selects the placement with the minimum potential energy. Further information may be found in Lazopoulos and Pirentis¹². Considering stress fibers made of material with non-convex strain energy density function, stress fibers' reorientation under uniaxial extracellular stretching is studied as a total potential energy minimization problem. There exist already studies explaining

* Mechanics Laboratory, Faculty of Applied Sciences (SEMFE) National Technical University of Athens, Athens, Greece.

the molecular structure of stress fibers, their development and their adhesion to the extracellular substrate. Langanger et al.¹³ describes how actin, a-actinin, filamin and myosin bipolar filament are interconnected to construct stress fibers. The model is described using principles of Finite Elasticity¹⁴, allowing for large strains. Adopting Maxwell's (global) criterion for stability (see Refs. 15,16,17), the stress fiber is simplified as a homogeneously contractile line deformable body (bar), reoriented under extracellular stretching, towards a direction globally minimizing the total potential energy. The model predicts that the degree of cell reorientation depends on the magnitude of the applied substrate stretching, on the state of cell contractility and the non-convexity parameter of the strain energy density, representing the influence of Rho. It is also proven the existence of oblique equilibrium directions with respect to the extracellular stretching^{2,4,5}. Further, the existence of different stable equilibrium states with the same (global) minimum value of the total potential energy, justifies the experimentally proved phenomenon², of coexistence of phases in stress fibers^{16,17}.

Actin cytoskeleton plays an important role in cell shape, motility and various cellular functions. The actin cytoskeleton is composed of actin filaments, which constantly undergo dis-assembly and re-assembly. In addition, experiments have shown that when cells were grown on a substrate subjected to mechanical stretching, the actin cytoskeletons of the cells were reorganized into bundles of actin filaments (stress fibers) oriented towards a specific direction. So, experimental evidence suggests that the actin cytoskeleton is reorganized with the substrate deformation.

It was shown that the frame of the cell (cytoskeleton) can be described as a tensegrity structure composed of actin microfilaments and intermediate filaments (tension components) and microtubules (compression components) (Fig. 7.1). The vertices of this tensegrity structure may support external loads or may be supports of the cell upon the substrate (focal adhesions).

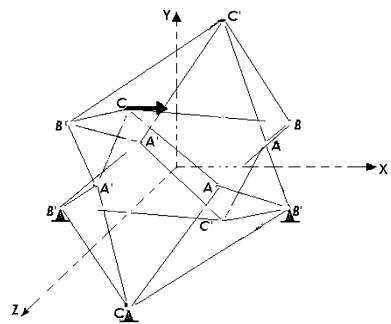


Figure 7.1. The tensegrity cytoskeleton model

In cell culture studies, a planar artificial substrate (e.g. a silicon membrane), is usually used for growing cells. When cells are grown on the substrate, they adhere to it through focal adhesions along the basal cell surfaces. The focal adhesions are discrete regions, which are composed of adhe-

sive proteins. Like short, discrete columns, the focal adhesions support the cell and link it with the underlying substrate. Besides the connection with the substrate, focal adhesions are also associated, via integrins, with termini of actin filaments. Therefore, tensions in actin filaments could be exerted on the substrate and substrate deformation can be transmitted to actin filaments.

The actin microfilaments and intermediate filaments compose the actin cytoskeleton of the cell which, under stretching of the extracellular matrix, may be reorganized as stress fibers.

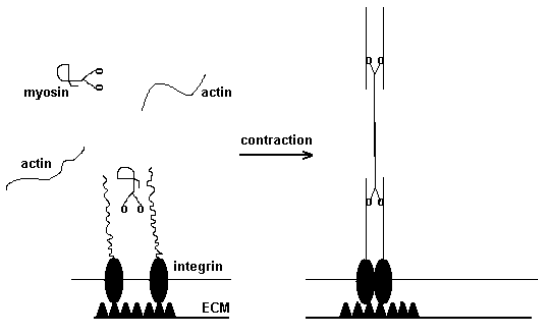


Figure 7.2. The focal adhesion mechanism and stress fiber formation

Activation of Rho results in active interaction of myosin with actin. The generation of tension aligns the actin filaments and aggregates integrins in the plane of the membrane.

Application of cyclic strain causes generally cells and their stress fibers to align perpendicular to the direction of stretching (Fig. 7.3), as has been demonstrated in many kinds of cells such as endothelial cells, fibroblasts, smooth muscle cells. Nevertheless, it has been noticed that smooth muscle cells and their stress fibers became obliquely oriented upon application of cyclic strain (Fig. 7.4).

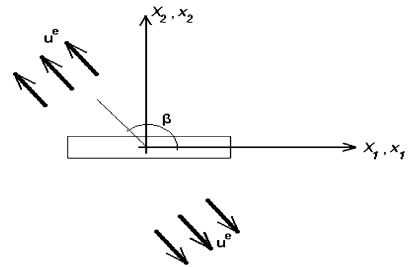


Figure 7.3. Reorientation of the adherent cell under extracellular stretching

This orientation was shown to be dependent on stretching amplitude within the range of 3.5-15%. Takemasa et al.² have shown correlation between oblique stress fibers orientation and the amplitude of cyclic strain.

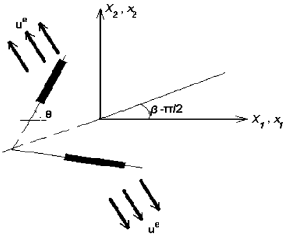


Figure 7.4. The oblique stress fibers direction

Wang et al.⁴ have presented experimental results of cell orientation depending on substrate stretching (Fig. 7.5). Before stretching, the distribution of orientations (defined by the orientation of the long axis) of the cells is the same in any direction of the plane of the extracellular matrix. However, after the application of the extracellular stretching the cells are oriented near the perpendicular direction to the stretching (Fig. 7.5, right panel).

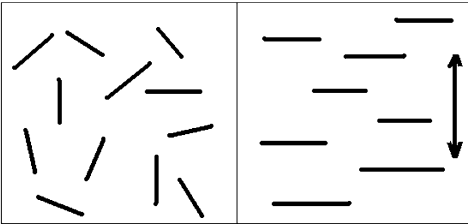


Figure 7.5. Adherent cells without substrate stretching (left), and under uniaxial stretching indicated by the arrow (right)

Figure 7.6 shows further experimental results where the cells have been oriented in a perpendicular direction to the direction of the initial stretching. Next, the stretching changed and aligned with the direction of the cells. In this case, as a result, the cells aligned again in the perpendicular direction of the new stretching course⁴.

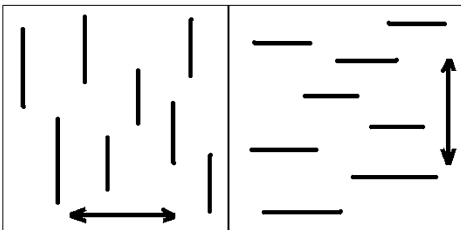


Figure 7.6. The orientation of the cells under various directions of the extracellular stretching

Takemasa et al.² have demonstrated experiments, in which two distinct directions coexisted, (Fig. 7.7). The phenomenon of coexistence of equilibrium placements has been appeared in many natural phenomena like the

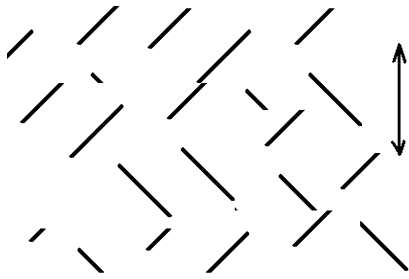


Figure 7.7. The coexistence of cell phases

cells under uni-axial or plane stretching.

meld of ice (where the two phases of the water and the ice coexist), the twinning of the crystals (where different crystal orientations coexist), in crystals transformations and generally in solids in two-phase problems like the elastoplastic problems.

The following discussion is an attempt to interpret the experimental evidence for the reorientation of the

7.2. MECHANICS PRELIMINARIES.

In this section, outline of the elastic equilibrium problem will be presented with the stability conventions. The most elementary elastic model is the spring. Consider the linear spring in Figure 7.8. The applied force is equal to:

$$F = kx \tag{7.1}$$

Then the energy differential is equal to:

$$dU = kx dx \tag{7.2}$$

Hence the deformation energy of the spring is equal to:

$$U = \frac{1}{2} kx^2 \tag{7.3}$$

Further, the total potential energy, V , of any system is equal to the deformation energy minus the work of the applied forces. Hence the total potential energy for the spring equals,

$$V = U - Fx = \frac{1}{2} kx^2 - Fx \tag{7.4}$$

We may draw the figure of V as a function of x for constant force F and we may imagine that the system is a small ball rolling on the potential surface V (Fig. 7.9). It is evident that due to friction, the ball will stop at the minimum value of the total potential energy. This is the equilibrium point. The equilibrium points are defined by the equation,

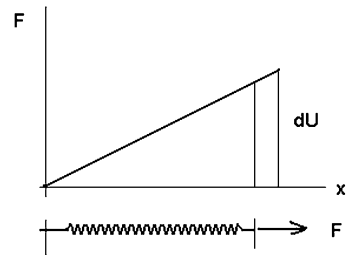


Figure 7.8. The linear spring elastic model

$$\frac{dV}{dx} = 0 \tag{7.5}$$

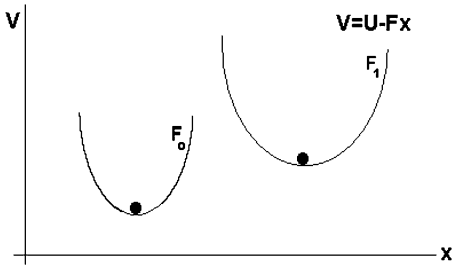


Figure 7.9. The potential surfaces

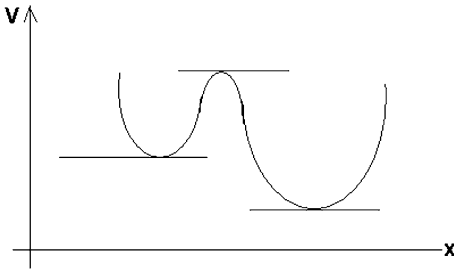


Figure 7.10. The three equilibrium points

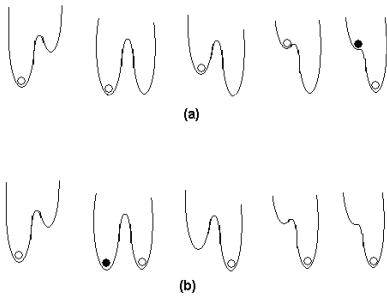


Figure 7.11. (a) The Local (Delay) stability convention. (b) Maxwell's (global) convention

If we perturb the ball from its equilibrium placement, the ball will return to the same equilibrium placement. This placement is called the stable equilibrium placement. Nevertheless, for the potential surface of [Figure 7.10](#), there exist three points satisfying the equilibrium eq. (7.5). Two of them are local minima and one is a maximum. Do both local minima define stable equilibrium placements? The answer depends on the stability convention. In fact there exist two distinct stability conventions (see the Ref. 15). The one is the local (delay) convention and the other is the global (Maxwell) convention.

Delay Convention. The system state remains in a stable or metastable equilibrium state until the state disappears ([Fig. 7.11a](#)).

Maxwell Convention. The system state is the one that globally minimizes the potential ([Fig. 7.11b](#)).

In the Appendix, the stability conventions will be discussed and clarified with some detail on the extension of a twin spring. Phenomena of hysteresis and coexistence of phases are also demonstrated.

Which is the proper convention? This question will be answered by the physics of the problem. Whenever hysteresis phenomena exist, the proper convention is the local.

However, demonstration of coexistence of phases phenomena suggests the adoption of Maxwell's convention. In the present case of the reorientation of the cells under extracellular strain, the experimental evidence of coexistence of phases phenomena indicate the adoption of Maxwell's (global) criterion.

Let us consider a body in its unstressed (reference) placement B_o with a point defined by the vector radius \mathbf{X} . In the deformed (current) placement B the point \mathbf{x} corresponds to the material (initial) point \mathbf{X} . The displacement vector \mathbf{u} is defined by, (see Fig. 7.12),

$$\mathbf{u} = \mathbf{x} - \mathbf{X} \quad (7.6)$$

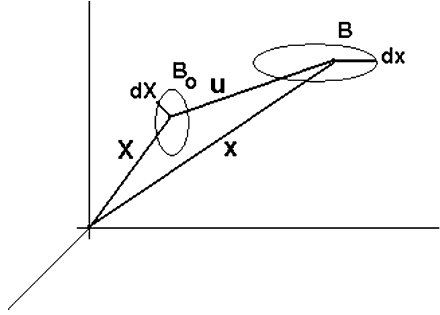


Figure 7.12. The reference and the current placements

Then any infinitesimal vector $d\mathbf{X}$ in the neighborhood of \mathbf{X} of the reference placement is mapped by $d\mathbf{x}$ in the neighborhood of the current placement \mathbf{x} . It is evident that ,

$$d\mathbf{x} = \frac{\partial \mathbf{x}}{\partial \mathbf{X}} d\mathbf{X} \quad (7.7)$$

The gradient of the current placement \mathbf{x} is called deformation gradient,

$$\mathbf{F} = \frac{\partial \mathbf{x}}{\partial \mathbf{X}} \quad (7.8)$$

The deformation gradient gives a picture of the deformation around the material point \mathbf{X} .

Now if \mathbf{m} is the unit vector in the direction of $d\mathbf{X}$, eq.(7.7) yields,

$$\frac{|d\mathbf{x}|^2}{|d\mathbf{X}|^2} = \frac{ds^2}{dS^2} = (\mathbf{F}\mathbf{m}) \cdot (\mathbf{F}\mathbf{m}) = \mathbf{m}^T \cdot (\mathbf{F}^T \mathbf{F}) \mathbf{m} \quad (7.9)$$

We call Lagrangean strain in the \mathbf{m} direction the quantity,

$$e = \frac{1}{2} \frac{ds^2 - dS^2}{dS^2} = \mathbf{m}^T \cdot \mathbf{E}\mathbf{m} = \mathbf{m}^T \cdot \frac{1}{2} (\mathbf{F}^T \mathbf{F} - \mathbf{I}) \mathbf{m} \quad (7.10)$$

where $\mathbf{E} = \frac{1}{2}(\mathbf{F}^T \mathbf{F} - \mathbf{I})$ is called the nonlinear Lagrangean strain tensor. In the linear elasticity where the deformations are small, the Lagrangean strain reduces to the linear strain ,

$$\varepsilon = \frac{ds - dS}{dS} \quad (7.11)$$

Furthermore, the strain energy function for a deformable body U is equal to :

$$U = U(\mathbf{E}) \quad (7.12)$$

with the (First Piola-Kirchhoff), stress tensor¹⁴,

$$\mathbf{S} = \frac{\partial U}{\partial \mathbf{F}} \quad (7.13)$$

The total potential energy V of the deformable body is equal to,

$$V = U - \mathbf{S}\mathbf{F} \quad (7.14)$$

7.3. THE NONLINEAR HOMOGENEOUS STRAIN FIELD OF A STRESS FIBER

The stress-fiber is considered as an extended string adherent to the substrate (Fig. 7.13). The focal adhesions are the supports of the string transferring the forces to the substrate. The mechanism of contractility induces focal adhesion and stress-fiber formation functions as follows: Integrins are the bridges transferring the forces from the stress-fibers to the extracellular matrix (see Fig. 7.2 and the Ref. 18). In quiescent cells, integrins are attached to the extracellular matrix. However, they are not aggregated to focal adhesions but they are dispersed. Inside the cell, the integrins are attached to actin filaments through some proteins. Nevertheless, the filaments are not bundled but they form a loose network. With the activation of Rho, phosphorylation of the myosin light chain takes place, resulting in change in myosin, myosin assembly and an active interaction with actin. The generation of tension aligns the actin filaments and aggregates integrins.

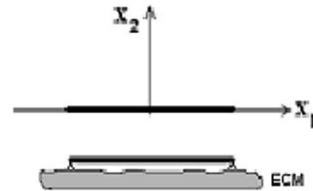


Figure 7.13. The stress-fiber and its supports

Furthermore, the stress fiber probes for the least total potential energy. Indeed, there exists a polymeric microstructural scission procedure, where the stress fiber probes for the least total potential energy with respect to all directions. In the case that there exists a direction with the lower total potential energy, the stress fiber disassembles and re-assembles in the latter direction. In fact, the present procedure looks like a modification of the polymeric scission theory¹⁹, just to include the co-existence of phases phenomena that are exhibited in the present problem. In some way, the Wang's model⁴ assumes the same. However the present model is not only valid to large deformations, but also proposes a mechanism for the reassembly of the stress-fibers, based upon the widely accepted energy principle. Indeed, the stress-fiber is considered as an elastic string reorganized *in the direction with the minimum total potential energy*.

Let us consider a stress fiber adherent on the substrate with zero extracellular stretching. The stress fiber is originally directed along the X_1 axis of the co-ordinate system X_1, X_2 (Fig. 7.14).

The stress fiber is prestressed with its deformation prescribed by the deformation gradient \mathbf{F}^o

$$\mathbf{F}^o = \begin{bmatrix} 1 + g^o & 0 \\ 0 & 1 \end{bmatrix} \quad (7.15)$$

where g^o denotes the displacement gradient due to prestress along the stress fiber. Furthermore, uniaxial stretching of the substrate in the direction β is superimposed to the prestressed stress fiber (Fig. 7.14). The deformation gradient of the superimposed uniaxial deformation, with reference to the initial coordinate system, is defined by,

$$\mathbf{F}^\beta = \mathbf{R}_\beta^T \begin{bmatrix} 1 + g^\beta & 0 \\ 0 & 1 \end{bmatrix} \mathbf{R}_\beta \quad (7.16)$$

where, g^β is the displacement gradient along the β direction due to the extracellular stretching and R_β is the rotation matrix of the coordinate system by an angle β ,

$$\mathbf{R}_\beta = \begin{bmatrix} \cos \beta & \sin \beta \\ -\sin \beta & \cos \beta \end{bmatrix} \quad (7.17)$$

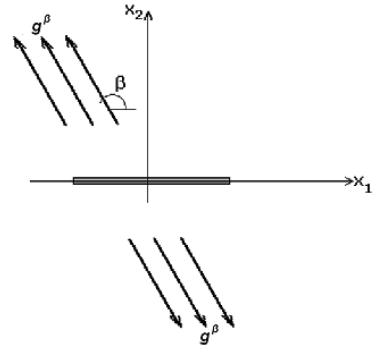


Figure 7.14. The geometry of the initial placement of the stress fiber and the extracellular stretching

and $()^T$ denoting the transpose matrix. Hence, the total deformation gradient of the stress fiber is defined by,

$$\mathbf{F} = \mathbf{F}^\beta \mathbf{F}^\vartheta \quad (7.18)$$

Due to the increased strain, the stress fiber disassembles and re-assembles in a current placement defined by the angle $\tilde{\vartheta}$ with respect to axis X_1 . At this current placement the stress fiber acquires the (global) minimum potential energy. Hence, the reference placement of the stress fiber has changed; in fact it has been rotated through an angle ϑ which is unknown (Fig. 7.15).

Since the prestress is a property imbedded in the stress fiber, the deformation gradient due to the prestress of the stress fiber in the ϑ direction is defined by,

$$\mathbf{F}^\vartheta = \mathbf{R}_\vartheta^T \begin{bmatrix} 1 + g^\vartheta & 0 \\ 0 & 1 \end{bmatrix} \mathbf{R}_\vartheta \quad (7.19)$$

where, the rotation matrix R_ϑ is defined similarly to R_β , eq.(7.15). In this case the total deformation gradient due to the superimposed extracellular stretching in the β direction and the prestress in the stress fiber in the ϑ direction is defined by,

$$\mathbf{F} = \mathbf{F}^\beta \mathbf{F}^\vartheta \quad (7.20)$$

The stress fiber should acquire the minimum total potential energy with respect to all directions ϑ . Since reorganization is observed at high extracellular strains (i.e.10-110%), finite elasticity procedures and methods will be followed. Let us recall that stress-fibers are reoriented not only in a direction perpendicular to the uniaxial extracellular stretching, but they align to the

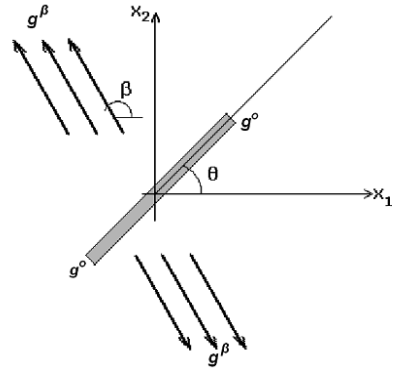


Figure 7.15. The reoriented reference placement of the stress fiber

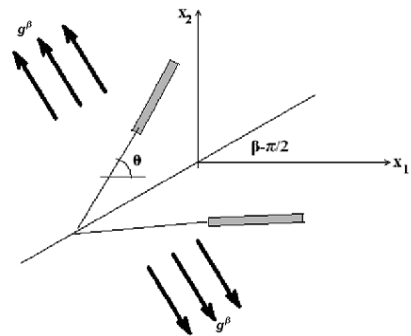


Figure 7.16. The coexistence of phases of the stress-fibers

direction of the extracellular stretching as well; they sometimes exhibit two distinct oblique directions (Fig. 7.16).

It is clear the presence of the non-linear elastic phenomenon of the co-existence of phases, occurring in the melting of ice and in the twinning of crystals^{16,17}. Those phenomena suggest the existence of non-convex strain energy density functions of the non-linear (Lagrangian) strain. Therefore, the assumption of the non-convex strain energy density function is not simple guessing, but an assumption dictated by the experimental evidence. Further, globally stable criteria will be adopted. These criteria justify the coexistence of phases phenomena observed in the experiments^{2,3}.

7.4. THE EQUILIBRIUM PLACEMENTS OF THE STRESS-FIBERS

Let us consider a plane elastic body in its unstressed (at ease) reference placement¹⁴. The material point $\mathbf{R} = (X_1, X_2)$ takes the current placement $\mathbf{r} = (x_1(X_1, X_2), x_2(X_1, X_2))$ under homogeneous deformation. The deformation gradient is defined by,

$$\mathbf{F} = \begin{bmatrix} \frac{\partial x_1}{\partial X_1} & \frac{\partial x_1}{\partial X_2} \\ \frac{\partial x_2}{\partial X_1} & \frac{\partial x_2}{\partial X_2} \end{bmatrix} \quad (7.21)$$

Hence, the Cauchy-Green right deformation tensor is given by,

$$\mathbf{C} = \mathbf{F}^T \mathbf{F} \quad (7.22)$$

and the Lagrangian strain tensor \mathbf{E} is defined by,

$$\mathbf{E} = \frac{1}{2}(\mathbf{C} - \mathbf{I}) = \begin{bmatrix} e_{11} & e_{12} \\ e_{21} & e_{22} \end{bmatrix} \quad (7.23)$$

Consider the prestressed stress-fiber, initially oriented along the X_1 direction; the stress fiber disassembles after the application of the extracellular stretching, and re-assembles in a direction forming an angle $\tilde{\vartheta}$ with the axis X_1 (Fig. 7.17).

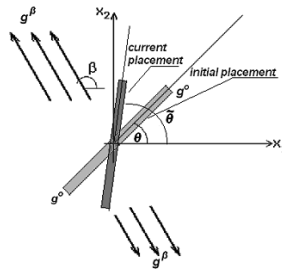


Figure 7.17. The current and initial placements of the stress fiber.

It is assumed that the stress fibers are not lost. They are created in a new direction. In this transplacement, the stress acquires the minimum of the total potential energy. It is evident, that this current placement corresponds to some new reference placement described by an angle ϑ , (Fig. 7.17). The unit vector $\boldsymbol{\eta}$ along this direction is defined by,

$$\boldsymbol{\eta} = [\cos \vartheta \quad \sin \vartheta]^T \quad (7.24)$$

Then, if ds denotes the deformed length of the initial length dS along the stress fiber,

$$\frac{ds}{dS} = (\boldsymbol{\eta}^T \cdot \mathbf{C} \boldsymbol{\eta})^{1/2} \quad (7.25)$$

and the displacement gradient along the stress fiber is equal to,

$$u_s = \frac{du}{dS} = \frac{ds}{dS} - 1 \quad (7.26)$$

Likewise, the Lagrangean strain e along the stress fiber is equal to,

$$e = (\boldsymbol{\eta}^T \cdot \mathbf{E} \boldsymbol{\eta})^{1/2} \quad (7.27)$$

Performing the computations with the help of Mathematica computerized algebra pack²⁰, the displacement gradient of the stress fiber is defined by,

$$u_s = -1 + \frac{1}{\sqrt{2}}(1 + g^o) \sqrt{\left(2 + 2g^\beta + (g^\beta)^2 + g^\beta(2 + g^\beta) \cos(2(\beta - \theta))\right)} \quad (7.28)$$

Let's recall that the Lagrangean strain e is defined by,

$$e = u_s + \frac{1}{2} u_s^2 \quad (7.29)$$

It has already been pointed out that the strain energy density of the stress fibers should be a non-convex function of the strain, because phenomena similar to the co-existence of phases have experimentally been

proved. Let us consider a fiber with the simplest non-convex strain energy per unit initial length equal to,

$$W = c_1 e^2 - c_2 e^4 + c_3 e^6 \quad (7.30)$$

with $c_1, c_2, c_3 > 0$. The strain energy density is objective, since it depends only upon the right Cauchy-Green deformation tensor. The strain energy density W is non-convex and c_2/c_1 denotes the non-convexity factor corresponding to the contribution of the Rho. It is evident that the strain energy density function, eq. (7.30), may be transformed to a function of the displacement gradient u_s due to eq. (7.29). Hence the first Piola-Kirchhoff stress along the axis of the fiber is defined by,

$$T = \frac{\partial W}{\partial u_s} = c_1(1+u_s) \left(-1+(1+u_s)^2 \right) - \frac{1}{2} c_2(1+u_s) \left(-1+(1+u_s)^2 \right)^3 + \frac{3}{16} c_3(1+u_s) \left(-1+(1+u_s)^2 \right)^5 \quad (7.31)$$

Let us recall that the length of the reorganized fibers is the same as the one of the disorganized ones. Without losing the generality, we may consider unit length of the stress fibers. Thus, the total potential of the unit length stress fiber is defined by,

$$V = W - T u_s = -\frac{1}{64} u_s^2 (2+u_s) \left(16c_1(2+3u_s) + u_s^2(2+u_s)^2 (-4c_2(6+7u_s)) + c_3 u_s^2 (2+u_s)^2 (10+11u_s) \right) \quad (7.32)$$

Recall that eq. (7.32) becomes a function of the pre-strain displacement gradient g^α , the extracellular uniaxial displacement gradient g^β and the difference $\beta - \vartheta$ of the angles of the reoriented initial placement direction of the stress fiber from the direction of the uniaxial extracellular stretching.

The equilibrium equation is expressed by the minimum of the potential V with the necessary condition,

$$\frac{\partial V}{\partial \vartheta} = 0 \quad (7.33)$$

Further, the stability of the solution demands that,

$$\frac{\partial^2 V}{\partial \vartheta^2} > 0 \quad (7.34)$$

Let us point out that performing the algebra,

$$\frac{\partial V}{\partial \vartheta} = \frac{\partial V}{\partial u_s} \frac{\partial u_s}{\partial \cos(2(\beta - \vartheta))} \sin(2(\beta - \vartheta)) = G(g^o, g^\beta, \beta - \vartheta) \sin(2(\beta - \vartheta)) = 0 \quad (7.35)$$

Hence there immediately exist two equilibrium solutions,

$$\beta = \vartheta \text{ and } \beta = \vartheta + \frac{\pi}{2} \quad (7.36)$$

The first solution aligns the reoriented initial placement of the stress fiber with the direction of the extracellular stretching, whereas the second to the perpendicular to the extracellular stretching. It is evident that those equilibrium solutions are valid whenever,

$$G(g^o, g^\beta, c_2/c_1, c_3/c_1, \beta - \vartheta) \neq 0 \quad (7.37)$$

for any ϑ . However, when

$$G(g^o, g^\beta, c_2/c_1, c_3/c_1, \beta - \vartheta) = 0 \quad (7.38)$$

with

$$\cos(2(\beta - \vartheta)) = \gamma \text{ and } |\gamma| \leq 1 \quad (7.39)$$

there exist two solutions ,

$$\vartheta = \beta \pm \frac{\arccos \gamma}{2} \quad (7.40)$$

symmetrically oriented to the direction of the extracellular stretching.

It is clear that γ depends upon the parameters of the problem, that are the initial pre-stress displacement gradient g^o , the displacement gradient of the superposed deformation g^β and non-convexity factor c_2/c_1 and the c_3/c_1 as well ($\gamma = \gamma(g^o, g^\beta, c_2/c_1, c_3/c_1)$).

7.5. GLOBALLY STABLE EQUILIBRIUM PLACEMENTS

According to the analysis presented in the former section, there exist many equilibrium placements of a stress-fiber under substrate stretching and some of them should be stable. Stability of equilibrium analysis requires the explicit stability criteria definition for the present problem. However, stability criteria come out from the adopted stability convention.

Nevertheless, the question is which convention should be adopted. It is up to the researcher to decide. There are some phenomena guiding the scientist to the proper stability convention. Indeed, the existence of hyste-

resis guides to the adoption of the local (delay) convention, however the phenomena of coexistence of phases guide to the Maxwell's convention. The experimental evidence for the stress-fibers assures coexistence of phases phenomena². Hence Maxwell's convention for stability is adopted for the present problem.

The solutions given by eqs. (7.36) and (7.39) are mutually exclusive in the sense that for a specific set of parameters ($g^o, g^\beta, c_2/c_1, c_3/c_1$) either eq.(7.22) or eq.(7.25) yields the global minimum of the total potential. By studying the stability of those solutions (see condition (7.34)) with the use of numerical methods, it turns out that low values of the pre-strain g^o and the displacement gradient g^β along the stress fiber, promote the stability of the solution $\vartheta = \beta$. Just describing the evolution of various equilibrium placements, the stress fibers are collinear to the direction of the extracellular stretching ($\beta = \theta$) when the values of their parameters are low. In that case, it is $G(g^o, g^\beta, c_2/c_1, c_3/c_1, 0) < 0$. In the critical state when $G(g^o, g^\beta, c_2/c_1, c_3/c_1, 0) = 0$, the phenomenon of the coexistence of phases will be shown up. In the Figure 7.18, the initial points (low boundary) of the evolution of the coexistence of phases have been drawn for various values of the pre-strain g^o . The region of co-existence of phases is extended to the right of each curve.

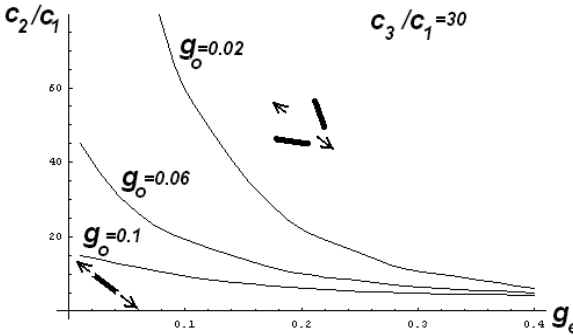


Figure 7.18. Region boundaries for the coexistence of phases.

Likewise, the region with the stress fiber aligning to the direction of the extracellular stretch is defined to the left of each curve. The higher the pre-strain is, the lower the non-convexity parameter is needed for the critical curves, indicating the contribution of the GTPase Rho. Increasing the extracellular stretching, the phenomenon of the co-existence of phases for the stress fibers is still present, since $G(g^o, g^\beta, c_2/c_1, c_3/c_1, \beta - \vartheta) = 0$ with β different from θ . The difference of the two angles ($\beta - \theta$) will absolutely increase, until the direction β of the extracellular stretching and the direction of the new initial placement of the stress fiber, defined by θ , become per-

pendicular. This placement is the limiting placement of the co-existence of phases of the stress fibers when the extracellular stretching or (and) the non-convex coefficient increases.

At this point, we may interpret the fact that the final equilibrium placement of the stress fiber, in long time, is transverse to the extracellular stretch direction. Wang et al.⁴ have experimentally proved that the phenomenon of the co-existence of phases of the stress fibers is not permanent but intermediate. Indeed, considering a co-existence of phases of the stress fibers placement with $G(g^o, g^\beta, c_2/c_1, c_3/c_1, \beta - \theta) = 0$ for some non-convexity parameter c_2/c_1 and assuming that the coefficient c_1 decreases with time, the non-convexity parameter c_2/c_1 increases, so that the two phases coincide in the limiting placement that is transverse to the extracellular stretch direction. In that placement the two phases disappear and one only stress fiber direction appears, perpendicular to the extracellular stretching.

Furthermore, the kind of the non-convexity of the strain energy density has its own contribution to the problem. In fact, if the non-convexity is strong then the co-existence of phases placements are exhibited with less extracellular strain. Of course, the non-convexity of the strain energy density depends upon the coefficients c_i , $i=1,2,3$. Since the ratio c_2/c_1 greatly contributes to the non-convexity of the strain energy density, this ratio will be called non-convexity factor. Higher values of the non-convexity ratio promote the limiting solution $\vartheta = \beta + \frac{\pi}{2}$, whereas low values of this ratio promote the solution $\vartheta = \beta$. In fact the non-convexity factor is related to the influence of Rho. The case with $c_2/c_1 = 0$ corresponds to the inhibition of Rho, while with $c_2/c_1 > 0$ Rho is activated. Let us point out that experiments have proved that activation of Rho reorients the stress-fibers in a transverse direction to the extracellular strain, whereas inhibition of Rho drives the stress-fibers in the direction of the extracellular stretching⁶.

It should be pointed out that the present theory may be shown without specific type of the strain energy density. The only restriction would be the non-convexity of the strain energy density function. However, the adopted strain energy density is of the simplest non-convex ones.

In the case of a group of fibers adherent to the substrate, (possibly included into a cytoskeleton) the present analysis proves that the stress fibers with weak Lagrangean strain that depends upon the contractile pre-strain, extracellular strain and small non-convexity parameter (inhibition of Rho), will be pointed towards direction of the uniaxial extracellular stretching, whereas in the case of strong contractile pre-strain, extracellular strain and

activation of Rho, the fibers will be directed towards direction transverse to the extracellular uniaxial stretch direction (Fig. 7.19).

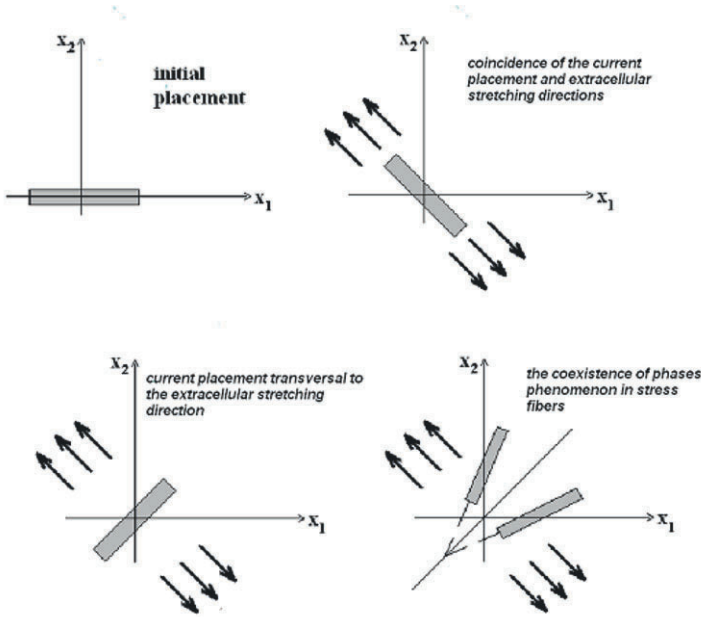


Figure 7.19. Summary of the reorientation of the stress-fibers.

7.6. APPLICATIONS

We consider the case when the displacement gradient due to pre-strain is $g^o = 0.04$, the displacement gradient due to extracellular stretching $g^\beta = 0.06$, the coefficient $c_2 = 10$ and the coefficients $c_1 = 1$ and $c_3 = 1$. By computing the total potential energy V , eq. (7.18), we get for the equilibrium placement $\vartheta = \beta$, the value $V|_{\vartheta=\beta} = -0.00843462$. However, at

$\vartheta = \beta + \frac{\pi}{2}$, the calculated value is $V|_{\vartheta=\beta+\frac{\pi}{2}} = -0.00164464$. The first equi-

librium placement is locally and globally stable, while, according to the eq.(7.32), the second placement is locally and globally unstable. No other solution exists in this case. Some critical extracellular strains may be computed for various values of the pre-strains. In fact for this stress fiber, for pre-strain displacement $g^o=0.02$ the critical extracellular strain is $g^e=0.103$; for $g^o=0.04$ the critical extracellular strain is $g^e=0.083$; for $g^o=0.08$ the critical extracellular strain is $g^e=0.103$. Increasing only the extracellular stret-

ching to $g^\beta = 0.14$, for $g^0=0.04$, two other solutions exist generated by eq. (7.36). The solutions are defined by the initial directions of the stress fibers, $\vartheta = \beta \pm 0.7$ in rad or $\vartheta = \beta \pm 40,1^\circ$. The criterion (7.34) assures that the placements are locally stable. Furthermore, they yield the same value of the total potential energy. Hence according to the global (Maxwell's) criterion for stability, these placements are equally accepted and co-exist (see Fig. 7.16). It is pointed out that the directions ϑ of the reoriented initial placements are not the directions of the current placements denoted by $\tilde{\vartheta}$. For the definition of the current directions $\tilde{\vartheta}$, the total deformation gradient has to be computed. For the parameters of the problem and further for the extracellular stretching direction $\beta = 2$ rad and $\vartheta = 2 - 0.70 = 1.30$ rad, the total deformation gradient, by applying the eq.(7.8), yields,

$$\mathbf{F} = \begin{bmatrix} 1.02663 & -0.0443836 \\ -0.0416243 & 1.15665 \end{bmatrix} \quad (7.41)$$

The deformed unit vector in the initial direction $\vartheta = 1.30$ rad is defined by the non-unit vector $\tilde{\boldsymbol{\eta}} = \mathbf{F}\boldsymbol{\eta}$, where $\boldsymbol{\eta}$ is the unit vector along the direction ϑ . It is found that

$$\tilde{\boldsymbol{\eta}} = (0.231856, 1.10336) \quad (7.28)$$

$$\text{Hence } \tan \tilde{\vartheta} = \frac{1.10336}{0.231856} = 4.75896 \text{ and } \tilde{\vartheta} = \arctan(4.75896) = 1.36368.$$

Thus the initial fiber direction at $\vartheta = 1.30$ rad or $\vartheta = 74.48^\circ$ deforms in the current fiber direction at $\tilde{\vartheta} = 1.36338$ or $\tilde{\vartheta} = 78.13^\circ$ (see Fig. 7.17). It is evident that a symmetric direction with respect to the extracellular stretching direction exists for the initial and current placements of the stress fibers. It turns out that the transverse to the extracellular stretching direction is revealed as the limiting placement of the co-existent phases when the various parameters of the pre-strain, extracellular stretch and non-convexity factor c_2/c_1 increase. Hence, that limiting placement is a global minimum. Therefore the stable solution is directed along the transverse to the direction of the extracellular stretching. Figure 7.19 presents all the possible equilibrium states of the stress fibers.

7.6. DISCUSSION

One evident question raises whether the non-convex strain energy density function assumption may be feasible or not. Of course, one could figure

out that given the peculiar ability of the stress-fiber to disassemble and reassemble, the non-convexity of the stress-fiber might not seem strange. Nevertheless, the structure of the stress-fiber, with its supports (focal adhesions), that has already been described in the Section 7.1, suggests that with slight sliding between the various components of the stress fiber, the introduced non-convex strain energy density may not be an imaginary ad hoc assumption but a realistic behavior.

It is evident that three main factors influence the proposed problem. These factors are the contractile strain (pre-strain), the measure of the extracellular strain and the non-convexity parameter. Hence the evolution of the fibers reorientation, with the increasing value of the extracellular strain, is described, first by the reorientation towards the direction of the extracellular stretching; then increasing the value of the extracellular stretching, the coexistence of two distinct reorientation directions is shown up; increasing further the value of the extracellular strain the reorientation towards the transverse direction to the extracellular strain will prevail, as a limiting co-existence of phases placement.

It is stated, as a final conclusion, that high contractility (prestrain), extracellular strain and non-convexity coefficient (activation of Rho) as well, promote the reorientation towards the transverse direction to the extracellular strain; on the contrary, small contractility (pre-strain), extracellular strain and non-convexity coefficient (inhibition of Rho) as well, promote the reorientation towards the direction of the extracellular strain.

References

1. Dartsch P.C., H. Haemmerle, Orientation response of arterial smooth muscle cells to mechanical stimulation. *Eur. J. Cell Biol.*, **41**:339-346, 1996.
2. Takemasa T., K. Sugimoto, K. Yamashita, Amplitude-dependent stress- fiber reorientation in early response to cyclic strain. *Exp Cell Res*, **230**:407-410, 1997.
3. Neidlinger-Wilke C., E.S. Grood, J. H.-C. Wang, R. A. Brand, L. Claes, Cell alignment is induced by cyclic changes in cell length: studies of cells grown in cyclically stretched substrates. *J Orthopaedic Res*, **19**:286-293, 2001.
4. Wang J.H.-C., P. Goldschmidt-Clermont, F. C.-P. Yin, Contractility affects stress-fiber remodeling and reorientation of endothelial cells subjected to cyclic mechanical stretching. *Ann Biomed Eng*, **28**:1165-1171, 2001.
5. Wang N., I. M. Tolić-Nørrelykke, J. Chen, S.M. Mijailovich, J.P. Butler, J.J. Fredberg, D. Stamenović, Cell prestress. I. Stiffness and prestress are closely associated in adherent contractile cells. *American Journal of Physiology: Cell Physiology*, **282**:C606-C616, 2002.
6. Kaunas R., P. Nguyen, S. Usami, S. Chien, Cooperative effects of Rho and mechanical stretch on stress-fiber organization. *Proc Natl Acad Sci USA*, **102**:15895-15900, 2005.

7. Butler J.P., I.M. Tolić-Nørrelykke, B. Fabry, J.J. Fredberg, Traction fields, moments, and strain energy that cells exert on their surroundings. *Am J Physiol: Cell Physiol*, **282**:C595-C605, 2002.
8. Bischofs I.B., U.S. Schwarz, Cell organization in soft media due to active mechanosensing. *Proc Natl Acad Sci USA*, **100**:9274-9279, 2003.
9. Bischofs I.B., S.A. Safran, U.S. Schwarz, Elastic interactions of active cells with soft materials. *Phys Rev E*, **69**, 021911, 2004
10. Lazopoulos K., D. Stamenovic, A mathematical model of cell reorientation in response to substrate stretching, *MCB*, **3**(1):43-48, 2006.
11. Lazopoulos K., D. Stamenovic, A mathematical model of cell reorientation in response to substrate stretching, Proceedings of the 5th World Congress of Biomechanics Munich July 29th-August 4th 2006, *Journal of Biomechanics* **39**, Sup. 1, S 584, 2006.
12. Lazopoulos K., A. Pirentis, Substrate stretching and reorganization of stress fibers as a Finite Elasticity problem, *IJSS*, **44**:8285-8296, 2007.
13. Langanger G., M. Moeremans, G. Daneels, S. Apolinary, M. De Brabander, J. De Mey, The molecular Organization of myosin in stress-fibers of cultured cells, *The J. of Cell Biol.* **102**:200-209, 1986.
14. Ogden R.W., *Non-linear elastic deformations*, Dover Publications, New York etc. 1997.
15. Gilmore R., *Catastrophe theory for scientists and engineers*. J. Wiley and Sons, New York, 1981.
16. Ericksen J.L., *Introduction to the Thermodynamics of Solids*. R.J. Knops, K.W. Morton (eds.), Chapman & Hall, London, chp. 3:39-61, 1991.
17. Pitteri M., G. Zanzotto, *Continuum models for phase transitions and twinning in crystals*, Chapman & Hall/CRC Boca Raton, 2002.
18. Chrzanowska-Wodnicka M., K. Burridge, Rho-stimulated contractility drives the formation of stress-fibers and focal adhesions, *Jnl of Cell Biol.*, **133**:1403-1415, 1996.
19. Rajagopal K.R., A.S. Wineman, A constitutive equation for non-linear solids which undergo deformation induced microstructural changes. *Int. J. of Plast.*, **8**:385-395, 1992.
20. Wolfram S., *The Mathematica book*. Third edition, Cambridge Univ. Press., Cambridge, 1996

APPENDIX

In this section, the importance of the stability criterion will be clarified. In fact there exist two distinct stability conventions (see the Ref. 15). The one is the local (delay) convention and the other is the global (Maxwell) convention.

Delay Convention. The system state remains in a stable or metastable equilibrium state until the state disappears.

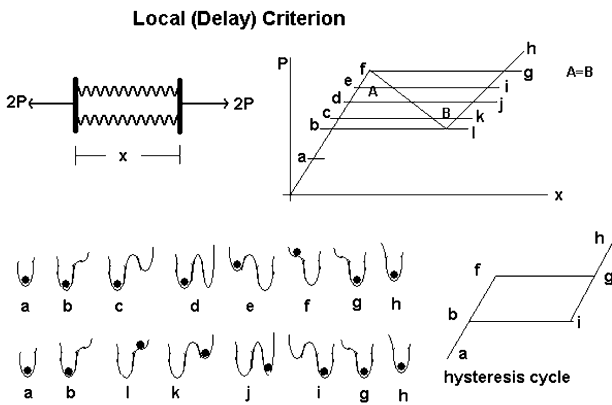
Maxwell Convention. The system state is the one that globally minimizes the potential.

The question is which convention should be adopted. It is up to the researcher to decide. There are some phenomena guiding the scientist to the proper stability convention. Indeed, the existence of hysteresis guides to the adoption of the local (delay) convention, however the phenomena of coexistence of phases suggest Maxwell's convention.

Extension of a twin spring problem

For clarification of the ideas we consider the extension of the twin spring, (Fig. 7.20). The twin spring is composed by two identical springs in parallel. The springs have a sectionally linear force P versus deformation x diagram. The total potential energy function V for low values of the displacement presents the unique local (and global) minimum. Nevertheless, by increasing the load, the situation becomes different because local and global minima do not coincide.

a) Deformation adopting the local (delay) criterion.



reaches to the placement h . Decreasing now the load, the system follows the $h-i$ section of the diagram. The point i is again a limiting point because two equilibrium placements coincide there to an inflection point. At decreasing further the loading, the system jumps to the placement b . Further decrease of the load, guides the system to the placement a . The cycle $bfgeb$ is called hysteresis cycle indicating the loss of the energy during this cycle. Adopting the local criterion for stability we expect just the same deformation of both springs of the twin spring structure.

b) Deformation adopting the global (Maxwell) criterion.

In this case, the equilibrium placements are defined by the placements of the global minima of the total potential energy function. There exist a load $P=P_M$ (Maxwell value) where two equal areas A and B are cut off from the diagram (Fig. 7.21).

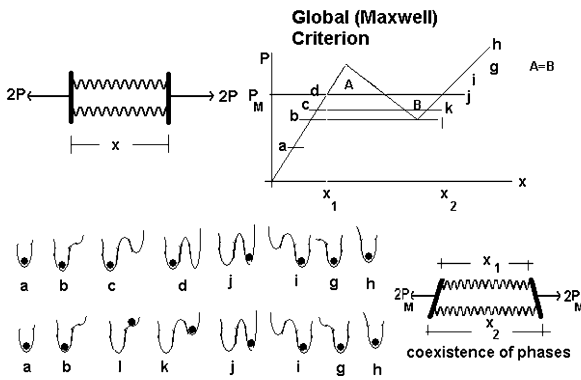


Figure 7.21. Deformation of the twin spring adopting the global (Maxwell) convention for stability

The function of the total potential energy V in this case exhibits two global minima. Therefore, the placements $a-d$ are the global minima of V . At the placement d there exists another global minimum j . So we may expect a deformation of the twin spring with different deformations ($x=d$, $x=i$). This is exactly the phenomenon of coexistence of phases where two different spring deformations coexist under the same load P_M . It is quite strange that the twin spring device accepts a stable placement at positions where each individual spring is unstable. At increasing the load, the twin spring becomes symmetric again following the path $g-h$. At decreasing the load, the deformation of the twin spring traces just the same path as in the local (delay) convention, i.e. the path $h-i-b-a$. These are the principles of pseudoelasticity, introduced by Ericksen¹⁶, who was solving the extension problem of a bar with non-convex strain energy density (Fig. 7.22).

**Ericksen's Pseudoelastic bar
(Coexistence of Phases)**

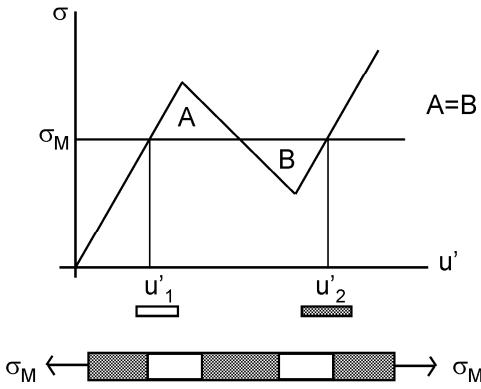


Figure 7.22. Coexistence of phases in an extended bar

In this case, continuous displacement fields are accepted but with possible discontinuous strain fields. Therefore, at the Maxwell value of the stress σ_M two strains u'_1 and u'_2 coexist forming regions of low (yellow) strain and high (green) one separated by the phase boundaries.

Various phenomena in solids, like twinning and phase transformations in crystals, are explained adopting the theory of pseudoelasticity.

ROLES OF MECHANICAL FORCES AND EXTRACELLULAR MATRIX PROPERTIES IN CELLULAR SIGNALING IN THE LUNG

Béla Suki^a
Erzsébet Bartolák-Suki^{a,b}

8.1. INTRODUCTION

The biomechanical properties of connective tissues play fundamental roles in the functioning of virtually every organ. These properties are critical determinants of how mechanical interactions of the body with its environment produce physical forces at the cellular level. In the lung for example, mechanical forces can directly influence function via cellular signaling¹ such as during lung development², surfactant release by alveolar epithelial cells³, the contractile properties of airway smooth muscle⁴, or tissue remodeling⁵. More generally, it is now recognized that mechanical interactions between cells and the extracellular matrix (ECM) have major regulatory effects on cellular physiology and cell-cycle kinetics which can lead to the reorganization and remodeling of the ECM^{6,7}. This in turn influences the macroscopic biomechanical properties and function of the organ.

Traditional biomechanics has focused on characterizing the macroscopic structural and mechanical properties of living tissues and organs by establishing a mathematical relation, called the constitutive equation, that describes how mechanical stresses (force per unit area) change in response to a change in the size and/or shape of a body. The constitutive equation is often nonlinear and can describe the static relationship between stress and strain. When the constitutive equation also

^a Department of Biomedical Engineering, Boston University, Boston, MA, USA.

^b CelluTraf Sci, Boston, MA, USA

characterizes the time-dependent or dynamic stress-strain properties, the tissue is usually referred to as viscoelastic. Virtually every living tissue displays viscoelastic behavior⁸. These constitutive equations are commonly determined from measured stress-strain relationships, and reflect behavior emergent from the mechanical properties of the individual constituents as well as their structural arrangement in the tissue⁸.

All connective tissues are composed of cells and ECM that includes water and a variety of biological macromolecules. The macromolecules that are most important in determining the mechanical properties of these tissues are collagen, elastin and proteoglycans (Fig. 8.1). Among the macromolecules, the most abundant and perhaps most critical for structural integrity is collagen. One might expect therefore that the amount of collagen in a tissue is the primary determinant of its mechanical properties. However, different connective tissues with similar collagen content can exhibit different mechanical behavior matching the specific needs of the organ⁸. During the last decade, the advent of novel imaging techniques⁹ and quantitative computational modeling¹⁰ have allowed the study of micromechanics of specific components of tissues and hence the ability to understand the relationship between tissue composition, microstructure, and macrophysiology. In particular, it has become evident that macrophysiology reflects both the mechanical properties of the individual components of the tissues, as well as the complexity of its structure¹¹.

This chapter will focus mostly on the lung and follow closely the material published in a recent review article¹². Specifically, first we will summarize the constituents of the connective tissue of the lung and their complex structural organization. Next, we will describe how the mechanical properties of the parenchyma arise from the constituents and structural organization of the alveolar walls. We will then argue that collagen is the single most important load bearing element within the alveolar duct and wall, and is critical to determining the homeostasis and cellular responses to injury. The deformation of the alveolar wall network is heterogeneous and hence the distribution of mechanical forces on the collagen is also heterogeneous in the lung. This heterogeneity in the ECM

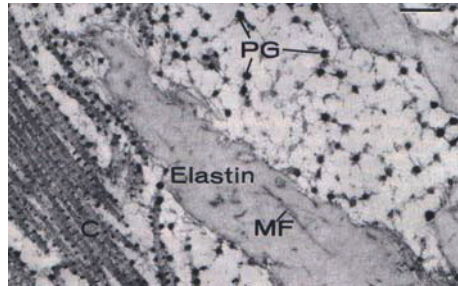


Figure 8.1 ECM structure including collagen (C), elastin, microfibrils (MF) and proteoglycans. (with permission from “Cell Biology of Extracellular Matrix”, Elizabeth Hay (ed.), Plenum Press, New York 1981)

properties likely plays a role in the regional distribution of cell signaling. Finally, we will summarize what is known about the interactions between the collagen network and cellular remodeling and how mechanotransduction might contribute to impaired lung function in a terminal disease, pulmonary emphysema.

8.2. MAIN CONSTITUENTS OF THE LUNG CONNECTIVE TISSUE

8.2.1. Properties of collagens

There are over 20 different types of collagen molecules. Most interstitial collagens (I, II, III, V, XI) are helical in structure, consisting of 3 polypeptide chains each of which is a left-handed coil of approximately 1000 amino acids and the 3 chains form a right-handed super helix¹³. These helical molecules are rod-like rigid structures with length and diameter of about 300 nm and 1.5 nm, respectively, and capable of spontaneous fibril forming¹⁴. The helical subunits are first assembled in the endoplasmic reticulum of interstitial cells in precursor form called procollagens which have amino and carboxyl terminal globular regions known as propeptides. These serve to solubilize the procollagen, and correctly align the individual peptide chains to facilitate helix formation¹⁴. Following secretion, the propeptides are enzymatically cleaved, which allows the collagen molecules to associate both axially and laterally to start forming fibrils. Apparently, type I collagen is thermally unstable at body temperature and folding of the least stable microdomains can trigger self-assembly of fibrils where the helices are protected from complete unfolding¹⁵. The lateral and axial growth of the fibrils appears to be, in part, determined through interactions with other matrix components such as proteoglycans¹⁶⁻¹⁸. The fibril structure itself also shows tremendous hierarchical complexity. For example, the lateral packing of molecules can exhibit significant fluid-like disorder^{16,19}. The collagen fibrils can further organize into thicker fibers through cross-linking of lysine and hydroxylysine residues present within the overlapping terminal helical and teleopeptide regions of the molecules¹⁴. These fibrils and fibers go on to form random such as lung tissue or cartilage or quasi-deterministic as networks (e.g. tendon) within an organ.

The interstitium of the lung parenchyma contains mostly type I and III collagen which provide the structural framework for the alveolar wall. Fiber thickness ranges from several hundred nm to well over a micron²⁰. The distribution of fiber thickness is skewed, and has a long “tail”²⁰ similar to a power law²¹, indicating broad variability of fiber structure.

This blend of deterministic order (exact amino sequence and axial packing) and random disorder (from fluid-like lateral packing to random networks) may partly be responsible for the existence of a broad range of time constants that characterizes the viscoelastic properties of the connective tissue of the lung^{22,23}. These collagen fibers in the parenchyma are further organized to form an axial fiber network extending down from the central airways to the alveolar ducts, a peripheral fiber network extending centrally from the visceral pleura, and a parenchymal interstitium, which connects the two²⁴.

Variations in the collagen content of the parenchyma during development^{25,26}, in fibrosis²⁷ or following *in vitro* digestion²⁸ have suggested an important role for these protein fibers in the biomechanical properties of the parenchyma.

8.2.2. Properties of elastic fibers

Elastic fibers are composed of elastin and microfibrils which are mostly fibrillin and fibullin²⁹. The elasticity of microfibrils is controversial and their role in lung elasticity has not been studied. Values of the Young's modulus of microfibrils were reported to be as low as 0.2 MPa³⁰, which is about 3-5 times lower than the stiffness of elastin^{8,31}, and as high as 96 MPa³², which is closer to that of the collagen⁸. The microfibrils often form a fibrous outer mantle surrounding the more amorphous elastin. The elastin is composed of insoluble flexible cross-linked polypeptides. While the 3D molecular structure of elastin fibers is not well understood^{16,33}, elastin organizes itself into easily extensible fibers and has a linear stress-strain relation up to 200% strain⁸. The distribution of the diameter and length of elastin fibers in the lung are skewed with long "tails," and appear similar to the distribution of collagen fiber properties. Thus, the elastic fibers exhibit significant structural heterogeneity and are also known to be mechanically connected to the collagen³⁴ via microfibrils and/or proteoglycans^{16,18,35}. Traditionally, elastin is thought to dominate lung elasticity at normal breathing lung volumes³⁶. However, a recent study comparing the effects of elastin and collagen digestion on the constitutive equation of parenchymal strips suggests that collagen may be equally important, even at lower lung volumes²⁸.

8.2.3. Properties of proteoglycans

Within the lung, collagen and elastin fibers of the connective tissues are embedded in a hydrated gel, often called the "ground substance". The composition of the matrix and the ratio of fiber to gel varies among tissues¹⁶ and change during maturation and with certain disease states³⁷. A

critical constituent of this matrix are the glycosaminoglycans (GAG), a family of highly charged polysaccharides¹⁶. There are several different types of GAGs (e.g., hyaluronic acid, chondroitin sulphate, dermatan sulphate, keratan sulphate) whose molecular weights vary over 3 orders of magnitude implying that the polymer chains can contain as many as 10^4 units with a huge variability in size and structure^{38,39}. Within the lung parenchyma, the most abundant GAGs are heparin sulfate and chondroitin sulfate. Most GAGs are usually covalently linked to a core protein to form proteoglycans. Similar to collagen, GAGs can also have secondary and tertiary structures by forming helical and randomly organized regions depending on the ionic environment and pH of the matrix³⁹. Proteoglycans can also associate ionically with one another to form large aggregates that exhibit an even higher level of hierarchical organization. Images of the proteoglycans obtained by electron microscopy reveal an extraordinarily complex structure^{38,40}. The majority of the above studies on proteoglycan mechanics has been done in cartilage and it is likely that the role of proteoglycans in lung function has been underestimated. Indeed, only a few studies have examined their role in lung mechanics^{11,41}.

8.2.4. Interstitial cells

The lung parenchyma contains a variety cell types. From the point of view of mechanics, the most important ones are the contractile cells including smooth muscle cells in the alveolar duct and vessel walls and the myofibroblasts and fibroblasts in the alveolar walls⁴². Stimulation of these cells with different agonists induce local internal stresses in the fiber network which can lead to changes in the viscoelastic properties of the lung tissue⁴³⁻⁴⁷. However, during contractile challenge, the mechanical properties of tissue strips have also been found to vary with the number of medium size airways in the sample⁴⁶. It is therefore possible that part of the previously observed changes in mechanics during agonist challenge were in fact related to smooth muscle contraction and airway-parenchymal interaction. Nevertheless, the viscoelastic properties of the lung parenchyma are only moderately affected by the active tone of the interstitial cells^{43,47}. A more important function of the interstitial cells is to actively remodel and repair the connective tissue during growth or following injury. As a result of such cellular processes, the nonlinear viscoelastic properties of the lung tissue can significantly change both at the organ and the alveolar wall levels⁴⁸. Thus, while cells contribute little to the biomechanical properties of the tissue in response to physical (e.g. deformation) or chemical (e.g. histamine challenge) stimuli over a short time period, they are responsible for the longer term maintenance as well as the remodeling of the composition and structure of the matrix.

8.2.5. Air-liquid interface and surface tension

The airways and alveoli are lined with a thin liquid film containing pulmonary surfactant which derives from type II epithelial cells. During the deflation of the lung from total lung capacity, the recoil pressure significantly decreases in fluid-filled compared to air-filled lung implying that the surface film significantly contributes to lung elasticity^{49,50}. In addition to its direct effects on recoil, the surfactant also influences lung macrophysiology by ensuring alveolar stability, and preventing collapse at low lung volume⁵¹. Among the various components of the surfactant, phospholipids and low molecular weight hydrophobic surfactant proteins play a critical role in determining its biophysical properties, and maintaining low surface tension⁵². The amount and composition of surfactant released by the type II epithelial cells into the air-liquid interface are largely determined by the dynamic stretching pattern of the lung parenchyma^{3,53,54}. The surfactant generates prestress on the alveolar ducts and by distorting their geometry, it indirectly alters the elastic properties of the associated connective tissues^{55,56}. For small deformations, similar to those that occur during normal tidal breathing, the hysteresis of the surface film is small and surface film viscoelasticity may be less important than lung tissue viscoelasticity⁵⁷. Indeed, tissue hysteresivity, defined as energy dissipation normalized by stored elastic energy per cycle⁵⁸, was found to be very similar in isolated lungs with intact surfactant and in lung tissue strips that lack air-liquid interface⁵⁹.

8.2.6. Interaction among the tissue components

Conventional histological or immunohistochemical techniques may not truly reflect the spatial orientations of different tissue components in vivo due to artifacts resulting from fixation. Recent atomic force microscopic studies have demonstrated the existence of ridges and filaments along the surface of unfixed, untreated collagen fibrils from rat tail tendon⁵⁹ which likely represent the core protein and the GAG side chains of proteoglycans, respectively. These data suggest that the organized network of proteoglycan aggregates have multiple interactions - including chemical and topological - with collagen fibril surfaces as well as with each other. Collagen may reinforce the proteoglycan/water gel and provide a safety limit against excessive stretching of the matrix. This results in a composite structure with significant load-bearing capacity over a wide range of external forces to which the lung is exposed. An additional level of structural complexity comes from the fact that the fibers of the lung parenchyma within the alveolar walls are arranged in a hexagonal-like lattice^{55,60}. By combining fluorescent imaging of the alveolar walls with

computational modeling following external deformation, it appears that interconnectedness of the alveolar wall network also contribute to parenchymal viscoelasticity⁴⁸.

8.3. MECHANICAL PROPERTIES OF THE NORMAL LUNG

8.3.1. Molecular, fibril and fiber elasticity

The structure of the lung is largely determined by the connective tissue network. The complex organization and the nonlinear mechanical properties of these tissue components lead to complex mechanical behavior. The Young's modulus of the type I collagen molecule has been estimated to be between 3 and 9 GPa^{14,61}. The elasticity of a single collagen molecule has been attributed to the existence of amino acid sequences along the triple helix that lack proline and hydroxyproline⁶². These regions are more flexible than other regions of the helix. Such variation of rigid and flexible regions likely has a significant effect on the fibril-forming ability and hence the elasticity of the fibrils. Additionally, the unfolding of thermally activated molecular kinks or “crimps” along the molecule may also contribute to molecular elasticity⁶³. The stress-strain curve of fibrils appears reasonably linear (up to 3-5% strain) with a modulus in the order of 0.5 to 5 MPa¹⁴. It is notable that the stiffness of elastin is at least 2 orders of magnitude smaller than that of collagen⁸. This is likely a result of the amorphous nature of elastin compared to the near crystalline organization of collagen fibers. Crimps also exist at the fibril and fiber level¹⁴ (Fig. 8.2).

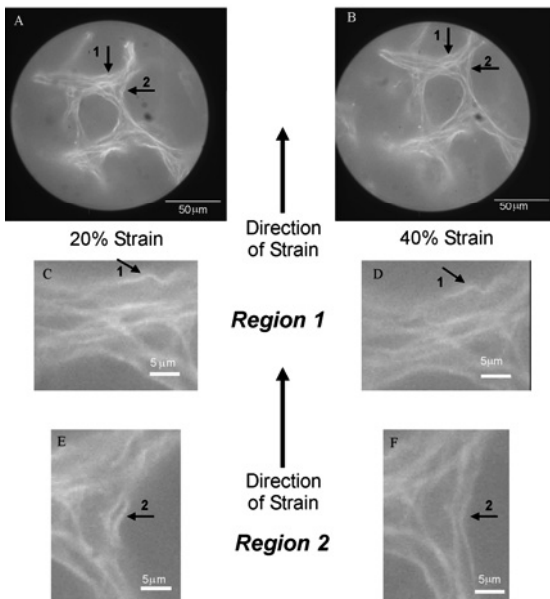


Figure 8.2. Collagen in alveolar walls at 20 (left) and 40% (right) uniaxial strain. Region 1 marks fibers perpendicular to strain, while region 2 has fibers parallel with strain. Magnified images show that fibers in region 2 unfold following strain, while those in region 1 remain wavy. (Brewer and Suki, unpublished).

When thicker fibers in the tissue are stretched, it is the crimps along the fibers that first unfold followed by an unfolding of the crimps in the fibrils⁶³. Further stretching the fibers result in stretching of the triple helices and the cross-links which also raises the possibility of slipping of molecules and fibrils within the fiber⁶⁴ (Fig. 8.3).

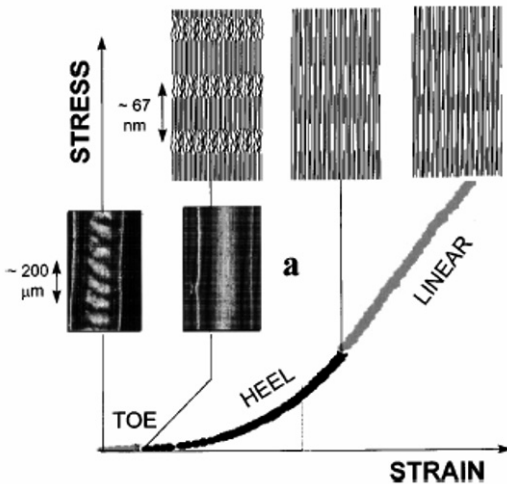


Figure 8.3. Stress-strain curve of collagen in tendon. Nonlinearity characterized by the heel region originates from the crimp (a) unfolding with stretching. (with permission from Ref. 64).

In addition to the elasticity of a single molecule, collagen fiber stiffness may depend on the number of fibrils through a given cross section, i.e. the diameter as well as the type of cross-linking between molecules and fibrils. Both increasing diameter and cross-linking tend to increase fiber stiffness in normal collagen^{14,65}. Furthermore, fibril length as well as small proteoglycan bridges between fibrils can contribute to the stiffness of collagen fibers¹⁰. The stress-strain curve of tendon composed of many fibrils arranged in parallel is nonlinear with a toe and a steep region^{66,67}. The toe region is usually attributed to the crimps along the fibrils which, upon stretching, straighten out⁶⁸ (Fig. 8.3). The composition of the fibrils and fibers is also important because fibers can contain a mixture of different collagen types. It has been argued that type I collagen is stiffer than type III⁶² implying that fiber stiffness can depend on the relative amounts of type I and type III within the fiber. Furthermore, there are notable species related differences. A small amount (5-10%) of variation in amino acid composition between bovine and equine collagen can lead to a 2-3 fold difference in elastic modulus of in vitro cross-linked collagen gels⁶⁵. All these factors can give rise to significant inter- and intra-species variability in the mechanical properties of the alveolar walls. However, as both mechanical and biochemical factors contribute to collagen production and assembly, it is likely that there are significant regional variabilities in

collagen fiber properties within a single lung. This variability is in addition to the different fiber content and mechanical properties of alveolar ducts and alveolar walls^{69,70}. The former has been argued to be stiffer and hence contribute more to lung elasticity at higher lung volume⁷¹. Such differences in local matrix stiffness may have important consequences on cell signaling as discussed below.

8.3.2. Elasticity of lung collagen, alveolar wall, tissue strip and whole lung

As shown in [Figure 8.3](#), the stress-strain curve of individual fibers may become linear once the crimps are unfolded. However, for larger lung tissue pieces and many other tissues, the stress-strain curve often exhibits exponential stiffening^{28,45,72,73}. The stress (σ) is related to the strain (ϵ) in the material for example during simple uniaxial stretching by the equation:

$$\sigma = A \epsilon \exp\{b\epsilon\} \quad (8.1)$$

where A is the amplitude of the stress-strain curve and can be related to the incremental elastic modulus near zero strain (as can be seen from a Taylor expansion of eq. (8.1)) and b is a nonlinearity parameter which is related to recruitment of fibers, i.e. the straightening of wavy fibers and perhaps folding of fibers in the direction of strain. Indeed, Maksym et al.^{74,75} showed that such behavior can be explained by the ensemble behavior of collagen fibers. They used a triangular network of line elements each containing a parallel combination of a crimped collagen and an elastin fiber. They found that the exponential nonlinearity could be explained by a power law distribution of collagen fiber properties. Based on morphometric data of collagen in the lung^{20,70}, this hypothesis may be reasonable and the distributed nature of collagen properties likely contribute to tissue elasticity. However, the collagen fibers are inside the alveolar walls which form a hexagonal-like network (Fig. 8.2). Triangular networks are inherently stable against shear or uniaxial stretching while hexagonal networks collapse under such deformations⁵⁵, and thus the model of Maksym et al.⁷⁵ may not be used to extract microscopic parameters of the tissue. The more realistic hexagonal geometry has important implications on the mechanism of alveolar wall deformation. Recently, simulations using a hexagonal network to mimic the observed deformation of the alveoli in normal, hypotonic and hypertonic solutions suggest that the folding of the alveolar wall and collagen during uniaxial stretching is elastically limited by the proteoglycan matrix¹¹. The reason is that the proteoglycans are highly sensitive to the osmolarity of the bath whereas collagen and elastin are much less sensitive. In hypertonic solution, the negatively charged proteoglycans collapse (low stiffness)

whereas in hypotonic solution they become inflated (high stiffness). Thus, the proteoglycans hinder the folding of collagen fibers into the direction of the macroscopic strain and so contribute to the elastic behavior of the tissue. A simple hexagonal model would be unable to mimic the stress-strain curve of lung tissue strip similar to that seen in [Figure 8.3](#) because such a model is unstable and angles of the hexagons collapse upon stretching and the model would show zero elasticity that is not observed (Note that a hexagonal model does not have this problem, it is stable).

Thus, a reasonable model needs to include both line element elasticity and a mechanism that hinders the collapse of angles. This can be achieved using an angular spring or bond-bending that resists the folding of two neighboring line elements. Such a model is shown in [Figure 8.4](#) for two configurations corresponding to two values of the bond-bending constant while the line element stiffness was kept constant. Notice that the minimum energy configuration of the same exact structure is very different when the bond-bending is low (left panel) or high (right panel). This means that 1) the macroscopic Poisson ratio (the negative of the axial strain normalized by the lateral strain) is significantly influenced by the mechanical interaction between collagen and proteoglycans; and 2) as shown in [Figure 8.4](#), the deformation pattern of the alveolar wall network does not follow the macroscopic deformation, i.e. it is not affine. However, by incorporating this mechanical interaction between collagen and proteoglycans into the hexagonal network model and comparing its stress-strain curve to measured data, the average absolute Young's modulus of a single alveolar wall can be calculated and it was estimated to be about 5 kPa. Furthermore, by taking into account the volume fraction of collagen fibers in the alveolar walls, a lower limit of collagen fiber stiffness in the alveolar wall was also estimated and a value of 300 kPa was obtained when tissue strips were stretched to 30% uniaxial macroscopic strain¹¹.

Figure 8.4. Nonlinearly elastic network model of lung parenchyma. Line elements are nonlinear springs and their folding is resisted by angular springs. When the angular spring (bond-bending) constant is low (a), the uniaxial stretching in the vertical direction results in large changes in angle. When the angular spring constant is high, stretching results in lengthening the line elements which is results in higher forces and hence more red color. The microscopic deformation is not affine, it does not follow the macroscopic deformation leading to significant heterogeneity both in structure and force distribution (color) which also depend on the bond-bending to line element stiffness ratio. (based on Cavalcante et al. J. Appl. Physiol. 2005). Please see the Figure on the page 269.

The elasticity of the whole lung can be described based on the quasi-static pressure-volume curve using various models that include surface tension, alveolar duct properties and constitutive equations for the lung fibers in an average alveolar duct unit^{55,56,76}. Another approach is the

distributed fiber models by Maksym and coworkers^{74,75} mentioned above that takes into account the heterogeneity of lung properties. It is likely that the stiffening behavior of the lung characterized by an exponential relation between transpulmonary pressure and lung volume similar to eq. (8.1) is related to the gradual recruitment of collagen fibers. This is a mechanism to protect the lung from failure at high lung volumes. Nevertheless, it remains difficult to directly relate any of the parameters in these models to the physico-chemical properties of collagen unless the spatial distribution of collagen and elastin⁷⁰ as well as the alveolar duct and septal geometry⁴² together with their distributed nature¹¹ are appropriately taken into account.

In summary, while the phenomenological quasi-static stress-strain curve of the lung tissue can be completely accounted for by various models, the relationship between the molecular organization of collagen and elastin fibers and the *in vivo* pressure-volume curve is not fully understood. Such a mechanistic link would obviously be valuable to better understand the pathophysiology observed in emphysema and fibrosis, two diseases in which the pressure-volume curve and hence the mechanical properties of the lung change in a manner that implies alteration in collagen elasticity.

8.4 EFFECTS OF MECHANICAL FORCES ON THE LUNG PARENCHYMA

8.4.1. Mechanical forces, cell signaling and biomechanical properties of the ECM

The lung tissue is constantly under a pre-existing tensile stress or prestress which is a result of the distension of the lung by the transpulmonary pressure. The regional distribution of the prestress is determined by the hydrostatic pressure in the pleural space and the shape of the lung^{77,78}. Additionally, prestress also changes cyclically and irregularly with breathing. This prestress in the alveolar walls is transferred through the ECM to the adhering cells with important consequences on cellular biophysics, biochemistry and phenotype⁷⁹. [Figure 8.5](#) shows lung tissue fixed in formalin and immunohistochemically labeled for types I and III collagen as well as cell nuclei. It can be seen that some nuclei appear rounded (green arrow) whereas some appear to be stretched in a direction parallel with the alveolar wall (blue arrow). This suggests that forces in the wall primarily carried by the collagen were transmitted to the nucleus.

Figure 8.5. Double-label immunohistochemistry of mouse lung tissue. The blue labels type I collagen, the brown corresponds to type III collagen and the pink is cell nucleus. It can be seen that some fibers are comprised of almost exclusively type I or type III collagen (black arrows), whereas at several locations, the two collagen types also appear to co-localize suggesting that they mix and form composite fibers (red arrow) where the color is intermediate between blue and brown. Magnification 1000. (Immunohistochemistry by E Bartolák-Suki). Please see the Figure on the page 269.

Such mechanical interactions between cells and the matrix are known to modulate cell contractility and myosin light chain phosphorylation⁸⁰, cell rheology⁸¹, focal adhesion assembly⁸², all of which are critical for control of cell adhesion, migration, growth, contractility and viability. Additionally, the mechanical properties of the ECM may influence angiogenesis⁸³, as well as connective tissue homeostasis itself⁸⁴. The direct interaction between the ECM and cellular biochemistry also has important implications for the biomechanical properties of the connective tissues.

It has been suggested by Ingber that cells in the interstitium sense mechanical forces via the integrin adhesion receptors that connect the cytoskeleton to the ECM⁸⁵. In addition to collagen, integrin receptors can also anchor to other ECM molecules such as fibronectin or laminin. However, since the collagen is the main load bearing component of the connective tissue, any prestress in the lung would likely be transferred from the collagen to the other ECM molecules. Although the exact molecular mechanisms by which this mechanotransduction occurs is not entirely clear⁸⁶, it has been found that modulation of stresses on the cell surface leads to a dynamic remodeling of focal adhesion⁸⁷. Thus, integrins serve as a mechanotransduction device and can activate various cellular processes⁷⁹ when the forces along the collagen change. For example, integrins have been shown to down regulate collagen alpha1(I) and up-regulate interstitial collagenase when fibroblasts were grown on a collagen matrix without prestress⁵. However, mechanical forces can also induce direct secretion of various growth factors that accelerate the remodeling of the matrix. For example, tensile force mediated up-regulation of the alpha1(I) procollagen gene was found to depend on the release of transforming growth factor beta (TGF- β)⁸⁸. Tensile force also appears to regulate the connective tissue growth factor that is able to stimulate extracellular protein release through a TGF- β independent pathway⁸⁹. Additionally, fibroblasts appear to respond differentially to various types of mechanical stimuli (e.g. uniaxial vs. biaxial deformation)⁹⁰. It is clear that the presence of specific types of mechanical forces and various signaling cues in the ECM jointly regulate how the cells create their microenvironment to maintain an optimal structure and biomechanical properties of an organ⁹¹. Thus, cells and the prestressed ECM live in a dynamic balance which results in a continuous remodeling of the matrix

with a rapid synthesis of collagen in the normal lung of about 10% of total collagen per day, 40% of which is immediately degraded⁹². A schematic diagram of the hierarchical transmission of mechanical stimuli from the level of the whole lung down to single cells and the various possible feedback loops controlling ECM remodeling and ultimately organ level mechanics are shown in Figure 8.6. We note however that several other important mechanisms related to the effects of mechanical forces of lung biology such as surfactant secretion³ or smooth muscle contractility^{4,80} are not considered here.

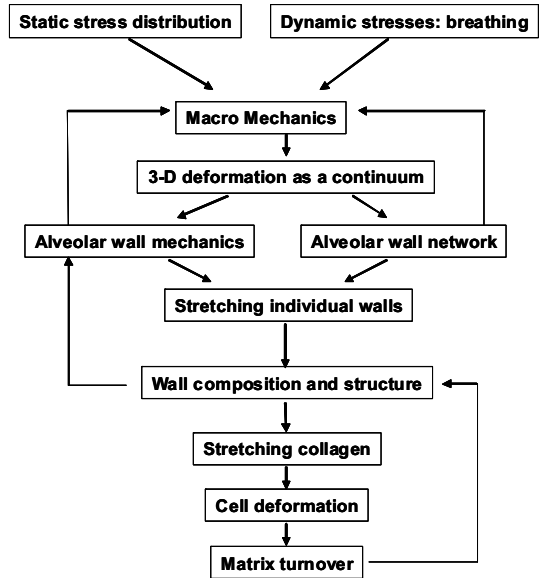


Figure 8.6. Schematic diagram of force transmission from the level of the whole lung to single cell with various feedback mechanisms influencing ECM composition and lung mechanics (with permission from Ref. 12).

8.4.2. Mechanical forces in the diseased lung

In diseases, the biochemical cues within the alveolar walls change either because of the expression of enzymes and/or cytokines or secondary to the injury that external agents such as cigarette smoke cause. The turnover half time of matrix molecules can drastically change. For example, an increased collagen mRNA expression in the lung was detected within 6 hours of elastase treatment of hamsters⁹³. In this case, matrix remodeling was directly initiated by the acute injury caused by elastase. It is conventional to think that diseases such as emphysema or fibrosis develop as a result of the changes in the biochemical microenvironment. However, as soon as the composition of the ECM is altered - either because of the direct injury or cellular remodeling - there are corresponding changes in the biomechanical properties of the matrix and consequently of the alveolar wall. Such alteration in matrix properties would lead to a change in the local deformation of the alveolar wall. The network of the alveoli

would then have to reorganize itself to satisfy the condition of mechanical equilibrium. Consequently, local prestress on the alveolar walls would change which in turn could have a feed back effect on cell signaling leading to further assembly of matrix molecules.

The possibility that mechanical forces contribute to the progression of emphysema has been put forth by West in 1971⁷⁸. He showed that the topological distribution of emphysema scores closely resembled the regional distribution of mechanical stresses in the lung due to its own weight. Consequently, he argued that mechanical forces should also contribute to the local development of tissue disease. This idea has been revisited more recently using imaging of the alveolar walls and simultaneously measuring the mechanical properties of tissue strips during uniaxial stretching⁶⁰. It was found that the alveolar walls from elastase-treated rats could break under the influence of mechanical forces akin to what would likely occur in vivo in the lung. The assumption that mechanical force contributed to tissue destruction was also consistent with Computed Tomography images⁹⁴. The breakdown of the alveolar network driven by mechanical forces has been shown to lead to significant heterogeneities at the parenchymal tissue level and it was argued that being the most important load bearing constituent of the alveolar wall, the collagen is expected to play a major role in this process⁹⁵.

At high lung volumes the collagen in the alveolar wall protects the parenchyma from rupture. Therefore, the fact that the alveolar walls in the emphysematous lung can break at strains corresponding to normal breathing suggests that the yield stress of the collagen must be weaker following the remodeling process induced by elastase treatment⁶⁰. Interestingly, in a more recent study it was reported that while the elastase treatment of mice led to a 50% increase in total collagen content of the lung, the stress at which tissue strips from these lungs failed decreased by ~50% compared to control⁹⁶. It is important to mention, however, that the mean linear intercept, a measure of alveolar airspace size, also increased. Since the number of alveolar walls that can support the stress per unit cross sectional area perpendicular to the direction of stretching is reduced, one may argue that the reduction in failure stress is simply due to the larger stress per alveolar wall in the emphysematous tissue. It has been argued, however, that the increase in mean linear intercept cannot fully explain the decrease in failure stress, especially when the collagen content per alveolar wall is increased⁹⁶. Therefore, despite increased collagen content per alveolar wall in the emphysematous lung, the wall stiffness is smaller than in healthy animals. Thus, the normal dynamic equilibrium between matrix turnover and mechanical forces is disturbed which would lead to additional feedback loops in [Figure 8.6](#). (e.g. direct injury to the alveoli leading to an alteration in matrix turnover and reduction in

collagen failure strength that ultimately results in the breakdown of alveolar wall network). Such feedback loops can represent a continuous deterioration of lung function and may offer an explanation for the progressive nature of emphysema⁹⁵. These findings are in stark contrast to the mechanics of the fibrotic lung in which total collagen content also increases but it is accompanied by an increase in stiffness^{27,97}. The conclusion is thus inescapable that following the remodeling process, the internal structural organization of the collagen fibers in the alveolar wall should be drastically different in the emphysematous and the fibrotic lung. Currently, it is unknown whether it is only the biochemical milieu that is responsible for the different matrix properties. It is possible that, as a feedback mechanism, the grossly different mechanical properties of the ECM also contribute to the different intracellular and/or extracellular assembly of the collagen. Finally, we have discussed that due to the network-like arrangement of the alveolar walls, there is a certain amount of heterogeneity of forces and corresponding mechanical properties in the lung. We can further speculate that the progression of emphysema and likely most other diseases should necessarily lead to an increasing spatial heterogeneity of tissue remodeling and biomechanical properties of the ECM because as we argued above, local changes in composition alter biomechanical properties and the distribution of mechanical forces which in turn can act as a feedback mechanism to produce additional remodeling.

8.5. SUMMARY

The connective tissue of the lung is not a static structure even during normal functioning. The tissue is the end result of a molecular hierarchical organization living in a dynamic balance between continuous breakdown and remodeling which is also modulated by mechanical forces. When this delicate dynamic balance is perturbed by external or internal chemical changes such as those occurring in a disease process or environmental stimuli, the system dynamically remodels itself by an excess or lack of producing or breaking up these large complex macromolecular structures. The result is a chemically and structurally different tissue with accordingly altered biomechanical properties. We have also argued that the changes in matrix stiffness will alter the mechanical forces on the cells which in turn may also influence the way cells remodel the interstitium. An important consequence is that a complete understanding of tissue biomechanics and lung function will not result solely from biochemical purification and biophysical study of the molecules. Connective tissues must be studied as an integrated system within their natural biochemical and mechanical environments. Additionally, to fully appreciate how diseases propagate

spatially in the tissue and how they progress with time, it will be essential to map the regional correlation between cell signaling, matrix composition and the local biomechanical properties of the tissue.

Acknowledgements

This work was supported by the National Heart, Lung, and Blood Institute Grants HL-59215.

References

1. Wirtz H.R., L.G. Dobbs, The effects of mechanical forces on lung functions. *Respir Physiol* **119**, 1-17, 2000.
2. Torday J.S., J. Sanchez-Esteban, L.P. Rubin, Paracrine mediators of mechanotransduction in lung development. *Am J Med Sci* **316**, 205-208, 1998.
3. Wirtz H.R., L.G. Dobbs, Calcium mobilization and exocytosis after one mechanical stretch of lung epithelial cells. *Science* **250**, 1266-1269, 1990.
4. Fredberg J.J., et al. Airway smooth muscle, tidal stretches, and dynamically determined contractile states. *Am J Respir Crit Care Med* **156**, 1752-1759, 1997.
5. Lambert C.A., E.P. Soudant, B.V. Nusgens, C.M. Lapiere, Pretranslational regulation of extracellular matrix macromolecules and collagenase expression in fibroblasts by mechanical forces. *Lab Invest* **66**, 444-451, 1992.
6. Breen E.C., Mechanical strain increases type I collagen expression in pulmonary fibroblasts in vitro. *J Appl Physiol* **88**, 203-209, 2000.
7. Carver W., M.L. Nagpal, M. Nachtigal, T.K. Borg, L. Terracio, Collagen expression in mechanically stimulated cardiac fibroblasts. *Circ Res* **69**, 116-122, 1991.
8. Fung Y.C., *Biomechanics: Mechanical Properties of Living Tissues*, Springer-Verlag, New York, 1993.
9. Cox G., et al. 3-dimensional imaging of collagen using second harmonic generation. *J Struct Biol* **141**, 53-62, 2003.
10. Redaelli A., et al. Possible role of decorin glycosaminoglycans in fibril to fibril force transfer in relative mature tendons--a computational study from molecular to microstructural level. *J Biomech* **36**, 1555-1569, 2003.
11. Cavalcante F.S., et al. Mechanical Interactions between Collagen and Proteoglycans: Implications for the Stability of Lung Tissue. *J Appl Physiol* **98**, 672-679, 2005.
12. Suki B., S. Ito, D. Stamenovic, K.R. Lutchen, E.P. Ingenito, Biomechanics of the lung parenchyma: critical roles of collagen and mechanical forces. *J Appl Physiol* **98**, 1892-1899, 2005.
13. Brown J.C., R. Timpl, The collagen superfamily. *Int Arch Allergy Immunol* **107**, 484-490, 1995.
14. Silver F.H., J.W. Freeman, G.P. Seehra, Collagen self-assembly and the development of tendon mechanical properties. *J Biomech* **36**, 1529-1553, 2003.
15. Leikina E., M.V. Merts, N. Kuznetsova, S. Leikin, Type I collagen is thermally unstable at body temperature. *Proc Natl Acad Sci U S A* **99**, 1314-1318, 2002.

16. Hukins D.W.L., *Connective tissue matrix*, Macmillan, London, 1984.
17. Hulmes D.J., T.J. Wess, D.J. Prockop, P. Fratzl, Radial packing, order, and disorder in collagen fibrils. *Biophys J* **68**, 1661-1670, 1995.
18. Raspanti M., A. Alessandrini, V. Ottani, A. Ruggeri, Direct visualization of collagen-bound proteoglycans by tapping-mode atomic force microscopy. *J Struct Biol* **119**, 118-122, 1997.
19. Holmes D.F., et al. Corneal collagen fibril structure in three dimensions: Structural insights into fibril assembly, mechanical properties, and tissue organization. *Proc Natl Acad Sci U S A* **98**, 7307-7312, 2001.
20. Sobin S.S., Y.C. Fung, H.M. Tremer, Collagen and elastin fibers in human pulmonary alveolar walls. *J Appl Physiol* **64**, 1659-1675, 1988.
21. Suki B., Fluctuations and power laws in pulmonary physiology. *Am J Respir Crit Care Med* **166**, 133-137, 2002.
22. Bates J.H., G.N. Maksym, D. Navajas, B. Suki, Lung tissue rheology and 1/f noise. *Ann Biomed Eng* **22**, 674-681, 1994.
23. Suki B., A.L. Barabasi, K.R. Lutchen, Lung tissue viscoelasticity: a mathematical framework and its molecular basis. *J Appl Physiol* **76**, 2749-2759, 1994.
24. Weibel E., J. Gil, in *Lung biology in health and disease*; v. **3**, 1-81, M. Dekker, New York, 1977.
25. Tanaka R., R. Al-Jamal, M.S. Ludwig, Maturational changes in extracellular matrix and lung tissue mechanics. *J Appl Physiol* **91**, 2314-2321, 2001.
26. Tanaka R., M.S. Ludwig, Changes in viscoelastic properties of rat lung parenchymal strips with maturation. *J Appl Physiol* **87**, 2081-2089, 1999.
27. Dolnikoff M., T. Mauad, M.S. Ludwig, Extracellular matrix and oscillatory mechanics of rat lung parenchyma in bleomycin-induced fibrosis. *Am J Respir Crit Care Med* **160**, 1750-1757, 1999.
28. Yuan H., et al. Effects of collagenase and elastase on the mechanical properties of lung tissue strips. *J Appl Physiol* **89**, 3-14, 2000.
29. Reinhardt D.P., et al. Fibrillin-1 and fibulin-2 interact and are colocalized in some tissues. *J Biol Chem* **271**, 19489-19496, 1996.
30. Thurmond F., J. Trotter, Morphology and biomechanics of the microfibrillar network of sea cucumber dermis. *J Exp Biol* **199**, 1817-1828, 1996.
31. Sherebrin M.H., S.H. Song, M.R. Roach, Mechanical anisotropy of purified elastin from the thoracic aorta of dog and sheep. *Can J Physiol Pharmacol* **61**, 539-545, 1983.
32. Sherratt M.J., et al. Fibrillin microfibrils are stiff reinforcing fibres in compliant tissues. *J Mol Biol* **332**, 183-193, 2003.
33. Kozel B.A., H. Wachi, E.C. Davis, R.P. Mecham, Domains in tropoelastin that mediate elastin deposition in vitro and in vivo. *J Biol Chem* **278**, 18491-18498, 2003.
34. Brown R.E., J.P. Butler, R.A. Rogers, D.E. Leith, Mechanical connections between elastin and collagen. *Connect Tissue Res* **30**, 295-308, 1994.
35. Kiely C.M., M.J. Sherratt, C.A. Shuttleworth, Elastic fibres. *J Cell Sci* **115**, 2817-1828, 2002.
36. Setnikar I., Origin and significance of the mechanical property of the lung. *Arch Fisiol* **55**, 349-374, 1955.

37. Juul S.E., M.G. Kinsella, T.N. Wight, W.A. Hodson, Alterations in nonhuman primate *M. nemestrina* lung proteoglycans during normal development and acute hyaline membrane disease. *Am J Respir Cell Mol Biol* **8**, 299-310, 1993.
38. Buckwalter J.A., L.C. Rosenberg, Electron microscopic studies of cartilage proteoglycans. Direct evidence for the variable length of the chondroitin sulfate-rich region of proteoglycan subunit core protein. *J Biol Chem* **257**, 9830-9839, 1982.
39. Scott J.E., Supramolecular organization of extracellular matrix glycosaminoglycans, in vitro and in the tissues. *Faseb J* **6**, 2639-2645, 1992.
40. Fratzl P., A. Daxer, Structural transformation of collagen fibrils in corneal stroma during drying. An x-ray scattering study. *Biophys J* **64**, 1210-1214, 1993.
41. Al Jamal R., P.J. Roughley, M.S. Ludwig, Effect of glycosaminoglycan degradation on lung tissue viscoelasticity. *Am J Physiol Lung Cell Mol Physiol* **280**, L306-315, 2001.
42. Weibel E., in: *Handbook of Physiology*, J. Mead (ed.), Am. Physio. Soc., Bethesda, pp. 89-110, 1986.
43. Dolhnikoff M., J. Morin, M.S. Ludwig, Human lung parenchyma responds to contractile stimulation. *Am J Respir Crit Care Med* **158**, 1607-1612, 1998.
44. Fredberg J.J., D. Bunk, E. Ingenito, S.A. Shore, Tissue resistance and the contractile state of lung parenchyma. *J Appl Physiol* **74**, 1387-1397, 1993.
45. Navajas D., G.N. Maksym, J.H. Bates, Dynamic viscoelastic nonlinearity of lung parenchymal tissue. *J Appl Physiol* **79**, 348-356, 1995.
46. Salerno F.G., M. Dallaire, M.S. Ludwig, Does the anatomic makeup of parenchymal lung strips affect oscillatory mechanics during induced constriction? *J Appl Physiol* **79**, 66-72, 1995.
47. Yuan H., E.P. Ingenito, B. Suki, Dynamic properties of lung parenchyma: mechanical contributions of fiber network and interstitial cells. *J Appl Physiol* **83**, 1420-1431; discussion 1418-1419, 1997.
48. Brewer K.K., et al. Lung and alveolar wall elastic and hysteretic behavior in rats: effects of in vivo elastase treatment. *J Appl Physiol* **95**, 1926-1936, 2003.
49. Bachofen H., J. Hildebrandt, M. Bachofen, Pressure-volume curves of air- and liquid-filled excised lungs-surface tension in situ. *J Appl Physiol* **29**, 422-431, 1970.
50. Gil J., H. Bachofen, P. Gehr, E.R. Weibel, Alveolar volume-surface area relation in air- and saline-filled lungs fixed by vascular perfusion. *J Appl Physiol* **47**, 990-1001, 1979.
51. Avery M.E., J. Mead, Surface properties in relation to atelectasis and hyaline membrane disease. *AMA J Dis Child* **97**, 517-523, 1959.
52. Ingenito E.P., et al. Biophysical characterization and modeling of lung surfactant components. *J Appl Physiol* **86**, 1702-1714, 1999.
53. Arold S.P., B. Suki, A.M. Alencar, K.R. Lutchen, E.P. Ingenito, Variable ventilation induces endogenous surfactant release in normal guinea pigs. *Am J Physiol Lung Cell Mol Physiol* **285**, L370-375, 2003.
54. Nicholas T.E., H.A. Barr, Control of release of surfactant phospholipids in the isolated perfused rat lung. *J Appl Physiol* **51**, 90-98, 1981.
55. Stamenovic D., Micromechanical foundations of pulmonary elasticity. *Physiol Rev* **70**, 1117-1134, 1990.

56. Wilson T.A., H. Bachofen, A model for mechanical structure of the alveolar duct. *J Appl Physiol* **52**, 1064-1070, 1982.
57. Schurch S., H. Bachofen, J. Goerke, F. Green, Surface properties of rat pulmonary surfactant studied with the captive bubble method: adsorption, hysteresis, stability. *Biochim Biophys Acta* **1103**, 127-136, 1992.
58. Fredberg J.J., D. Stamenovic, On the imperfect elasticity of lung tissue. *J Appl Physiol* **67**, 2408-2419, 1989.
59. Sakai H., et al. Hysteresivity of the lung and tissue strip in the normal rat: effects of heterogeneities. *J Appl Physiol* **91**, 737-747, 2001.
60. Kononov S., et al. Roles of mechanical forces and collagen failure in the development of elastase-induced emphysema. *Am J Respir Crit Care Med* **164**, 1920-1926, 2001.
61. Sasaki N., S. Odajima, Stress-strain curve and Young's modulus of a collagen molecule as determined by the X-ray diffraction technique. *J Biomech* **29**, 655-658, 1996.
62. Silver F.H., I. Horvath, D.J. Foran, Mechanical implications of the domain structure of fiber-forming collagens: comparison of the molecular and fibrillar flexibilities of the alpha-chains found in types I-III collagen. *J Theor Biol* **216**, 243-254, 2002.
63. Misof K., G. Rapp, P. Fratzl, A new molecular model for collagen elasticity based on synchrotron X-ray scattering evidence. *Biophys J* **72**, 1376-1381, 1997.
64. Fratzl P., et al. Fibrillar structure and mechanical properties of collagen. *J Struct Biol* **122**, 119-122, 1998.
65. Angele P., et al. Influence of different collagen species on physico-chemical properties of crosslinked collagen matrices. *Biomaterials* **25**, 2831-2841, 2004.
66. Sasaki N., S. Odajima, Elongation mechanism of collagen fibrils and force-strain relations of tendon at each level of structural hierarchy. *J Biomech* **29**, 1131-1136, 1996.
67. Stromberg D.D., C.A. Wiederhielm, Viscoelastic description of a collagenous tissue in simple elongation. *J Appl Physiol* **26**, 857-862, 1969.
68. Giraud-Guille M.M., L. Besseau, Banded patterns in liquid crystalline phases of type I collagen: relationship with crimp morphology in connective tissue architecture. *Connect Tissue Res* **37**, 183-193, 1998.
69. Denny E., R.C. Schroter, Relationships between alveolar size and fibre distribution in a mammalian lung alveolar duct model. *J Biomech Eng* **119**, 289-297, 1997.
70. Mercer R.R., J.D. Crapo, Spatial distribution of collagen and elastin fibers in the lungs. *J Appl Physiol* **69**, 756-765, 1990.
71. Mercer R.R., J.M. Laco, J.D. Crapo, Three-dimensional reconstruction of alveoli in the rat lung for pressure-volume relationships. *J Appl Physiol* **62**, 1480-1487, 1987.
72. Fukaya H., C.J. Martin, A.C. Young, S. Katsura, Mechanical properties of alveolar walls. *J Appl Physiol* **25**, 689-695, 1968.
73. Mijailovich S.M., D. Stamenovic, R. Brown, D.E. Leith, J.J. Fredberg, Dynamic moduli of rabbit lung tissue and pigeon ligamentum propatagiale undergoing uniaxial cyclic loading. *J Appl Physiol* **76**, 773-782, 1994.

74. Maksym G.N., J.H. Bates, A distributed nonlinear model of lung tissue elasticity. *J Appl Physiol* **82**, 32-41, 1997.
75. Maksym G.N., J.J. Fredberg, J.H. Bates, Force heterogeneity in a two-dimensional network model of lung tissue elasticity. *J Appl Physiol* **85**, 1223-1229, 1998.
76. Denny E., R.C. Schroter, The mechanical behavior of a mammalian lung alveolar duct model. *J Biomech Eng* **117**, 254-261, 1995.
77. Hubmayr R.D., Perspective on lung injury and recruitment: a skeptical look at the opening and collapse story. *Am J Respir Crit Care Med* **165**, 1647-1653, 2002.
78. West J.B., Distribution of mechanical stress in the lung, a possible factor in localisation of pulmonary disease. *Lancet* **1**, 839-841, 1971.
79. Giancotti F.G., E. Ruoslahti, Integrin signaling. *Science* **285**, 1028-1032, 1999.
80. Polte T.R., G.S. Eichler, N. Wang, D.E. Ingber, Extracellular matrix controls myosin light chain phosphorylation and cell contractility through modulation of cell shape and cytoskeletal prestress. *Am J Physiol Cell Physiol* **286**, C518-528, 2004.
81. Rosenblatt N., S. Hu, J. Chen, N. Wang, D. Stamenovic, Distending stress of the cytoskeleton is a key determinant of cell rheological behavior. *Biochem Biophys Res Commun* **321**, 617-622, 2004.
82. Chen C.S., J.L. Alonso, E. Ostuni, G.M. Whitesides, D.E. Ingber, Cell shape provides global control of focal adhesion assembly. *Biochem Biophys Res Commun* **307**, 355-361, 2003.
83. Ingber D.E., Mechanical signaling and the cellular response to extracellular matrix in angiogenesis and cardiovascular physiology. *Circ Res* **91**, 877-887, 2002.
84. Chiquet M., A.S. Renedo, F. Huber, M. Fluck, How do fibroblasts translate mechanical signals into changes in extracellular matrix production? *Matrix Biol* **22**, 73-80, 2003.
85. Ingber D., Integrins as mechanochemical transducers. *Curr Opin Cell Biol* **3**, 841-848, 1991.
86. Shyy J.Y., S. Chien, Role of integrins in endothelial mechanosensing of shear stress. *Circ Res* **91**, 769-775, 2002.
87. Davies P.F., C. Shi, N. Depaola, B.P. Helmke, D.C. Polacek, Hemodynamics and the focal origin of atherosclerosis: a spatial approach to endothelial structure, gene expression, and function. *Ann N Y Acad Sci* **947**, 7-16; discussion 16-17, 2001.
88. Gutierrez J.A., H.A. Perr, Mechanical stretch modulates TGF-beta1 and alpha1I collagen expression in fetal human intestinal smooth muscle cells. *Am J Physiol* **277**, G1074-1080, 1999.
89. Schild C., B. Trueb, Mechanical stress is required for high-level expression of connective tissue growth factor. *Exp Cell Res* **274**, 83-91, 2002.
90. Berry C.C., C. Cacou, D.A. Lee, D.L. Bader, J.C. Shelton, Dermal fibroblasts respond to mechanical conditioning in a strain profile dependent manner. *Biorheology* **40**, 337-345, 2003.

91. Huiskes R., R. Ruimerman, G.H. van Lenthe, J.D. Janssen, Effects of mechanical forces on maintenance and adaptation of form in trabecular bone. *Nature* **405**, 704-706, 2000.
92. McAnulty R.J., G.J. Laurent, Collagen synthesis and degradation in vivo. Evidence for rapid rates of collagen turnover with extensive degradation of newly synthesized collagen in tissues of the adult rat. *Coll Relat Res* **7**, 93-104, 1987.
93. Lucey E.C., R.H. Goldstein, P.J. Stone, G.L. Snider, Remodeling of alveolar walls after elastase treatment of hamsters. Results of elastin and collagen mRNA in situ hybridization. *Am J Respir Crit Care Med* **158**, 555-564, 1998.
94. Mishima M., et al. Complexity of terminal airspace geometry assessed by lung computed tomography in normal subjects and patients with chronic obstructive pulmonary disease. *Proc Natl Acad Sci U S A* **96**, 8829-8834, 1999.
95. Suki B., K.R. Lutchen, E.P. Ingenito, On the progressive nature of emphysema: roles of proteases, inflammation, and mechanical forces. *Am J Respir Crit Care Med* **168**:516-521, 2003.
96. Ito S., et al. Tissue heterogeneity in the mouse lung: effects of elastase treatment. *J Appl Physiol* **97**, 204-212, 2004.
97. Goldstein R.H., E.C. Lucey, C. Franzblau, G.L. Snider, Failure of mechanical properties to parallel changes in lung connective tissue composition in bleomycin-induced pulmonary fibrosis in hamsters. *Am Rev Respir Dis* **120**, 67-73, 1979.

ENZYME SIGNALING: IMPLICATIONS FOR TISSUE ENGINEERING

Erzsébet Bartolák-Suki*

“Tissue engineering/regenerative medicine is an emerging multidisciplinary field involving biology, medicine, and engineering to improve the health and quality of life by restoring, maintaining, or enhancing tissue and organ function. In addition to having a therapeutic application, tissue engineering can have diagnostic applications.” NIH.

In recent years, the development and ongoing process of this multidisciplinary approach led to the ability to perform tissue and organ replacement resulting in the improvement of health care.

Generally speaking, nothing in nature lives in a complete isolation without some form of interaction with the environment. This is particularly important for engineered materials including biomaterials, single cells, or transplanted whole organs of artificial or native origin. The broad variety of interactions ranging from mechanical (pressure, tension, shear stress), through chemical-molecular (covalent bonds, ionic bonds, hydrogen bonds, Van der Waals bonds) to inter-cellular (cell-to-cell signaling, or cell-to-extracellular matrix, ECM signalling through receptors), play important roles in creating such devices or tissue substitutes. The large accumulated knowledge that has allowed the advancement and development of appropriate biological tissue substitutes or biomaterials has emerged mostly from studies characterizing the basic mechanisms of cell-ECM interactions during development or remodelling such as wound healing.

This chapter will discuss some of the basic principles of how cells communicate by means of extracellular signaling molecules with special

* CelluTraf Sci, Boston, MA, USA.

emphasis on enzyme function. Particular attention will be paid to a relatively recent discovery of a new form of signalling by protease enzymes. Examples of certain key events during signaling such as proliferation, differentiation and cell death as the result of the interaction among cells, ECM and enzyme containing biomaterials will be presented with relevance to tissue engineering.

9.1. INTRODUCTION

Cells communicate with their neighbours and their environment by sending and receiving information in the form of chemical **signals**¹. The signaling molecules operate over various distances: endocrine signaling acts on distant target cells, paracrine signaling affects adjacent target cells whereas in autocrine signaling the target sites are on the same cells. Often, these signals, also called ligands, are sensed by receptors on the cell surface, but some ligands can also bind to intracellular receptors (e.g., cytosolic receptors or nuclear receptors). Once the ligands are captured by their receptors, the extra cellular signals converted into intracellular **second messenger** signals that ultimately make the cells to respond by for example dividing, moving, differentiating or even triggering programmed cell death. The external signals may activate a cell through **enzyme-related receptors** (tyrosine kinase-linked receptors for interferons and erythropoietins or receptors with intrinsic enzymatic activity: intrinsic tyrosine kinase activity of NGF, PDGF receptors), G-protein coupled receptors (for serotonin, glucagon, epinephrine) or ion channels (activated by acetylcholine, GABA). When the receptor sensing signal is a catalyst such as an enzyme, the response can be substantially amplified. Thus, cell signaling governs and coordinates cell actions. Errors in cell signaling can lead to serious diseases including atherosclerosis, diabetes, cancer, immune diseases, etc. Thus, by understanding cell signaling, we will have a better chance to treat these diseases.

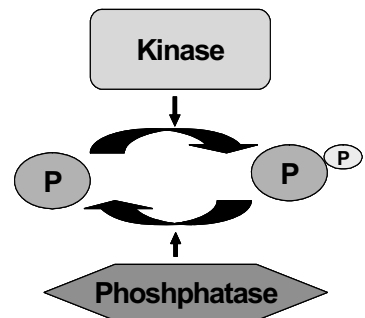
There is much information in the literature on special signaling events and to different depth. This chapter will focus in more detail on a special form of extracellular signaling by enzymes such as proteinases (serine or serine-threonin proteinases) and, in more depth, by metalloproteinases (MMPs) including their activation and inactivation.

9.2. GENERAL PROPERTIES OF ENZYMES

Enzymes are proteins and they accelerate and hence catalyze chemical reactions². In cells, almost all processes need enzymes to lower the activation energy of a reaction in order to occur at significant rates. One of the salient features of an enzyme is that it is selectively specific to its reactions to be catalyzed and it has high fidelity to the choice of substrate. This specificity is accomplished by the complementary shape and by the charge and hydrophilic/hydrophobic characteristics of the enzyme and its substrate resulting in chemoselectivity, regioselectivity and stereospecificity. Enzyme activity can be affected by other molecules such as **inhibitors** to block or decrease its activity or **activators** to increase its activity³. It is interesting to note that many drugs and poisons are enzyme inhibitors. Temperature, chemical environment such as pH and substrate concentration also influence enzyme activity among other factors. When designing biomaterials, all of these factors have to be considered.

Enzymes serve a wide variety of functions in living organisms. Perhaps the most well known is their function in **metabolism**⁴. A perfect example is how they chew food throughout the digestive system. However, enzymes do have other important functions and can not be substituted in **signal transduction**^{1,5}. Cells respond to external cues using a limited number but spatially and temporally well organized **signaling pathways** involving multiple interacting cascades to initiate signal propagation. One of the best studied example is the activation of epidermal growth factor receptor (EGFR)⁶, a tyrosine kinase receptor (RTK) by epidermal growth factor (EGF) initiating the cascade of phospholipase C- γ (PLC γ), phosphatidylinositol 3-kinase (PI3K)-AKT/protein kinase B (PKB) and extracellular signal-regulated kinase (ERK)/mitogen activated kinase (MAPK) pathways. The complexity of the individual components in signaling pathways masks the more universal motifs of cell signaling networks using kinases and phosphatases as shown in [Figures 9.1](#) and [9.2](#).

Figure 9.1. One site phosphorylation-dephosphorylation cycle. The “One site phosphorylation-dephosphorylation cycle” uses a pair of enzymes to activate-deactivate a protein. A typical example is the functionally reciprocal kinases-phosphatases but others such as the small GTPase Switch Proteins (e.g., Ras) alone serve as the activator-deactivator through GTP-GDP.



In the **one site phosphorylation cycle** (Fig. 9.1), the protein (P) is phosphorylated by a kinase to yield the phosphorylated (activated) form of protein (P^P), which is dephosphorylated by an opposing phosphatase. In the **cascade cycles**, if P is an enzyme and activated, the phosphorylated protein P^P becomes the kinase in the next cycle (Fig. 9.2). P^P1 is the kinase in cycle 2 and P^P2 is the kinase in cycle 3. Negative or positive feedbacks are regulators of the reaction as shown in the figure.

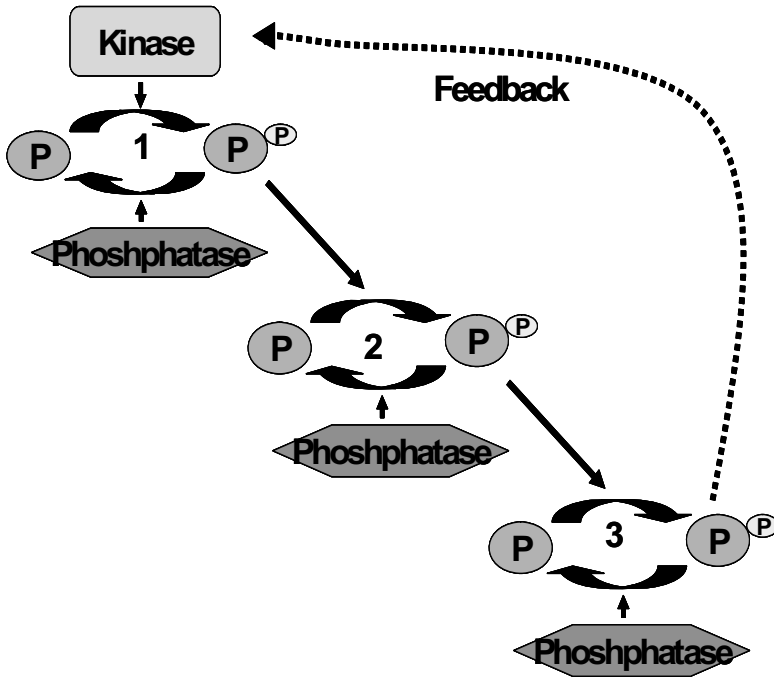


Figure 9.2. Cascade activation cycle. The cascade cycle consists of interconnected “one site cycles” where the phosphorylated substrate protein itself is an enzyme, which becomes the kinase in the next cycle. An example of the cascade activation cycle is the Receptor Tyrosine Kinase (RTK)/Ras GTPase/MAP kinase (MAPK) signaling pathway which is used repeatedly during development to control many different biological processes.

It is well understood that life could not exist without enzymes. Besides their broad range of functions as metabolic enzymes or second messengers, they can also act as signaling molecules in a special manner, while utilizing their fundamental properties. **Matrix metalloproteinases, MMPs**, and other type of proteinases (serine or serine-threonin proteinases) can act as “unconventional ligands” in signal activation. These enzymes can liberate “real” ligands like TGF β , EGF, IGF from their ECM or cell surface storage⁷⁻⁹ and hence initiate or increase their signaling or by

cleaving them can block or silence their effect. This type of activation, called transactivation, can also be achieved by the cleavage of the receptor itself like in the case of IGFR by trypsin or tryptase¹⁰. **Receptor shedding** occurs when an enzyme or enzymes cleave a receptor and prevents it from activation by its signaling ligand as in the case of growth hormone receptor (GHR)¹¹. The tumor necrosis factor- α - converting enzyme (TACE) also known as ADAM17 (metalloproteinase) cleaves the GHBP (GH binding protein) from GHR and subsequently the γ -secretase pinches off the carboxyl terminus of the truncated GHR. Besides preventing the receptor from activation, the released GHBP act as competitive antagonist for other GHRs; on the other hand, the free cytoplasmic carboxyl-terminal peptide can serve as a transcription factor. Recently, a new form of receptors was discovered called **protease activated receptors (PARs)**¹². The four family members of PARs are G-protein coupled receptors that are normally activated by proteolytic exposure of an occult tethered ligand. The PAR1, 3, and 4 are activated by thrombin and PAR2 is activated by trypsin, tryptase and Factor Xa. These receptors can also transactivate each other, such as PAR1 by PAR1 or PAR2 by PAR1. Endocytosis and subsequent lysosomal degradation are major processes in their inactivation.

9.3. METALLOPROTEINASES IN SIGNALING

MMPs are capable of degrading all kinds of ECM proteins as well as a number of bioactive molecules. They are known to be involved in the cleavage of cell surface receptors modulating their action, in the release and activation/inactivation of cytokines or chemokines and even in the release of apoptotic ligands such as FAS¹³. Among the many biological effects, MMPs influence various cell behaviors such as migration, proliferation, differentiation and cell death. These broad ranges of physiologic and pathologic roles make the MMPs ideal candidates for scientists from many fields to develop compounds in order to enhance or inhibit their function.

9.3.1. MMPs in diseases

In cancer research, there is a considerable interest in the cell types responsible for producing MMPs¹⁴. It is important to note that most MMPs in tumors are produced by the stromal cells rather than the cancer cells. However, cancer cells are producing Extracellular Matrix Metalloproteinase Inducer (EMMPRIN)¹⁵ and stimulate fibroblasts through direct cell contact to produce MMP1, 2, 3 and MMP14. The tissue inhibitors of MMPs, TIMP1 and TIMP2^{16,17}, are also expressed in increased levels in malignant stromal cells. MMP2 and MMP9 cleave a major protein com-

ponent of the basement membranes, the type IV collagen¹⁸. The breakdown of the basement membrane in turn makes the propagation of malignant cells easier. The membrane type (MT-MMP) MMP14 and MMP1 have also been implicated in enhancing cancer cell migration^{19,20}. Another important consequence of the cleavage of collagen type IV is that it exposes a cryptic site with affinity for the $\alpha v\beta 3$ integrin, a transmembrane adhesion receptor, and subsequently leads to the enhancement of angiogenesis²¹. However, other MMPs such as the MMP12, the macrophage-derived metalloelastase, generate angiostatin by the cleavage of plasminogen, a powerful inhibitor of tumor angiogenesis²². It is clear from the above examples that these multi purpose proteinases can have cancer enhancement effects, as well as anti tumor effects. On one hand, in cancer, the increased levels of growth factors (FGF, EGF and IGF) released from the cell surface by MMPs enhance cell proliferation; on the other hand, release and activation of ECM stored TGF β can lead to the inhibition of cell proliferation. Therefore, these signaling events indicate that MMPs are capable of inducing both positive and negative effects during carcinogenesis.

Just like in cancer research, there has been a long-standing interest in identifying the roles of MMPs in cardiovascular diseases²³⁻²⁵. Numerous studies have demonstrated increased levels of MMPs, especially MMP2 and MMP9, in atherosclerosis as well as aneurysm formation. Again, the degradation of ECM within the atherosclerotic plaque and plaque rupture point to the importance of MMP activation.

It is also of note that MMPs play important roles in the pathogenesis in many other clinical conditions including inflammatory diseases such as rheumatoid and osteoarthritis or various lung diseases such as asthma, cystic fibrosis, bronchiectasis and acute respiratory distress syndrome, or skin conditions including ulcer.

9.3.2. Types and Structure of MMPs

MMPs are zinc dependent endopeptidases and belong to the metzincin superfamily of proteases²⁶. The metzincins contain a highly conserved motif with three histidines (HExGHHxxGxxH) that bind to zinc at the catalytic site. The prodomain of MMPs at the C-terminal portion contain the other conserved motif with a cysteine residue (PRCGxPD) which also binds to the zinc preventing enzyme activation. The MMPs with astacins, serraly-sins and adamalysins form the four multi-gene families of metzincins.

Since the first member, MMP1 was discovered four decade ago by Jerome Gross and Charles Lapiere, more than 20 related zinc-dependent enzymes have been described in the MMP family²⁷. These enzymes based on the order of discovery have a name as a numbering system as well as has a descriptive name based on the preferred substrate.

The MMPs share three common domains in their structure: the pro-peptide, the catalytic domain and the haemopexin-like C-terminal domain. MMPs are synthesized with the pro-peptide domain to prevent early activation by occupying the active site zinc in the catalytic domain. The hinge region links the catalytic and haemopexin domains. The C-terminal domain determines substrate specificity and is the site for interaction with TIMP's. MMP7 is the smallest lacking the haemopexin domain. Additional structural domains lead to membrane type MMPs containing an additional 20 amino acid transmembrane domain and a small cytoplasmic domain (MMP14, MMP15, MMP16 and MMP24) or a glycosylphosphatidyl inositol linkage which attaches these proteins to the cell surface (MMP17 and MMP25). MMP2 and MMP9 contain fibronectin-like domains. Some MMPs have a prohormone convertase cleavage site (Furin-like) in their pro-peptide domain including MMP-23A and MMP-23B. The following panel below represents the structural similarity as well as the heterogeneity of MMPs (Fig. 9.3).

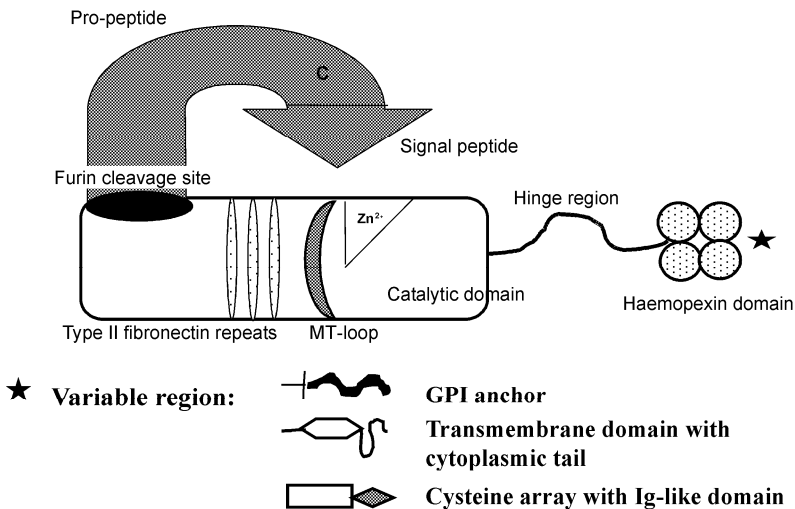


Figure 9.3. Structural similarity and the heterogeneity of MMPs. MMPs share several common domains in their structure including a pro-peptide domain, a catalytic domain, a hinge region and a haemopexin-like C-terminal domain. Additional structural domains are a transmembrane domain and a small cytoplasmic domain or a glycosyl-phosphatidyl inositol linkage that attaches some MMPs to the cell surface. MMP2 and MMP9 contain fibronectin-like domains too. Some MMPs have a prohormone convertase cleavage site (Furin-like) in their pro-peptide domain.

The **Figure 9.4** summarizes the classification of MMPs into further subgroups. This classification is based on the variable region such as GPI anchor, transmembrane domain with a cytoplasmic tail or a cysteine array. The fibronectin repeats and furin cleavage site are also used in the classification (**Fig. 9.4**).

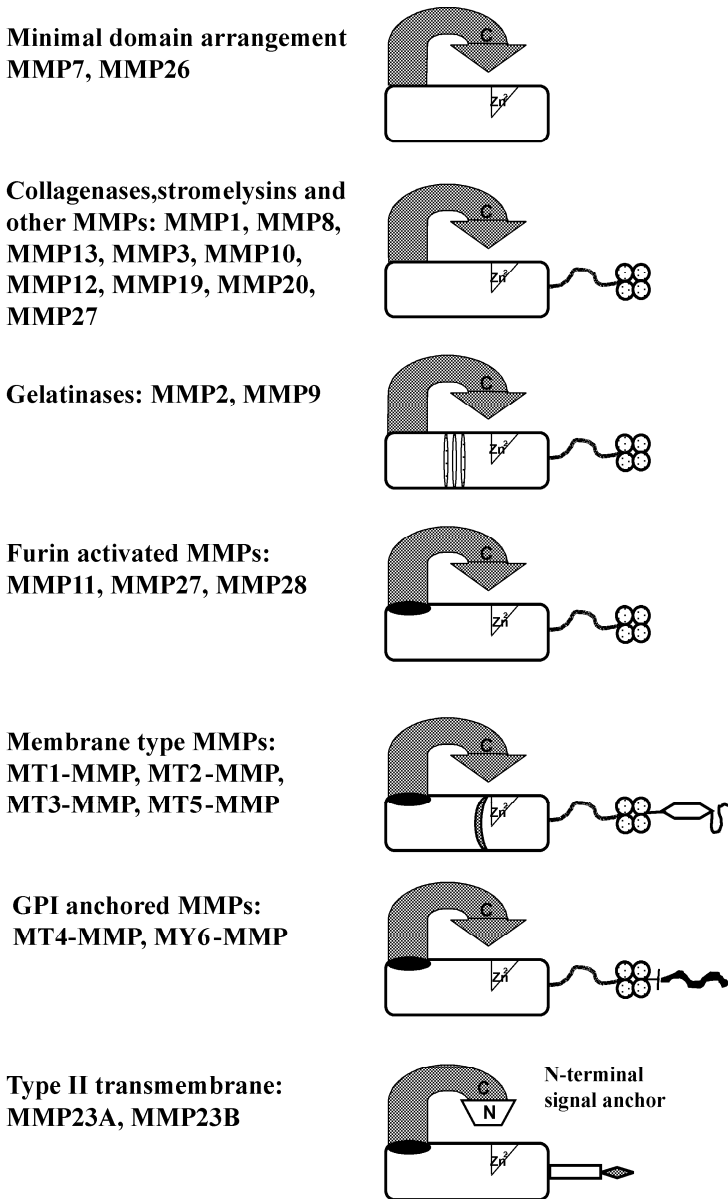


Figure 9.4. Classification of MMPs into further subgroups. This panel is a schematic representation of the subgroups. This classification is based on the variable regions of MMPs such as the GPI anchor, the transmembrane domain with a cytoplasmic tail or the cysteine array. The fibronectin repeats and the furin cleavage site are also used in the classification.

9.3.3. Activation and inhibition of MMPs

Most MMPs are secreted as inactive proenzymes and are subsequently activated most likely nearby the plasma membrane by other MMPs or by serine proteinases such as plasmin (Fig. 9.5)²⁸. The *in vivo* activation of MMPs is under tight control at several levels^{29,30}. At the transcriptional level, their amount (which is very low) is tightly regulated positively or negatively by a reciprocal feedback loop through growth factors and cytokines such as growth factors (EGF, HGF, TGF β), interleukins (IL-1, IL-6) or TNF α . Post-transcriptionally, MMP activity is restricted by the latency through the propeptide. MMPs that contain furin-like recognition domains in their propeptides (MMP11, MT-MMPs and MMP28) can be activated in the trans-Golgi network by some serine proteases such as subtilisin. The activation of secreted MMPs depends on the disruption of the prodomain – catalytic domain interaction, which may occur by proteolytic removal of the propeptide or conformational changes. The MT-MMPs which are anchored to the cell membrane by their C-terminal transmembrane domain or by a glycosylphosphatidylinositol anchor, also play major roles in the activation processes of several non-membrane anchored MMPs. The catalytic activity of MMPs is specifically inhibited by the tissue inhibitors of MMPs (TIMPs). The inter-functional relationship among those molecules are the best known for gelatinase A (MMP-2) and B (MMP-9) which are mostly present as latent enzymes complexed to their specific inhibitor, TIMP-2 and TIMP-1, respectively.

The activation of MMP-2, the most understood one among the MMPs, involves ternary interactions^{31,32}. The C terminal domains of MMP-2 and TIMP-2 form a heterodimeric pro-MMP-2/TIMP-2 complex. Binding of the N-terminal part of TIMP-2 of this complex to the catalytic site of MT1-MMP localizes the pro-MMP2 to the cell surface, allowing its activation by a neighboring MT1-MMP. The control of pericellular activation of MMPs requires tight regulation by local activation or silencing. The catalytic activity of MMP-2, MMP-9 as well as MT1-MMP is inhibited by the membrane associated glycoprotein, RECK^{33,34}. The other form of the silencing mechanism of MMPs involves a less understood general clearance mechanism, endocytosis by binding to the low density lipoprotein receptor related protein (LRP)³⁵. From the description above, it is clear that the activation and inhibition processes are highly regulated and interconnected. It is likely that there are still many other activation pathways to be discovered.

Activation and inhibition of MMPs

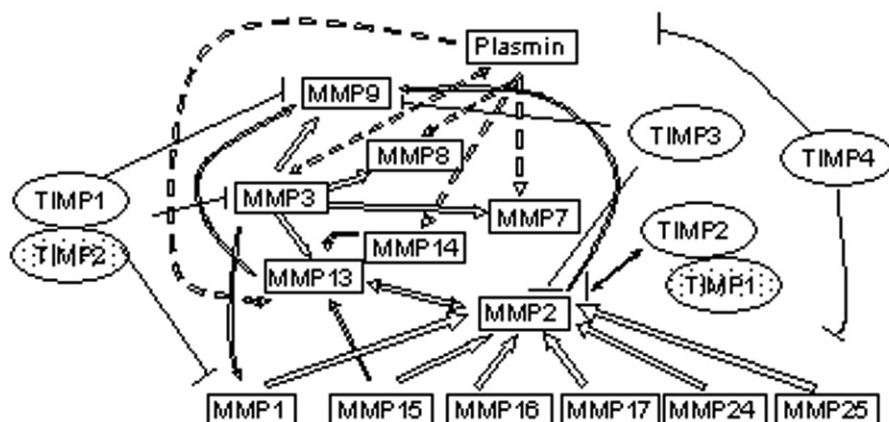


Figure 9.5. MMP activation and inactivation. This panel summarizes the known activation of MMPs by other MMPs (solid arrows) and by a serine protease, plasmin (dashed arrows). The inhibition of TIMPs is also shown (strong inhibitors are in solid ovals and weaker inhibitors are in dotted ovals). Note, that TIMP2 has a bi-functional role on MMP2: the MT1- MMP mediated proMMP2 activation requires some TIMP2 (black double headed arrow) to make the activation process happen, whereas a greater concentration of TIMP2 inhibits MMP2. The TIMP4 is an inhibitor of all MMPs without any preference.

9.3.4. Pharmacological manipulations of MMPs

In the previous section, we introduced the clinical importance and relevance of MMPs. Scientists from many fields together with clinicians have attempted to develop inhibitors for MMPs and some even reached the level of clinical trial with more or less success³⁶⁻³⁹.

The synthetic inhibitors generally contain a chelating group which binds tightly to the catalytic zinc atom preventing MMP activation. Commonly used chelating groups include hydroxamates, carboxylates, thiols and phosphinyls. To make these inhibitors more specific, the drug design includes various binding elements on the MMP of interest and these specific MMP inhibitors share the success and requirement to their usefulness. A number of inhibitors such as the drug *trocade* proved promising for the treatment of symptoms in animal models of arthritis^{40,41}. Unfortunately, human trials have not replicated the laboratory results. Most of these inhibitors turned out to be highly toxic, as for example the drug *marimastat* due to its non-selectivity⁴²⁻⁴⁴. In an interesting twist, researchers found that an old class of antibiotics, the tetracyclines, in fact acts as broad-spectrum MMP inhibitors. Indeed, the only MMP inhibitor that has

been approved so far as a drug is the *Collagenex's Periostat*, a tetracycline for the treatment of periodontitis in clinical use^{45,46}.

It is important to realize that depression, silencing or inhibition as well as induction of MMPs can occur through ECM signaling which can further trigger an array of signaling events through transactivation of growth factor receptors and other molecules⁴⁷⁻⁴⁹. Therefore, in order to avoid adverse side effects or toxicity, the above factors have to be taken into consideration when designing various biomaterials. Figure 9.6 is a schematic diagram summarizing some of these events.

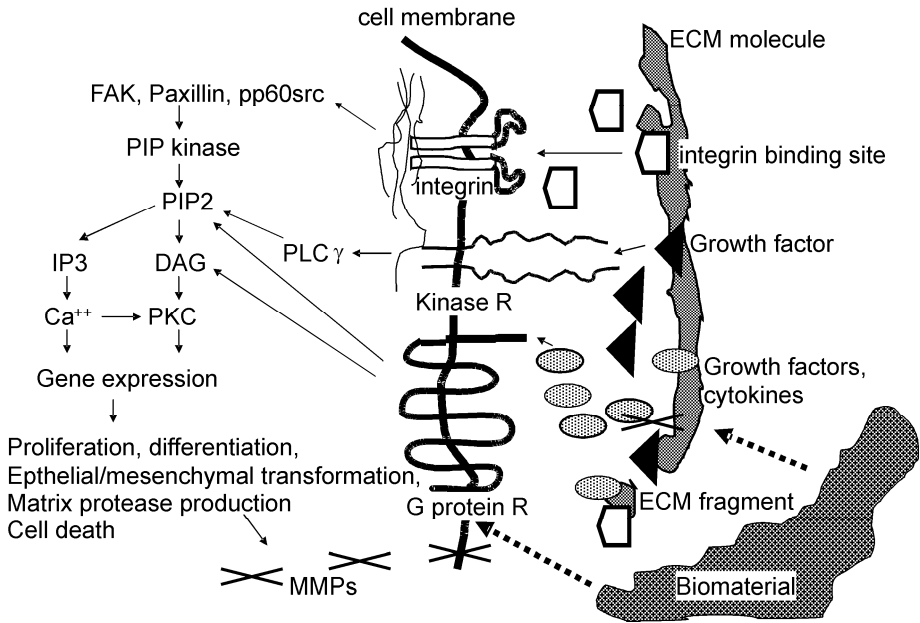


Figure 9.6. Signaling cascade between cells and ECM. The major elements involved in the signaling events including second messengers and MMPs can occur as a result of biomaterial implantation. The biomaterial interacts directly with the ECM as well as with the cell surface including receptors and integrins.

The signaling cascade between cells and ECM is conveyed through integrins and proteoglycan receptors (not shown in Fig. 9.6), when both binds for example to different domains of fibronectin, an ECM molecule⁵⁰⁻⁵². Integrin activates its focal adhesion molecules leading to weakening or strengthening cell adhesion which influences cell migration. Integrins through gene expression also modify the level of MMPs hence the degradation of ECM and cell migration. The secreted MMPs activate or inactivate cell surface receptors by transactivation or receptor shedding through degrading the ECM and hence liberating ECM bound growth factors re-

sulting in gene activation that is involved in cell proliferation, cell transformation or cell death.

9.4. GENERAL CONSIDERATIONS FOR TISSUE ENGINEERING

In general, the goal in designing tissue or organ replacement is to simulate nature as closely as possible. When developing a tissue replacement, we have to consider several factors in a biological system:

1) When placed in the body, any biomaterial can have nonspecific biological effects by simply inducing changes in the local mechanical environment⁵³. As an example of how mechanical factors can induce MMPs, [Figure 9.7A](#) below demonstrates that the level of MMP2 is increased by 4 hours of cyclic stretching of a lung tissue strip (S) compared to a non-stretched control tissue strip (C). These immunoblots were obtained from lung tissue homogenates and LC represents loading control to validate the effect. Another immediate event that can occur after biomaterial implantation is a locally initiated physical trauma with subsequent complex hypoxic tissue response called necrosis, a type of cell death⁵⁴. In the so called coagulative necrosis, the lung architecture is still recognizable with bubbly appearance (disappearance of stainable nuclei), different sizes of swollen or shrunk nuclei (pyknosis), fragmented nuclei (karyorrhexis) and fading of chromatin material (karyolysis) as shown on a hematoxylin-eosin (H&E) stained tissue slide in [Figure 9.7B](#). (Both A and B are the author's unpublished data).

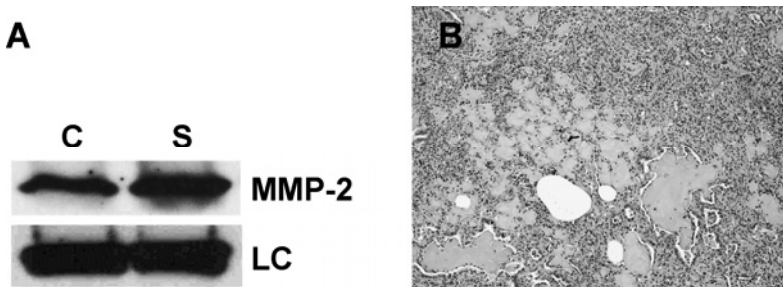


Figure 9.7. Examples of the non-specific effects following biomaterial implantation. (A) Western blot analyses of lung tissue strips for MMP2 after 4 hours of cyclic stretch. (B) H&E stained tissue slide represents necrotic tissue response after biomaterial implantation.

2) An important consideration in biomaterial design is to avoid or minimize an adverse immune response that can cause inflammation and/or rejection⁵⁵⁻⁵⁷. At the same time, it is also crucial to maintain a minimal

immune response in a spatial-temporal manner that prevents unwanted complications. After biomaterial implantation using for example hydrogels, inflammatory cells can and will infiltrate the engineered material to resolve it. The examples in [Figure 9.8A](#) and [B](#) below are representative images showing two types of inflammatory cells, lymphocytes and macrophages, in response to the implantation of thrombin containing hydrogel specifically labeled by immuno-histo-chemistry (IHC). The dark pink labels are the specific cells, lymphocytes ([Fig. 9.8A](#)) and macrophages ([Fig. 9.8B](#)); all cell nuclei appear as blue. The macrophage is the key cell type in the immune protection operating in a nonspecific defense mode and augmented by specific immunologic mechanisms as well. The innate immune lymphocytes may co-regulate the Th1-mediated response for induction of this moderate host defense⁵⁸.

Figure 9.8. Immune response following biomaterial implantation detected by IHC. Images of immunohistochemically labeled tissue sections represent (A) lymphocytes (pink dots) and (B) macrophages (pink dots) infiltrating into the biomaterial. Please see the Figure on the page 269.

3) Another important factor in the design of biomaterials is to create a proper substrate for cell survival and differentiation either for the implanted cells or attracted native cells⁵⁹. Biocompatible implants composed of ECM molecules seeded with autologous or heterologous cells are very promising. The addition of immunosuppressing drugs, growth and differentiating factors to these bio-substrates as well as agonists or antagonist to modulate ECM-cell interactions can potentially increase the success of tissue replacements. The basic RGD peptide sequence is already in intense use to manipulate cell attachment through its binding to integrins. Skin, cartridge and bone replacements as well as artificial cornea matrices benefited from it with the use of other ECM components such as collagens or proteoglycans. In the example images in [Figure 9.9](#), cell proliferation is very intense supporting cell survival by a thrombin containing biomaterial. Image (A) represents all proliferating cells (dark blue) regardless of cell type labeled by an antibody for Proliferating Cell Nuclear Antigen, PCNA, which is a protein that acts as a processivity factor for DNA polymerase delta in eukaryotic cells. The two other images are examples of special cell types. In image (B), numerous proliferating fibroblasts are present labeled by IHC to blue color with a fibroblast surface protein and in image (C), epithelial-to-mesenchymal and fibroblast-to-myofibroblasts transformed cells are labeled brown color by α -smooth muscle actin, a “motor” molecule. In this biomaterial system one of the goals was to attract fibroblasts to the matrices and help support the transformation of these cells to contractile phenotype.

Figure 9.9. Cell proliferation and transformation in biomaterial *in vivo* detected by IHC. Image (A) represents proliferating cells (dark blue) regardless of cell type labeled by an antibody for PCNA. Every cell nuclei are labeled green. In image (B), numerous proliferating fibroblasts are present labeled (blue) with a fibroblast surface protein. In image (C), epithelial-to-mesenchymal and fibroblast-to-myofibroblast transformed cells are present labeled by α -smooth muscle actin (brown), while all other cell nuclei are labeled pink on both images. Please see the Figure on the page 270.

4) It is crucial to maintain a balanced microenvironment of the host and the tissue replacement with appropriate cues to sustain correct cell function toward repair and/or regeneration⁵⁹⁻⁶⁶. Unfortunately, today very little is known about the crosstalk between the ECM and the implanted cells and complex materials. To evaluate the long term effects, well designed *in vivo* studies are needed toward elucidating the biomaterial-induced remodeling. Some examples are shown here applying thrombin containing biomaterial that were designed for epithelial cell regeneration (Fig. 9.10A), new vessel formation (Fig. 9.10B) and to natural collagen deposition (Fig. 9.10C). In this figure, IHC was used to label E-cadherin, an epithelial specific adhesion molecule; von Willebrand factor, a glycoprotein produced in endothelial cells and collagen type I antibody. The numerous newly formed epithelial cells appear blue, the newly formed vessels appear pink as a tube like structure and the newly deposited collagen is brown.

Figure 9.10. Biomaterial-induced remodeling detected by IHC. Epithelial cell (blue) regeneration is induced (A), new vessel (pink tubes) formation is obtained (B) and natural collagen deposition is maintained (C) after long term biomaterial implantation during regeneration and wound healing, while the cell nuclei are labeled either pink (A) or green (B and C). Please see the Figure on the page 270.

One should also realize that the above 4 main factors that we highlighted as perhaps the most important ones for successful tissue engineering are not necessarily exclusive. Indeed, with all the complexity of the biological world, the introduction of man-made materials in the body can generate further unwanted and unexpected results. For example, when the implanted biomaterial generates new ECM by depositing collagen or vessels, the mechanical properties of the native-biomaterial complex can undergo alterations. Such changes in stiffness will likely elicit additional feedback mechanisms involving cell signaling and subsequent MMP activation which in turn can influence the original process of deposition itself. Therefore, even though the name “Tissue Engineering” implies the rigorous use of engineering principles for rational optimization of tissue implants, it is still crucially important to advance step by step using carefully and systematically executed experiments in which all aspects of the bio-

material-native tissue interaction is examined. Therefore, to better understand the homeostasis between host environment and tissue replacement material is a fundamental must!

Finally, today organ transplantation is still broadly used even though it is very expansive and not always readily available. As a rapidly developing new field, tissue engineering should be able to offer a more consistent and faster solution in a less cost demanding way than organ replacement and hence has the potential for improving the quality of life.

Acknowledgements

This work was supported by CelluTraf. Sci. Boston. The author wishes to thank Bela Suki for his valuable comments.

References and suggested readings

1. Lodish H.F., P.T. Matsudaira, C. Kaiser, M. Krieger, Molecular cell biology, 1 v. (various pagings), W.H. Freeman and Company, New York, 2004.
2. Baynes J.W., M.H. Dominiczak, Medical biochemistry, xii, 693, Elsevier Mosby, Philadelphia, Pa., 2005.
3. Price N.C., L. Stevens, Fundamentals of enzymology: the cell and molecular biology of catalytic proteins, 478, Oxford University Press, Oxford ; New York, 1999.
4. Nutritional and Metabolic Diseases Chapter of on-line textbook "Introduction to Genes and Diseases" from NCBI.
5. Sandy J.R., R.W. Farndale, Second messengers: regulators of mechanically-induced tissue remodelling. *Eur J Orthod* **13**, 271-8, 1991.
6. Reynolds A.R., C. Tischer, P.J. Verveer, O. Rocks, P.I. Bastiaens, EGFR activation coupled to inhibition of tyrosine phosphatases causes lateral signal propagation. *Nat Cell Biol* **5**, 447-53, 2003.
7. Varro A., et al. Increased gastric expression of MMP-7 in hypergastrinemia and significance for epithelial-mesenchymal signaling. *Am J Physiol Gastrointest Liver Physiol* **292**, G1133-40, 2007.
8. Kakizoe E., et al. Isoform-selective upregulation of mast cell chymase in the development of skin fibrosis in scleroderma model mice. *J Invest Dermatol* **116**, 118-23, 2001.
9. Smith N.J., H.W. Chan, J.E. Osborne, W.G. Thomas, R.D. Hannan, Hijacking epidermal growth factor receptors by angiotensin II: new possibilities for understanding and treating cardiac hypertrophy. *Cell Mol Life Sci* **61**, 2695-703, 2004.
10. Moller A.V., et al. Glycosaminoglycans increase levels of free and bioactive IGF-I in vitro. *Eur J Endocrinol* **155**, 297-305, 2006.
11. Baumann G., S.J. Frank, Metalloproteinases and the modulation of GH signaling. *J Endocrinol* **174**, 361-8, 2002.
12. O'Brien P.J., M. Molino, M. Kahn, L.F. Brass, Protease activated receptors: theme and variations. *Oncogene* **20**, 1570-81, 2001.

13. Wang W.S., P.M. Chen, H.S. Wang, W.Y. Liang, Y. Su, Matrix metalloproteinase-7 increases resistance to Fas-mediated apoptosis and is a poor prognostic factor of patients with colorectal carcinoma. *Carcinogenesis* **27**, 1113-20, 2006.
14. Overall C.M., C. Lopez-Otin, Strategies for MMP inhibition in cancer: innovations for the post-trial era. *Nat Rev Cancer* **2**, 657-72, 2002.
15. Nabeshima K., et al. Emmpirin (basigin/CD147): matrix metalloproteinase modulator and multifunctional cell recognition molecule that plays a critical role in cancer progression. *Pathol Int* **56**, 359-67, 2006.
16. Yasui W., et al. Molecular-pathological prognostic factors of gastric cancer: a review. *Gastric Cancer* **8**, 86-94, 2005.
17. Neth P., et al. The Wnt signal transduction pathway in stem cells and cancer cells: influence on cellular invasion. *Stem Cell Rev* **3**, 18-29, 2007.
18. Takahashi C., et al. Regulation of matrix metalloproteinase-9 and inhibition of tumor invasion by the membrane-anchored glycoprotein RECK. *Proc Natl Acad Sci USA* **95**, 13221-6, 1998.
19. Bando E., et al. Immunohistochemical study of MT-MMP tissue status in gastric carcinoma and correlation with survival analyzed by univariate and multivariate analysis. *Oncol Rep* **5**, 1483-8, 1998.
20. Iida J., J.B. McCarthy, Expression of collagenase-1, MMP-1) promotes melanoma growth through the generation of active transforming growth factor-beta. *Melanoma Res* **17**, 205-13, 2007.
21. Moschos S.J., L.M. Drogowski, S.L. Reppert, J.M. Kirkwood, Integrins and cancer. *Oncology (Williston Park)* **21**, 13-20, 2007.
22. Kerkela E., et al. Metalloelastase (MMP-12) expression by tumour cells in squamous cell carcinoma of the vulva correlates with invasiveness, while that by macrophages predicts better outcome. *J Pathol* **198**, 258-69, 2002.
23. Chau K.Y., et al. Plasma levels of matrix metalloproteinase-2 and -9 (MMP-2 and MMP-9) in age-related macular degeneration. *Eye*, 2007.
24. Nanni S., et al. Matrix metalloproteinases in premature coronary atherosclerosis: influence of inhibitors, inflammation, and genetic polymorphisms. *Transl Res* **149**, 137-44, 2007.
25. Lin S.J., et al. Salvianolic acid B attenuates MMP-2 and MMP-9 expression in vivo in apolipoprotein-E-deficient mouse aorta and in vitro in LPS-treated human aortic smooth muscle cells. *J Cell Biochem* **100**, 372-84, 2007.
26. Stocker W., W. Bode, Structural features of a superfamily of zinc-endopeptidases: the metzincins. *Curr Opin Struct Biol* **5**, 383-90, 1995.
27. Nagase H., J.F. Jr. Woessner, Matrix metalloproteinases. *J Biol Chem* **274**, 21491-4, 1999.
28. Zucker S., K. Doshi, J. Cao, Measurement of matrix metalloproteinases (MMPs) and tissue inhibitors of metalloproteinases (TIMP) in blood and urine: potential clinical applications. *Adv Clin Chem* **38**, 37-85, 2004.
29. Murphy G., et al. Mechanisms for pro matrix metalloproteinase activation. *Apmis* **107**, 38-44, 1999.
30. Cauwe B., P.E. Van den Steen, G. Opdenakker, The biochemical, biological, and pathological kaleidoscope of cell surface substrates processed by matrix metalloproteinases. *Crit Rev Biochem Mol Biol* **42**, 113-85, 2007.

31. Santos-Martinez M.J., C. Medina, P. Jurasz, M.W. Radomski, Role of metalloproteinases in platelet function. *Thromb Res*, 2007.
32. Schulz R., Intracellular targets of matrix metalloproteinase-2 in cardiac disease: rationale and therapeutic approaches. *Annu Rev Pharmacol Toxicol* **47**, 211-42, 2007.
33. Oh J., et al. The membrane-anchored MMP inhibitor RECK is a key regulator of extracellular matrix integrity and angiogenesis. *Cell* **107**, 789-800, 2001.
34. Takeuchi T., et al. The membrane-anchored matrix metalloproteinase (MMP) regulator RECK in combination with MMP-9 serves as an informative prognostic indicator for colorectal cancer. *Clin Cancer Res* **10**, 5572-9, 2004.
35. Guo Y., et al. Blocking Wnt/LRP5 signaling by a soluble receptor modulates the epithelial to mesenchymal transition and suppresses met and metalloproteinases in osteosarcoma Saos-2 cells. *J Orthop Res* **25**, 964-71, 2007.
36. Fingleton B., MMPs as therapeutic targets-Still a viable option? *Semin Cell Dev Biol*, 2007.
37. Shangari N., T.S. Chan, K. Chan, S. Huai Wu, P.J. O'Brien, Copper-catalyzed ascorbate oxidation results in glyoxal/AGE formation and cytotoxicity. *Mol Nutr Food Res* **51**, 445-55, 2007.
38. Howes J.M., R.D. Theakston, G.D. Laing, Neutralization of the haemorrhagic activities of viperine snake venoms and venom metalloproteinases using synthetic peptide inhibitors and chelators. *Toxicon* **49**, 734-9, 2007.
39. Kung H.N., et al. Involvement of NO/cGMP signaling in the apoptotic and anti-angiogenic effects of beta-lapachone on endothelial cells in vitro. *J Cell Physiol* **211**, 522-32, 2007.
40. Hemmings F.J., M. Farhan, J. Rowland, L. Banken, R. Jain, Tolerability and pharmacokinetics of the collagenase-selective inhibitor Trocade in patients with rheumatoid arthritis. *Rheumatology (Oxford)* **40**, 537-43, 2001.
41. Close D.R., Matrix metalloproteinase inhibitors in rheumatic diseases. *Ann Rheum Dis* **60 Suppl 3**, iii62-7, 2001.
42. Bloomston M., E.E. Zervos, A.S. Rosemurgy, 2nd. Matrix metalloproteinases and their role in pancreatic cancer: a review of preclinical studies and clinical trials. *Ann Surg Oncol* **9**, 668-74, 2002.
43. Failes T.W., T.W. Hambley, Towards bioreductively activated prodrugs: Fe(III) complexes of hydroxamic acids and the MMP inhibitor marimastat. *J Inorg Biochem* **101**, 396-403, 2007.
44. Tonn J.C., et al. Effect of synthetic matrix-metalloproteinase inhibitors on invasive capacity and proliferation of human malignant gliomas in vitro. *Int J Cancer* **80**, 764-72, 1999.
45. Murakami S., R. Nakashima, E. Yamashita, T. Matsumoto, A. Yamaguchi, Crystal structures of a multidrug transporter reveal a functionally rotating mechanism. *Nature* **443**, 173-9, 2006.
46. Burggraf D., A. Trinkl, M. Dichgans, G.F. Hamann, Doxycycline inhibits MMPs via modulation of plasminogen activators in focal cerebral ischemia. *Neurobiol Dis* **25**, 506-13, 2007.
47. Birkedal-Hansen H., Proteolytic remodeling of extracellular matrix. *Curr Opin Cell Biol* **7**, 728-35, 1995.

48. Ohbayashi H., K. Shimokata, Matrix metalloproteinase-9 and airway remodeling in asthma. *Curr Drug Targets Inflamm Allergy* **4**, 177-81, 2005.
49. Lijnen H.R., Matrix metalloproteinases and cellular fibrinolytic activity. *Biochemistry (Mosc)* **67**, 92-8, 2002.
50. Hynes R.O., Cell-matrix adhesion in vascular development. *J Thromb Haemost* **5 Suppl 1**, 32-40, 2007.
51. Adair B.D., M. Yeager, Electron microscopy of integrins. *Methods Enzymol* **426**, 337-73, 2007.
52. Huebsch N.D., D.J. Mooney, Fluorescent resonance energy transfer: A tool for probing molecular cell-biomaterial interactions in three dimensions. *Biomaterials* **28**, 2424-37, 2007.
53. Suki B., S. Ito, D. Stamenovic, K.R. Lutchen, E.P. Ingenito, Biomechanics of the lung parenchyma: critical roles of collagen and mechanical forces. *J Appl Physiol* **98**, 1892-9, 2005.
54. Garcia Y., A. Breen, K. Burugapalli, P. Dockery, A. Pandit, Stereological methods to assess tissue response for tissue-engineered scaffolds. *Biomaterials* **28**, 175-86, 2007.
55. Castro G.R., B. Panilaitis, E. Bora, D.L. Kaplan, Controlled release biopolymers for enhancing the immune response. *Mol Pharm* **4**, 33-46, 2007.
56. Taylor P.M., Biological matrices and bionanotechnology. *Philos Trans R Soc Lond B Biol Sci* **362**, 1313-20, 2007.
57. Weintraub W.S., The pathophysiology and burden of restenosis. *Am J Cardiol* **100**, 3K-9K, 2007.
58. Oviedo-Orta E., A. Bermudez-Fajardo, S. Karanam, U. Benbow, A.C. Newby, Comparison of MMP-2 and MMP-9 secretion from T helper 0, 1 and 2 lymphocytes alone and in coculture with macrophages. *Immunology*, 2007.
59. Fedorovich N.E., et al. Hydrogels as extracellular matrices for skeletal tissue engineering: state-of-the-art and novel application in organ printing. *Tissue Eng* **13**, 1905-25, 2007.
60. Bagnaninchi P.O., Y. Yang, A.J. El Haj, N. Maffulli, Tissue engineering for tendon repair. *Br J Sports Med* **41**, e10; discussion e10, 2007.
61. Metcalfe A.D., M.W. Ferguson, Tissue engineering of replacement skin: the crossroads of biomaterials, wound healing, embryonic development, stem cells and regeneration. *J R Soc Interface* **4**, 413-37, 2007.
62. Saettele T.M., et al. Use of porcine dermal collagen as a prosthetic mesh in a contaminated field for ventral hernia repair: a case report. *Hernia* **11**, 279-85, 2007.
63. Bolland B.J., S. Tilley, A.M. New, D.G. Dunlop, R.O. Oreffo, Adult mesenchymal stem cells and impaction grafting: a new clinical paradigm shift. *Expert Rev Med Devices* **4**, 393-404, 2007.
64. Lee S.H., H. Shin, Matrices and scaffolds for delivery of bioactive molecules in bone and cartilage tissue engineering. *Adv Drug Deliv Rev* **59**, 339-59, 2007.
65. Kimura Y., Y. Tabata, Experimental tissue regeneration by DDS technology of bio-signaling molecules. *J Dermatol Sci* **47**, 189-99, 2007.
66. Kontakis G.M., J.E. Pagkalos, T.I. Tosounidis, J. Melissas, P. Katonis, Bioabsorbable materials in orthopaedics. *Acta Orthop Belg* **73**, 159-69, 2007.

HYDROGELS IN TISSUE ENGINEERING

Biancamaria Baroli*

10.1. INTRODUCTION

Tissue engineering (TE) aims to provide an alternative to organ transplantation when all the other treatments failed by using three main strategies. First, the utilization of isolated cells, which has the great advantage to replace just the cells that are really needed and to eventually –genetically– manipulate them before infusion. This strategy allows for minimal invasive surgery, but there is always the possibility of immunological rejection or failure in maintaining new functions. The second approach is that of using ‘tissue inducing substances’ like, for instance, growth factors or cytokines. However, drawbacks of this solution are purification and large-scale production issues, and it will always be necessary to have a system to deliver the bioactive molecule to its target. Finally, the third strategy utilizes cells that are placed on, or within, matrices. In this case, we can have ‘closed systems’ where cells are entrapped within, or encapsulated in a biomaterial, and ‘open systems’ where cells are attached on the external surfaces of an appropriately shaped biomaterial before, in both cases, being implanted in the receiving body (Fig. 10.1).¹

Thus, TE investigates in three main, but interconnected, areas: cells, tissue inducing substances, and materials. Hydrogels belong to a class of material used for regenerative and biomedical applications due to their ability to retain a great quantity of water, good biocompatibility, low interfacial tension, and minimal mechanical and frictional irritation.^{3,4}

* Dipartimento Farmaco Chimico Tecnologico, Università di Cagliari, Cagliari, Italy.

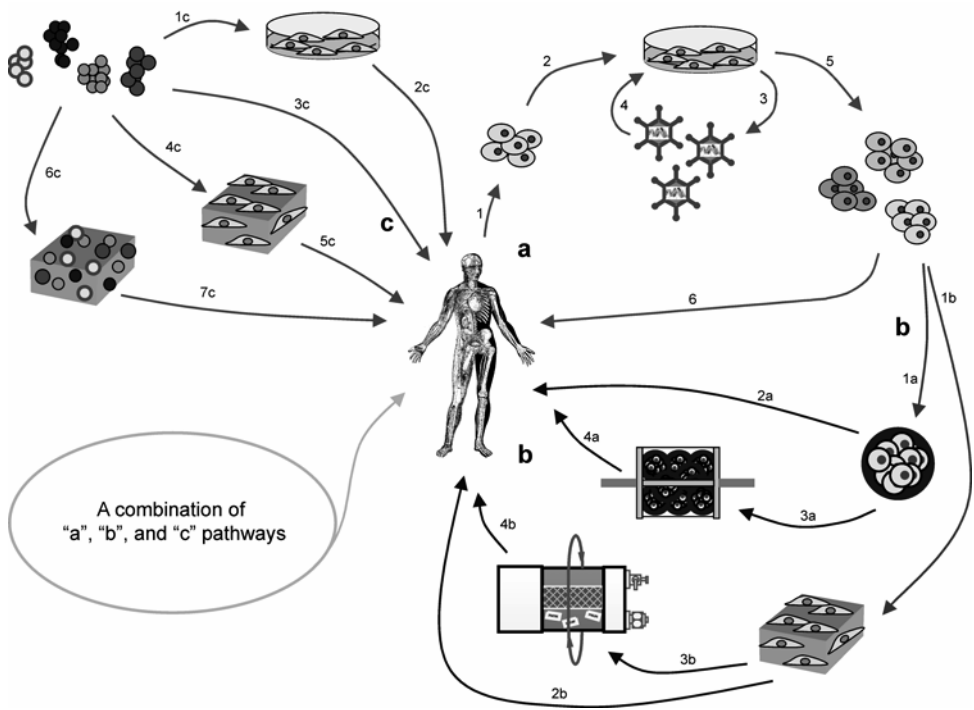


Figure 10.1. Tissue engineering strategies. To regenerate an organ, TE may take profit of cells explanted from an individual (pathway a, 1), which can be cultivated and differentiated in vitro (a, 2), possibly genetically modified (a, 3-4), and expanded (a, 5) prior to be re-infused, preferentially, in the same individual (a, 6). This approach is hardly using any engineering expertise, since the final goal is sufficient number of cells with certain characteristics. Then, everything is left to nature. However, according to the pathway b, these same cells could be engineered before re-exposure to all the signals (e.g. mechanical, molecular) of the human body. For instance, they could be encapsulated (b, 1a) and implanted in the body (b, 2a) to act as an artificial organ (e.g., artificial pancreas), or encapsulated and utilized in a bioreactor (b, 3a) to serve as an external (b, 4a) artificial organ (e.g. artificial liver). In a different approach, cells (b, 1b) could be seeded on scaffolds and directly implanted in the body (b, 2b), or after a period of in vitro cultivation using bioreactors (b, 3b). During this time, different environmental signals could be controlled, and consequently the ones that more efficiently guide the cells toward a desired path could be revealed (e.g. differentiation towards particular cell type or increased extracellular matrix production). Consequently, exposing cells to controlled signals increases the probability that the implanted construct (scaffold + cells) will better integrate within the host. The third major approach is based on using tissue-inducing substances (pathway c) that can be added in all types of in vitro cultures (c, 1c) prior to re-infusing the exposed cells in the body. Alternatively, these molecules could be administered, delivered, and/or targeted to the exact location where a regeneration is desired. However, this solution is difficult to achieve since formulation, stability, integrity, and many other issues related to tissue-inducing molecules and their carriers may arise. More approachable and controllable strategies are instead those that use such molecules in vitro either on cells cultivated on scaffolds (c, 4c) and implanted (c, 5c), or encapsulated in a scaffold (c, 6c) to be implanted (c, 7c). Finally, it should be mentioned that regeneration may be also achieved by combined approaches of pathways a, b, and c, and others not illustrated inhere. Adapted with permission from Ref. 2.

This lecture aims to introduce the student to this class of materials by describing what hydrogels are, how they can be classified, their methods of preparation, their properties, how they can be characterized, and finally their biomedical applications.

10.2. WHAT IS A HYDROGEL?

The term hydrogel is composed of ‘hydro’ (= water) and ‘gel’, and it refers to aqueous (water-containing) gels, or, to be more precise, to polymer networks that are insoluble in water, where they swell to an equilibrium volume but retaining their shapes.⁴

The hydrophilicity of the network is due to the presence of chemical residues such as $-\text{OH}$, $-\text{COOH}$, $-\text{CONH}-$, $-\text{CONH}_2$, $-\text{SO}_3\text{H}$, and others. Nevertheless, it is also possible to produce hydrogels containing a significant portion of hydrophobic polymers, by blending or copolymerizing hydrophilic and hydrophobic polymers, or by producing interpenetrating or semi-interpenetrating networks with hydrophilic polymer networks.⁵

The insolubility of the gel in water is instead due to the presence of a three-dimensional network, where an equilibrium between dispersing (acting on hydrated chains) and cohesive (preventing further penetration of water) forces exists.^{3,6,7} These cohesive forces are generated by covalent bonds between the chains of the polymer network (chemical hydrogel), or by cooperative and associative forces such as (1) hydrophobic associations/Van der Waals forces, (2) micellar packing, (3) hydrogen bonding, (4) ionic bonding, (5) crystallizing segments, or (6) combinations of the above (physical hydrogel).²⁻⁷ In a first approximation, we can image a hydrogel to have a structure similar to those shown in [Figure 10.2](#), but three-dimensionally organized.

As mentioned earlier, these structures expand when the hydrogel is put in contact to water. However, these materials can be also designed to swell or shrink when they are exposed to particular signals such as temperature, pH, ionic strength, electrical field, particular aqueous solution composition, and light as it was on command.^{8,9}

Finally, hydrogels can be classified as (1) natural or synthetic; (2) degradable or non-degradable; (3) physical or chemical hydrogels; (4) homopolymer, copolymer, block-copolymer, or multipolymer hydrogels, interpenetrating or semi-interpenetrating polymer networks; (5) neutral, cationic, anionic, amphiphilic hydrogels; (6) amorphous or semi-crystalline hydrogels; (7) matrix, film, membrane, microsphere, or microcapsule. They can be also classified using their chemical family names.

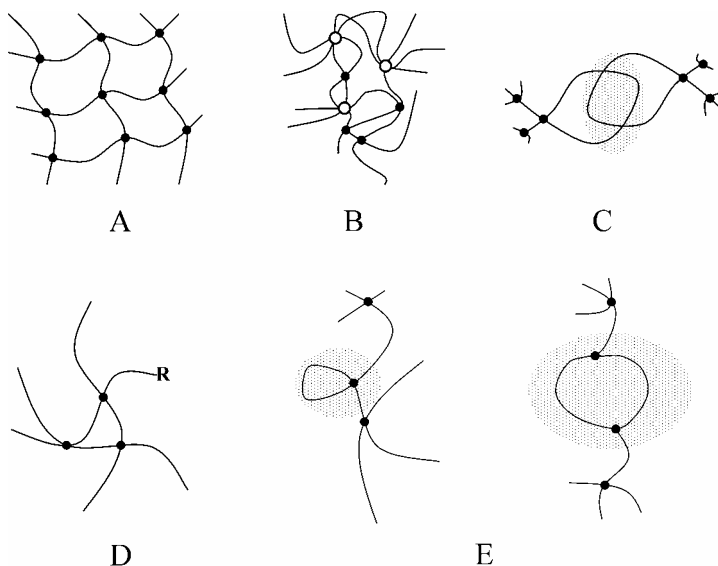


Figure 10.2. Hydrogel structure. This figure shows (A) a well-ordered tetra-branched network (ideal in most of the cases) where covalent or non-covalent junctions are visualized as filled dots; (B) a random multi-branched (clear and filled dots) network; (C) a network with some chain entanglements (shaded); (d) a network with a reactive moiety (R), which is considered a defect; (E) two networks exhibiting some loops in their structure (shaded), which are considered defects since they do not contribute to mechanical strength or other physical properties. Adapted with permission from Ref. 2.

10.3. METHODS OF PREPARATION

Methods of preparation of hydrogels have been extensively reviewed in literature.²⁻⁹ In this paragraph, they will be grouped in those that are used to produce chemical and physical gels.

10.3.1. Chemical hydrogel preparation

Chemical hydrogels are produced by crosslinking starting materials through chemical reactions (polymerization, but not limited to) or irradiation (UV, gamma-rays, X-rays, electron beams). Synthetic and natural starting materials (monomers, macromonomers, polymers) should have, or should be modified to have, vinyl residues (e.g.; acrylic acid, methacrylic acid, (meth)-acrylamide, hydroxyethylmethacrylate, glycidil acrylate, cinnamic acid, and vinyl pyrrolidone; Fig. 10.3). These monomers are then polymerized in presence of crosslinking agents bearing di- or multi-vinyl residues.¹⁰⁻¹²

Nevertheless, starting materials possessing other functional residues might be crosslinked using other chemical reactions. For instance, gelatin

and albumin can be crosslinked by using dialdehyde, while cystein-bearing peptides through cystein bonds.¹³⁻¹⁸

Finally, those functional residues providing hydrophilicity ($-\text{OH}$, $-\text{COOH}$, $-\text{CONH}-$, $-\text{CONH}_2$) can also be crosslinked with residues having complementary reactivity (e.g.; amine-carboxylic acid, isocyanate-hydroxyl, isocyanate-amine). Among these, examples of crosslinking (1) with aldehydes; (2) by addition or condensation reactions; (3) by high energy irradiation of polymer not bearing vinyl groups; and (4) by using enzymes have been reported.¹³⁻¹⁸

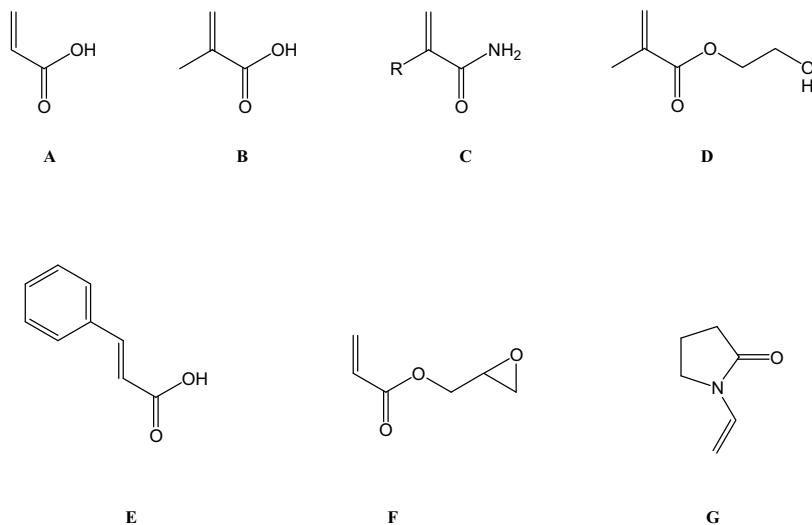


Figure 10.3. Polymerizable vinyl modifiers. This figure shows some molecules used to functionalize starting materials to be used to prepare hydrogels. In particular, acrylic acid (a); methacrylic acid (b); (meth-)acrylamide (c) where R is respectively a $-\text{CH}_3$ or and $-\text{H}$; 2-hydroxyethylmethacrylate (d); cinnamic acid (e); glycidil acrylate (f); vinyl pyrrolidone (g) are presented. adapted with permission from Ref. 2.

10.3.2. Physical hydrogel preparation

Physical hydrogels are receiving great attention because they are produced without any chemical reaction, which make them suitable for cell and sensitive molecule (e.g.; cytokine) encapsulation because they avoid the use (and then removal) of toxic or extremely reactive molecules (even part of the unreacted monomer) used to initiate chemical crosslinking reactions.^{2,19}

10.3.2.1. Hydrogels obtained by ionic interactions

Maybe the best-known hydrogels of this type are alginate and chitosan. Alginate can be crosslinked with calcium ions and has been used for cell and protein encapsulation.²⁰⁻²⁴ Chitosan²⁵⁻²⁸ has been instead crosslinked with glycerophosphate disodium salt, producing gels at 37°C, which make this formulation suitable to be injected subcutaneously as a liquid. This thermo-hydrogel has been used for cartilage and bone tissue engineering applications.²⁹

In these two cases, the hydrogel is formed because two polymer chains bearing anionic or cationic residues react with (at least) divalent counter ions (Fig. 10.4.2). However, other interactions are possible. For instance, dextran/potassium hydrogel is formed when potassium ions fit in the cage formed by the six oxygen atoms of three dextran chains. In addition, it is also possible to crosslink anionic and cationic polymers among each other (Fig. 10.4.1), as chitosan with dextran sulfate or alginate.³⁰

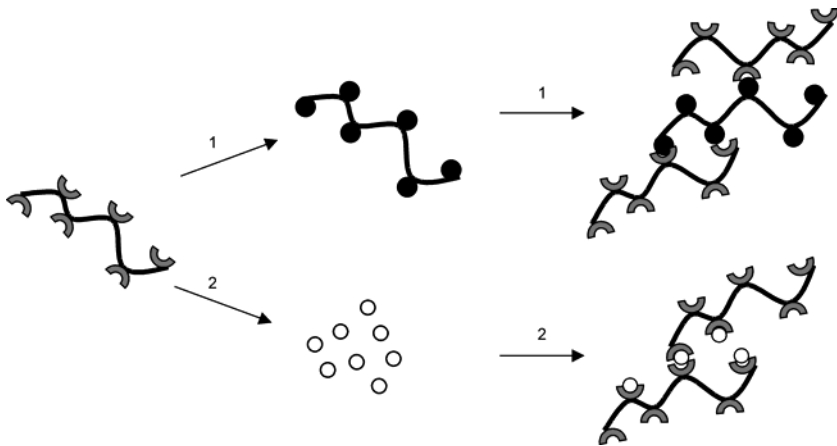


Figure 10.4. Hydrogel formation by ionic interactions. This figure shows (1) reticulation between oppositely charged polymers (e.g. alginate-chitosan), and (2) reticulation between a charged polymer and its counter ions (e.g. alginate-Ca⁺⁺).

10.3.2.2. Hydrogels obtained by crystallization

Hydrogels obtained by crystallization are formed when parts of the polymer chain crystallize and act as crosslinking sites within the network, as shown in Figure 10.5.

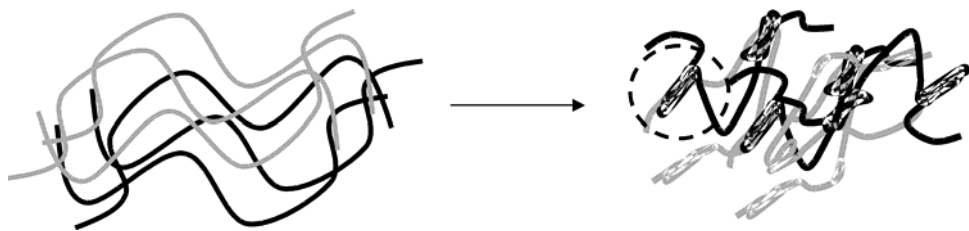


Figure 10.5. Formation of a hydrogel by crystallization. This figure shows different randomly organized polymer chains, whose segments, here and there, crystallized together (marked by the circle) forming crosslinking sites.

Examples of such hydrogels are PVA [poly(vinyl alcohol)] after a cycle of freeze-thawing, a concentrated solution of dextran 6000 incubated at room temperature, and isotactic poly(methacrylic acid).³¹⁻³³

10.3.2.3. Hydrogels obtained from amphiphilic block and graft co-polymers

Amphiphilic block and graft co-polymers have the ability to self-assemble in different phases, such as micellar, lamellar and others, which can then eventually compose hydrogels. In here, hydrophobic moieties are segregated and aggregated among each other. Thus, the hydrogel is formed by hydrophobic interactions and supramolecular organization³⁴⁻³⁸ (Fig. 10.6).

Examples of such polymers are those composed of a water-soluble backbone to which hydrophobic chains, bearing hydrophilic residues, are attached, or block copolymer where hydrophilic and hydrophobic units are the internal or external segments of the backbone. In this latter case, two well-known polymers may be cited. The copolymers PEO-*b*-PPO-*b*-PEO and PPO-*b*-PEO-*b*-PPO (known as Pluronics[®], and that are FDA approved for in vivo applications), and PEG-PLGA-PEG and PLGA-PEG-PLGA. It should be highlighted that this class of molecules should not be confused with those that form hydrogels by hydrophobic interaction or dehydration [e.g.; poly(N-isopropylacrylamide), or hydroxypropylmethyl cellulose] but without a particular supramolecular organization.

Pluronics[®], and in particular the F-127, has been investigated for the production and use of hydrogel scaffolds for TE of cartilage, and drug delivery both in its cubic and micellar (nanocarrier) phases.³⁹ PEG-PLGA-PEG and PLGA-PEG-PLGA have been studied for drug delivery, from which molecules are released by diffusion and degradation processes. These polymers exhibit also UCST and LCST properties (see paragraph 10.4.2.), which in some cases can provide additional features.

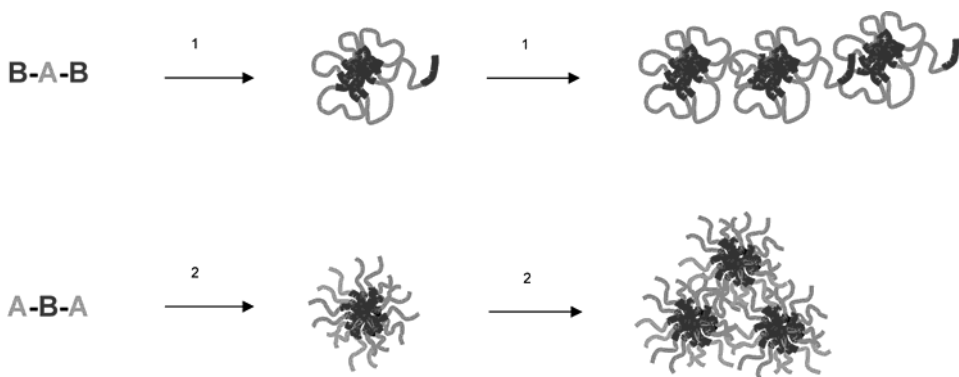


Figure 10.6. Gelation process of amphiphilic polymers. This figure shows the gelation process of two block copolymers: (1) the Type BAB block copolymer is composed of two external hydrophobic segments and a central hydrophilic one; (2), the Type ABA block copolymer is composed of two external hydrophilic segments and a central hydrophobic one. At low concentration both type of molecules will form micelles once a critical micellar concentration (cmc) or critical micelle temperature (cmt) is reached. By increasing the concentration of polymers, micelles will start to overlap and gelation will occur. Though, micelle structure and inter-micelle interactions will depend on the structure of the block copolymer, and on the length of the blocks.

10.3.2.4. Hydrogels obtained by hydrogen bond interactions

Hydrogen bonds can occur between proton donor (e.g. carboxylic and hydroxylic groups, amine and amide) and proton acceptor (e.g.; oxygen, nitrogen, and halogen atoms, which have a lone pair electrons, and/or unsaturated residues) groups. Therefore, polymers or polymers blends bearing such groups may gel due to these interactions. Examples of such polymers are: PVA, PVA/PEO blends, polyacrylamide/polyacrylic acid blends, gelatin, and others.⁴⁰⁻⁴⁴ Another fascinating hydrogel was inspired by DNA structure: in this case, oligodeoxyribonucleotides (ODN) were grafted on poly(*N,N*-dimethylacrylamide-co-*N*-acryloyloxysuccinimide). Gelation occurred by adding free or grafted complementary ODN.¹³

10.3.2.5. Hydrogels obtained by protein interactions

With advances in protein engineering is now possible to (a) produce protein with desired repeating units, (b) graft desired units on synthetic polymers, (c) graft coiled coils (i.e.; left-handed superhelices of two or more right-handed alpha-helices) on synthetic polymers. These hybrids are able to form hydrogels in response to temperature and pH changes, due to the interactions between proteic residues. In addition, other remarkable

self-assembled hydrogel scaffolds for drug and cell encapsulation were designed starting from biotin-avidin (Fig. 10.7) and antigen-antibody (not shown) reactions.⁴⁵⁻⁴⁷

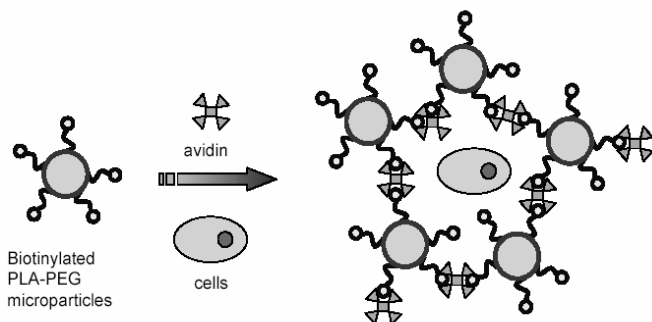


Figure 10.7. Formation of a self-assembled hydrogel scaffold obtained by reacting biotinylated microparticles with avidin.

10.4. HYDROGEL PROPERTIES

In this section, some of the properties that are important for tissue engineering applications will be briefly described. More in depth mathematical descriptions may be found elsewhere.^{2,48-50}

10.4.1. Swelling

As it was mentioned earlier, hydrogels have the ability to swell up to an equilibrium when put in contact with water.^{2,5,6,48-52} In this process, the osmotic swelling is counterbalanced by the network elasticity generating a net force known as swelling pressure (P_{sw}), which is equal to zero at equilibrium when using pure water, and which complies with the following equation:

$$P_{sw} = k \times C^n \quad (10.1)$$

where k and n are constants and C is the polymer concentration.

Swelling can also be described by describing the increase in weight, volume, or length. Thus the weight amount of water up-taken by the hydrogel (W_w) is given by:

$$W_w = \frac{WH_w - DH_w}{WH_w} \quad (10.2)$$

where ' WH_w ' and ' DH_w ' are respectively the wet and dry hydrogel weights.

If we would like to refer to the dry state of the hydrogel, we would have to talk about ‘hydration’, which is instead described as a percent of hydration ($H\%$), and thus by the following expression:

$$H\% = \frac{100 \times (WH_w - DH_w)}{DH_w} \quad (10.3)$$

In addition, while the percent of swelling does not exceed 100, the percent of hydration does. Then, the degree of swelling (D_{sw}) is given by:

$$D_{sw} = \frac{WH_w}{DH_w} \quad D_{sw} \geq 1 \quad (10.4)$$

whereas the swelling ratio (R_{sw}) by:

$$R_{sw} = D_{sw} \frac{d_0}{d_{sw}} = \frac{WH_v}{DH_v} \quad (10.5)$$

where ‘ d_0 ’ is the density of the hydrogel in the dry state, ‘ d_{sw} ’ the density of the swollen gel, ‘ WH_v ’ and ‘ DH_v ’ are respectively the volumes of the hydrogel in the wet and dry states. Another useful equation that describes the volume fraction of the polymer in the swollen hydrogel at equilibrium and 25°C (v_2) is the following:

$$v_2 = \frac{\frac{m_p}{d_p}}{\frac{m_p}{d_p} + \frac{m_s}{d_s}} \quad (10.6)$$

where ‘ m_p ’ and ‘ m_s ’ are the weights of the dry polymer and solvent, while ‘ d_p ’ and ‘ d_s ’ their respective densities.

Finally, it should be mentioned that as swelling occurs, molecules entrapped within the hydrogel will be delivered outside according to the well known Fick’s law. However, an exhaustive release from a hydrogel used as a drug delivery system will comprise of diffusion, polymer degradation, and other physico-chemical parameters of the hydrogel.

10.4.2. Responsive hydrogels

The term “responsive hydrogel” indicates a particular hydrogel that is able to undergo volume phase (swell or shrink) or sol-gel phase transitions in response to physical and/or chemical stimuli, such as a critical pH, ionic strength, temperature, electric field, a non-solvent solvent ratio, light, and pressure, to cite some.^{2,8,9,53} Many of these stimuli have been used to trigger the controlled delivery of active molecules in particular situations.

Nevertheless, in this paragraph, a particular attention will be given to temperature responsive hydrogels, because this property allows for minimal invasive implantation of a liquid formulation that will be transformed in hydrogel in in-vivo conditions. These type of hydrogels can be classified as negatively or positively thermosensitive gels, or thermally reversible gels.

In particular, the negatively thermosensitive gels are those showing a lower critical solution temperature (LCST) behavior (Fig. 10.8), which means that the gel collapses as temperature increases (e.g.; Poly(*N,N*-diethylacrylamide [PDEAAM], Pluronics[®], Tetronics[®]). Positively thermosensitive gels will instead dissolve as temperature will increase, and are known to have an upper critical solution temperature (UCST; Fig. 10.8).

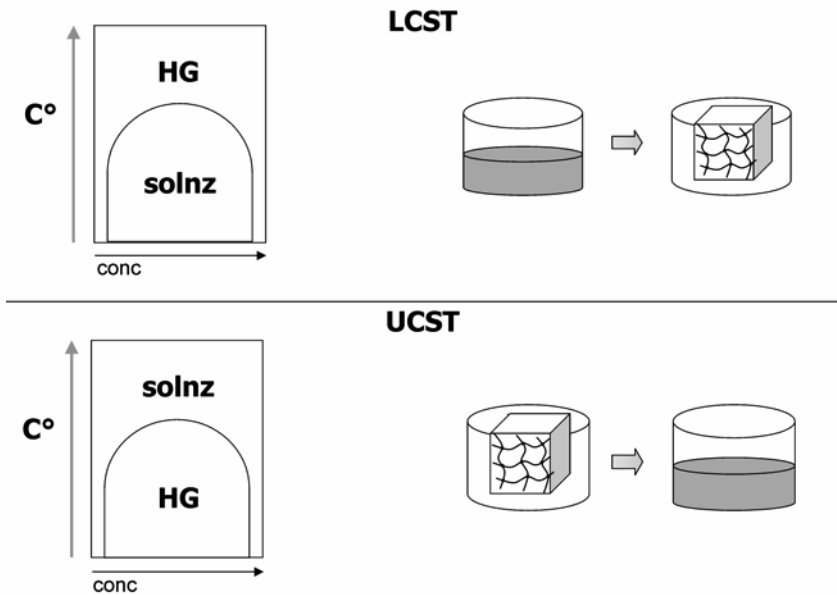


Figure 10.8. Phase separation in LCST and UCST polymer solution as a function of temperature and polymer concentration.

10.4.3. Surface properties

Whereas swelling and diffusion are properties that depend on chemical composition and structure of the internal network, for the applications discussed in this lecture, surface properties are also very important for cell adhesion (or in some cases cell adhesion resistance), thrombogenicity,⁵⁴⁻⁵⁸ and biocompatibility.⁵⁹⁻⁶² In general, the great amount of water entrapped

within the hydrogel is considered an advantageous property for compatibility.⁶³ However, ionic properties may then smooth benefits arising from water content. In fact, a negatively charged surface will have a good blood compatibility, but poor cell growth, which could be instead enhanced by increasing the positive charges.⁵ In addition, to improve adherent cell attachment on hydrogel matrices/scaffolds, RGD sequences have been bound to hydrophilic polymers.⁶⁴⁻⁶⁸ The ionic character of hydrogel may also control (among other parameters) membrane selectivity. This is very important for encapsulated cells, since those pores within gel matrix that assure transport of nutrients and cell product can be clogged by circulating protein-ionic group interactions.^{3,5,20}

10.4.4. Degradability

Degradation of hydrogel may occur accordingly to different pathways. Backbone degradation will generate low molecular weight, and generally soluble units. This type of degradation is typical of hydrophilic polymer networks, hydrophilic-hydrophobic copolymer networks, physical blends of hydrophilic and hydrophobic-but-degradable polymers. However, the majority of hydrophilic polymers are not degradable, but they become degradable by using degradable cross-linkers (e.g. azo-aromatic compounds, oligopeptides, and macromolecules: intact proteins, functionalized protein, modified polysaccharides). In addition, in hydrogels obtained from natural polymers it is common that both backbone and crosslinker degradations occur simultaneously. Finally, in those hydrogels designed to also deliver active molecules, degradation may occur by degrading pendant chains, used as spacers, but to which molecule of interest are generally linked. Mechanisms of hydrogel degradation comprise solubilization by erosion or by a pH-induced increase in ionic charges, hydrolysis, hydrolysis followed by dissolution, and enzyme-catalyzed degradation.

10.5. METHODS OF CHARACTERIZATION

Hydrogel can be characterized by using the following test methods. Polymer density is normally measured picnometrically using an inert liquid. The equilibrium swelling is determined by weighing the swollen hydrogel and the vacuum dried hydrogel. The volume swelling is calculated by measuring dried and swollen hydrogel. Mechanical properties normally investigated are tensile strength, strain-at-break, stress corresponding to a given deformation, and viscoelastic behavior.

Wettability is normally evaluated measuring the contact angle (θ), which is expressed, for flat surfaces, by the Young-Dupr ee equation:

$$\gamma_{SV} = \gamma_{SL} + \gamma_{LV} \times \cos\theta \quad (10.7)$$

where ‘ γ ’ is the solid/vapor (SV), solid/liquid (SL), or liquid/vapor (LV) interfacial tension.

10.6. BIOMEDICAL / TISSUE ENGINEERING APPLICATIONS

Hydrogels have been extensively used for diagnostics, therapeutic devices and implants for short- and long-term applications.^{2-9,69-75} A short list is proposed in [Table 10.1](#). Among therapeutics, adsorbent coatings for blood perfusion, hemodialysis membranes, blood oxygenators, degradable drug delivery systems, medicated and soft contact lenses should be mentioned. Implants include intraocular lenses, artificial corneas, eye capillary drains, vitreous humor replacements, soft tissue substitutes/replacements, burn dressing, bone ingrowth sponges, urethral prostheses, artificial larynges, plastic surgery, scleral buckling implants for retinal surgery, suture coatings, soft palate replacements. Finally, as pure TE products, we should mention temporal artificial skin substitutes, membranes used to prevent post-operation adhesion and to promote healing, hydrogels produced in-vivo by using in-situ photopolymerization, hydrogels for cell encapsulation and consequently corporal and extra-corporal bioartificial or biohybrid organs (e.g., artificial pancreas, artificial liver). It should be said that, due to their aqueous environment, hydrogels can protect encapsulated cells also from immune response, though maintaining good transport of nutrients and cell products. In addition, hydrogels have been used for tissue engineering of cartilage, bone, neural tissue, vocal matrix, ligaments, heart valves and aortic heart valves, skeletal muscle, human cornea, hair follicles, and trachea. Hydrogels have been also used to culture fibroblasts, preadipocytes, insulinoma cell lines, bone marrow stromal cells, mesenchymal amniocytes, pancreatic islet cells, granulosa cell-oocyte complexes, human umbilical vein endothelial cells, hepatocytes, osteoblasts, smooth muscle cells, schwann cells, and to support the chondrogenic differentiation of mesenchymal stem cells, the chondrogenic differentiation of adipose-derived adult stem cells, peripheral nerve regeneration, and brain lesion healing.

Nevertheless, it should not be forgotten that hydrogels have also some disadvantages. They may be difficult to handle, generally mechanical weak, difficult to produce as pre-fabricated matrix, and difficult to be sterilized. In addition, unreacted monomers and initiators may cause some toxicity.

Table 10.1. Hydrogels used in biomedical / tissue engineering applications

Polymer Name	Acronym	Utilization/Application
Poly(vinyl alcohol)	PVA	Blood compatible
Polyacrylamide	PAAm	Blood compatible
Poly(N-vinyl pyrrolidone)	PNVP	Blood compatible
Poly(hydroxyethyl methacrylate)	PHEMA	Blood compatible
Poly(ethylene oxide)	PEO	Blood compatible
Poly(ethylene glycol)	PEG	Blood compatible
Poly(ethylene glycol) monomethyl ether	PEGME	Blood compatible
Cellulose		Blood compatible
PHEMA copolymerized with NVP		Contact lenses
Methylacrylic acid	MAA	Contact lenses
Butyl methacrylate	BMA	Contact lenses
Methyl methacrylate	MMA	Contact lenses
3-methoxy-2-hydroxypropylmethacrylate	MHPM	Contact lenses
PHEMA/poly(ethylene terephthalate)	PHEMA/PFTE	Artificial tendons, other medical applications
Cellulose acetate		Artificial kidney
PVA, cellulose acetate		Membranes for plasmapheresis
PNVP, PHEMA, cellulose acetate		Artificial livers
PVA, PHEMA		Artificial skin
Terpolymers of HEMA, MMA, NVP		Mammoplasty
PHEMA, P(HEMA-co-MMA)		Maxillofacial reconstruction
PVA		Vocal cord reconstruction
PHEMA-b-siloxane		Sexual organ reconstruction
PVA, poly(glyceryl methacrylate)		Ophthalmic application
Poly(acrylic acid)	PAA	Ophthalmic application
PVA, HEMA, MMA		Articular cartilage
PVA, HEMA, MMA		Controlled drug delivery
PGA, PLA,PLA-PGA, PLA-PEG, chitosane, dextran, dextran-PEG, polycyanoacrylate, fumaric acid-PEG, sebacic acid 1,3-bis(p-carboxyphenoxy) propane		Biodegradable hydrogels
PHEMA, PVA, PNVP		Neutral non-degradable HG
Poly(ethylene-co-vinyl acetate)	PEVAc	Neutral non-degradable HG
PAAm, PAA, PMAA		pH-sensitive non-degradable HG
Poly(diethylaminoethyl methacrylate)	PDEAEMA	pH-sensitive non-degradable HG
Poly(dimethylaminoethyl methacrylate)	PDMAEMA	pH-sensitive non-degradable HG
P(MAA-g-EG), P(PAA-g-EG)		Complexing non-degradable HG
Poly(N-isopropyl acrylamide)	PNIPAAm	Temperature sensitive non-degradable HG
PNIPAAm/PAA, PNIPAAm/PMAA		pH/temperature sensitive non-degradable HG

Finally, two interesting methods of hydrogel scaffold preparation are presented.

Polymer solutions that undergo temperature-induced phase separation have been used for the production of printable hydrogels, as shown in [Figure 10.9](#). Most interesting polymers are those possessing a LCST

temperature close to body temperature, since it is possible to introduce both cells and/or sensitive molecules. Blends are generally printed over a temperature-controlled stage drop-by-drop or as a continuum fiber in multiple layers.

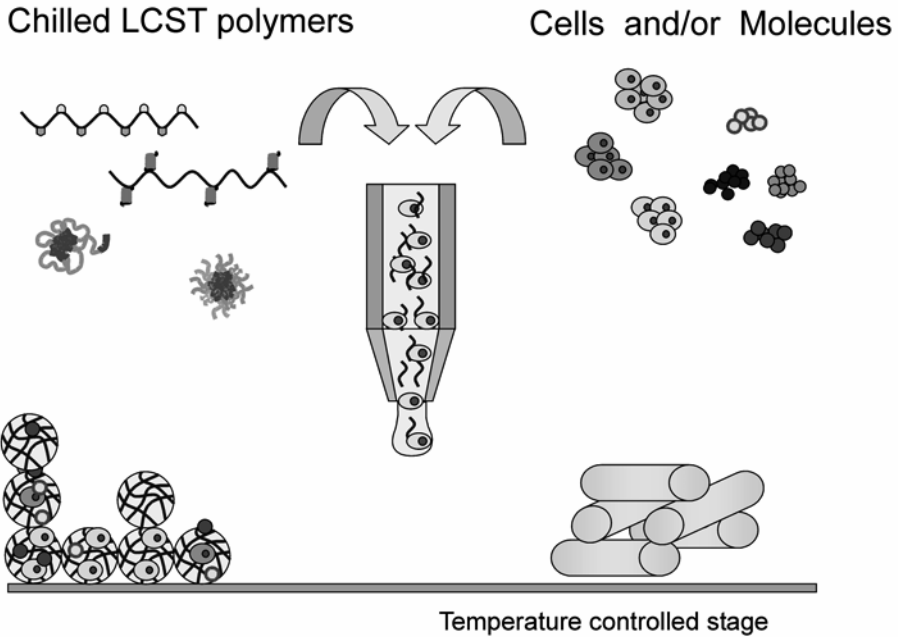


Figure 10.9. Schematic representation of a printable hydrogel.

The other approach to produce hydrogel scaffold reminds a salt leaching technique (Fig. 10.10). In this case, a bed of poly(methyl methacrylate) microspheres (Fig. 10.10.A) will be filled with a monomer solution, which opportunely polymerized, will form a composite matrix (Fig. 10.10.B). Following microspheres dissolution (Fig. 10.10.C), a perfectly ordered porous structure will be obtained.

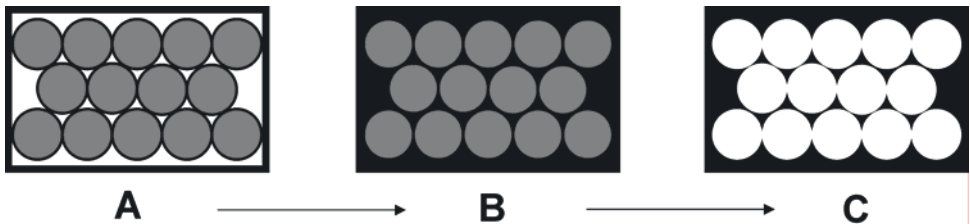


Figure 10.10. Schematic representation of hydrogel scaffold production. Explanation within the text.

Acknowledgements

This work was supported by Fondazione Banco di Sardegna (protocol number 2003.0476) and by MIUR (Prin 2005, protocol number 2005035525).

References and suggested readings

1. Langer R., J.P. Vacanti. Tissue engineering. *Science* **260**(5110):920-926, 1993.
2. Baroli B., Hydrogels for tissue engineering and delivery of tissue-inducing substances, *J. Pharm. Sci.*, **96**(9), 2197-223, 2007.
3. Hoffman A.S., Hydrogels for biomedical applications, *Adv. Drug Deliver. Rev.*, **43**, 3-12, 2002.
4. Chen J., S. Jo, K. Park, Degradable Hydrogels, in *Handbook of biodegradable polymers*, A.J. Domb, J. Kost, D.M. Wiseman (Eds). Hardwood academic publishers, pp. 203-230, 1997.
5. K udela V., Hydrogels, in *Polymers: biomaterials and medical applications*, J.I. Kroschwitz (Ed). John Wiley and Sons, NY, pp 228-252, 1989.
6. Peppas N.A., P. Bures, W. Leobandung, H. Ichikawa, Hydrogels in pharmaceutical formulations, *Eur. J. Pharm. Biopharm.*, **50**(1), 27-46, 2000.
7. Guenet J.M., *Thermoreversible gelation of polymers and biopolymers*. Academic Press, London, 1992.
8. Jeong B., S.W. Kim, Y.H. Bae, Thermosensitive sol-gel reversible hydrogels, *Adv. Drug Deliver. Rev.*, **54**(1), 37-51, 2002.
9. Qiu Y., K. Park, Environment-sensitive hydrogels for drug delivery, *Adv. Drug Deliver. Rev.*, **53**(3), 321-339, 2001.
10. Odian G., *Principles of polymerization*. John Wiley and Sons, Inc., NY, pp 149-150, 1991.
11. Elisseeff J., K. Anseth, D. Sims, W. McIntosh, M. Randolph, R. Langer, Transdermal photopolymerization for minimally invasive implantation, *Proc. Natl Acad. Sci. USA*, **96**(6), 3104-3107, 1999.
12. Nguyen K.T., J.L. West, Photopolymerizable hydrogels for tissue engineering applications, *Biomaterials*, **23**(22), 4307-4314, 2002.
13. Hennink W.E., C.F. van Nostrum, Novel Crosslinking methods to design hydrogels, *Adv. Drug Deliver. Rev.*, **54**(1), 13-16, 2002.
14. Wathier M., C.S. Johnson, T. Kim, M.W. Grinstaff. Hydrogels formed by multiple peptide ligation reactions to fasten corneal transplants, *Bioconjugate Chem.*, **17**(4), 873-876, 2006.
15. Ghosh K., X.D. Ren, X.Z. Shu, G.D. Prestwich, R.A. Clark, Fibronectin functional domains coupled to hyaluronan stimulate adult human dermal fibroblast responses critical for wound healing, *Tissue Eng.*, **12**(3), 601-613, 2006.
16. Rizzi S.C., J.A. Hubbell, Recombinant protein-co-PEG networks as cell-adhesive and proteolytically degradable hydrogel matrixes. Part I: Development and physicochemical characteristics, *Biomacromolecules*, **6**(3), 1226-1238, 2005.

17. Ehrick J.D., S.K. Deo, T.W. Browning, L.G. Bachas, M.J. Madou, S. Danert, Genetically engineered protein in hydrogels tailors stimuli-responsive characteristics, *Nat. Mater.*, **4(4)**, 298-302, 2005.
18. Plunkett K.N., K.L. Berkowski, J.S. Moore, Chymotrypsin responsive hydrogel: application of a disulfide exchange protocol for the preparation of methacrylamide containing peptides, *Biomacromolecules*, **6(2)**, 632-637, 2005.
19. Baroli B., Photopolymerization in drug delivery, tissue engineering and cell encapsulation: issues and potentialities, *J. Chem. Technol. Biotechnol.*, **81(4)**, 491-499, 2006.
20. Zimmermann H., D. Zimmermann, R. Reuss, P.J. Feilen, B. Manz, A. Katsen, M. Weber, F.R. Ihmig, F. Ehrhart, P. Gessner, M. Behringer, A. Steinbach, L.H. Wegner, V.L. Sukhorukov, J.A. Vasquez, S. Schneider, M.M. Weber, F. Volke, R. Wolf, U. Zimmermann, Towards a medically approved technology for alginate-based microcapsules allowing long-term immunoisolated transplantation, *J. Mater. Sci. – Mater. Med.*, **16(6)**, 491-501, 2005.
21. Visted T., R. Bjerkvig, P.O. Enger, Cell encapsulation technology as a therapeutic strategy for CNS malignancies, *Neuro-oncology* **3(3)**, 201-210, 2001.
22. Uludag H., P. De Vos, P.A. Tresco, Technology of mammalian cell encapsulation, *Adv. Drug Deliver. Rev.*, **42(1-2)**, 29-64, 2000.
23. Gombotz W.R., D.K. Pettit, Biodegradable polymers for protein and peptide drug delivery, *Bioconjugate Chem.*, **6(4)**, 332-351, 1995.
24. Dai C., B. Wang, H. Zhao, Microencapsulation peptide and protein drugs delivery system, *Colloids Surf. B - Biointerfaces*, **41(2-3)**, 117-120, 2005.
25. Jayakumar R., N. Nwe, S. Tokura, H. Tamura, Sulfated chitin and chitosan as novel biomaterials, *Int. J. Biol. Macromol.*, **40(3)**, 175-181, 2007.
26. Shi C., Y. Zhu, X. Ran, M. Wang, Y. Su, T. Cheng, Therapeutic potential of chitosan and its derivatives in regenerative medicine, *J. Surg. Res.*, **133(2)**, 185-192, 2006.
27. Berger J., M. Reist, J.M. Mayer, O. Felt, N.A. Peppas, R. Gurny, Structure and interactions in covalently and ionically crosslinked chitosan hydrogels for biomedical applications, *Eur. J. Pharm. Biopharm.*, **57(1)**, 19-34, 2004.
28. Borchard G., Chitosans for gene delivery, *Adv. Drug Deliver. Rev.*, **52(2)**, 145-150, 2001.
29. Chenite A., C. Chaput, D. Wang, C. Combes, M.D. Buschmann, C.D. Hoemann, J.C. Leroux, B.L. Atkinson, F. Binette, A. Selmani, Novel injectable neutral solutions of chitosan form biodegradable gels in situ, *Biomaterials*, **21(21)**, 2155-2161, 2000.
30. Kuo C.K., P.X. Ma, Ionically crosslinked alginate hydrogels as scaffolds for tissue engineering: part 1. Structure, gelation rate and mechanical properties, *Biomaterials*, **22(6)**, 511-521, 2001.
31. Hassan C.M., N.A. Peppas, Structure and morphology of freeze/thawed PVA hydrogels, *Macromolecules*, **33(7)**, 2472-2479, 2000.
32. Gu Z.Q., J.M. Xiao, X.H. Zhang, The development of artificial articular cartilage-PVA-hydrogel, *Biomed. Mater. Eng.*, **8(2)**, 75-81, 1998.
33. Stenekes R.J., H. Talsma, W.E. Hennink, Formation of dextran hydrogels by crystallization, *Biomaterials*, **22(13)**, 1891-1898, 2001.

34. Salem A.K., F.R.A.J. Rose, R.O.C. Oreffo, X. Yang, M.C. Davies, J.R. Mitchell, C.J. Roberts, S. Stolnik-Trenkic, S.J.B. Tendler, P.M. Williams, K.M. Shakesheff, Porous Polymer and Cell Composites That Self-Assemble In Situ, *Adv. Mater.*, **15(3)**, 210-213, 2003.
35. Cao Y., A. Rodriguez, M. Vacanti, C. Ibarra, C. Arevalo, C.A. Vacanti, Comparative study of the use of poly(glycolic acid), calcium alginate and pluronics in the engineering of autologous porcine cartilage, *J. Biomater. Sci. Polym. Ed.*, **9(5)**, 475-87, 1998.
36. Jeong B., Y.H. Bae, D.S. Lee, S.W. Kim, Biodegradable block copolymers as injectable drug-delivery systems, *Nature*, **388(6645)**, 860-862, 1997.
37. Chu B., Structure and Dynamics of Block Copolymer Colloids, *Langmuir*, **11(2)**, 414-421, 1995.
38. Alexandridis P., J.F. Holzwarth, T.A Hatton, Micellization of Poly(ethylene oxide)-Poly(propylene oxide)-Poly(ethylene oxide) Triblock Copolymers in Aqueous Solutions: Thermodynamics of Copolymer Association, *Macromolecules*, **27(9)**, 2414-2425, 1994.
39. Shah J.C., Y. Sadhale, D.M. Chilukuri, Cubic phase gels as drug delivery systems, *Adv. Drug Deliver. Rev.*, **47(2-3)**, 229-250, 2001.
40. Bromberg L.E., E.S. Ron, Temperature-responsive gels and thermogelling polymer matrices for protein and peptide delivery, *Adv. Drug Deliver. Rev.*, **31(3)**, 197-221, 1998.
41. Lin W.C., D.G. Yu, M.C. Yang, Blood compatibility of novel poly(gamma-glutamic acid)/polyvinyl alcohol hydrogels, *Colloids Surf. B – Biointerfaces*, **47(1)**, 43-49, 2006.
42. Oh K.S., S.K. Han, Y.W. Choi, J.H. Lee, J.Y. Lee, S.H. Yuk, Hydrogen-bonded polymer gel and its application as a temperature-sensitive drug delivery system, *Biomaterials*, **25(12)**, 2393-2398, 2004.
43. Petrini P., M.C. Tanzi, C.R. Moran, N.B. Graham, Linear poly(ethylene oxide)-based polyurethane hydrogels: polyurethane-ureas and polyurethane-amides, *J. Mater. Sci. – Mater. Med.*, **10(10/11)**, 635-639, 1999.
44. Bray J.C., E.W. Merrill, Poly(vinyl alcohol) hydrogels for synthetic articular cartilage material, *J. Biomed. Mater. Res.*, **7(5)**, 431-443, 1973.
45. Wang C., R.J. Stewart, J. Kopecek, Hybrid hydrogels assembled from synthetic polymers and coiled-coil protein domains, *Nature*, **397(6718)**, 417-420, 1999.
46. Salem A.K., F.R.A.J. Rose, R.O.C. Oreffo, X. Yang, M.C. Davies, J.R. Mitchell, C.J. Roberts, S. Stolnik-Trenkic, S.J.B. Tendler, P.M. Williams, K.M. Shakesheff, Porous polymer and cell composites that self-assemble in situ, *Adv. Mater.*, **15(3)**, 210-213, 2003.
47. Miyata T., N. Asami, T. Urugami, A reversibly antigen-responsive hydrogel, *Nature*, **399(6738)**, 766-769, 1999.
48. Flory P.J., J. Rehner Jr., Statistical mechanics of cross-linked polymer networks. II. Swelling, *J. Chem. Phys.*, **11**, 521-526, 1943.
49. Flory P.J., J. Rehner Jr., Statistical mechanics of cross-linked polymer networks. I. Rubberlike elasticity, *J. Chem. Phys.*, **11**, 512-520, 1943.
50. Flory P.J., *Principles of Polymer Chemistry*, Cornell University Press, Ithaca, 1953.

51. Lustig S.R., N.A. Peppas, Solute diffusion in swollen membranes .9. Scaling laws for solute diffusion in gels, *J. Appl. Polymer Sci.*, **36**, 735-747, 1988.
52. Canal T., N.A. Peppas, Correlation between Mesh Size and Equilibrium Degree of Swelling of Polymeric Networks, *J. Biomed. Mater. Res.*, **23**, 1183-1193, 1989.
53. Ron E.S., L.E. Bromberg, Temperature-responsive gels and thermogelling polymer matrices for protein and peptide delivery, *Adv. Drug Deliver. Rev.*, **31(3)**, 197-221, 1998.
54. Duncan A.C., M.V. Sefton, J.L. Brash, Effect of C4-, C8- and C18-alkylation of poly(vinyl alcohol) hydrogels on the adsorption of albumin and fibrinogen from buffer and plasma: limited correlation with platelet interactions, *Biomaterials*, **18(24)**, 1585-1592, 1997.
55. Gemmell C.H., J.P. Black, E.L. Yeo, M.V. Sefton, Material-induced up-regulation of leukocyte CD11b during whole blood contact: material differences and a role for complement, *J. Biomed. Mater. Res.*, **32(1)**, 29-35, 1996.
56. Llanos G.R., M.V. Sefton, Immobilization of poly(ethylene glycol) onto a poly(vinyl alcohol) hydrogel: 2. Evaluation of thrombogenicity, *J. Biomed. Mater. Res.*, **27(11)**, 1383-1391, 1993.
57. Strzinar I., M.V. Sefton, Preparation and thrombogenicity of alkylated polyvinyl alcohol coated tubing, *J. Biomed. Mater. Res.*, **26(5)**, 577-592, 1992.
58. Llanos G.R., M.V. Sefton, Heparin-poly(ethylene glycol)-poly(vinyl alcohol) hydrogel: preparation and assessment of thrombogenicity, *Biomaterials*, **13(7)**, 421-424, 1992.
59. Kaluzny J.J., W. Jozwicki, H. Wisniewska, Histological biocompatibility of new, non-absorbable glaucoma deep sclerectomy implant, *J. Biomed. Mater. Res. B: Appl. Biomater.*, **81**, 403-409, 2007.
60. Maruoka S., T. Matsuura, K. Kawasaki, M. Okamoto, H. Yoshiaki, M. Kodama, M. Sugiyama, M. Annaka, Biocompatibility of polyvinylalcohol gel as a vitreous substitute, *Curr. Eye Res.*, **31(7-8)**, 599-606, 2006.
61. Shim W.S., J.H. Kim, H. Park, K. Kim, I. Chan Kwon, D.S. Lee, Biodegradability and biocompatibility of a pH- and thermo-sensitive hydrogel formed from a sulfonamide-modified poly(epsilon-caprolactone-co-lactide)-poly(ethylene glycol)-poly(epsilon-caprolactone-co-lactide) block copolymer, *Biomaterials*, **27(30)**, 5178-5185, 2006.
62. Rucker M., M.W. Laschke, D. Junker, C. Carvalho, A. Schramm, R. Mulhaupt, N.C. Gellrich, M.D. Menger, Angiogenic and inflammatory response to biodegradable scaffolds in dorsal skinfold chambers of mice, *Biomaterials*, **27(29)**, 5027-5038, 2006.
63. Chellat F., M. Tabrizian, S. Dumitriu, E. Chornet, P. Magny, C.H. Rivard, L. Yahia, In vitro and in vivo biocompatibility of chitosan-xanthan polyionic complex, *J. Biomed. Mater. Res.*, **51(1)**, 107-116, 2000.
64. Hern D.L., J.A. Hubbell, Incorporation of adhesion peptides into nonadhesive hydrogels useful for tissue resurfacing, *J. Biomed. Mater. Res.*, **39(2)**, 266-76, 1998.
65. Burdick J.A., K.S. Anseth, Photoencapsulation of osteoblasts in injectable RGD-modified PEG hydrogels for bone tissue engineering, *Biomaterials*, **23(22)**, 4315-4323, 2002.

66. Park K.H., K. Na, S.W. Kim, S.Y. Jung, K.H. Park, H.M. Chung, Phenotype of hepatocyte spheroids behavior within thermo-sensitive poly(NiPAAm-co-PEG-g-GRGDS) hydrogel as a cell delivery vehicle, *Biotechnol. Lett.*, **27(15)**, 1081-1086, 2005.
67. Yang F., C.G. Williams, D.A. Wang, H. Lee, P.N. Manson, J. Elisseeff, The effect of incorporating RGD adhesive peptide in polyethylene glycol diacrylate hydrogel on osteogenesis of bone marrow stromal cells, *Biomaterials*, **26(30)**, 5991-5998, 2005.
68. Park K.H., K. Na, S.Y. Jung, S.W. Kim, K.H. Park, K.Y. Cha, H.M. Chung, Insulinoma cell line (MIN6) adhesion and spreading mediated by Arg-Gly-Asp (RGD) sequence conjugated in thermo-reversible gel. *J. Biosci. Bioeng.*, **99(6)**, 598-602, 2005.
69. An Y., J.A. Hubbell, Intraarterial protein delivery via intimately-adherent bilayer hydrogels, *J. Control. Release*, **64**, 205-15, 2000.
70. Hubbell J.A., Hydrogel systems for barriers and local drug delivery in the control of wound healing, *J. Control. Release*, **39**, 305-313, 1996.
71. Elisseeff J., *et al*, Photoencapsulation of chondrocytes in poly(ethylene oxide)-based semi-interpenetrating networks, *J. Biomed. Mater. Res.*, **51**, 164-171, 2000.
72. Jen A.C., M.C. Wake, A.G. Mikos, Hydrogels for cell immobilization, *Biotechnol. Bioeng.*, **50**, 357-364, 1996.
73. Peppas N.A., Y. Huang, M. Torres-Lugo, J.H Ward, J. Zhang, Physicochemical foundations and structural design of hydrogels in medicine and biology, *Annu. Rev. Biomed. Eng.*, **2**, 9-29, 2000.
74. Chiellini F., F. Petrucci, E. Ranucci, R. Solaro, in *Biomedical Polymers and Polymer Therapeutics*, E. Chiellini, J. Sunamoto, C. Migliaresi, R.M. Ottenbrite, D. Cohn, (Eds.), Kluwer, NY, 1999, pp. 63-74.
75. Hennink W.E., *et al*. in *Biomedical Polymers and Polymer Therapeutics*, E. Chiellini, J. Sunamoto, C. Migliaresi, R.M. Ottenbrite, D. Cohn, (Eds.), Kluwer, NY, 2001, pp.3-18.

BIOREACTORS IN TISSUE ENGINEERING

Warren L. Grayson^a, Gordana Vunjak-Novakovic^a, Bojana Obradovic^b

11.1. INTRODUCTION: WHAT ARE TISSUE-ENGINEERING BIOREACTORS?

The underlying philosophy guiding the design and development of advanced bioreactors for tissue engineering purposes is to provide environmental conditions that enable metabolically active cells in three-dimensional (3D) spatial arrangements to reconstruct functional tissues¹. This requires that cells receive adequate supplies of nutrients to maintain their viability, along with ‘relevant’ biological, physiological and mechanical signals to guide their differentiation along a chosen lineage-pathway. These signals are necessarily tissue-specific, and may be determined by characterizing and expressing key properties of the native tissue environments as parameters that can be reconstructed and varied experimentally. Therefore tissue engineering bioreactors serve two major purposes – optimizing transport requirements and providing micro-environmental control – in order to stimulate an agglomeration of cells into forming immature tissue (Fig. 11.1.).

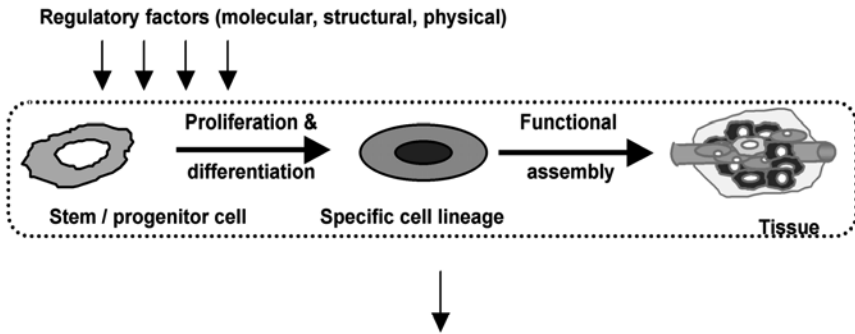
The tissue engineering bioreactors presented in this chapter demonstrate in their overall design a predominantly qualitative understanding of the biological environments within the tissue combined with knowledge of the tissue’s structure and functional mechanics. Universal design elements include improved mass transfer, adequate gas exchange to the bulk culture media, regular replenishment of spent medium, and temperature/pH control. Advanced designs incorporate physiological levels of biophysical stimuli to account for specific structure-function relationships of the tissue and to exert greater influence over cellular differentiation and development into functional tissue-constructs. The examples of tissue engineering

^a Columbia University, New York, NY, U.S.A.

^b Faculty of Technology and Metallurgy, University of Belgrade, Belgrade, Serbia

bioreactors provided illustrate the incorporation of universal requirements and emphasize how design specificity is influenced by tissue types.

Learning from nature...



...and translating into tissue engineering technologies

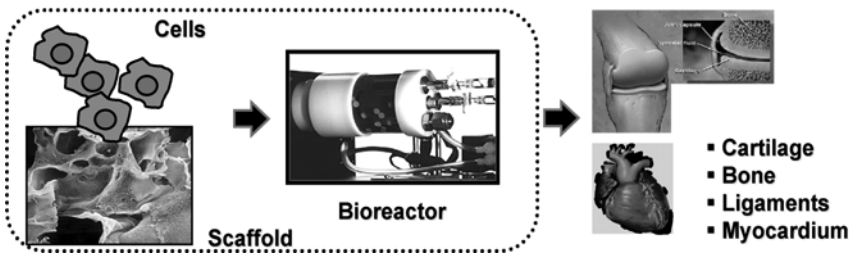


Figure 11.1. Tissue engineering strategy. In the body certain factors guide stem or progenitor cell differentiation and assembly into tissues. One approach to tissue engineering is to adopt the various regulatory factors that guide tissue development *in vivo* and introduce these elements in controlled manner into the *in vitro* cellular microenvironment. *In vitro*, the spatial organization of cells is guided by the scaffolds and regulatory factors are controlled within the bioreactor microenvironment.

11.2. MASS TRANSPORT CONSIDERATIONS

It is challenging to provide efficient mass-transport to cells within tissue constructs. The most influential metabolic factor limiting the *in vitro* growth of tissues is the oxygen concentration as oxygen has low solubility in culture medium. In native tissues, the diffusion of oxygen is limited to less than 200 μm from the closest artery. Oxygen diffusion into tissue constructs is also limiting². Consequently, the size of tissue constructs that can be grown *in vitro* is severely limited by diffusional constraints^{3,4}. Increasing oxygen transport from the bulk of the medium to cells in the inner re-

gions is achieved primarily by providing convectional transport via perfusion or scaffold deformation. However, both perfusion and deformation are heavily dependent on the scaffold's internal architecture and both impart intrinsic mechanical signals to cells. These forces, depending on the cell type, may further stimulate tissue growth or may be detrimental to cell survival. The system design and method of increasing mass transport must therefore be chosen with special consideration to cell type and their ability to withstand biophysical forces. Some examples of different strategies for oxygen supply to the cultivated tissues and cells and mathematical modeling of oxygen transport are presented in the Chapter 12.

11.3. BIOPHYSICAL REGULATION

The cells within various tissues in the body are subjected to mechanical and physiological microenvironments which correlate specifically with the function of the tissue. For example, chondrocytes within cartilage and osteocytes within bone are exposed to deformational compressive loads, cardiomyocytes, neurons and even osteocytes to electrical signals, and fibroblasts in tendons and ligaments to extensional dynamic strains. It has been shown that the application of these intrinsic biophysical signals to cells *in vitro* enhances their differentiation along specific lineages into mature phenotypes⁵. Thus, using bioreactors to apply these stimuli to cells within three-dimensional scaffold arrangements improves the expression of functional tissue phenotypes. Many bioreactors have been developed with the objective of utilizing 'bio-mimetic' approaches to tissue development. For this chapter, three specific examples of bioreactors for engineered bone, cartilage and cardiac tissues are provided.

11.3.1. Engineered Bone

The skeleton is a major structural component within our bodies, bearing considerable load and serving as attachment points for muscles to enable locomotion. Intuitively, it might be expected that compressive forces would be major biophysical stimuli enhancing the development of tissue-engineered bone scaffolds. However, in the native bone, it is hypothesized that cells are not stimulated by the direct compression. Instead, the bending and compression in long bones during various exercises (such as walking) results in interstitial fluid flow in the canalicular spaces, which in turn, imparts shear stresses to osteocytes^{6,7}. It is these forces that provide anabolic stimuli to the cells *in vivo*. A similar mechanism is not possible *in vitro* as cells within scaffolds are not contained within canalicular spaces and gross compression of scaffolds cannot be transduced to cells. Addi-

tionally, the compressive strains experienced in bone are on the order of 0.1 %^{8,9}, which is difficult to impart experimentally since the thickness of tissue-engineered bone constructs are typically on the order of a few millimeters. Hence, bone forming cells within engineered constructs are exposed to convective flow and its associated shear stresses.

Convective flow through scaffolds is achieved using *perfusion bioreactors* and improves nutrient transfer to central regions of constructs^{10,11}. These bioreactors enable controlled flow of culture medium *through* the interstices of porous scaffolds into which bone-forming cells have been seeded¹¹. The scaffolds are confined so that medium is forced directly through the pore spaces in tortuous flow paths dictated by the internal architecture of the scaffolds¹². A ‘bone-bioreactor’ developed in our laboratory enables the perfusion of up to six scaffolds simultaneously (Fig. 11.2). The wells housing the scaffolds are arranged radially so that as culture medium (containing osteogenic supplements) enters through a central core, it is distributed to six channels leading to each of the wells. There are similar pressure drops through each channel and scaffolds with narrow ranges of resistances are chosen to facilitate even distribution of flow. Medium exiting the scaffolds enters a shared ‘reservoir’ and is re-circulated. Using decellularized bone and bone marrow-derived mesenchymal stem cells, it was found that superficial flow-velocities up to 400 $\mu\text{m}/\text{sec}$ enhanced bone formation and tissue distribution¹³. The flow-rates used correlated with estimated shear stresses in the range of 0.007 – 0.01 Pa. This estimate is one or more orders of magnitude lower than estimates for the native tissues (~ 3 Pa)^{6,7,14} or for those used in monolayer studies with osteoblasts (1 – 3 Pa)¹⁵. Yet, after five weeks of culture there was evidence of increased mineralization, and the expression of bone specific markers by the cells.

Other studies have resulted in variable findings. One such study reported considerably lower linear velocities to be detrimental to osteoblast survival¹⁶ while others have shown a dose-dependent response to shear stress¹⁷ with linear velocities up to 640 $\mu\text{m}/\text{sec}$ to be beneficial to tissue formation¹⁸. This emphasizes the need for systematic studies elucidating the upper limits of shear that can be tolerated by cells in scaffolds.

Figure 11.2 Engineered bone. (A) Schematic of perfusion bioreactor with six wells for housing six constructs. Cut-off view (right) depicts the interstitial flow of medium through the scaffolds in the wells. (B) The effects of seeding density and flow-rates on cell distribution in the scaffolds. First row: H&E stains demonstrating that at low-seeding and high flow (LS-HF) cells grow more uniformly throughout the scaffolds than cells grown at low-seeding: low flow (LS-LF) or high seeding-low flow (HS-LF)(scale bar = 1 mm). Second row: Higher magnification images of scaffold edges showing that cells also pack more densely at higher flow rates (scale bars = 200 μm). Third row: SEM images of representative scaffolds (scale bar = 1 mm).

11.3.2. Engineered Cartilage

Articular cartilage is a soft, mostly avascular tissue lining bone ends in synovial joints and providing almost frictionless load bearing. The tissue contains relatively low number of cells (chondrocytes) embedded in abundant extracellular matrix, consisting of a fibrous network of collagen type II and glycosaminoglycan (GAG)-rich proteoglycans. Articular cartilage is exposed to high compressive loads, which it absorbs and distributes to enable joint mobility. The functionality of the native (and engineered) tissues therefore, is characterized primarily by its ability to withstand both static and dynamic compressive forces. Cartilage tissue engineering was investigated in variety of bioreactors including static and mixed flasks, rotating vessels, perfusion cartridges, packed bed bioreactors, and bioreactors with mechanical stimulation¹⁹. Among these, bioreactors with mechanical stimulation were especially designed to imitate the native cell environment and provide dynamic loading to the cultivated tissues²⁰⁻²⁵.

The most outstanding results for mechanically competent engineered cartilage to date have been obtained with the encapsulation of chondrocytes at high densities into hydrogels and maintained in culture medium. The mechanical properties achieved in these systems using various cultivation regimes have been remarkable after eight weeks of culture, even exceeding the stiffness of native cartilage in some cases²⁶. It was seen that providing carefully regulated dynamic loads (mimicking physiological loading) to the constructs enhanced their mechanical properties over this period²⁰. Loading was done utilizing unconfined compression with an impermeable plunger (Fig. 11.3). The parameters for dynamic compression using bioreactors were optimized empirically at 10% strain and 1 Hz for 3 hrs daily²⁷. It was found that longer duty cycles did not improve the mechanical properties of the constructs²⁸. Importantly, it was also shown that the mechanical stimulation of the constructs did not result in higher GAG or collagen contents, suggesting that the major impact of mechanical stimulation was enhanced organization, but not production, of new matrix by cells²⁵.

While the bioreactors are essential for imparting mechanical forces, it should be noted that providing mechanical stimulation in tandem with biological (TGF- β or IGF) factors had synergistic effects on growing constructs²⁴. The timing and duration of these stimuli also affected construct development: When TGF- β is administered only during the first two weeks and then stopped, chondrocyte-laden agarose constructs exhibited enhanced GAG deposition with a correlating increase in mechanical properties^{29,30}. Also, beginning dynamic compression after two weeks of culture rather than day 0 resulted in enhanced properties²⁶.

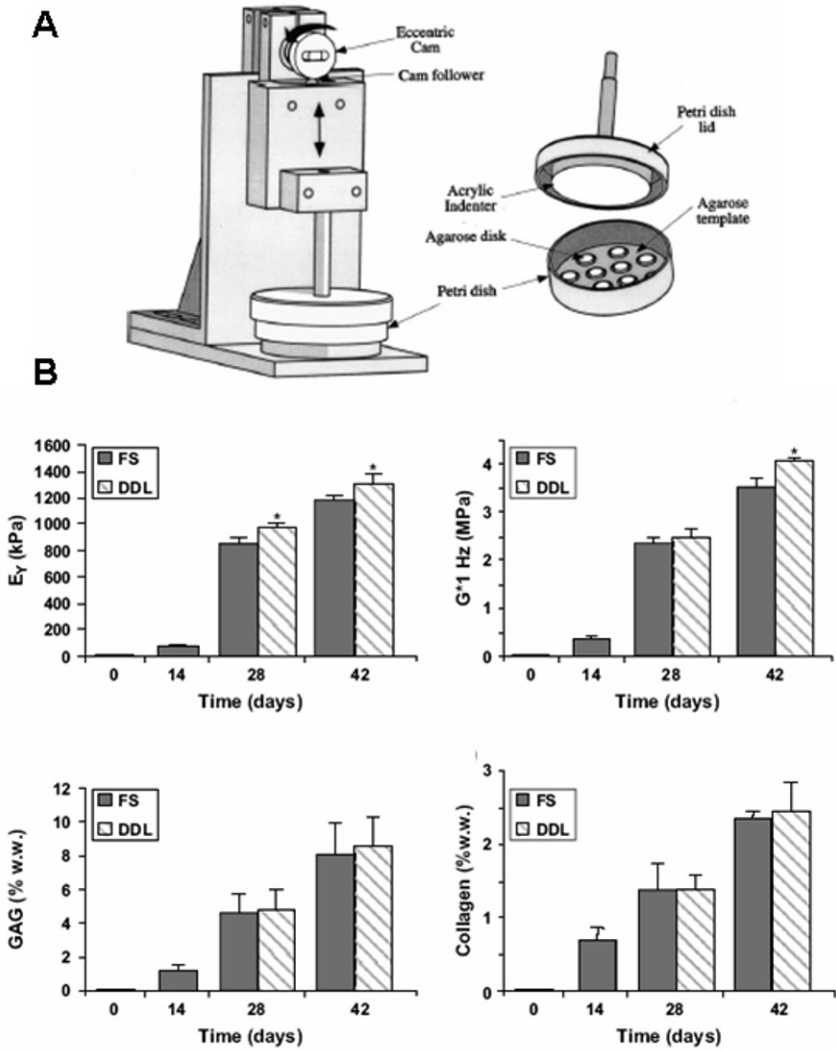


Figure 11.3. Engineered cartilage. (A) Schematic of bioreactor used for dynamic deformational loading (DDL) of chondrocyte-seeded agarose disks. (Reprinted with permission from [27]). (B) The effects of DDL compared to free-swelling (FS) cultures on the development of engineered cartilage constructs is small but significant: (Top left) Young's moduli of engineered cartilage is in the range of native cartilage. However, moduli of DDL constructs at 28 and 42 days are statistically higher than those of FS constructs. (Top right) Comparison of dynamic moduli of DDL and FS constructs. Dynamic modulus of DDL constructs is statistically higher at day 42. (Bottom) GAG and collagen levels are identical for FS and DDL constructs suggesting that the differences in mechanical properties are due to differences in arrangement, but not amount, of matrix molecules. (Adapted with permission from [26]).

11.3.3. Engineered Myocardium

The coordinated contraction of myocytes in the native heart is responsible for pumping thousands of liters of blood through blood vessels daily. The synchronicity of these cells is possible through their intrinsic electro-mechanical coupling, which is specific to their phenotype. The primary characterization of engineered myocardium therefore is their inherent capability to transduce applied electrical signals into a coordinated contractile response. Cardiomyocytes cultured to confluence in tissue culture flasks exhibit localized contractions³¹. Similarly, when encapsulated in collagen sponges at high densities, rat cardiomyocytes are able to contract the sponge significantly in response to an applied electrical stimulation³². However, it has been shown that applying electrical pulses to the collagen-cell constructs over an 8-day period during their cultivation considerably improves the cellular differentiation and tissue development of the constructs³².

The bioreactor employed in this case was a Petri dish modified with two parallel carbon electrodes spaced 6 mm apart along their length to sandwich the collagen sponges (6 mm × 8 mm × 1.5 mm) (Fig. 11.4). Square electrical pulses were applied (2 ms, 1 Hz) at 5 V/cm (above native threshold values). As with the development of cartilage described in the previous section the temporal application of these impulses is also crucial: A three-day delay prior to initiation of electrical stimulation was found to be optimal to construct development. At the end of the cultivation period there was a noticeable difference between stimulated and non-stimulated constructs. Stimulated constructs exhibited 7-fold increases in the fractional change in area of the constructs during each contraction relative to non-stimulated constructs. Electrical stimulation also induced considerable changes in the ultra-structure of the engineered grafts enabling them to appear much more like the native tissues than non-stimulated constructs (Fig. 11.4).

11.4. SUMMARY

Bioreactor technologies have enabled widespread advances in the field of tissue engineering. Numerous examples exist besides those mentioned in the chapter. For example, bioreactors have also been used to engineer blood vessels³³ and ligaments³⁴. Future advances in engineering functional tissues depend in large part on furthering our understanding of the processes guiding fetal tissue development as well as natural healing responses. Such knowledge could enable the design of bioreactors that more precisely control the dose as well as spatial and temporal variations in the

application of signals, stimulating the development of tissues that more closely resemble their native counterparts in structure and function. Bioreactors may also be essential for cultivating large tissues *in vitro*, such as clinically-relevant sizes of engineered bone. Hence, the development of larger, more complex, functional tissues may require the development of even more advanced bioreactors.

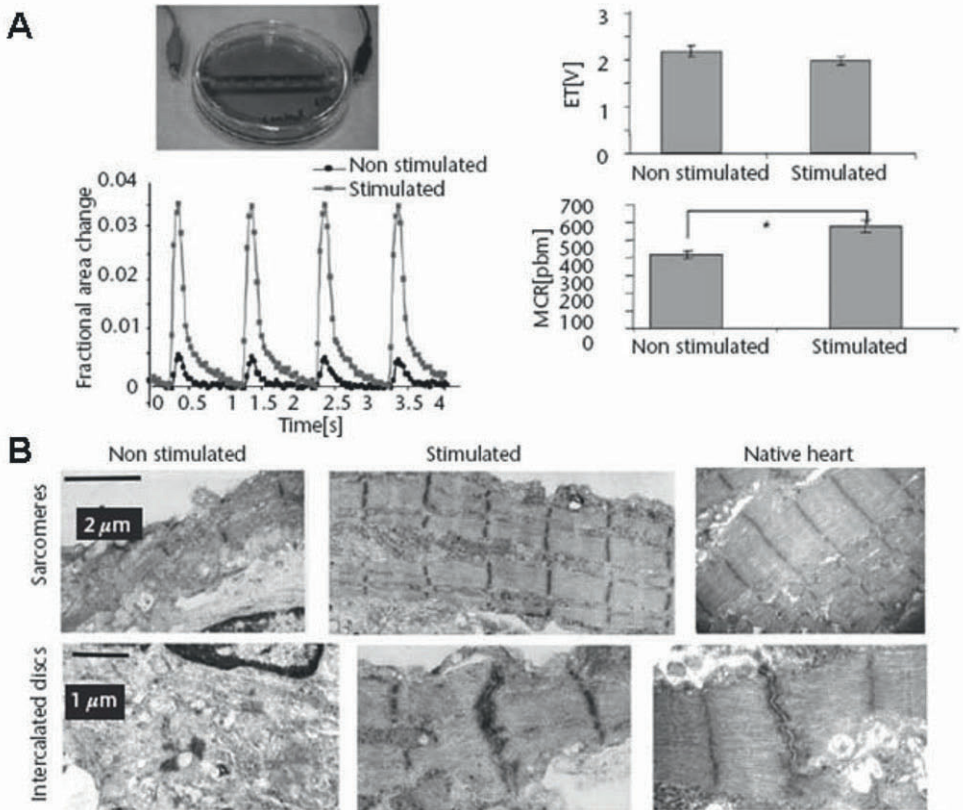


Figure 11.4. Engineered myocardium. (A) (Clockwise from the top left) Bioreactor for electrical stimulation of tissue-engineered cardiac constructs. Seeded collagen constructs are housed between two parallel carbon electrodes. Excitation threshold of stimulated and non-stimulated constructs. Maximum capture rate of stimulated versus non-stimulated constructs. Comparison of fractional area change in surface area during contractions in response to applied electrical stimuli. (B) Comparisons of the ultrastructure of non-stimulated, stimulated and native heart tissues. (Taken with permission from [32]).

Acknowledgements

This work was supported by National Institutes of Health (R01 DE16525, R01 HL076485 and P41-EB002520) awarded to GVN and Mandl Connective Tissue Research Fellowship (WLG).

References

1. Chao P.H.G., W. Grayson, G. Vunjak-Novakovic, Engineering cartilage and bone using human mesenchymal stem cells. *J. Orthop. Sci.* **12**, 398-404, 2007.
2. Griffith L.G., M.A. Swartz, Capturing complex 3D tissue physiology in vitro. *Nature Rev. Mol. Cell Biol.* **7**, 211-224, 2006.
3. Bursac N. et al. Cardiac muscle tissue engineering: toward an in vitro model for electrophysiological studies. *Am. J. Physiol. Heart Circ. Physiol.* **277**, H433-H444, 1999.
4. Martin I., D. Wendt, M. Heberer, The role of bioreactors in tissue engineering. *Trends Biotechnol.* **22**, 80-86, 2004.
5. Freshney R.I., B. Obradovic, W.L. Grayson, C. Cannizzaro, G. Vunjak-Novakovic, Principles of Tissue Culture and Bioreactor Design. in *Principles of Tissue Engineering*, R.P. Lanza, R. Langer, J. Vacanti (eds.), Academic Press, pp. 155 - 181, 2007.
6. You J.D., S.C. Cowin, M.B. Schaffler, S. Weinbaum, A model for strain amplification in the actin cytoskeleton of osteocytes due to fluid drag on pericellular matrix. *Journal of Biomechanics* **34**, 1375-1386, 2001.
7. Han Y.F., S.C. Cowin, M.B. Schaffler, S. Weinbaum, Mechanotransduction and strain amplification in osteocyte cell processes. *Proc Natl Acad Sci U S A*, **101**, 16689-16694, 2004.
8. Rubin C.T., L.E. Lanyon, Regulation of Bone-Formation by Applied Dynamic Loads. *J. Bone Joint Surg. Am.* **66A**, 397-402, 1984.
9. Fritton S.P., K.J. McLeod, C.T. Rubin, Quantifying the strain history of bone: spatial uniformity and self-similarity of low-magnitude strains. *J. Biomechanics* **33**, 317-325, 2000.
10. Glowacki J., S. Mizuno, J.S. Greenberger, Perfusion enhances functions of bone marrow stromal cells in three-dimensional culture. *Cell Transplantation* **7**, 319-326, 1998.
11. Bancroft G.N., V.I. Sikavitsas, A.G. Mikos, Design of a flow perfusion bioreactor system for bone tissue-engineering applications. *Tissue Eng.* **9**, 549-554, 2003.
12. Porter B., R. Zael, H. Stockman, R. Guldberg, D. Fyhrie, 3-D computational modeling of media flow through scaffolds in a perfusion bioreactor. *J. Biomechanics* **38**, 543-549, 2005.
13. Grayson W.L., S. Bhumiratana, C. Cannizzaro, P.H.G. Chao, D.P. Lennon, A.I. Caplan, G. Vunjak-Novakovic, Increased Perfusion Rate and Cell-Seeding Density Enhance Tissue Engineering of Human Bone. *Tissue Eng.*, In Press.
14. Zeng Y., S.C. Cowin, S. Weinbaum, A Fiber-Matrix Model for Fluid-Flow and Streaming Potentials in the Canaliculi of an Osteon. *Ann. Biomed. Eng.* **22**, 280-292, 1994.
15. Jacobs C.R. et al. Differential effect of steady versus oscillating flow on bone cells. *J Biomechanics* **31**, 969-976, 1998.
16. Cartmell S.H., B.D. Porter, A.J. Garcia, R.E. Guldberg, Effects of medium perfusion rate on cell-seeded three-dimensional bone constructs in vitro. *Tissue Eng.* **9**, 1197-1203, 2003.

17. Sikavitsas V.I., G.N. Bancroft, H.L. Holtorf, J.A. Jansen, A.G. Mikos, Mineralized matrix deposition by marrow stromal osteoblasts in 3D perfusion culture increases with increasing fluid shear forces. *Proc Natl Acad Sci U S A*, **100**, 14683-14688, 2003.
18. Bancroft G.N. et al. Fluid flow increases mineralized matrix deposition in 3D perfusion culture of marrow stromal osteoblasts in a dose-dependent manner. *Proc Natl Acad Sci U S A*, **99**, 12600-12605, 2002.
19. Radisic M., B. Obradovic, G. Vunjak-Novakovic, Functional tissue engineering of cartilage and myocardium: bioreactor aspects, in: *Scaffolding in Tissue Engineering*, P.X. Ma, J. Elisseeff (eds.), Marcel Dekker, pp. 491-520, 2005.
20. Mauck R.L. et al. Functional tissue engineering of articular cartilage through dynamic loading of chondrocyte-seeded agarose gels. *J. Biomech. Eng.* **122**, 252-260, 2000.
21. Mauck R.L., S.L. Seyhan, G.A. Ateshian, C.T. Hung, Influence of seeding density and dynamic deformational loading on the developing structure/function relationships of chondrocyte-seeded agarose hydrogels. *Ann. Biomed. Eng.* **30**, 1046-1056, 2002.
22. Demarteau O., M. Jakob, D. Schafer, M. Heberer, I. Martin, Development and validation of a bioreactor for physical stimulation of engineered cartilage. *Biorheology*, **40**, 331-336, 2003.
23. Demarteau O., D. Wendt, A. Braccini, M. Jakob, D. Schafer, M. Heberer, I. Martin, Dynamic compression of cartilage constructs engineered from expanded human articular chondrocytes. *Biochem. Bioph. Res. Co.* **310**, 580-588, 2003.
24. Mauck R.L., S.B. Nicoll, S.L. Seyhan, G.A. Ateshian, C.T. Hung, Synergistic action of growth factors and dynamic loading for articular cartilage tissue engineering. *Tissue Eng.* **9**, 597-611, 2003.
25. Mauck R.L., C.C.B. Wang, E.S. Oswald, G.A. Ateshian, C.T. Hung, The role of cell seeding density and nutrient supply for articular cartilage tissue engineering with deformational loading. *Osteoarth. Cartilage* **11**, 879-890, 2003.
26. Lima E.G. et al., The beneficial effect of delayed compressive loading on tissue-engineered cartilage constructs cultured with TGF-beta 3. *Osteoarth. Cartilage* **15**, 1025-1033, 2007.
27. Hung C.T., R.L. Mauck, C.C.B. Wang, E.G. Lima, G.A. Ateshian, A paradigm for functional tissue engineering of articular cartilage via applied physiologic deformational loading. *Ann. Biomed. Eng.* **32**, 35-49, 2004.
28. Mauck R.L., C.C. Wang, Q.Q. Cheng, N. Gabriel, E.S. Oswald, G.A. Ateshian, C.T. Hung, Optimization of parameters for articular cartilage tissue engineering with deformational loading. in *Trans. ORS 305*, New Orleans, LA, 2003.
29. Byers B.A. et al., Transient TGF-beta3 and constant dexamethasone treatment synergistically enhance maturation and functional properties of chondrocyte-laden hydrogels. in *Trans. ORS Vol. 31*, 794, Chicago, IL, 2006.
30. Byers B.A. et al., Temporal exposure of TGF-beta3 under serum-free conditions enhances biomechanical and biochemical maturation of tissue-engineered cartilage. in *Trans. ORS Vol. 31*, 43, Chicago, IL, 2006.
31. Radisic M. et al., High-density seeding of myocyte cells for cardiac tissue engineering. *Biotechnol. Bioeng.* **82**, 403-414, 2003.

32. Radisic M. et al., Functional assembly of engineered myocardium by electrical stimulation of cardiac myocytes cultured on scaffolds. *Proc Natl Acad Sci U S A*, **101**, 18129-18134, 2004.
33. Niklason L.E. et al., Functional arteries grown in vitro. *Science* **284**, 489-493, 1999.
34. Altman G.H. et al. Advanced bioreactor with controlled application of multi-dimensional strain for tissue engineering. *J Biomech. Eng.* **124**, 742-749, 2002.

APPROACHES TO MATHEMATICAL MODELING OF TISSUE ENGINEERING SYSTEMS

Bojana Obradovic*

12.1. INTRODUCTION

Tissue engineering (TE) is one of the new strategies aiming to address the problem of tissue failure by *in vitro* cultivation of functional tissue equivalents (please see the Chapter 1). Ideally, engineered tissues can serve to replace damaged or diseased tissues providing appropriate tissue composition, biosynthetic activity, full integration with the host tissue, and normal tissue function. In addition, functional constructs can also serve as physiologically relevant models for *in vitro* studies of tissue development and help distinguishing the effects of specific environmental signals (cell derived, biochemical and physical) from the complex milieu of factors present *in vivo*. The ultimate aim of these studies is to establish fundamental correlations between *in vitro* cultivating conditions, cell response, and resulting structural and functional properties of the engineered tissue. Such correlations provide fundamental understanding of processes during the *in vitro* tissue regeneration as well as strategies for design of optimal cultivation conditions.

Mathematical modeling is a valuable tool in the analysis of complex systems, which are thus described by the use of mathematical language. General aims of mathematical modeling could be illustrated by instructions in drawing as in [Figure 12.1](#). In order to represent any complex process in nature we use tools to extract characteristic features important for the particular application. If the aim is to represent the natural object as vivid as possible it will require a lot of skill and effort to

* Faculty of Technology and Metallurgy, University of Belgrade, Belgrade, Serbia.

capture all different features, such as different nonregular shapes, light reflections etc (e.g. Fig. 12.1b).

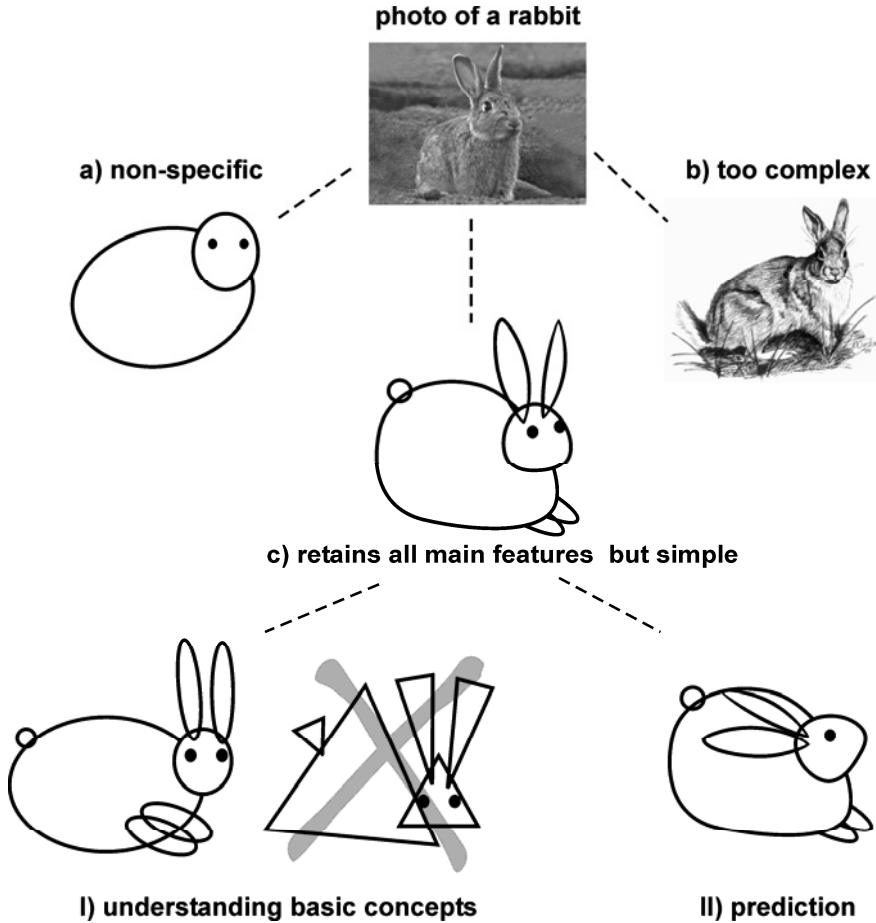


Figure 12.1. Mathematical modeling illustrated by drawings of a rabbit: a) very simple model but non-specific; b) very close to the natural appearance but very complex; c) simple model that is clearly recognized as a drawing of a rabbit. Still, the required level of complexity will depend on the particular application (e.g. artistic drawing vs. a symbol or a logo). Mathematical modeling (I) reveals fundamental concepts of a process such as basic shapes underlying the drawing of a rabbit, and clearly indicates wrong assumptions (e.g. circles and ellipses could form a rabbit shape, while triangles could be skewed and rotated but the shape of a rabbit can not be achieved), and (II) provides means to predict the process behavior in altered situations.

Nevertheless, it should be kept in mind that even such complex drawings are still models since they capture the object at only one level (in the case of a drawing it is a two-dimensional representation of a three-dimensional object). However, in many cases such complex models are not necessary (for instance, if we want to make a drawing of a rabbit for a

child, we will want to make a drawing as simple as possible but still recognizable, as shown in example on Fig. 12.1c). So, in the process of modeling, we reduce the complexity and simplify the features until we come to the suitable representation. Still, it should be noted that the needed level of complexity depends on the desired application.

Main goals of mathematical modeling are fundamental understanding of the process mechanisms and predictions of the process operation and outcomes in the case of an unforeseeable event. Only based on the knowledge of fundamental principles governing a particular process, it is possible to predict how the process will behave in all circumstances. Mathematical modeling aims at defining such principles by (i) formulating the model based on experimental observations and a set of assumptions, (ii) estimating the model parameters, and (iii) validating the model by comparisons of the model predictions with the experimental data. It is important to note that not only the proper mathematical model is important, as the final goal, but also the very process of mathematical modeling is valuable, by helping to distinguish among possible mechanisms and clearly showing non-appropriate assumptions (Fig 12.1).

A mathematical model usually describes a system by a set of variables and a set of equations that establish relationships between the variables. The variables represent some properties of the system, for example, concentrations of chemical species or viable cells, fluid velocity and tissue size. The actual model is the set of functions that describe the relations between different variables. The model also contains parameters, which are used to fit the model to the system that it describes. In conventional modeling using explicit mathematical functions, model parameters are determined by curve fitting. Mathematical modeling of TE systems is generally applied to define at least one of the following: (i) define *in vitro* cultivation conditions, (ii) characterize engineered tissues, and (iii) correlate cultivating conditions to the cell response and tissue properties¹.

In this lecture, the focus will be given to the TE approach based on autologous cells, biodegradable scaffolds, and bioreactors (Fig. 12.2). In this approach, the scaffold serves as a structural and logistic template for tissue development. The structure of the scaffold determines the transport of nutrients, metabolites and regulatory molecules to and from the cells *i.e.* the local cell environment. On the other hand, the bioreactor design governs the overall hydrodynamic, mass and heat transfer conditions at the tissue surfaces^{2,3,4}. In this lecture, basic strategies for characterization of bioreactor cultivating conditions will be outlined and some attempts to formulate mathematical models correlating environmental conditions with the cell response and engineered tissue structure will be presented.

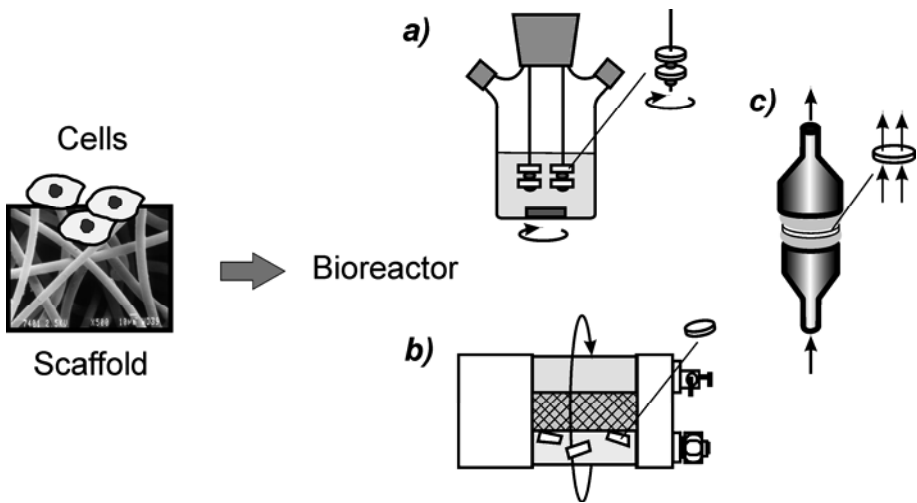


Figure 12.2. Tissue engineering systems: isolated cells are seeded onto polymer scaffolds and cultivated in bioreactors such as a) stirred flask (tissue constructs are fixed and exposed to the turbulent medium flow), b) rotating bioreactor (the bioreactor is rotated such that the tissue constructs are freely suspended in laminar medium flow and settling at a stationary point), c) bioreactor with medium perfusion through the tissue construct (interstitial medium flow through the tissue is provided)^{2,3}.

12.2. CHARACTERIZATION OF *IN VITRO* CULTIVATING CONDITIONS

Functional tissue engineering attempts to recapitulate aspects of the environment present *in vivo* during native tissue development and thereby stimulate the cells to regenerate functional tissues *in vitro*. In order to define the cell microenvironment it is necessary to define both bioreactor conditions and conditions within the scaffold/engineered tissue. Basically, it is necessary to determine hydrodynamic conditions, mass transport rates and velocity, stress, and concentration fields in the culture system. Temperature gradients are usually avoided in tissue cultures but in some cases it may be necessary to solve energy balances and define heat transfer rates, too.

Velocity and stress fields are determined by solving momentum balances in differential form, which provides point-by-point information. Conservation of momentum is based on the Newton's second law of motion and for a nonaccelerating control volume (CV)* it is defined as:

* In analyses of fluids in motion, it is convenient to use the concept of a control volume, which is an arbitrary volume in space through which the fluid flows.

$$\left(\begin{array}{c} \text{sum of all} \\ \text{forces acting} \\ \text{on the CV} \end{array} \right) = \left(\begin{array}{c} \text{momentum} \\ \text{outflow} \end{array} \right) - \left(\begin{array}{c} \text{momentum} \\ \text{inflow} \end{array} \right) + \left(\begin{array}{c} \text{rate of momentum} \\ \text{accumulation} \\ \text{in the CV} \end{array} \right) \quad (12.1)$$

The mathematical formulation of the eq. (12.1) will depend on flow regime and fluid properties in the given system. For laminar flow of an incompressible Newtonian fluid, the eq. (12.1) becomes a well known Navier-Stokes equation.

Concentration fields of chemical species in the bioreactor and the engineered tissue are determined by formulating and solving mass balances in differential forms. Conservation of mass for a control volume is defined as:

$$\left(\begin{array}{c} \text{mass} \\ \text{inflow} \end{array} \right) + \left(\begin{array}{c} \text{mass} \\ \text{produced} \\ \text{in the CV} \end{array} \right) = \left(\begin{array}{c} \text{mass} \\ \text{outflow} \end{array} \right) + \left(\begin{array}{c} \text{rate of mass} \\ \text{accumulation} \\ \text{in the CV} \end{array} \right) \quad (12.2)$$

where it is assumed that the tissue component is produced in the CV. For the components that are consumed in the CV, the second term on the left-hand side of the eq. (12.2) will have the negative sign and will signify the mass consumed in the CV.

In order to solve governing equations for the given system, it is necessary to set initial and boundary conditions, which could also present a difficulty. Some of the frequently used boundary conditions are shown in [Table 12.1](#).

Table 12.1. Examples of boundary conditions frequently used in systems with fluid flow

Boundary condition	Explanation
symmetry	in all axes and planes of symmetry of the system, velocity/ concentration profiles are also symmetrical (velocity/ concentration gradient is 0)
no-slip	at the fluid-solid interfaces, the fluid velocity is equal to the velocity of the solid wall

12.2.1. Hydrodynamic environment

Hydrodynamic factors in the culture system can affect the engineered tissue in at least two ways: via associated effects on mass transport between the developing tissue and culture medium (*e.g.* oxygen, nutrients, growth factors), and by physical stimulation of the cells (*e.g.* shear, pressure). Fluid flow provides convective transport of biochemical species

to the tissue, which is enhanced as compared to the transport by diffusion only in a stagnant fluid. On the other hand, high shear stresses imposed by fluid in motion on tissue surfaces could induce cell dedifferentiation and formation of a fibrous tissue⁵.

In order to define shear and velocity fields in a bioreactor it is necessary to determine the flow regime and then to formulate and solve the overall mass and momentum balances. In TE bioreactors, laminar flow is usually preferred over the turbulent flow regime. Laminar flow occurs at low fluid velocities such that the fluid flows in undisturbed layers and this flow regime is characterized by the molecular mechanism of momentum transfer. Turbulent flow occurs at high velocities and is characterized by high-frequency velocity fluctuations superimposed on the mean fluid motion. Momentum is transferred by random, three-dimensional motions of fluid particles (eddies). The flow regime can be determined by the value of a dimensionless parameter, the Reynolds number, Re :

$$Re = \frac{\rho \bar{\omega} L}{\mu} \quad (12.3)$$

where ρ is the fluid density, μ is the fluid viscosity, $\bar{\omega}$ is the average flow velocity, and L is the characteristic length (for the flow in pipes, it is the pipe diameter). In general, most of the fluid flow found in nature (*e.g.* rivers, winds) is turbulent, while the flow in living organisms (*e.g.* blood flow, urine) is mostly laminar.

TE bioreactor systems usually exhibit complex geometries with engineered tissues disturbing the fluid flow such that the momentum balances, generally described by the eq. (12.1), cannot be solved analytically. For these systems, it is necessary to use numerical methods and computational fluid dynamic (CFD) modeling to obtain shear and velocity fields. An example of fluid flow modeling in a stirred flask with porous, disc-shaped scaffolds for cartilage tissue engineering (Fig 12.2a) is presented in the Box 12.1.

Box 12.1.

In the stirred flask bioreactor, the scaffolds seeded with cells, are threaded onto needles and positioned apart using segments of silicone tubing. Two to four needles with two or three scaffolds apiece are fixed to the stopper and exposed to the culture medium mixed by a magnetic stirrer (Fig. 12.2a). Medium flow is turbulent with the mean fluid velocity of about 5 cm/s and a shear stress of about 0.2 Pa at the tissue surfaces⁶. In order to determine local velocities and shear stresses at the tissue surfaces, a realizable k - ϵ eddy viscosity model⁷ could be applied. The parameter k , the

turbulent kinetic energy, is determined from the momentum balance (eq. 12.1), while the energy dissipation rate, ε , is determined from a new transport equation (Sucosky, unpublished). In addition, since the scaffold is porous until significant amounts of tissue are accumulated, the medium flow through scaffolds was incorporated in the model.

The governing equations were solved using experimentally determined parameters⁸ and the software package FLUENT 6.1. The obtained velocity and shear stress fields for the top scaffold are shown in [Figures 12.3 and 12.4](#), respectively.

Figure 12.3. Predictions of fluid flow: mean-velocity vector and contour fields observed at time $t=0$ in the vicinity of the top scaffold threaded onto the reference needle (the square represents the cross-section of the construct while the circle represents the cross-section of the silicone spacer placed in-between two scaffolds) (Sucosky, unpublished) Please see the Figure on the page 270.

Figure 12.4. Predictions of shear stresses: mean-shear stress magnitudes obtained on two different views of the surface of the top scaffold threaded onto the reference needle. The black arrow indicates the flow direction (Sucosky, unpublished). Please see the Figure on the page 271.

It can be noted that shear and velocity fields are highly non-uniform with inner scaffold surfaces exposed to the highest shear stress. Such flow conditions can be expected to induce a non-uniform tissue development.

12.2.2. Modeling of mass transfer

12.2.2.1. Mass transport through the tissue by diffusion

Mass transfer to the cells in cultivated tissues can be analyzed in terms of internal and external transfer rates. Internal transfer designates the transport of nutrients, regulatory molecules, gases and metabolites within the tissue construct. It depends on scaffold properties and it usually occurs by molecular diffusion. External transfer indicates the transport between the bulk fluid and the tissue surface and it depends on hydrodynamic properties in the bioreactor. The external liquid-solid mass transfer is usually described by the film theory, which assumes that the resistance to mass transport is concentrated in a thin film adherent to the solid surface⁹ ([Fig. 12.5a](#)).

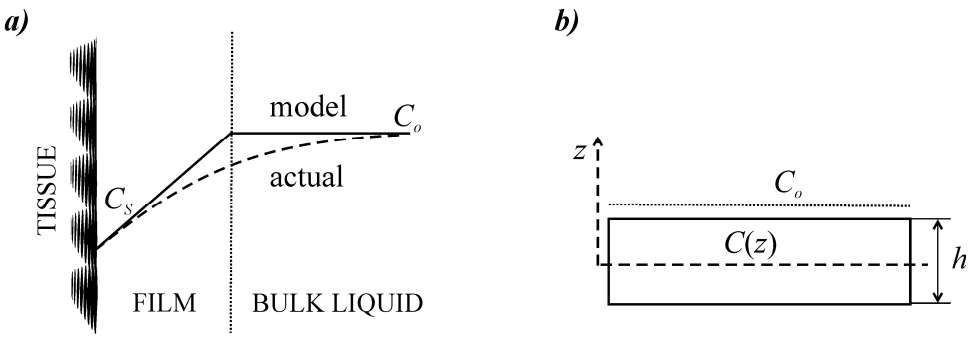


Figure 12.5. Film theory model of liquid-solid mass transfer. a) It is assumed that the concentration change from the bulk liquid (C_o) to the tissue surface (C_s) occurs linearly within a thin film. b) Model of one-dimensional mass transfer from the bulk medium (C_o) to the rectangular construct of a thickness h , in which the concentration is a function of the z coordinate (the construct thickness is considered negligible compared to the length so that the end effects are neglected).

The average molar flux, N , of the species that is transferred from the bulk medium through the film is described as:

$$N = k(C_o - C_s) \quad (12.4)$$

where C_o and C_s are the molar concentrations in the bulk medium and at the tissue surface, respectively, and the parameter k is the mass transfer coefficient in the liquid film and, actually, the ratio of the diffusion coefficient in the liquid and the film thickness.

One of the common methods to evaluate k and the importance of the film mass transfer resistance is based on evaluation of dimensionless parameters. Reynolds number is the ratio of convective to viscous effects and is calculated by the eq. (12.3) in which the length L is a characteristic length for the tissue construct (e.g. for a particle or a cell lump it is the particle/lump diameter). Schmidt number (Sc) is the ratio of the momentum diffusivity (i.e. kinematic viscosity, $\nu = \mu / \rho$) and mass diffusivity:

$$Sc = \frac{\nu}{D_L} \quad (12.5)$$

where D_L is the diffusion coefficient in the liquid phase. The Re and Sc numbers provide an insight in the importance of convection in the bioreactor environment and can be generally related to the parameter k by the Sherwood number (Sh), which is the ratio of external diffusion and mass diffusivity. In two-phase reactors with solid spherical particles, commonly accepted correlation is^{10,11}:

$$\text{Sh} = \frac{k d_p}{D_L} = 2 + 0.6 \text{Re}^{1/2} \text{Sc}^{1/3} \quad (12.6)$$

where d_p is the particle diameter.

This case of mass transport to the tissue and cells can be illustrated by mass transport modeling of a species that is supplied by medium and consumed by cells in the cultivated tissue. For a simplified case of a thin rectangular tissue construct of a thickness h such that the transfer is carried out only through the upper and bottom surfaces in the z direction (Fig. 12.5b), the mass balance is:

$$\frac{\partial C}{\partial t} = D_t \frac{\partial^2 C}{\partial z^2} - Q \quad (12.7)$$

$$\left(\begin{array}{c} \text{rate of} \\ \text{accumulation} \end{array} \right) = \left(\begin{array}{c} \text{net inflow} \\ \text{by diffusion} \end{array} \right) - \left(\begin{array}{c} \text{rate of} \\ \text{consumption} \end{array} \right)$$

where C is the concentration of the species in the tissue, D_t is the diffusion coefficient in the tissue, and Q is the consumption rate by cells. In order to solve the eq. (12.7) it is necessary to set the initial and boundary conditions as given in the Table 12.2. According to the film theory, the mass flux emerging through the tissue surface has to be equal to the flux that is supplied through the film (the boundary condition **a** in the Table 12.2). However, in cases where the consumption rate is much lower than the diffusion rate or where the medium velocity around the tissue is sufficient to diminish the film thickness, mass transfer resistance in the film could be neglected. In these cases, the concentration at the tissue surface can be set as equal to the concentration in the bulk medium (the boundary condition **b** in the Table 12.2).

Table 12.2. Initial and boundary conditions for one-dimensional mass transfer from the bulk medium to the cultivated tissue

Initial conditions	$t = 0$	$0 \leq z < h/2$	$C = C_o$	the concentration within the tissue is equal to that in the culture medium
		$z = 0$	$\frac{\partial C}{\partial z} = 0$	symmetry condition along the tissue axis
Boundary conditions	$t \geq 0$	$z = h/2$	a) $k(C_o - C_s) = D_t \frac{\partial C}{\partial z}$	the flux through the liquid film is equal to the flux through the tissue surface
			b) $C_s = C_o$	the concentration at the tissue surface is equal to that in the bulk medium

In the Box 12.2, a very simple example of one dimensional oxygen diffusion through the cultivated tissue is presented.

Box 12.2.

In the simple case of one-dimensional oxygen diffusion from the bulk medium to the cultivated tissue presented in the Figure 12.5b, oxygen concentration within the tissue could be described by the eq. (12.7). The oxygen consumption rate, Q , depends on the cell distribution in the tissue, which is generally non-uniform and can change over the cultivation time as the cells proliferate or synthesize the extracellular matrix (ECM). So, the oxygen consumption rate as a function of z and t should be known and inserted into the eq. (12.7), which is then numerically solved. In the simplest case, we can assume that the cell distribution through the tissue is uniform and that the oxygen consumption rate is constant. In this case, oxygen is steadily supplied to the tissue and consumed by the cells so that the concentration in the steady state is independent of time and the concentration profile within the tissue is constant. The eq. (12.7) in this case becomes the ordinary, second order, differential equation:

$$\frac{d^2C}{dz^2} = \frac{Q}{D_t} \quad (12.8)$$

In order to estimate the importance of the film resistance, we will assume laminar flow conditions with the medium velocity of 2 cm/s, corresponding to that found in the rotating bioreactor¹² (Fig. 12.2b). In addition, we will consider the cartilage tissue construct, 2 mm thick, and assume the construct thickness as the characteristic length for evaluation of dimensionless parameters. Oxygen consumption rate by cartilage cells can be assumed as $Q = 2.23 \cdot 10^{-4}$ mM/s and oxygen diffusion coefficient in the tissue can be set as half of that in water, $D_t = 1.5 \cdot 10^{-5}$ cm²/s^[13]. The medium properties and the oxygen diffusion coefficient will be assumed as those in water (*i.e.* $\nu = 1 \cdot 10^{-6}$ m²/s; $D_L = 3 \cdot 10^{-5}$ cm²/s) and the oxygen concentration in medium will be set as 0.125 mM (corresponding to that measured in rotating bioreactors and stirred flasks). Re, Sc, and Sh numbers can be calculated according to eqs. (12.3), (12.5), and (12.6), respectively, to yield the value of $k = 4.2 \cdot 10^{-3}$ cm/s. The eq. (12.8) can be readily integrated:

$$\frac{dC}{dz} = \frac{Q}{D_L} z + A_1 \quad (12.9)$$

where A_I is the integration constant. Application of the first boundary condition (Table 12.2) results in $A_I = 0$, while the second boundary condition (condition **a**, Table 12.2), provides estimation of the oxygen concentration at the tissue surface, C_s :

$$C_s = C_o - \frac{Qh}{2k} = 0.120 \text{ mM}$$

The estimated value of the oxygen concentration at the tissue surface is only 4 % lower than the bulk oxygen concentration and shows that in the present case, the rate of oxygen diffusion through the film is much higher than the consumption rate by the cells. So, in this case it is acceptable to apply the boundary condition **b** in the Table 12.2 so that the integration of the eq. (12.9) yields the oxygen concentration profile (Fig. 12.6):

$$C = C_o - \frac{Q}{8D_t} h^2 \left(1 - 4 \frac{z^2}{h^2} \right) \quad (12.10)$$

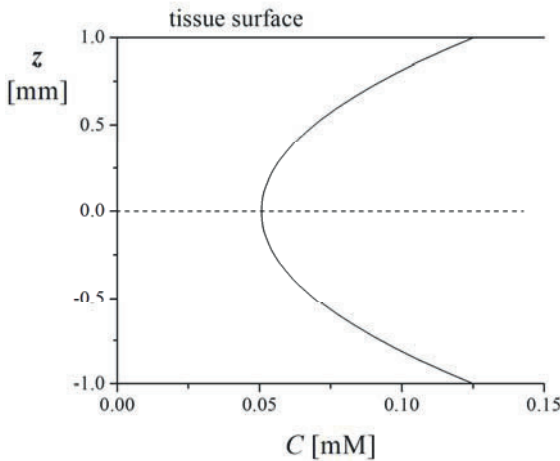


Figure 12.6. Oxygen concentration profile within a cultivated tissue construct: 2 mm thickness, with the constant oxygen consumption rate of $Q = 2.23 \cdot 10^{-4}$ mM/s and the oxygen diffusion coefficient of $D_t = 1.5 \cdot 10^{-5}$ cm²/s, calculated according to the eq. (12.10). For the given set of parameters, O₂ concentration decreases from the value of $C_s = 0.125$ mM in the bulk medium and at the tissue surface to a minimum at the central axis.

Even such a crude model of oxygen transport to the tissue is useful to grossly indicate if the tissue is depleted of oxygen and if the oxygen transfer is a limiting factor for cell survival and proliferation.

12.2.2.2. Enhancement of mass transport through the tissue by convection

For cultivation of cells that demand efficient delivery of particular species such as oxygen in cultures of cardiomyocytes, or specific growth factors in stem cell cultures, mass transport can be enhanced by introduction of fluid flow within the cultivated tissue. In this way, the convective mass transport is provided and carried out by the fluid flow in addition to molecular diffusion. Convective transport through the cultivated tissue can be established in bioreactors with medium perfusion through porous scaffolds seeded with cells (Fig. 12.2c). The scaffolds are secured between two gaskets in a cartridge and perfused by the medium at velocities usually adjusted to correspond to blood velocities in capillaries in native tissues. Such systems were used for tissue engineering of myocardium^{14,15,16}, cartilage^{17,18,19}, and bone^{20,21,22}.

Mass transport through the cultivated tissue in these cases can be illustrated by a mathematical model of oxygen transport and consumption in engineered cardiac constructs²³. The model is based on the standard Krogh cylinder model, which was developed for modeling of oxygen transport through capillaries in muscles. The construct is divided into an array of cylindrical domains, each representing a channel with medium flow surrounded with a tissue space (Fig. 12.7). Only flow in axial, z , direction in the channel lumen is assumed and no convective flow in the tissue region. Both axial and radial diffusion are taken into account in the tissue region with assumptions of a constant cell density and a constant diffusion coefficient.

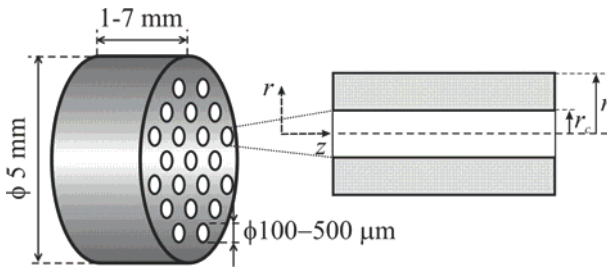


Figure 12.7. Schematics of the tissue construct with a parallel channel array (r_c -channel radius, r_t -one half of the center-to-center spacing between the channels)

At a steady state, oxygen transport through the channels can be described according to:

$$D_L \frac{1}{r} \frac{\partial}{\partial r} \left(r \frac{\partial C_L}{\partial r} \right) - \omega \frac{\partial C_L}{\partial z} = 0 \quad (12.11)$$

$$\left(\begin{array}{c} \text{net inflow} \\ \text{by diffusion} \end{array} \right) - \left(\begin{array}{c} \text{net outflow} \\ \text{by convection} \end{array} \right) = 0$$

where ω is the axial velocity, D_L is the diffusion coefficient in the liquid phase and C_L is the local oxygen concentration in the channel. In the eq. (12.11) only radial diffusion is taken into account while diffusion in axial direction is neglected as compared to the convective transport.

Governing equation for oxygen distribution in the tissue region can be expressed as:

$$D_t \left[\frac{1}{r} \frac{\partial}{\partial r} \left(r \frac{\partial C_t}{\partial r} \right) + \frac{\partial^2 C_t}{\partial z^2} \right] - Q = 0 \quad (12.12)$$

$$\left(\begin{array}{c} \text{net inflow} \\ \text{by diffusion} \end{array} \right) - \left(\begin{array}{c} \text{rate of} \\ \text{consumption} \end{array} \right) = 0$$

where D_t is the diffusion coefficient of oxygen in the tissue space, Q is the oxygen consumption rate and C_t is the local oxygen concentration in the tissue space.

The consumption of oxygen can be described according to Michaelis-Menten kinetics:

$$Q = \frac{Q_m C_t}{C_m + C_t} \quad (12.13)$$

where Q_m is the maximum rate of oxygen consumption, and C_m is the C_t at the half-maximal consumption rate. Boundary conditions are listed in the [Table 12.3](#) for the tissue construct of the length L , the channel radius r_c , and the half distance between centres of two channels r_t .

Table 12.3. Boundary conditions for the porous tissue construct of the length L , channel radius r_c , and half distance between centres of two channels r_t .

	Channel	Tissue annulus	
$z = 0$	$0 \leq r < r_c$ $C_L = C_{in}$	$0 \leq r < r_t$ $C_t = C_{in}$	O ₂ concentration at the construct entrance is equal to that in the inlet medium, C_{in}
$z = L$	$0 \leq r < r_c$ $C_L = C_{out}$	$0 \leq r < r_t$ $C_t = C_{out}$	O ₂ concentration at the construct exit is equal to that in the outlet medium, C_{out}
$0 \leq z \leq L$	$r = 0$ $\partial C_L / \partial r = 0$	$r = r_t$ $\partial C_t / \partial r = 0$	symmetry conditions
$0 \leq z \leq L$ $r = r_c$	$D_L \frac{\partial C_L}{\partial r} = D_t \frac{\partial C_t}{\partial r}$	$C_L = C_t$	equal fluxes of O ₂ at the interface; concentrations of O ₂ in the medium and the tissue are the same

The model was solved using finite element method and a commercial software FEMLAB. Oxygen concentration profiles obtained for one set of parameters for a scaffold seeded with cardiomyocytes are shown in [Figure 12.8](#).

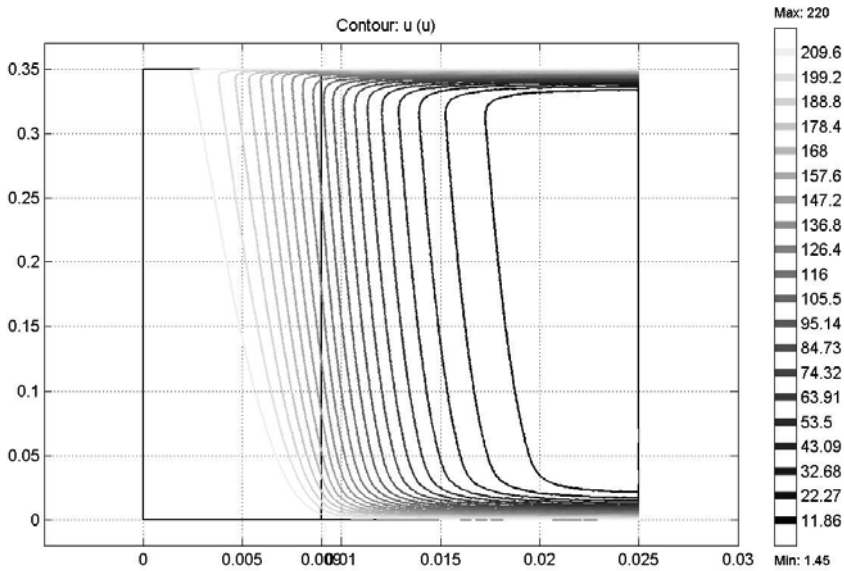


Figure 12.8. Model predictions: oxygen distribution in and around a channel in the cardiac tissue construct of the length $L = 0.35$ cm, channel radius $r_c = 0.09$ mm, and the tissue space radius $r_t = 0.25$ mm. Contours of the constant oxygen concentrations are shown over the tissue length [cm] vs. channel and tissue space radius [cm] (half-channel shown). Dashed line shows the channel-tissue interface. Model parameters: $Q_m = 38 \mu\text{M/s}$; $C_m = 13 \mu\text{M}$; $D_L = 2.4 \cdot 10^{-5} \text{ cm}^2/\text{s}$; $D_t = 2.0 \cdot 10^{-5} \text{ cm}^2/\text{s}$; $C_{in} = 220 \mu\text{M}$; $C_{out} = 190 \mu\text{M}$; average medium velocity in channels $\bar{w} = 1.0 \text{ cm/s}$. (adapted with permission from the Ref. 23)

According to the model, even at high velocities through the tissue ($\sim 1 \text{ cm/s}$), oxygen would be almost completely depleted in the tissue region $\sim 150 \mu\text{m}$ thick around the channel wall, indicating that the minimal wall-to-wall spacing between the channels in a scaffold seeded with cardiomyocytes should be $\sim 300 \mu\text{m}$. At the given velocity, enough oxygen was supplied to the cells for the entire length of the channel. However, if the velocity is decreased in order to decrease the shear rate (*e.g.* to prevent washout of cells immediately after inoculation) the oxygen supply would dramatically decrease indicating that supplementation of the culture medium with oxygen carriers (*e.g.*, perfluorocarbon emulsion) may be necessary for functional cardiac TE^{16,24}.

12.3. CORRELATIONS OF CULTIVATING CONDITIONS WITH THE CELL RESPONSE AND TISSUE PROPERTIES

The final aim of mathematical modeling in TE is development of integrated models relating bioreactor conditions (i.e. flowrate, scaffold geometry and porosity, administration of regulatory molecules) to the cell microenvironment (i.e. local shear stresses and concentrations of regulatory molecules) and tissue responses (i.e. cell proliferation, synthesis of ECM components). The ultimate goal is to identify and optimize cultivation conditions for engineering of functional tissue equivalents.

Development of such models strongly relies on experimental data and tissue characterization that has to be extended to the micro- and molecular levels in order to validate the model predictions and assumptions. In this section, two mathematical models attempting to correlate bioreactor cultivation conditions to the cell response and tissue properties in cartilage TE will be presented.

12.3.1. Correlations of hydrodynamic conditions with the tissue growth

Articular cartilage, as briefly described in the Chapter 11, is an avascular tissue containing only one cell type, the chondrocyte, which generates and maintains the ECM consisting of glycosaminoglycan (GAG)-rich proteoglycans confined within a network of collagen type II fibers²⁵. During the normal function, articular cartilage is exposed to high compressive stresses (as high as 6 – 18 MPa), which are dynamically applied as the joints move during normal daily activities (e.g. walking, sitting, jumping)²⁶. It is thus commonly assumed that biomechanical stimuli will affect the *in vitro* regeneration of functional cartilage tissue (please see examples in the Chapter 11).

Rotating bioreactors (Fig. 12.2b) were shown to promote *in vitro* regeneration of cartilaginous tissue, presumably due to efficient mass transfer and suitable hydrodynamic environment⁵. These bioreactors are configured as two concentric cylinders, the inner of which is porous and covered by a silicone membrane in order to provide gas exchange. The bioreactor is rotated as a solid body around its horizontal axis and tissue constructs are freely suspended in culture medium in the annular space. The rotation rate is adjusted to maintain each construct settling at a stationary point within the bioreactor. The flow conditions were characterized as dynamic and laminar, with tissue constructs settling in a tumble-slide regime associated with fluctuations in fluid pressure, velocity, and shear¹². Cultivation of chondrocytes seeded onto fibrous polyglycolic acid (PGA) scaffolds resulted in engineered tissue constructs

that increased in size and weight over time and regenerated uniformly cartilaginous matrix^{27,5}. The growth of tissue constructs was shown to be carried out by formation of new tissue at the periphery²⁷.

In order to validate the hypothesis of beneficial effects of hydrodynamic environment on cartilage tissue constructs, Lappa²⁸ postulated a model that predicts shear and velocity fields in the rotating bioreactor and relates these fields to the tissue growth. It was assumed that the mass, M , deposited at the tissue surface is proportional to the shear stress, τ , and concentration of some limiting nutrient, C_n , as:

$$\frac{\partial M}{\partial t} \sim \sqrt{\tau} C_n \quad (12.14)$$

Momentum (Navier-Stokes equation) and mass balances for the liquid phase were formulated to define velocity, shear stress and concentration fields and to couple them with the local growth of the tissue given by the eq. (12.14). The model was solved numerically to predict the growth of disc-shaped constructs (initially 5 mm in diameter, 2 mm thick) and the construct shape after 6 weeks of cultivation in rotating bioreactors (Fig. 12.9). Qualitative similarity of the model predictions (Fig. 12.9a) with the experimental results (Fig. 12.9b) could be discerned. In addition, overlay of the construct histological cross-section over calculated velocity and shear stress fields (Fig. 12.10) indicates the highest growth in the areas of higher shear stresses.

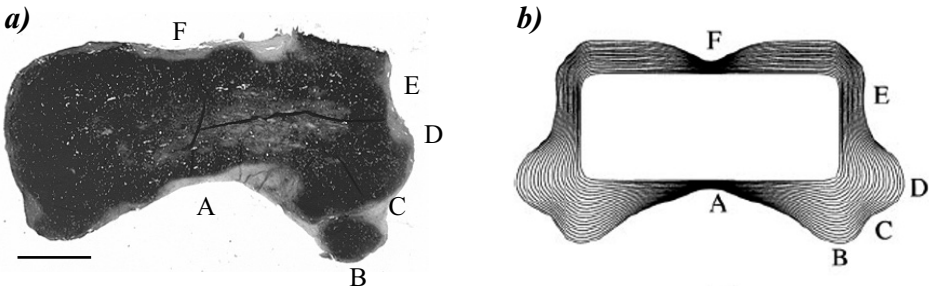


Figure 12.9. Cartilage tissue construct after 6 weeks of cultivation in the rotating bioreactor. a) Histological cross-section stained with safranin O; scale bar: 1 mm. b) Prediction of the tissue growth: snapshots of the construct shape versus time (white rectangular shape indicates the initial construct shape; $\Delta t = 14.5$ h). From Lappa M., Organic tissues in rotating bioreactors: fluid-mechanical aspects, dynamic growth model, and morphological evolution, *Biotechnol. Bioeng.*, **84**, 518-532, 2003, (Ref. 28). Reprinted with permission of Wiley-Liss, Inc., a subsidiary of John Wiley & Sons, Inc.

Figure 12.10. Velocity field (lines) and nondimensional shear stress distribution (color surfaces, $\times 10^{-8}$) at 40 days of cultivation. The experimental histological cross-section of cartilage construct cultured for six weeks has been superimposed on the independently computed tissue-shape and on the velocity and shear stress distributions at the same time. From Lappa M., Organic tissues in rotating bioreactors: fluid-mechanical aspects, dynamic growth model, and morphological evolution, *Biotechnol. Bioeng.*, **84**, 518-532, 2003, (Ref. 28). Reprinted with permission of Wiley-Liss, Inc., a subsidiary of John Wiley & Sons, Inc. Please see the Figure on the page 271.

Results of this modeling study support the hypothesis that optimal hydrodynamic and biomechanical environment could stimulate *in vitro* growth and regeneration of functional cartilaginous tissues.

12.3.2. Mathematical model of GAG accumulation in engineered cartilage constructs

Skeletally mature articular cartilage is an avascular tissue that is supplied by oxygen and nutrients from the synovial fluid (the fluid filling and lubricating joints and cartilage surfaces) by a combination of diffusive and convective transports during joint compression²⁹. In adult cartilage there is thus a steep gradient of oxygen and nutrients such that deep zones are at low oxygen tensions. At these conditions, adult cartilage has practically no capacity for growth or self-repair. In contrast, immature cartilage is vascularized and efficiently supplied with oxygen and nutrients and exhibits high biosynthetic activity. In addition, oxygen concentration in culture medium was shown to significantly affect the *in vitro* chondrogenesis such that low oxygen concentrations (42.7 ± 4.5 mmHg as compared to 86.5 ± 7.3 mmHg) suppressed the growth of both native and engineered cartilage^{30,31}.

In order to interpret experimental findings of tissue growth and ECM deposition and to quantify the effects of oxygen, a mathematical model was formulated, which yielded concentrations of glycosaminoglycan (GAG) as a function of time and position within constructs cultivated in rotating bioreactors¹³. Production of GAG was taken as a marker of chondrogenesis based on previous findings that GAG deposition in engineered constructs coincided with deposition of collagen type II²⁷.

GAG concentration profiles within tissue constructs can be analysed as a function of GAG synthesis by the cells, diffusion of newly synthesised and not yet incorporated and immobilized GAG, and the resulting accumulation within the tissue matrix. The governing equation for GAG distribution within a disc-shaped tissue construct (Fig. 12.11) over cultivation time, t , is:

$$\frac{\partial C_G}{\partial t} = D_G \left(\frac{\partial^2 C_G}{\partial r^2} + \frac{1}{r} \frac{\partial C_G}{\partial r} + \frac{\partial^2 C_G}{\partial z^2} \right) + Q_G \quad (12.15)$$

$$\left(\begin{array}{c} \text{rate of} \\ \text{accumulation} \end{array} \right) = \left(\begin{array}{c} \text{net inflow} \\ \text{by diffusion} \end{array} \right) + \left(\begin{array}{c} \text{rate of} \\ \text{synthesis} \end{array} \right)$$

where r and z are cylindrical coordinates (GAG concentration is independent of θ due to symmetry), C_G is the GAG concentration, D_G is the coefficient of GAG diffusion within the tissue, and Q_G is the rate of GAG synthesis. In healthy cartilage *in vivo*, GAG concentration within the tissue is maintained at a constant level by a balance between GAG synthesis and catabolism³². Accordingly, the GAG synthesis rate was formulated as product inhibited with C_l denoting the maximum GAG concentration, corresponding to that found *in vivo*. In addition, the central hypothesis of the model was that the rate of GAG synthesis depends on the local oxygen concentration (C_{O_2}) according to the first order kinetics. The GAG synthesis rate can be then expressed as:

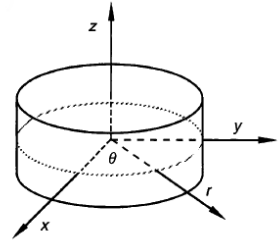


Figure 12.11. Disc-shaped construct: cylindrical coordinates are used (at the construct center: $z, r, \theta = 0$)

$$Q_G = \rho \cdot k \cdot \left(1 - \frac{C_G}{C_l} \right) \cdot C_{O_2} \quad (12.16)$$

where ρ is the cell density, and k is the apparent synthesis rate constant, which incorporated the effects of all other parameters affecting GAG synthesis rate.

Oxygen concentration within the tissue was assumed to be governed by oxygen transport from culture medium to the cells and cellular consumption (Michaelis-Menten kinetics), that is:

$$\frac{\partial C_{O_2}}{\partial t} = D_{O_2} \left(\frac{\partial^2 C_{O_2}}{\partial r^2} + \frac{1}{r} \frac{\partial C_{O_2}}{\partial r} + \frac{\partial^2 C_{O_2}}{\partial z^2} \right) - \rho \cdot \frac{Q_m C_{O_2}}{C_m + C_{O_2}} \quad (12.17)$$

$$\left(\begin{array}{c} \text{rate of} \\ \text{accumulation} \end{array} \right) = \left(\begin{array}{c} \text{net inflow} \\ \text{by diffusion} \end{array} \right) - \left(\begin{array}{c} \text{rate of} \\ \text{consumption} \end{array} \right)$$

where D_{O_2} is the oxygen diffusion coefficient in constructs, Q_m is the maximum rate of oxygen consumption, and C_m is the C_{O_2} at the half-maximum consumption rate. The model also incorporated experimentally

observed growth of tissue constructs and temporal changes in the cell density. The initial and boundary conditions are listed in the [Table 12.4](#) with the assumption of negligible external mass transfer resistances.

Model parameters were determined experimentally and the governing equations (eq. (12.15) with incorporated eq. (12.16) for GAG and eq. (12.17) for O_2) were solved numerically.

Table 12.4. Initial and boundary conditions for a disc-shaped construct of a diameter d and thickness h .

Initial conditions	$t = 0$	$0 \leq r < d/2;$ $0 \leq z < h/2$	$C_G = 0$ $C_{O_2} = C_{O_2}^o$	GAG concentration within the construct is negligible; oxygen concentration is equal to that in the bulk medium ($C_{O_2}^o$)
	$t \geq 0$	$r = d/2; 0 \leq z \leq h/2$ $z = h/2; 0 \leq r \leq d/2$	$C_G = 0$ $C_{O_2} = C_{O_2}^o$	GAG and oxygen concentrations at construct surfaces are equal to those measured in the bulk medium
Boundary conditions	$t > 0$	$r = 0;$ $0 \leq z \leq h/2$	$\frac{\partial C_G}{\partial r} = 0$	symmetry conditions $\frac{\partial C_{O_2}}{\partial r} = 0$
		$z = 0;$ $0 \leq r \leq d/2$	$\frac{\partial C_G}{\partial z} = 0$	

The model predicted a gradual decrease of oxygen concentration from the construct surface towards its centre, as a result of oxygen consumption by the cells. Due to the higher total number of cells and larger diffusion distances, the decrease in oxygen concentration was markedly higher in 6-week as compared to 10-day constructs ([Fig. 12.12a](#)).

In order to validate the model, a high-resolution (40 μm) image analysis method was applied to measure the local GAG concentrations in histological tissue sections (Martin et al., 1999). As shown in [Figure 12.12b](#), the qualitative and quantitative agreements of the model predictions with experimental data for both time points were excellent (average SD = ± 0.2 % wet weight GAG). In addition, the model was also validated by satisfactory predictions of GAG concentration profiles in constructs cultivated under low oxygen tension¹³. This modeling study has indicated the importance of oxygen concentration for GAG synthesis, in particular in the beginning of cultivation (about first 10 days of culture).

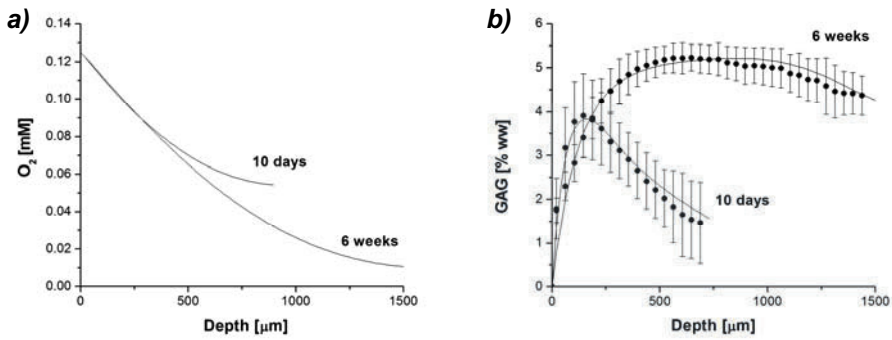


Figure 12.12. Mathematical model predictions: oxygen and GAG concentration profiles within tissue constructs cultivated in rotating bioreactors at medium oxygen concentration of 0.125 mM (80 mmHg). a) Spatial profiles of oxygen distribution after 10 days and 6 weeks of culture (model predictions). b) Spatial profiles of GAG distribution after 10 days and 6 weeks of culture (data points: measured by image processing; lines: model predictions) (adapted with permission from the Ref. 13).

Mathematical models presented here, although only grossly approximating the processes of GAG accumulation and growth of tissue engineered cartilage under *in vitro* conditions, indicated some of the mechanisms and parameters affecting tissue regeneration.

12.4. CONCLUSION

Tissue engineering can potentially provide a basis for systematic, controlled *in vitro* studies of tissue regeneration, growth, and function. Mathematical modeling is a powerful tool for analysis of complex systems and can be used for examination of biological systems in terms of precise equations with well-defined parameters in order to explore complicated biochemical and biophysical mechanisms in a systematic manner. Mathematical modeling in TE is used for (i) assessment of cultivation parameters, (ii) characterization of engineered tissues, and (iii) correlations of *in vitro* cultivation conditions with cell response and tissue structure and function. As information is accumulated about biochemical pathways and cell structure and function, integrated models relating bioreactor macro environment to the cellular microenvironment and intracellular processes could be developed with the aim to provide a tool for understanding and optimizing the cultivation of functional equivalents of native tissues for potential clinical applications.

Acknowledgements

Parts of this text and several figures are adapted from papers of dr M. Lappa, dr P. Succosky, and dr P. Neitzel. This work is supported by the Ministry of Science of the Republic of Serbia, grants 1776 (2001-2005) and 142075 (2006-2010).

Summary objectives

After completing study of this chapter, you should be able to do the following:

- define mathematical modeling;
- define applications and aims of mathematical modeling in TE;
- state conservation laws of momentum and mass in general forms for a CV;
- define flow regimes and the criterion for regime determination;
- define mechanisms of mass transport by diffusion and by convection;
- explain the film theory regarding applications in TE systems;
- state some of the initial and boundary conditions used in TE systems;
- recognize and distinguish among terms in mass balance equations;
- generally describe examples of mathematical modeling of TE systems (approaches, aims, and general findings and significance).

References

1. Obradovic B., M. Radisic, G. Vunjak-Novakovic, Oxygen transport in tissue engineering systems: cartilage and myocardium, *FDMP: Fluid Dynamics and Materials Processing*, **3**, 189-202, 2007.
2. Freed L.E., G. Vunjak-Novakovic, Tissue engineering bioreactors, in: *Principles of Tissue Engineering*, R.P. Lanza, R. Langer, J. Vacanti (eds), Academic Press, pp. 143-156, 2000.
3. Radisic M., B. Obradovic, G. Vunjak-Novakovic, Functional tissue engineering of cartilage and myocardium: bioreactor aspects, in: *Scaffolding in Tissue Engineering*, P.X. Ma, J. Elisseeff (eds.), Marcel Dekker, pp. 491-520, 2005.
4. Freshney R.I., B. Obradovic, W. Grayson, C. Cannizzaro, G. Vunjak-Novakovic, Principles of tissue culture and bioreactor design, in: *Principles of Tissue Engineering*, R.P. Lanza, R. Langer, J. Vacanti (eds.), Elsevier, Inc, pp. 155-183., 2007.
5. Vunjak-Novakovic G., I. Martin, B. Obradovic, S. Treppo, A.J. Grodzinsky, R. Langer, L.E. Freed, Bioreactor cultivation conditions modulate the composition and mechanical properties of tissue engineered cartilage, *J. Orthop. Res.*, **17**, 130-138, 1999.

6. Vunjak-Novakovic G., L.E. Freed, R.J. Biron, R. Langer, Effects of mixing on the composition and morphology of tissue engineered cartilage, *AIChE J.*, **42**, 850-860, 1996.
7. Shih T.H., W.W. Liou, A. Shabbir, J. Zhu., A new $k-\epsilon$ eddy-viscosity model for high Reynolds number turbulent flows - Model development and validation, *Comput. Fluids*, **24**, 227-238, 1995.
8. Sucusky P., D.F. Osorio, J.B. Brown, G.P. Neitzel, Fluid mechanics of a spinner-flask bioreactor, *Biotechnol. Bioeng.*, **85**, 34-46, 2004.
9. Bird B.R., W.E. Stewart, E.N. Lightfoot, *Transport Phenomena*, Wiley, 2006.
10. Obradovic B., V.A. Nedovic, B. Bugarski, R.G. Willaert, G. Vunjak-Novakovic, Immobilised cell bioreactors, in: *Focus on Biotechnology*, Vol. 8a: *Fundamentals of Cell Immobilisation Biotechnology*, V. Nedovic, R.G. Willaert (eds.), Kluwer Academic Publishers, Dordrecht, pp. 411-436, 2004.
11. Martin Y., P. Vermette, Bioreactors for tissue mass culture: design, characterization, and recent advances, *Biomaterials*, **26**, 7481-7503, 2005.
12. Freed L.E., G. Vunjak-Novakovic, Cultivation of cell-polymer tissue constructs in simulated microgravity, *Biotechnol. Bioeng.*, **46**, 306-313, 1995.
13. Obradovic B., J.H. Meldon, L.E. Freed, G. Vunjak-Novakovic, Glycosaminoglycan deposition in engineered cartilage: experiments and mathematical model, *AIChE J.* **46**, 1860-1871, 2000.
14. Carrier R.L., M. Rupnick, R. Langer, F.J. Schoen, L.E. Freed, G. Vunjak-Novakovic, Perfusion improves tissue architecture of engineered cardiac muscle, *Tissue Eng.* **8**, 175-188, 2002.
15. Radisic M., L. Yang, J. Boublik, R.J. Cohen, R. Langer, L.E. Freed, G. Vunjak-Novakovic, Medium perfusion enables engineering of compact and contractile cardiac tissue, *Am. J. Physiol. Heart Circ. Physiol.*, **286**, H507-H516, 2004.
16. Radisic M., H. Park, F. Chen, J.E. Salazar-Lazzaro, Y. Wang, R.G. Dennis, R. Langer, L.E. Freed, G. Vunjak-Novakovic, Biomimetic approach to cardiac tissue engineering: Oxygen carriers and channeled scaffolds, *Tissue Eng.*, **12**, 1-15, 2006.
17. Dunkelman N.S., M.P. Zimmer, R.G. Lebaron, R. Pavelec, M. Kwan, A.F. Purchio, Cartilage production by rabbit articular chondrocytes on polyglycolic acid scaffolds in a closed bioreactor system, *Biotechnol. Bioeng.*, **46**, 299-305, 1995.
18. Pazzano D., K.A. Mercier, J.M. Moran, S.S. Fong, D.D. DiBiasio, J.X. Rulfs, S.S. Kohles, L.J. Bonassar, Comparison of chondrogenesis in static and perfused bioreactor culture, *Biotechnol. Prog.*, **16**, 893-896, 2000.
19. Meinel L., B. Obradovic, V. Karageorgiou, M. Radisic, H. Park, L.E. Freed, D. Kaplan, G. Vunjak-Novakovic, Biophysical regulation of adult human mesenchymal stem cells in engineered tissues, Proceedings of the Annual Meeting of the AIChE, San Francisco, Nov. 16-21, 2003, pp. 477d: 1-17.
20. Bancroft G.N., V.I. Sikavitsas, J. van den Dolder, T.L. Sheffield, C.G. Ambrose, J.A. Jansen, A.G. Mikos, Fluid flow increases mineralized matrix deposition in 3D perfusion culture of marrow stromal osteoblasts in a dose-dependent manner, *Proc. Natl. Acad. Sci. U.S.A.*, **99**, 12600-12605, 2002.
21. Meinel L., V. Karageorgiou, R. Fajardo, B. Snyder, V. Shinde-Patil, L. Zichner, D. Kaplan, R. Langer, G. Vunjak-Novakovic, Bone tissue engineering using

- human mesenchymal stem cells: effects of scaffold material and medium flow, *Annals Biomed. Eng.*, **32**, 112–122, 2004.
22. Holtorf H.L., J.A. Jansen, A.G. Mikos, Flow perfusion culture induces the osteoblastic differentiation of marrow stromal cell-scaffold constructs in the absence of dexamethasone, *J. Biomed. Mater. Res.* **72A**, 326-334, 2005.
 23. Obradovic B., M. Radisic, G. Vunjak-Novakovic, Tissue engineering of cartilage and myocardium, in: *Focus on Biotechnology*, Vol. 8b: *Applications of Cell Immobilisation Biotechnology*, V. Nedovic, R.G. Willaert (eds.), Springer Dordrecht, Berlin, Heidelberg, New York, pp. 99-133, 2005.
 24. Radisic M., H. Park, S. Gerecht-Nir, C. Cannizzaro, R. Langer, G. Vunjak-Novakovic, Biomimetic approach to cardiac tissue engineering, *Philos. Trans. Royal Soc. London – B Biol. Sci.*, **362**, 1357-1368, 2007.
 25. Buckwalter J.A., H.J. Mankin, Articular cartilage: degeneration and osteoarthritis, repair, regeneration, and transplantation, *Instr. Course Lect.* **47**, 487-504, 1998.
 26. Ateshian G.A., C.T. Hung, Functional properties of native articular cartilage. In *Functional Tissue Engineering*, F. Guilak, D.L. Butler, S.A. Goldstein, D.J. Mooney (eds.), Springer-Verlag, New York, pp. 46-68, 2003
 27. Freed L.E.; A.P. Hollander, I. Martin, J.R. Barry, R. Langer, G. Vunjak-Novakovic, Chondrogenesis in a cell-polymer-bioreactor system, *Exp. Cell Res.*, **240**, 58-65, 1998.
 28. Lappa M., Organic tissues in rotating bioreactors: fluid-mechanical aspects, dynamic growth model, and morphological evolution, *Biotechnol. Bioeng.*, **84**, 518-532, 2003.
 29. O'Hara B.P., J.P.G. Urban, A. Maroudas, Influence of cyclic loading on the nutrition of articular cartilage, *Ann. Rheum. Dis.*, **49**, 536–539, 1990.
 30. Obradovic B., L.E. Freed, R. Langer, G. Vunjak-Novakovic, Bioreactor studies of natural and engineered cartilage metabolism, Proceedings of the Topical Conference on Biomaterials, Carriers for Drug Delivery, and Scaffolds for Tissue Engineering, N.A. Peppas, D.J. Mooney, A.G. Mikos, L. Brannon-Peppas (eds.), pp. 335-337. AIChE, New York. 1997.
 31. Obradovic B., R.L. Carrier, G. Vunjak-Novakovic, L.E. Freed, Gas exchange is essential for bioreactor cultivation of tissue engineered cartilage, *Biotechnol. Bioeng.*, **63**, 197 1999.
 32. Hascall V.C., J.D. Sandy, C.J. Handley, Regulation of proteoglycan metabolism in articular cartilage, in: *Biology of the synovial joint*, Archer, C.W. (ed.). Harwood Academic Publishers, Chpt 7., 1999.

COMPUTATIONAL MODELING OF TISSUE SELF-ASSEMBLY*

Adrian Neagu^{a,c}, Ioan Kosztin^a, Karoly Jakab^a, Bogdan Barz^a,
Monica Neagu^c, Richard Jamison^a and Gabor Forgacs^{a,b}

13.1. THE MODELING APPROACH TO MORPHOGENESIS

Starting from the beginning of the 20th century, theoretical models of living tissues have evolved along two distinct conceptual lines. The first of these views considers the tissue as a set of discrete, interacting cells, whereas the other treats it as a continuum, and monitors cell densities instead of individual cells¹. Here we briefly describe a few of these models. The interested reader can find further details in the cited literature.

The continuum approach, promoted by Murray and Oster, uses the methods of continuum mechanics and allows for modeling tissues built of realistic numbers of cells (see ref [2], and refs. therein). The distribution of cells of various types throughout the tissue is described in terms of their densities, whereas their morphogenetic rearrangements are treated as fluxes. The method has been applied for studying developmental morphogenesis, dermal wound healing, contraction, scar formation and vasculogenesis¹. The latter phenomenon may occur in vivo via two different mechanisms: (i) *vasculogenesis*, a term used for de novo vessel

* Article published as: Neagu A, Kosztin I, Jakab K, Barz B, Neagu M, Jamison R, Forgacs G. (2006) *Modern Physics Letters B*, 20:1217-1231, DOI: 10.1142/S0217984906011724, <http://www.worldscinet.com/mplb/mplb.shtml>.

^a Department of Physics and Astronomy, University of Missouri-Columbia, Columbia, MO, U.S.A.

^b Department of Biology, University of Missouri-Columbia, Columbia, MO, U.S.A.

^c Department of Biophysics and Medical Informatics, Victor Babeş University of Medicine and Pharmacy Timișoara, Timișoara, Romania.

formation by the self-assembly of an endothelial cell population, and (ii) *angiogenesis*, the formation of capillary vessels by endothelial cell sprouting from preexisting vessels. (Endothelial cells represent the major component of small blood vessels and line the internal face of large ones. Besides endothelial cells, capillaries also feature attached pericytes, a cell type responsible for the stability of capillary vessels.)

Growing large, vascularized organ replacements in the laboratory is one of the major challenges of tissue engineering. Therefore, understanding the intimate mechanisms of vasculogenesis is vital for building perfusable tissue constructs. Starting from a cell population randomly distributed on the planar surface of a homogeneous extracellular matrix, the model of Murray et al.² predicts the emergence of interconnected filamentous structures of cells that are similar to a vascular network. The results are in good agreement with in vitro experiments on endothelial cells seeded on Matrigel³.

One of the most important principles of developmental biology, which inspired numerous discrete cell models, is the *differential adhesion hypothesis* (DAH)⁴. It states that (i) cell adhesion corresponds to cell-type-dependent energies and (ii) the constituent cells of a tissue are motile enough to reach the lowest energy configuration. The DAH withstood the test of time, being confirmed by many experiments. This principle leads to a close analogy between true liquids and living tissues made of adhesive and motile cells, such as most embryonic and some artificial tissues⁵.

A considerable number of discrete cell models rely on DAH. Monte Carlo simulations of the large- N Potts model from statistical physics reproduced experimental findings regarding the segregation of different cell populations and the mutual engulfment of adjacent tissue fragments⁶. In this model the tissue is represented on a lattice, each cell spans several lattice sites, and has a unique identification number; the average number of sites per cell is maintained around a target value via an elastic energy term containing a Lagrange multiplier. The simulations are based on the Metropolis algorithm, accounting for cell migration and shape changes in systems made of up to several thousand cells⁷. These simulations suggested that cell motility may be ascribed to an effective, temperature-like parameter⁸.

Recent computational models of in vivo morphogenesis, besides DAH, also include chemical signaling, i.e., chemotaxis, cell differentiation and extracellular matrix production^{9,10}. The process of culmination of the cellular slime mold *Dictyostelium discoideum* under the condition of scarce food supply, was simulated in two dimensions by combining the Glazier and Graner model⁷ with a set of partial differential equations able to describe cAMP signaling. The model is defined by parameters characteristic to the subcellular level and is able to predict phenomena that

involve the self-organization of thousands of cells. In this respect, this model bears the potential to characterize the morphogenetic impact of genes whose function is elucidated at the subcellular level¹⁰. Slime mold aggregation has also been described using a distinct, force-based, three-dimensional (3D) model, in which individual amoebae are treated as viscoelastic ellipsoids with type-dependent adhesion apparatus, intrinsic motility and cAMP-mediated signaling capacity⁹.

13.2. IN SILICO TISSUE ENGINEERING

Tissue engineering (TE) is a rapidly developing field of biomedical research, which aims to repair, replace or regenerate damaged tissues (please see the Chapter 1). It exploits biological morphogenesis, a self-assembly process that gives birth to a large variety of structures in living systems. TE employs a large variety of techniques meant to engage cells into forming tissues¹¹ (see also the web page <http://www.nsf.gov/pubs/2004/nsf0450/>). It is hard to overestimate the importance of the field, given that growing organs in vitro could solve the problem of transplantable organ shortage. TE evolved in close relationship with regenerative medicine, and proved successful in developing various functional organ modules. These may be used for in vivo tissue repair, may promote tissue regeneration, and can also be used for testing new drugs. The clinical success of TE depends on finding a suitable cell source, on optimizing scaffolds or hydrogels that support cell growth, differentiation and assembly, on building bioreactors able to provide physiological conditions for the engineered tissues, and, most importantly, on the development of techniques able to assure long-enough shelf life for the tissue construct to reach the patient¹².

The success of the theoretical methods currently used to describe both in vivo and in vitro rearrangements of cell populations motivated recent attempts of modeling phenomena of interest in TE. In order to be efficient in screening alternative experimental designs and in offering hints for related laboratory studies, computational tissue engineering must properly account for the dynamics of cell populations in the presence of scaffolds and extracellular matrices that on the one hand guide cell behavior and, on the other hand, are subject to degradation and restructuring by cells. Several groups are presently engaged in this endeavor. For example, a recent computational model describes the movement of fibroblasts within an acellular dermal matrix of oriented fibers¹. The simulations predict the dynamics of matrix invasion as a function of various parameters, such as fiber size distribution, packing density, and matrix morphometry. The scaffold is generated by a random walk algorithm and the fibroblast

movement along the fibers is described by a five-state Markovian process of directional change. The hopping of cells between nearby fibers is simulated using the Monte Carlo method. The simulations are remarkable also from the point of view of the computational platform they use, a versatile 3D modeling and animation package, MAYA (Alias, Toronto, ON, Canada; <http://www.alias.com>). It incorporates an onboard programming language, along with physics simulation, visualization, and animation engines. The computational model is meant as a supplement for experimental efforts to streamline the workflow of matrix design.

In the context of bone and cartilage morphogenesis *in vitro*, hierarchical computational techniques have been employed to design anatomically shaped 3D scaffolds with controlled porosity and chemical composition via solid free-form fabrication¹³. The method proved useful for improving the mechanical properties of scaffolds and resulted in accelerated tissue formation.

Computer simulations, serving as proof-of-concept *in silico* experiments, may also speed up the development of new technologies. As an example, we present results related to the modeling of artificial organs built from spheroids containing tens of thousands of cells. The self-assembly of these cell aggregates resembles the fusion of adjacent liquid drops, thus justifying the name of “bioink” given to the cell aggregates used in bioprinters. Their computer-controlled, layer-by-layer deposition into a supportive hydrogel (also referred to as “biopaper”) goes by the name of bioprinting^{14,15}. Model assumptions and parameter estimations are based on experiments. Simulations of similar systems starting from new initial configurations, with same or modified conditions, are used to optimize future experiments. In the following we describe the employed computer simulation method along with some of the obtained results.

13.3. A LATTICE MODEL OF LIVING TISSUES

We first build a lattice model of a system of living cells in a culture medium or an extracellular matrix, and then turn to simulate its evolution using the Metropolis Monte Carlo method.

Our goal is to describe the self-assembly of cells within tissue constructs made of hundreds of thousands of cells. Therefore, in contrast to the Glazier-Graner model^{6,7} our program focuses on the types of particles present on each lattice site rather than following cell shape changes or monitoring the position of individual cells.

For computational simplicity, we discretize the space and represent the biological system on a cubic lattice. Each lattice site is occupied either by a cell, or a similar-sized volume element of the embedding medium.

Figure 13.1 depicts the 2D version of the model that enables us to explain the significance of the terms in the total interaction energy:

$$E = \sum_{i,j} [J(\sigma_{i,j}, \sigma_{i,j+1}) + J(\sigma_{i,j}, \sigma_{i+1,j+1}) + J(\sigma_{i,j}, \sigma_{i+1,j}) + J(\sigma_{i,j}, \sigma_{i+1,j-1})] \quad (13.1)$$

The occupancy of a given site, (i, j) , is specified by a type index, $\sigma_{i,j}$, which can take two values, namely 0 for a medium (type 1) particle, and 1 for a cell (type 2) particle. A given cell interacts with its neighbors either directly, via cell adhesion molecules (e.g., cadherins) or indirectly by binding to extracellular matrix filaments via integrins. In our model adhesivities are associated to contact interaction energies also referred to as bond energies. Note that these bond energies are not to be confused with the binding energies associated to true chemical bonds. The bond energies are effective quantities that besides the energies of the involved chemical bonds also depend on their dynamics. Each term on the right hand side of eq. (13.1) can take the values $J(0,0) = -\varepsilon_{11}$, $J(1,1) = -\varepsilon_{22}$ or $J(1,0) = J(0,1) = -\varepsilon_{12}$. The ε 's are positive quantities and represent the mechanical work needed to disrupt the corresponding bond.

The second law of thermodynamics tells us that such a system will evolve towards the less structured, highest symmetry state that has maximum entropy. In the associated biological problem, however, we are dealing with an open system, so the principle of maximum entropy does not necessarily imply less structure in the emergent cellular pattern. That is why, for example, the differential adhesion hypothesis is not a direct consequence of the second law of thermodynamics. DAH has its origin in experiments like that of Figure 13.2, showing that an irregular tissue fragment placed in a nonadhesive environment spontaneously rounds up, as a liquid droplet would⁵. This experiment indicates that the rearrangement of cells is dictated by interfacial forces: the tissue rounds up in order to minimize the area exposed to the tissue culture medium. (A sphere is the geometrical object of smallest surface area for a given volume).

Figure 13.1. A simplified, two-dimensional square-lattice model. Sites are occupied by cells (green), or volume elements of medium or extracellular matrix (gray). A cell is considered to interact to the same extent with nearest or next-nearest neighbors. Cells interact with adjacent cells (red) and with the surrounding medium (blue). In order to avoid double-counting, only half of the depicted bonds are attributed to the given cell (see eq. 13.1) Please see the Figure on the page 271.

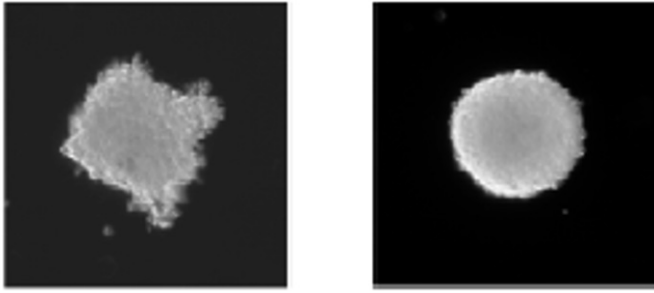


Figure 13.2. Spontaneous rounding of irregular tissue fragments during 24 hours of incubation.

The total interaction energy may be rewritten in terms of interfacial contributions. To this end, consider a configuration of N_1 particles of type 1, out of which N_1^I are located on the 1-2 interface while the rest, N_1^B , reside in the bulk. A similar partitioning may be done for the type 2 particles as well. Thus, eq. (13.1) can be rewritten as

$$E = -\frac{1}{2} \left[N_1^B n_n \epsilon_{11} + N_2^B n_n \epsilon_{22} + \sum_{i_1=1}^{N_1^I} (n_{1i_1} \epsilon_{11} + n_{2i_1} \epsilon_{12}) + \sum_{i_2=1}^{N_2^I} (n_{2i_2} \epsilon_{22} + n_{1i_2} \epsilon_{12}) \right] \quad (13.2)$$

where the factor $1/2$ cancels the double counting of interacting pairs. The dummy index i_1 (i_2) runs over interfacial particles of type 1 (2), whereas n_{1i_1} (n_{2i_1}) stands for the number of type 1 (2) neighbors interacting with the type 1 particle labeled by i_1 . A similar notation holds for the type 2 interfacial particles labeled by i_2 .

The simulations are performed for systems of finite size, such that cells are coaxed to move within the medium. With these boundary conditions, it is technically convenient to maintain an immobile medium layer on the frontier of the system. The contribution to the interaction energy coming from this layer is constant and, therefore, it can be discarded. Thus we are dealing with particles lying in the interior of the system with n_n significant neighbors ($n_n = 8$ in two dimensions and $n_n = 26$ in three dimensions); therefore $n_{1i_1} = n_n - n_{2i_1}$ and $n_{2i_2} = n_n - n_{1i_2}$, which leads to

$$E = -\frac{1}{2} \left[\left(N_1^B + N_1^I \right) n_n \varepsilon_{11} + \left(N_2^B + N_2^I \right) n_n \varepsilon_{22} + \left(\varepsilon_{12} - \varepsilon_{11} \right) \sum_{i_1=1}^{N_1^I} n_{2i_1} + \right. \\ \left. + \left(\varepsilon_{12} - \varepsilon_{22} \right) \sum_{i_2=1}^{N_2^I} n_{1i_2} \right] \quad (13.3)$$

Both sums in eq. (13.3) yield the total number of heterotypic bonds $\sum_{i_1=1}^{N_1^I} n_{2i_1} = \sum_{i_2=1}^{N_2^I} n_{1i_2} = B_{12}$. Indeed, the first is obtained by cumulating the numbers of type 2 particles in the significant neighborhood of each interfacial particle of type 1, whereas the second one is the sum of the numbers of type 1 particles around all type 2 particles from the 1-2 interface. Thus, the total adhesive interaction energy, both in 2D and 3D, becomes

$$E = \gamma_{12} B_{12} - \frac{1}{2} N_1 n_n \varepsilon_{11} - \frac{1}{2} N_2 n_n \varepsilon_{22} \quad (13.4)$$

where B_{12} is the number of 1-2 bonds, directly proportional to the area of the interface, and

$$\gamma_{12} = \frac{\varepsilon_{11} + \varepsilon_{22}}{2} - \varepsilon_{12} \quad (13.5)$$

is the interfacial tension parameter. During simulations that do not include cell proliferation, differentiation and death the last two terms on the right hand side of eq. (13.4) are constant and, therefore, they may be omitted.

Canonical Monte Carlo simulations using $E = \gamma_{12} B_{12}$ yielded results in qualitative agreement with experiments on living tissue self-assembly¹⁴. This expression is remarkable, since it does not depend on the strengths of all types of interactions, but only on their combination, γ_{12} .

In the case of a complex tissue of several cell types and media, the total interaction energy, under the constraint of constant numbers of particles of each type, is given by

$$E = \sum_{\substack{i,j=1 \\ i < j}}^T \gamma_{ij} \cdot B_{ij} \quad (13.6)$$

where T is the number of particle types in the system and $\gamma_{ij} = \frac{1}{2}(\epsilon_{ii} + \epsilon_{jj}) - \epsilon_{ij}$ are the interfacial tension parameters. One can easily show that there are $T(T-1)/2$ independent γ_{ij} parameters.

The *interfacial tension*, σ_{12} , defined as the interaction energy corresponding to the unit area of the interface, may be obtained from γ_{12} by assuming that each of the n_n bonds formed between a cell particle and its neighbors stems from adhesive interactions acting on an average cell membrane area of S_c/n_n , where S_c is the cytoplasmic membrane area of a typical cell from the simulated population. Under this simplifying assumption, which does not take into account the eventuality of the clustering of adhesion molecules, one infers $\sigma_{12} = \gamma_{12} n_n / S_c$.

Tissue surface tension (TST) is defined as the energy of the unit area of interface between a biological tissue and cell culture medium, experimentally accessible via a specially designed parallel plate compression apparatus. During the last decade TST has been measured for several tissue types, and allowed to predict the sorting behavior of heterotypic tissues⁵. In the framework of our lattice model the surface tension of a tissue is given by $\sigma = \epsilon_{22} n_n / (2S_c)$, where the index 1 refers to cell culture medium and 2 to cells, and it has been assumed that ϵ_{11} and ϵ_{12} are negligible in comparison to the cell-cell work of adhesion, ϵ_{22} . Note that the latter may be assessed using the measured values of the tissue surface tension along with an estimate of the cell surface area.

13.4. MONTE CARLO SIMULATIONS OF THE SELF-ASSEMBLY OF LIVING CELLS

A convenient way for studying energetically driven conformational changes of a system is the Monte Carlo method¹⁶. This name stands for a large collection of computational algorithms that involve the use of random numbers. It is important to pay attention to the choice of the random number generator – a numerical algorithm that actually generates pseudo-random numbers. Correlations between the terms of the generated sequence may have important impact on the results. Our simulations are based on a random number generator of L'Ecuyer with Baym–Durham shuffle¹⁷.

Tissue evolution is followed using a version of the Metropolis algorithm adapted for the biological problem at hand. The initial state is constructed based on the known composition and shape of the studied biological system. Then, a conformational change is made by identifying

interfacial cells, picking one of them by chance and exchanging it with an adjacent, randomly chosen, medium particle. The corresponding change of adhesive energy, ΔE , is calculated, and the new conformation is accepted with a probability

$$P = \min(1, \exp(-\Delta E/E_T)) \quad (13.7)$$

The move is readily accepted if it leads to a decrease of the energy. However, in the opposite case, the move may also be accepted albeit with a probability less than one, (given by the Boltzmann factor). In practice this decision is made by generating a random number, r , with uniform distribution between 0 and 1, and accepting the new conformation provided that $r < \exp(-\Delta E/E_T)$.

A Monte Carlo step (MCS) is defined as the sequence of operations during which each interfacial cell has been given the chance to move once.

Such an algorithm is suitable for the study of fluids with velocity-independent interactions¹⁶, therefore it provides a natural framework for investigating the consequences of tissue liquidity. Its technical implementation also requires creativity, since multiple decision steps can be made efficiently by relying on algebraic operations instead of nested *if* statements. For instance, in a system of T types of particles by assigning type indices as $\sigma_1 = 0$ and $\sigma_i = 100^{i-2}$ for $i = 2, \dots, T$, the nature of the neighbors of a given site may be easily inferred from the sum of their type indices. Let us illustrate this in some particular situations: For the highlighted cell of Figure 13.1 this sum would be 3, showing that the cell is surrounded by 3 cells and 5 medium particles. Had one of the adjacent cells been of another type, the sum would have been equal to 102, yielding one neighbor of type 3, two of type 2 and five of type 1.

From the biological point of view the above stochastic rules mean that a cell actively explores its neighborhood, being able to exchange position with adjacent cells or to reorganize the extracellular matrix from their vicinity. The latter process is known to involve both mechanical traction forces and enzymatic activity by matrix metalloproteases (MMPs). The DAH tells that cells are able to keep track of partial success in lowering their adhesive energy by building more/stronger bonds with their surroundings.

In the acceptance probability (eq. 13.7) E_T is a measure of cell motility, the analogue of the energy of thermal fluctuations in true liquids. It is referred to as the energy of biological fluctuations, being related to cytoskeleton-driven cell membrane ruffling, and has been estimated for certain cell types⁸. Our relevant model parameters are the ratios obtained by dividing the interfacial tension parameters by E_T . This implies that a

highly cohesive tissue made of very motile cells is assumed to behave just as a less cohesive one which consists of less motile cells.

Finally, we demonstrate the simulation methods described above in two biologically relevant cases, namely cell sorting and directed self-assembly of cells into constructs of controlled shape.

It is a well known experimental fact that distinct cell types from a cell aggregate spontaneously segregate. Measurements have revealed that in segregated cell aggregates the most cohesive population occupies the central region, being surrounded by the less cohesive one (Fig. 13.3). A measure of tissue cohesivity is its surface tension, an experimentally accessible quantity, which predicts the sorting hierarchy⁵. In the simulations of Figure 13.4 we started with a 3D cell aggregate of linear size of 30 cell diameters, made of about 32000 cells of two different types, in roughly equal amounts, randomly intermixed. Comparison with the experimental result allows to determine the relative magnitudes of the interfacial tension parameters.

Figure 13.3. Starting with a random mix of two distinct cell populations, within a day of incubation in a hanging drop assay the cells sort out, cells of the most adhesive type being surrounded by those of the less adhesive one. The aggregate diameter is about 300 μm . Please see the Figure on the page 271.

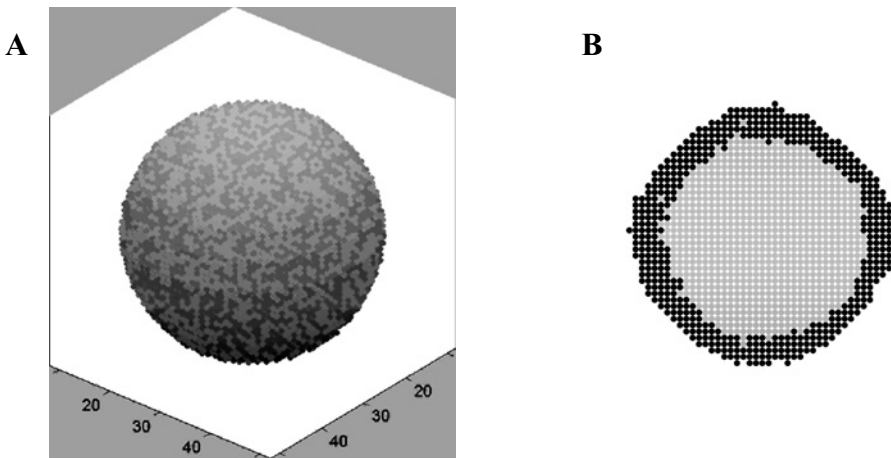


Figure 13.4. Simulation of cell sorting in a 3D aggregate of 16 789 cells of type 2 (light gray) and 16 612 cells of type 3 (dark gray). The surrounding medium (consisting of type 1 particles) is not shown. The initial state (A) contains a random mixture of the two populations, whereas the result of 2×10^5 MCS is a completely sorted equilibrium conformation of the system (B), shown in cross-section. Compare with the experimental result of Figure 13.3. The interfacial tension parameters, expressed in units of E_T are: $\gamma_{12} = 1.5$, $\gamma_{13} = 0.5$, $\gamma_{23} = 0.3$.

Note that the values given in the caption of [Figure 13.4](#) are consistent with the experimental observation that the cell type from the interior has higher adhesivity than that from the periphery. Indeed, according to eq. (13.5) $\gamma_{12} = \varepsilon_{22}/2$ and $\gamma_{13} = \varepsilon_{33}/2$ because the cells do not interact significantly with the cell culture medium (type 1); we conclude that the mechanical work needed to disrupt a bond between two model cells is three times lower in the case of the external (type 3) population ($\varepsilon_{33} = 1; \varepsilon_{22} = 3.$)

Once the parameters are estimated on the basis of experiments, the model may be employed for predicting possible outcomes of the spontaneous self-assembly of cells in a system of complex shape and composition.

In the evolving technology of organ printing, successive layers of cell aggregates and an embedding hydrogel are placed on top of each other and tissue liquidity is supposed to lead to subsequent fusion of the artificial tissue droplets, giving rise to constructs of desired shape. The *in silico* study of post printing cellular rearrangement may offer hints regarding the conditions needed to coax the cells to build the needed configuration. It has been shown that the properties of the supportive hydrogel are vital in this respect¹⁵. This has been verified both *in silico* and *in vitro*. Modeling results are shown in [Figure 13.5a-d](#), whereas the experimental validation is depicted in [Figure 13.5e-h](#).

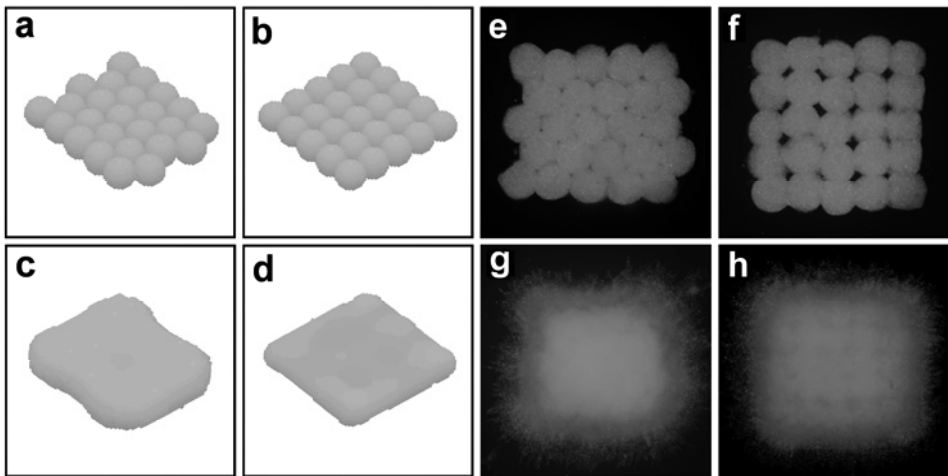


Figure 13.5. Sheet formation depends on the initial configuration and the tissue-matrix interfacial tension. Model cell aggregates, 925 cells each, packed initially in a hexagonal (a) and square lattice (b), after 250,000 MCS evolve into configurations shown in panels c ($\gamma_{cg}/E_T=0.8$) and d ($\gamma_{cg}/E_T=1.4$), respectively. For identical parameters, fusion from the hexagonal initial configuration is considerably faster. Similar structures of 25 aggregates of CHO cells (500 μm in diameter) were embedded in collagen type I (e and f). Compact sheets after 144 hours of incubation are shown in panels g and h.

Spherical cell aggregates prepared from Chinese Hamster Ovary (CHO) cells transfected with N cadherins and histone-attached yellow fluorescent protein (for adhesion and fluorescence microscopy observations, respectively), were embedded in 1.0 mg/ml collagen type I hydrogel in 2D close packed and grid-like geometries (Fig. 13.5e,f). (For a detailed description of the protocol of manufacturing spherical aggregates, see the ref [14]).

Figure 13.6A depicts a model system of a “printed” tubular structure of two cell and two gel types. Suitable energetic conditions, expressed by the values of the interfacial tension parameters that incorporate cell-cell and cell-matrix adhesion energies lead to tissue conformations that are similar to blood vessels (Fig. 13.6B). The plot from Figure 13.7, shows that our algorithm indeed generates conformations of lower and lower energy.

Figure 13.6. Post-printing cell sorting and aggregate fusion in a blood vessel like construct. The initial state (A) consists of 100 cell aggregates, closely packed along a tube of gel (tan). Each cell spheroid contains 257 cells; about 30 % are endothelial (green) cells, randomly intermixed with the smooth muscle (red) cell population. The outcome of the 10^5 MCS simulation (B) indicates that spontaneous endothelialization is possible under suitable energetic conditions. In our model these are expressed by the values of the interfacial tension parameters (see eq. 13.6):

$\gamma_{12} = 1.8, \gamma_{13} = 1.2, \gamma_{14} = 0.7, \gamma_{23} = 0.7, \gamma_{24} = 1.2, \gamma_{34} = 0.4$. Illustrations rendered with the program VMD¹⁸. Please see the Figure on the page 272.

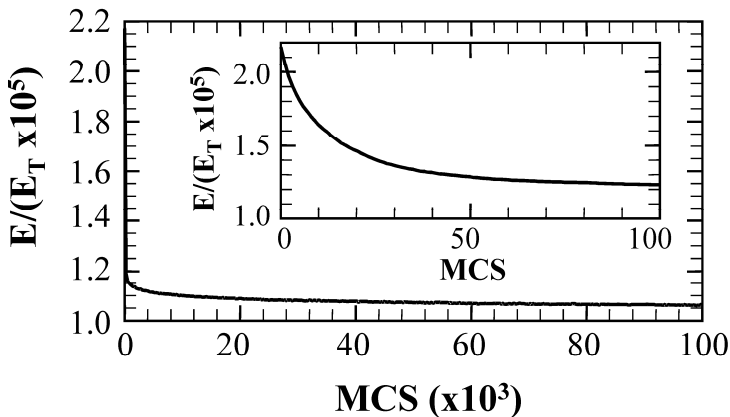


Figure 13.7. The total adhesive energy expressed in units of the biological fluctuation energy, E_T , vs. number of elapsed MCS.

Especially the first hundred MCS, corresponding to cell sorting and adjacent aggregate fusion, result in a sudden drop of the energy (Fig. 13.7,

insert). This is followed by a regime of slow decrease, indicating that the tubular structure of Figure 13.6B is a long-lived metastable state. According to this *in silico* experiment we expect that, provided that the technical difficulties of building such systems in the laboratory can be overcome, the self-assembled tube can be transferred into a pulsed-flow bioreactor that will provide biomimetic conditions for tissue maturation.

Acknowledgements

This work was supported in part by NSF FIBR – 0526854, VIASAN 313/2004 and CEEEX 11/2005.

References

1. Semple J.L., N. Woolridge, C.J. Lumsden, *In vitro*, *in vivo*, *in silico*: Computational systems in tissue engineering and regenerative medicine, *Tissue Eng.* **11**: 341–356, 2005.
2. Murray J.D., D. Manoussaki, S.R. Lubkin, R.B. Vernon, A mechanical theory of *in vitro* vascular network formation, in: *Vascular morphogenesis: In vivo, in vitro, and in mente*, C.D. Little, V. Mironov, E.H. Sage (eds.), Birkhauser, Boston, 1998.
3. Manoussaki D., S.R. Lubkin, R.B. Vernon, J.D. Murray, A mechanical model for the formation of vascular networks *in vitro*. *Acta Biotheoretica* **44**: 271–282, 1996.
4. Steinberg M.S., Reconstruction of tissues by dissociated cells, *Science* **137**: 762–763, 1963.
5. Forgacs G., S.A. Newman, *Biological Physics of the Developing Embryo*. Cambridge University Press, New York, 2005.
6. Graner F., J.A. Glazier, Simulation of biological cell sorting using a two-dimensional extended Potts model, *Phys. Rev. Lett.* **69**: 2013–2016, 1992.
7. Glazier J.A., F. Graner, Simulation of the differential adhesion driven rearrangement of biological cells, *Phys. Rev. E* **47**: 2128–2154, 1993.
8. Beysens D., G. Forgacs, J.A. Glazier, Cell sorting is analogous to phase ordering in fluids. *Proc. Natl. Acad. Sci. USA* **97**: 9467–9471, 2000.
9. Palsson E., H.G. Othmer, A model for individual and collective cell movement in *Dictyostelium discoideum*, *Proc. Natl. Acad. Sci. USA* **97**: 10448–10453, 2000.
10. Maree A.F.M, P. Hogeweg, How amoeboids self-organize into a fruiting body: Multicellular coordination in *Dictyostelium discoideum*, *Proc. Natl. Acad. Sci. USA* **98**: 3879–3883, 2001.
11. Langer R., J.P. Vacanti, Tissue engineering, *Science* **260**: 920–926, 1993.
12. Griffith L.G., G. Naughton, Tissue engineering – Current challenges and expanding opportunities, *Science* **295**: 1009–1014, 2002.

13. Hollister S.J., Porous scaffold design for tissue engineering. *Nature Materials* **4**: 518–524, 2005.
14. Jakab K., A. Neagu, V. Mironov, R.R. Markwald, G. Forgacs, Engineering biological structures of prescribed shape using self-assembling multicellular systems, *Proc. Natl. Acad. Sci. USA* **101**: 2864–2869, 2004.
15. Neagu A., K. Jakab, R. Jamison, G. Forgacs, Role of physical mechanisms in biological self-organization. *Phys. Rev. Lett.* **95**:178104-1 – 4, 2005.
16. Amar J.G., The Monte Carlo method in science and engineering. *Computing in Science & Engineering* **8**: 9-19, 2006.
17. Press W.H., S.A. Teukolsky, W.T. Vetterling, B.P. Flannery, *Numerical Recipes in C⁺⁺: The Art of Scientific Computing*, Third Edition, Cambridge Univ. Press, Cambridge, U.K., pp. 403–418, 2007.
18. Humphrey W., A. Dalke, K. Schulten, VMD - Visual Molecular Dynamics, *J. Molec. Graphics* **14**: 33–38, 1996.

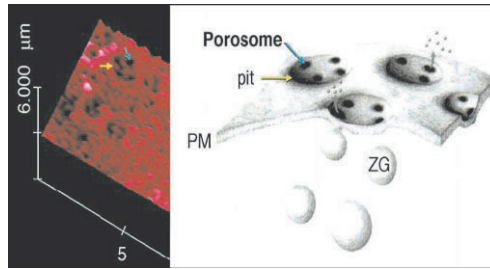


Figure 3.2

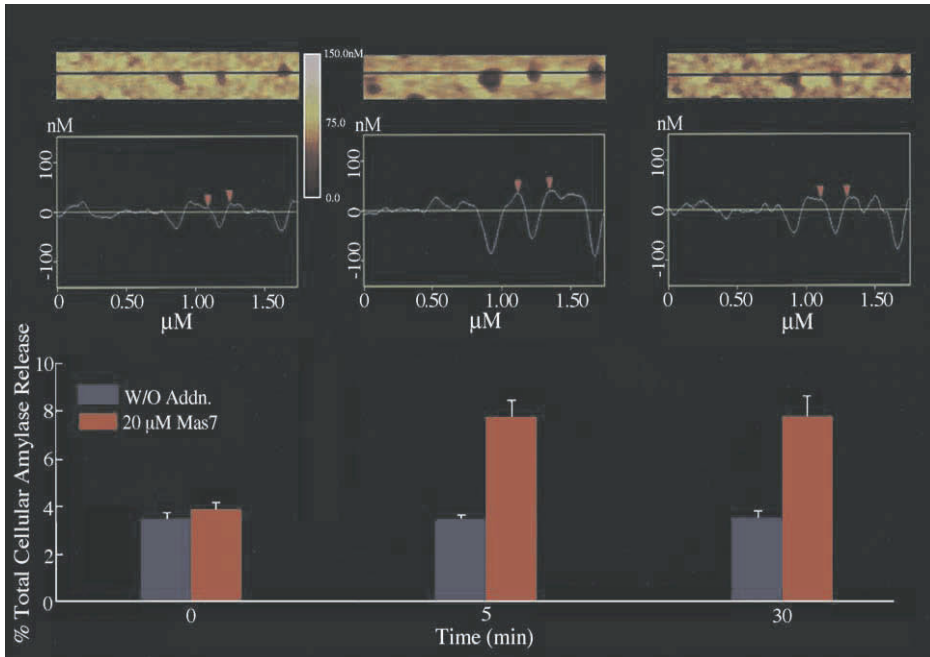


Figure 3.3

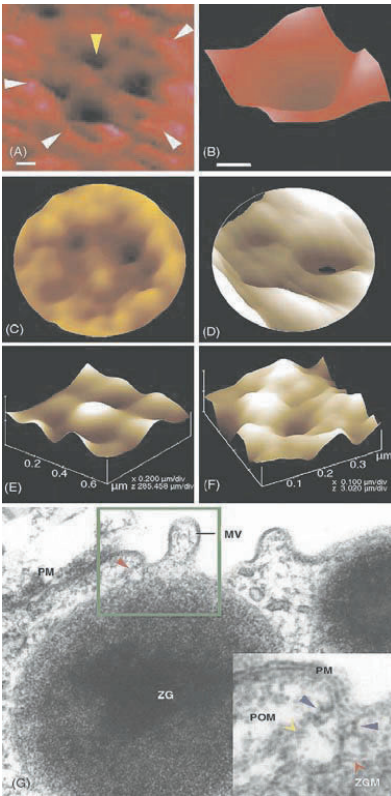


Figure 3.4

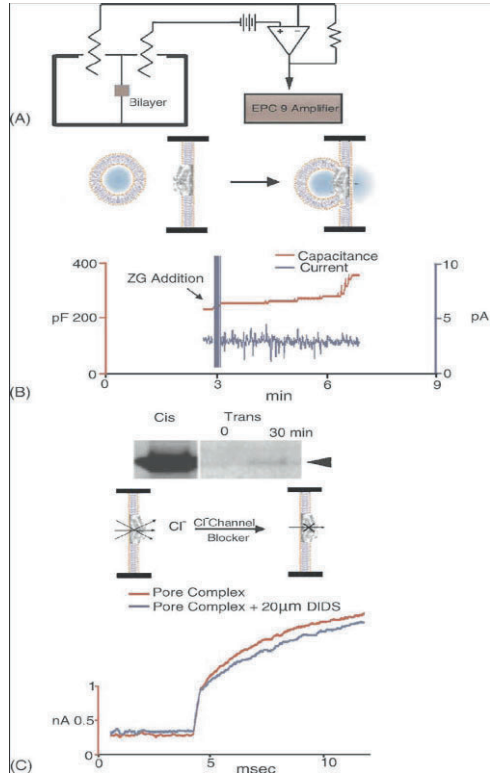


Figure 3.9

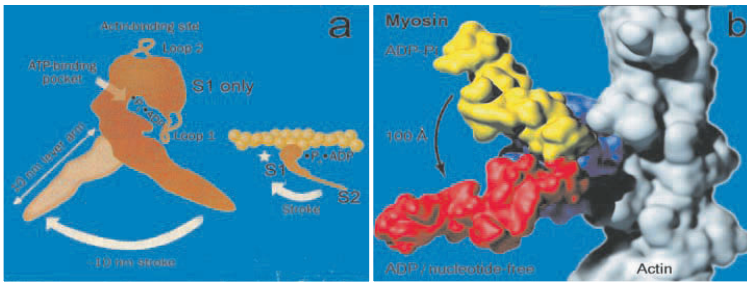


Figure 4.4

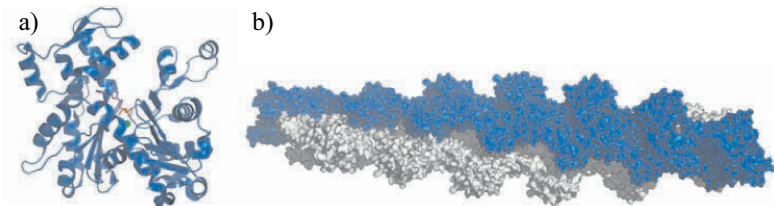


Figure 4.5.

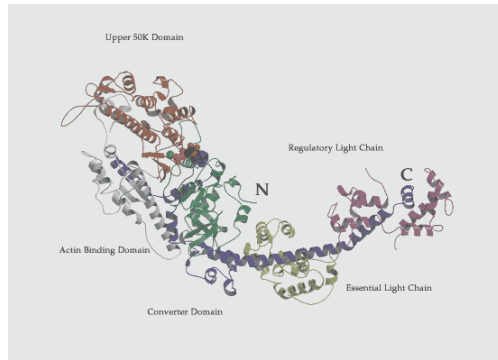


Figure 4.6

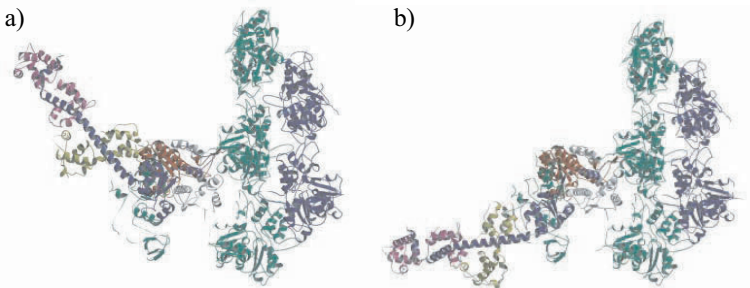


Figure 4.7

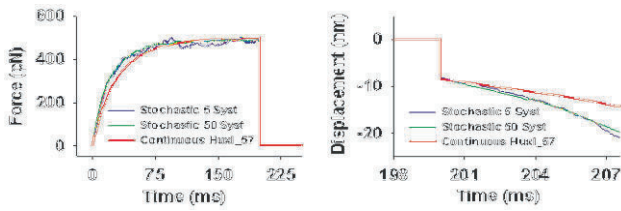


Figure 4.14

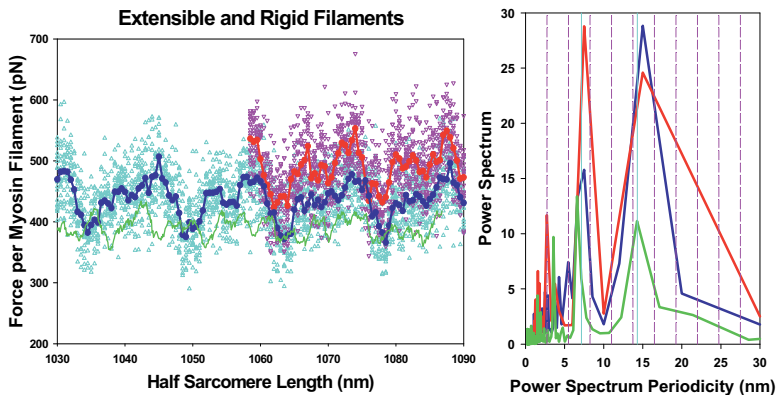


Figure 4.16

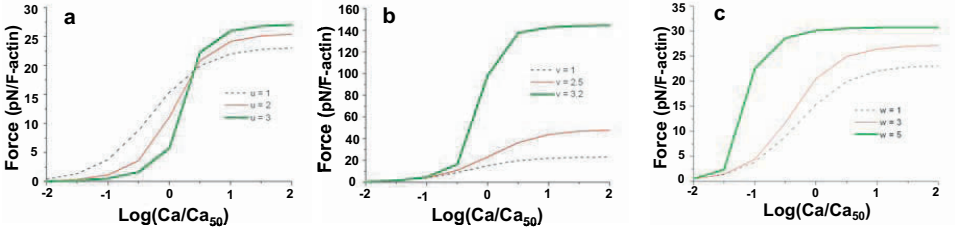


Figure 4.19

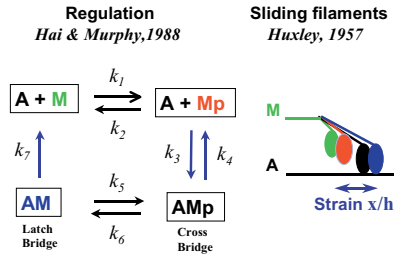


Figure 4.21

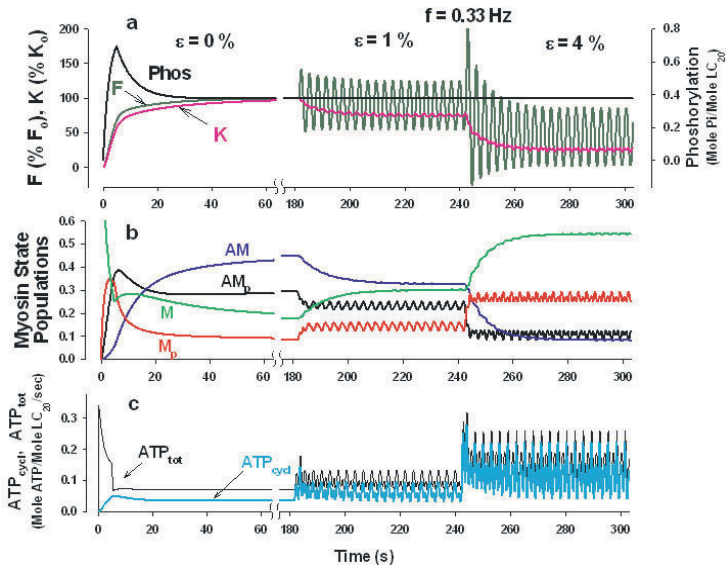


Figure 4.22

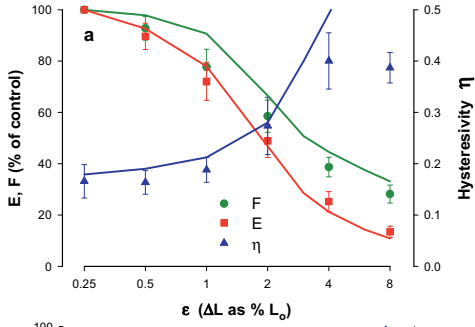


Figure 4.23

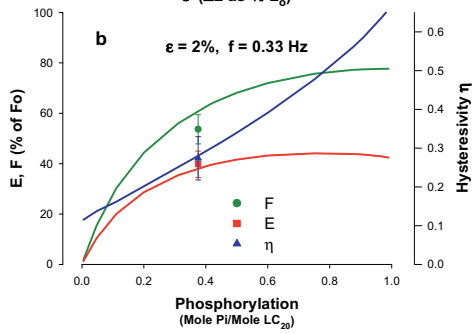


Figure 4.23

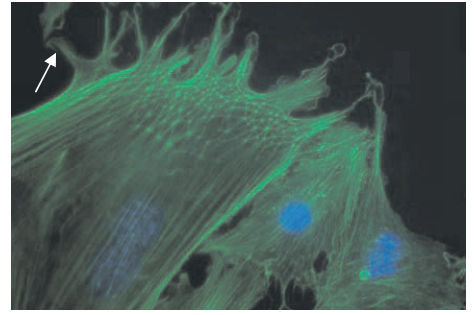


Figure 5.1

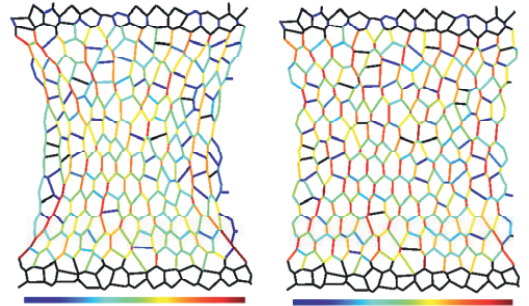


Figure 8.4

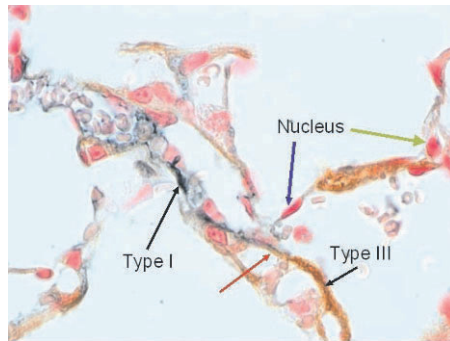


Figure 8.5

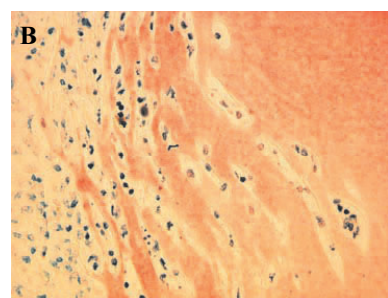
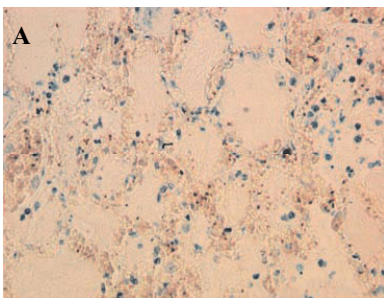


Figure 9.8

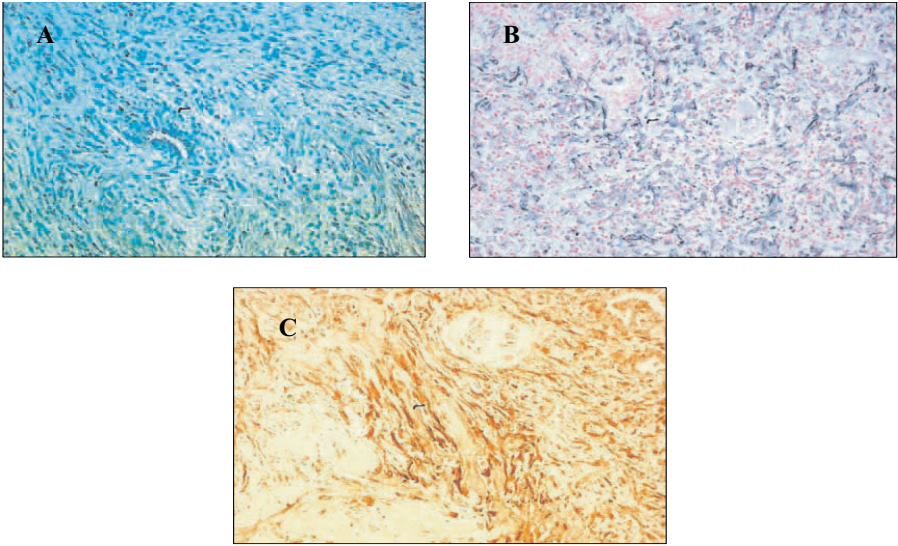


Figure 9.9

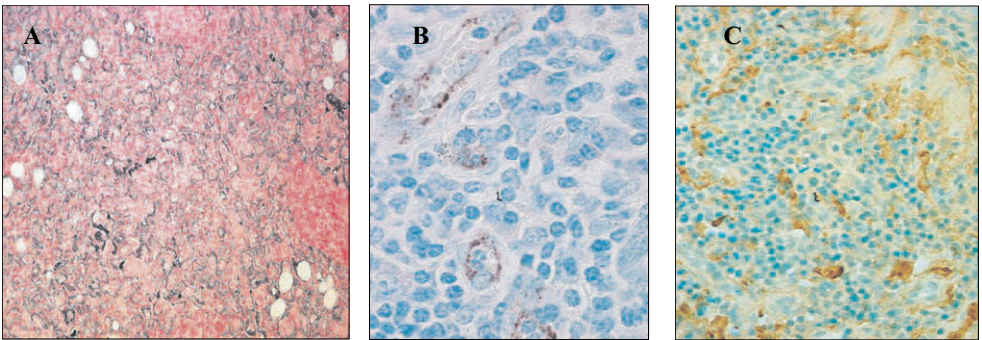


Figure 9.10

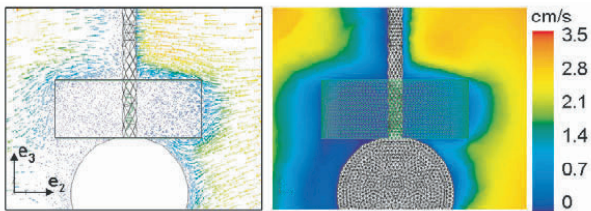


Figure 12.3

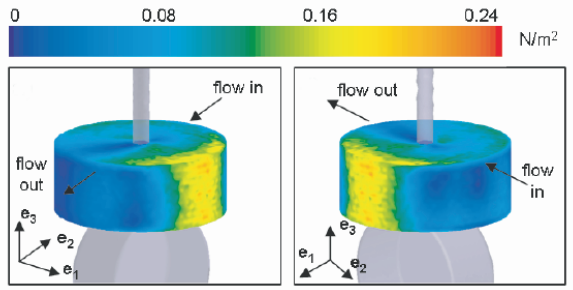


Figure 12.4

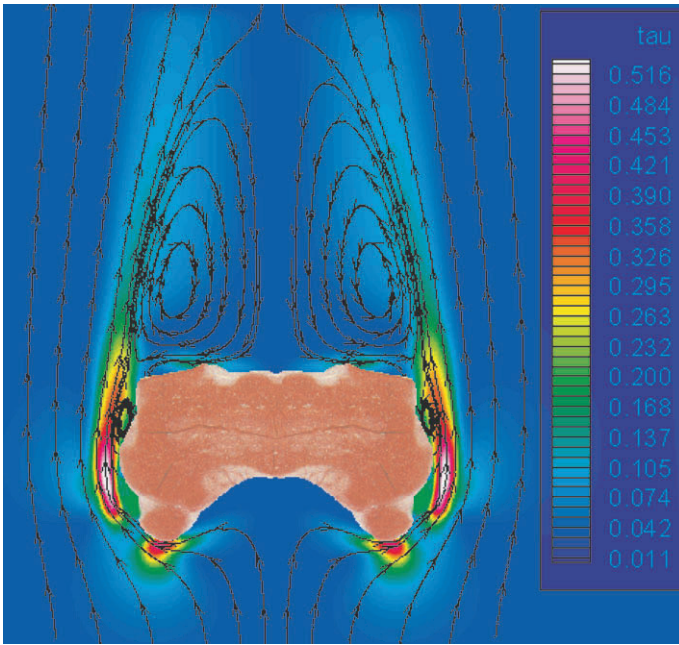


Figure 12.10

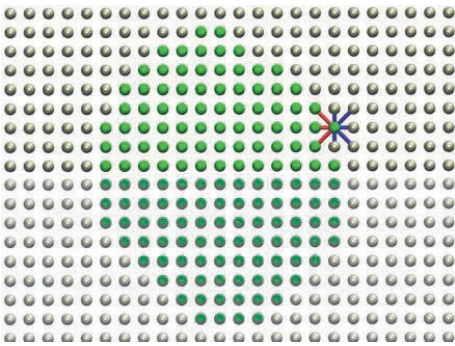


Figure 13.1.

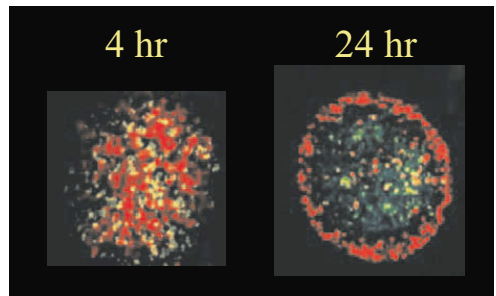


Figure 13.3.

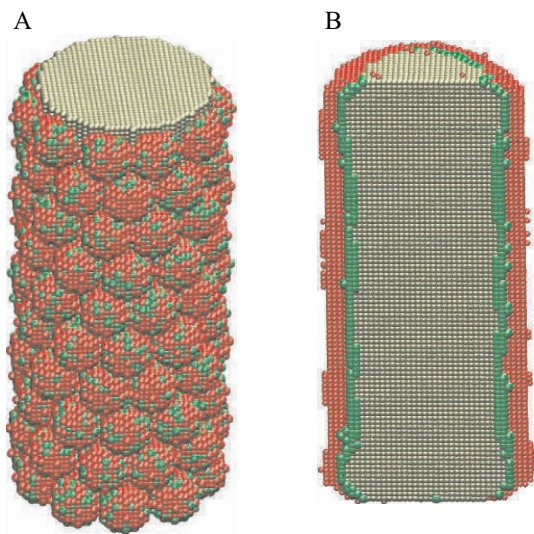


Figure 13.6

Index

A

actin filaments 45-47, 100, 109, 135-137, 142
activation energy 61, 75, 108-109, 181
affine model 101, 103
alginate 202
atomic force microscope 28-29, 123

B

biodegradable 210, 230
biomimetic 263
bioreactor 198, 217-224, 230, 232-235, 237, 239, 242-244, 247, 253, 263
- perfusion 209, 219-221, 231, 239
- rotating 47, 221, 231, 237, 242-244, 247
bone 5, 191, 202, 209, 219-221, 224, 239, 254

C

cardiac 59, 219, 224, 239, 241
cartilage 160, 162, 202-203, 209-210, 219, 221-223, 233, 237, 239, 242-245, 247, 254
Cauchy-Green right deformation tensor 145
cell
- death 180, 183, 190
- organization 119-123, 125-127, 130, 132, 218, 253
- secretion 28, 40
- matrix contacts 121-123, 130-131
cellular mechanics 99
chitosane 210
collagen 22-23, 25, 119, 122, 130, 159-173, 189, 191-192, 221-224, 242, 244, 261-262
contractile force 44, 70, 92, 101, 108
convection 219, 235, 239-240, 248
creep 110-113
cross-bridge cycle 47-48, 50, 57-58, 68, 74, 78
cytoskeleton 18, 92, 121-122, 130, 136-137, 150, 169, 259

D

deformation 57, 64, 103, 108, 123-124, 126, 135-137, 139, 141-145, 147, 148, 152, 155-156, 159, 162-164, 166-167, 169-170, 208, 219, 222
- dynamic loading 103, 221
- gradient 141, 143-145, 152
- large deformations 135, 143

delay convention for stability 155
dextran 202-203, 210
differential adhesion hypothesis (DAH) 252, 255, 259
differentiation 119-121, 130, 180, 183, 191, 198, 209, 217-219, 223, 233, 252, 257
diffusion 203, 206-207, 218, 233-240, 244-246, 248
discrete cell models 252
DNA code 11-13, 16-18, 21, 24
dynamic modulus 103, 222

E

elastic (storage) modulus 103, 96, 104, 107, 165, 166
elasticity 96, 110, 112-113, 123-125, 127, 130, 135-136, 142, 144, 156-157, 161, 163-168, 205
elastin 159, 161, 164, 166, 168
electrical stimulation 223-224
emphysema 160, 168, 170-172
enzymes 27, 170, 180-184, 187, 201
extracellular matrix 179, 183, 198, 221, 237, 252, 254-255, 259

F

FAK 125
fibrosis 72, 161, 168, 170, 184
film theory 234-236, 248
finite elasticity 135-136, 144
First Piola-Kirchhoff stress tensor 142, 147
flow regime 232-233, 248
focal adhesions 93, 95, 110, 122, 131-132, 136-137, 142, 153

G

global minimum 136, 144, 149, 152, 155-156
glycosaminoglycan 162, 221, 242, 244

H

HHM 80, 83, 85
hydrodynamic conditions 231, 242
hydrogel 130, 191, 197, 199-211, 221, 253-254, 261-262

I

information 2, 9-24, 29, 62, 71-72, 135, 180, 231, 247
integrins 97, 122, 137, 142, 169, 189, 191, 255

K

kinases 80, 123, 181
Krogh cylinder model 239

L

Lagrangean strain 141-142, 145-146, 150
lung 4-5, 84, 158-164, 166-173, 184, 190, 221

M

magnetic cytometry 97-98, 104, 106, 120, 123
mass transfer 217, 234-236, 242, 246
mathematical modeling 219, 228-230, 242, 247-248
Maxwell's convention for stability 149
mechanical effects 84, 120, 130
mechanosensing 121-122, 130
membrane fusion 27-28, 37-41
metalloproteinases 180-183
Metropolis algorithm 252, 258
microenvironment 169-170, 192, 217-219, 231, 242, 247
microtubules 18-20, 92-93, 95-97, 99-103, 110, 136
momentum balance 231-234
Monte Carlo 57-58, 62, 71, 111, 129, 252, 254, 257-259
muscle 3, 6, 44-47, 49-57, 59, 62-73, 79-80, 82-84, 96-98, 101-104, 106-108, 119, 137, 158, 162, 170, 191-192, 209, 219, 239, 262
myosin filaments 45-46, 53-57, 62, 68, 71, 80

O

organ printing 261
oxygen 3, 5, 17, 19, 202, 204, 209, 218-219, 232, 237-241, 244-247

P

perfusion 209, 219-221, 231, 239
phosphatases 80, 123, 181
PIP
poly(ethylene glycol) 210
poly(ethylene oxide) 210
poly(methyl methacrylate) 211
poly(vinyl alcohol) 203, 210

polyacrylamide 96, 120, 204, 210
polyglycolic acid 242
polymer dynamics 27-28, 30-37, 40-41
porosome 27-28, 30-37, 40-41
power law 104-106, 108-114, 160, 166
prestress 143-145, 163, 168-169, 171
probabilistic model 52, 54, 69, 71
proliferation 180, 183-184, 190-192, 238, 242, 257
proteoglycans 159-163, 166-167, 191, 221, 242

R

red blood cells 5-6
remodeling 72, 92, 106, 108, 113, 119, 135, 158, 160, 162, 169-172, 192
reorientation 135-137, 139, 141, 151, 153
rheology 109, 112-114, 169
- dynamic rheological behavior 106-107

S

salt leaching 211
sarcomeric model 57
scaffold 8, 198, 203, 205, 208, 210-211, 218-220, 230-231, 233-234, 239, 241-242, 253-254
self-assembly 160, 251-252, 254, 257-258, 260-261
shear stress 101, 179, 219-220, 233-234, 242, 243-244
signal transduction 181
signaling cascade 189
skin cancer 22, 23
stiffness 52, 55, 63-67, 71, 80, 82-83, 95-98, 101-103, 105, 108, 110, 112, 121, 126-128, 130-131, 161, 164-167, 171-172, 192, 221
stochastic model 52, 54, 69-71
stress fibers 110, 121, 126, 135-138, 142-144, 146-147, 149-152
substrate mechanics 120-122, 125, 130, 132

T

tensegrity 106-107, 113, 136
TIMP 183, 185, 187-188
tissue engineering 197-198, 202, 205, 209-210, 217-218, 221, 223, 228, 231, 233, 247, 252-253
- bone 202, 209, 219, 239
- cardiac 219, 224, 241
- cartilage 160, 162, 202-203, 209, 219, 221-223, 233, 237, 239, 242-245, 247, 254
tissue 258-263
- liquidity 259, 261

- organization 127, 253
- surface tension 163, 167, 258, 260

traction microscopy 96, 98, 104

tropomyosin 55-56, 64, 72, 76

troponin 55, 59, 64, 72-73, 75

V

velocity field 233-234, 243-244

viscous (loss) modulus 103

CIP - Каталогизација у публикацији
Народна библиотека Србије, Београд

CIP

606:61(082)

CELL and Tissue Engineering / redactor
Bojana Obradović. - Belgrade : Academic Mind :
#University, #Faculty of Technology and Metallurgy ;
Berlin : Springer, 2011 (Belgrade : Planeta print). -
[10], 275 str. : ilustr. ; 24 cm

Tiraž 300. - Str. [4-5]: Preface / Bojana Obradovic.

Napomene i bibliografske reference uz tekst. -
Bibliografija uz većinu radova. - Registar.

ISBN 978-86-7466-408-7 (AM)

ISBN 978-3-642-21912-2 (Springer)

а) Биотехнологија - Зборници

COBISS.SR-ID 184888844
